Investigation of Marine-derived Bacteria for Bioactive Natural Products

by

Thomas P. Wyche

A dissertation submitted in partial fulfillment
of the requirements for the degree of

Doctor of Philosophy
(Pharmaceutical Sciences)

at the
UNIVERSITY OF WISCONSIN-MADISON
2014

Date of oral examination: May 5, 2014

The dissertation is approved by the following members of the Final Oral Committee:
Tim S. Bugni, Assistant Professor, Pharmaceutical Sciences
Richard P. Hsung, Professor, Pharmaceutical Sciences
Charles T. Lauhon, Associate Professor, Pharmaceutical Sciences
Lingjun Li, Associate Professor, Pharmaceutical Sciences
Michael G. Thomas, Associate Professor, Bacteriology

ABSTRACT

This dissertation focuses on the discovery and development of bioactive natural products derived from marine invertebrate-associated bacteria. Natural products have historically played an important role in the development of therapeutics, but several challenges still hinder natural product drug discovery. Methods for improving the efficiency of natural product discovery are overviewed in Chapter 1.

The discovery of cytotoxic agent thiocoraline and five novel analogs from a marine-derived bacterium (*Verrucosispora* sp. WMMA107) is described in Chapter 2. The analogs provided insight to thiocoraline's structure-activity relationship and biosynthesis.

Thiocoraline was investigated against carcinoid tumors in Chapter 3. Thiocoraline caused a decrease in cell proliferation and activation of the Notch pathway. Formulation of thiocoraline in polymeric micelles allowed for *in vivo* studies, which demonstrated that thiocoraline slowed carcinoid tumor progression.

The discovery of five new antibacterial lipopeptides (peptidolipins B-F) from a marine-derived bacterium (*Nocardia* sp. WMMB215) is described in Chapter 4. The *Nocardia* sp. was selected for investigation based on principal component analysis (PCA) of LCMS data of a group of bacterial strains.

PCA was utilized to select one bacterial strain (*Actinomadura* sp. WMMB499) that produced three classes of novel natural products that are discussed in Chapters 5-7. In Chapter 5, the discovery of four novel natural products (halomadurones A-D), which activate the Nrf2-ARE pathway, is described. Additionally, a method is described for ^{13}C-incorporation of microbial-derived natural products and acquisition of a ^{13}C-^{13}C COSY, which allows for rapid structure elucidation of the carbon backbone.

The discovery of a potent novel antibiotic (ecteinamycin) from strain WMMB499 is described in Chapter 6. The structure of ecteinamycin was determined in part by use of a ^{13}C-^{13}C COSY. Ecteinamycin showed potent bacterial inhibition, especially against *C. difficile*. Initial mechanism of action studies suggested ecteinamycin is an ionophore antibiotic that depolarizes cell membranes.

The discovery of novel antifungal natural products (forazoline A and B) from strain WMMB499 is described in Chapter 7. The structure of forazoline A was rapidly determined in part by acquisition of a ^{13}C-^{13}C COSY and ^{13}C-^{15}N HMQC. Forazoline A demonstrated *in vivo* efficacy against *Candida albicans*. Initial mechanism of action studies suggested forazoline A disrupts fungal cell membranes.

Acknowledgments

First, I would like to thank my advisor, Prof. Tim Bugni, for his guidance, patience, and continual support through the past five years. His passion for science and teaching will stay with me for the rest of my career. I would also like to thank my thesis committee: Prof. Richard Hsung, Prof. Charles Lauhon, Prof. Lingjun Li, and Prof. Michael Thomas for their advice and support.

I would like to thank all members of the Bugni group for all of their support. I would especially like to thank Dr. Yanpeng Hou, who helped me a great deal my first two years of graduate school, as well as Navid Adnani, a friend and colleague, without whom my time in graduate school would not be the same. I also would like to thank Dr. Greg Ellis, Emmanuel Vazquez-Rivera, and Doug Braun for their advice and insight.

The work entailed in this dissertation would not be possible without dozens of other people, many I will not be able to mention. However, there are a few people that cannot be forgotten. Dr. Herb Chen allowed me to work in his lab for several months pursuing work on thiocoraline; while working in the Chen lab, Dr. Renata Jaskula-Sztul taught me a great deal about cancer cell biology. The Analytical Instrumentation Facility in the School of Pharmacy and the National Magnetic Resonance Facility at Madison (NMRFAM) provided great resources for me to learn the ins-and-outs of NMR and mass spectrometry. From those facilities, I would especially like to acknowledge Gary Girdaukus and Dr. Milo Westler. I would also like to thank the UW School of Pharmacy and the NIH for funding.

Finally, I would not be where I am today without the love and support of my family and friends. I especially want to thank my parents, Phil and Ellen, and my brother Steve, for their

relentless support, love, and generosity. Lastly, my time in graduate school would not be the same without my dog Maddux, whose wagging tail brought a smile to my face every day I returned home from lab.

Table of Contents

List of Tables

List of Figures

List of Compounds

Compound - number page no.

Abbreviations

ARE	antioxidant response element
ASW	artificial seawater
ATCC	American type culture collection
c	concentration
C	Celsius
CD	circular dichroism
COSY	correlation spectroscopy
°	degree
DFT	density functional theory
DMSO	dimethyl sulfoxide
DNA	deoxyribonucleic acid
dqf	double-quantum filtered
EC_{50}	effective concentration 50%
ESI-MS	electrospray ionization mass spectrometry
FDLA	1-fluoro-2,4-dinitrophenyl-5-leucine amide
FT-IR	Fourier transform infrared
g	gram
GC	gas chromatrography
h	hour
hPAP	human placental alkaline phosphatase
Hz	hertz
HMBC	heteronuclear multiple bond correlation

HPLC	high-performance liquid chromatography
HRMS	high resolution mass spectrometry
HSQC	heteronuclear single quantum coherence
HSQMBC	heteronuclear single quantum multiple bond correlation
IC_{50}	inhibitory concentration 50%
INADEQUATE	incredible natural abundance double quantum transfer experiment
IR	infrared
L	liter
LB	Luria-Bertani
LC	liquid chromatography
m/z	mass/charge
MHz	megahertz
MIC	minimum inhibitory concentration
MeOH	methanol
μg	microgram
min	minute
mL	milliliter
MMFF	Molecular Mechanics Force Field
MPA	α-methoxy-α-phenylacetyl
MRSA	methicillin-resistant *Staphylococcus aureus*
MS	mass spectrometry
MSSA	methicillin-sensitive *Staphylococcus aureus*
MSTD	multi-standard

MTT	3-[4,5-dimethylthiazol-2-yl]-2,5-diphenyltetrazolium bromide
nm	nanometer
NMR	nuclear magnetic resonance
NOE	nuclear Overhauser enhancement
NP	natural product
Nrf2	nuclear factor E2-related factor
OD	optical density
OR	optical rotation
PCA	principal component analysis
PBS	phosphate buffered saline
PCR	polymerase chain reaction
PK	pharmacokinetic
ppm	parts per million
ROESY	rotating frame Overhauser enhancement spectroscopy
RT	retention time
rt	room temperature
SAR	structure-activity relationship
TOCSY	total correlation spectroscopy
UPLC	ultra-performance liquid chromatrography
UV	ultraviolet
VRE	vancomycin-resistant *Enterococcus*
WMMA	Wisconsin Marine Microbe (collection A)
WMMB	Wisconsin Marine Microbe (collection B)

Chapter 1:

Recent Advancements in Tools for Natural Products Drug Discovery

Portions of this chapter have been previously published as:

Adnani, N.; Ellis, G.A.; Kwan, J.; Wyche, T.P.; Schmidt, E.; Bugni, T.S. Emerging Trends for Stimulating Natural Products Drug Discovery. In *Natural Products Analysis: Instrumentation, Methods, and Applications*; Havlicek, V.; Spizek, J. Eds.; Wiley: Hoboken, NJ, 2014.

1.1. Introduction

Natural product discovery was documented for the first time in 2600 B.C. on a clay tablet in Mesopotamia.[1] Oils from *Cupressus sempervirens* (Cypress) and *Commiphora* species (myrrh), which are still used today, were found to treat coughs, colds, and inflammation.[1] Natural product drug discovery continued to grow, especially in the area of medicinal herbs, with records in China in 1100 B.C., Greece in 100 A.D., and throughout Europe in the Dark and Middle Ages.[1] However, it was not until the early 1970's, more than 4500 years after the first documentation of natural product drug discovery, that drug discovery gained a foothold in the marine environment. With the development of technology to explore the marine environment, such as SCUBA, manned submersibles, and remotely operated vehicles (ROVs), collection of marine samples became more accessible, and as a result, publications of complex, bioactive natural products from the marine environment began to surface.[2]

Despite thousands of years of natural product research, advanced analytical tools for determining the chemical structures of these bioactive natural products did not arise until the twentieth century. The first mass spectrometer was built by J.J. Thomson in the early 1900's.[3] Nuclear magnetic resonance (NMR) was first described in 1938 by Isidor Rabi,[4] and the first NMR spectrometer for liquids and solids was developed in 1946 by Bloch[5] and Purcell.[6] These advancements in analytical technology provided a boost for natural products drug discovery, but even at the advent of marine natural products drug discovery, in the early 1970's, structure elucidation was still a long and cumbersome procedure.

As analytical instrumentation continued to develop through the end of the twentieth century, the discovery of novel natural products began to reach unprecedented levels. This increased discovery led to the 2004 FDA approval of ziconotide (Prialt™), the first drug from the marine environment to be approved in the United States.[7,8] Ziconotide, a peptide originally isolated from a marine cone snail, ushered in the approval of several other marine-derived drugs in subsequent years, including Halaven™ (**1**)[9] and Yondelis™ (**2**).[10]

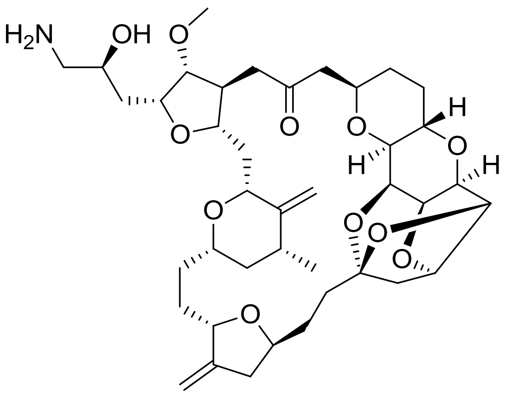

1

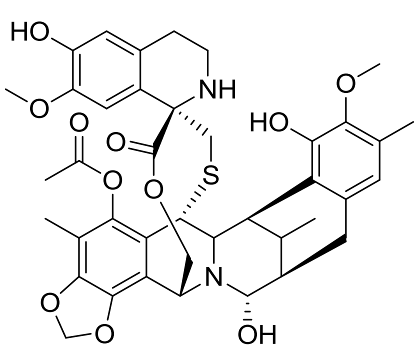

2

Even with the successful approval of several marine-derived drugs, pharmaceutical companies have deemphasized natural products discovery – in many cases eliminating all operations – in recent years.[11] This downsizing of natural product research has been caused in part by the challenges of the "hit-to-lead" process, which continues to be a major bottleneck in the natural product drug discovery timeline. One of the major obstacles in the hit-to-lead process is chemical rediscovery. For example, the rate of rediscovery of known antibiotics in soil-derived actinobacteria is estimated at about 99.5%.[12] In addition to chemical rediscovery, structure elucidation of complex natural products can often be a time-consuming task.

Futhermore, even when a structure is published, it is not always correct: between 1996 and 2010, about 260 natural products were misassigned.[13]

To address these issues, recent methods have been developed, many coinciding with advancements in analytical technology, aimed at minimizing the natural products bottleneck. To address chemical rediscovery, metabolomics methods have been developed to improve strain selection and media optimization, among other parts of the discovery process. Determination of the absolute configuration of natural products, which contain unique, complex chemical scaffolds, is often the last and most challenging step in structure elucidation, and a variety of methods have been developed to determine the absolute configuration of different types of molecules.

1.2. Metabolomics

Traditional methods for natural product drug discovery, in general, have relied on a brute-force method in which large numbers of extracts are examined and purification is guided by bioactivity. However, these methods can be costly and time-consuming. Often times, the bioactivity-guided fractionation, followed by structure elucidation, results in the discovery of a known compound of little interest. More recently, methods have been developed for the dereplication, or identification of known compounds, of natural products. Such dereplication has been accomplished at the strain level using metabolomic analysis of liquid chromatography-mass spectrometry (LCMS) data[14] and for previously identified compounds using several analytical approaches (e.g., UV,[15] NMR,[16,17] mass spectrometry,[18,19] or a combination thereof[20,21]). In this section, the focus will be on metabolomics tools that have been used to rapidly dereplicate known chemistry, leading to the discovery of novel natural products. At the same time, metabolomics has gained a foothold in other areas of natural product research, including understanding biochemical pathways and investigating phytochemicals, and will be discussed briefly in this section. These methods have utilized technological advancements in mass spectrometry (MS) and NMR, as well as various databases and software.

Multivariate analysis, studying more than one outcome variable at a time, has been used in numerous fields in order to better analyze large sets of data, but not until recently has the field of natural products adopted some of these methods to stimulate its research – in particular, drug discovery. Principal Component Analysis (PCA) is one of these statistical tools that has begun to gain a foothold in natural products drug discovery research. A primary example utilizing multivariate analysis in natural products starts with LCMS data, which contains *m/z*-RT pairs as well as an intensity for each *m/z*. Manually analyzing large sets of LCMS data – for example, from bacterial-derived metabolites – can be a challenging and time-consuming procedure. Instead, “buckets” for the *m/z*-RT pairs (with respective intensity) can be generated and compiled into a table, and PCA can be used to reduce the dimensionality of the data through multivariate analysis and plot most of the variance between samples in three dimensions (Figure 1.1). This variance can be visualized in a 2D plot of the principal component (PC) axes. The Scores plot shows the overall variance amoung the samples (for example, extracts from bacterial strains) while the Loadings plots shows the variance of the *m/z*-RT pairs (for example, metabolites produced by the bacterial strains). The distance between two samples in the Scores plot represents the amount of variance between them; if the samples have nearly identical chemistry, the samples will be in close proximity in the Scores plot, but if the samples have very different chemistry, the samples will be located farther apart in the Scores plot (Figure 1.1). Programs for PCA analysis include SIMCA (Umetrics AB, Umeå, Sweden), MATLAB (The MathWorks Inc., Natick, MA, USA), R packages, ProfileAnalysis (Bruker Daltonik GmbH, Bremen, Germany), XCMS,[22] and MZMine2.[23] After the data analysis is complete, several natural product databases (e.g., Antibase,[24] MarinLit,[25] and NAPRALERT[26]) are commercially available to facilitate dereplication.

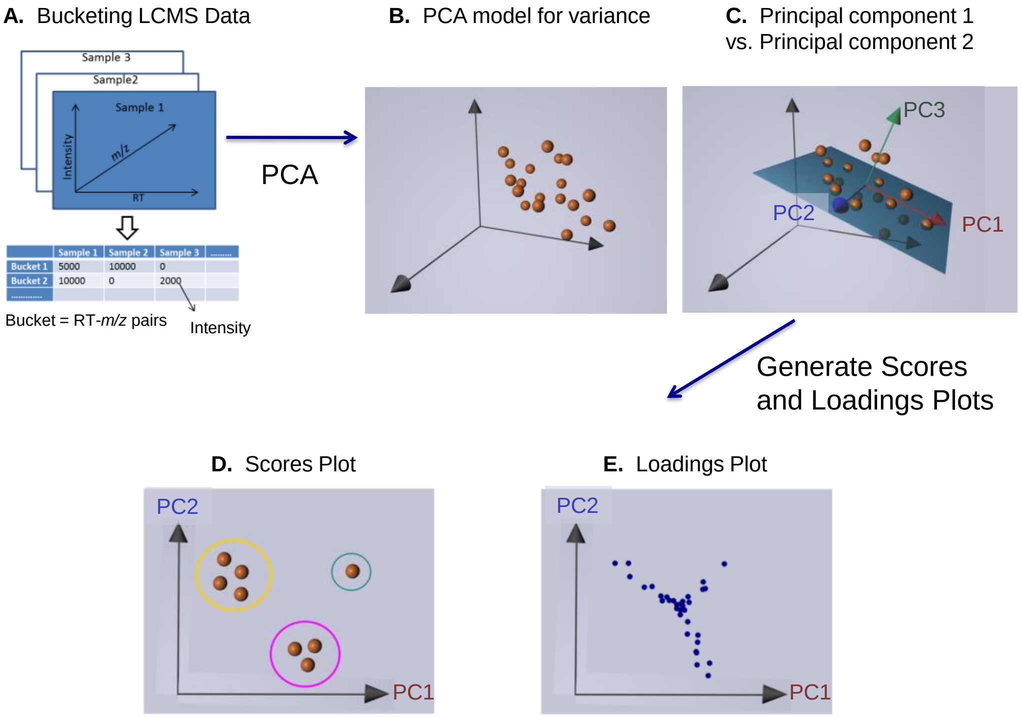

Figure 1.1. PCA analysis. (A) Data from each LC/MS analysis of a sample (representing 1 putative NP-producing strain each) are condensed into buckets by retention time (RT)-mass-to-charge (*m/z*) pairs (roughly corresponding to a separate compound each) and the peak intensity for each bucket specified for each sample. (B) PCA condenses the data and plots the variance. (C) Planes can be constructed in the 3D plot by principal component axes (PC planes). (D) Each plane can generate a Scores Plot, grouping samples (i.e. strains) with similar buckets and intensities together. In this example, three groups can be assigned which should have different chemistry from each other. (E) A Loadings plot is also generated. Each point corresponds to a bucket (i.e. compound). The plot is geometrically related to the Scores plot and depicts those compounds causing the most variance between groups. For example, the sample/strain in the upper-right hand corner of the Scores Plot varies from the other groups, and this can be mostly attributed to this strain containing different intensities/amounts of the compounds in the upper-right hand corner of the Loadings plot as compared to other samples/strains.

Krug *et al.* first demonstrated the utility of LCMS-based metabolomics and PCA in bacteria by examining 9 *Myxococcus* strains in comparison to the *M. xanthus* DK1622 reference.[27] Several known compounds, such as myxalamid A (**3**), as well as several putative new natural products, were rapidly identified using this methology. Krug *et al*. expanded their LCMS-based metabolomics and PCA studies by examining 98 myxobacteria strains, all from the same species (*Myxococcus xanthus*).[28] These strains were collected from 78 locations worldwide, including 20 isolates from the same location. The *M. xanthus* DK1622 strain was used as a reference. LCMS of extracts from these 98 strains, followed by a metabolomics analysis that included PCA, resulted in the identification of 37 putative novel natural products, comprising about 80% of the metabolites produced by *M. xanthus*. Additionally, PCA showed that the chemistry produced by different *M. xanthus* strains from the same location do not produce the exact same chemistry.

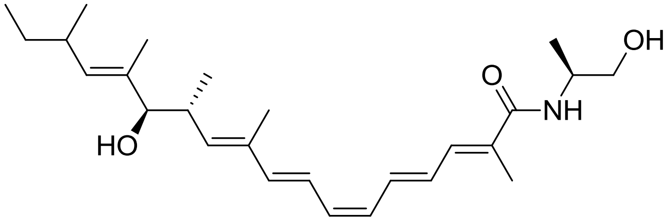

3

Bugni and co-workers investigated LCMS-based metabolomics as a tool for strain selection for developing natural product libraries.[14] In a proof-of-concept study, 47 bacterial strains cultivated from tropical ascidians were analyzed by LCMS and PCA. While some of the strains were identical by morphology and 16S rDNA sequences, the PCA analysis showed that the chemistry produced by the strains was different. The 47 strains formed into 7 groups based on the secondary metabolites produced. In addition to investigating PCA as a method for bacterial strain selection, the work demonstrated that PCA can be useful for rapidly identifying unique chemistry within a group of bacterial strains; often times, this chemistry can be novel. A family of polyenepyrones (**4-6**) were rapidly discovered with this method.

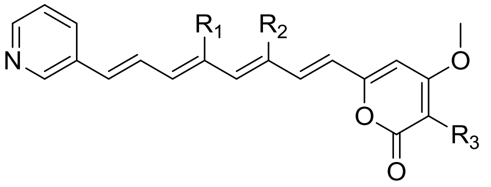

4 $R_1 = CH_3$ $R_2 = H$ $R_3 = CH_3$
5 $R_1 = H$ $R_2 = CH_3$ $R_3 = CH_3$
6 $R_1 = H$ $R_2 = CH_3$ $R_3 = H$

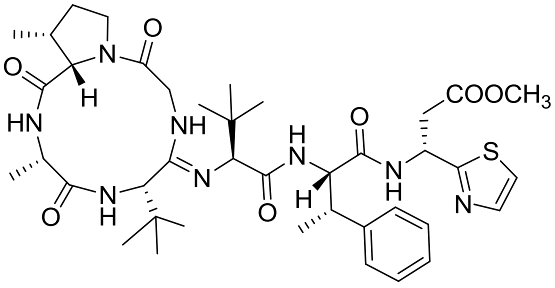

7

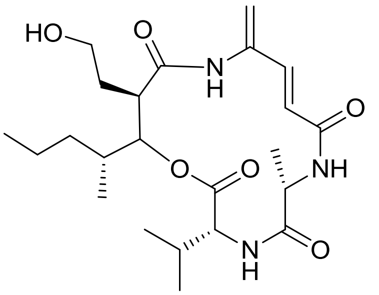

8

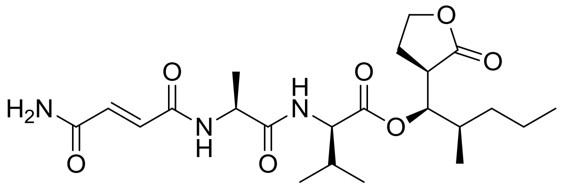

9

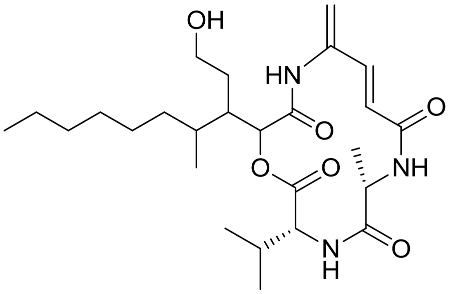

10

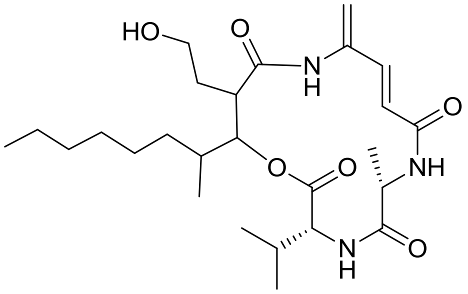

11

PCA has been successfully used for strain selection and the discovery of novel natural products in several other instances. Fifty bacterial extracts were analyzed by LCMS/PCA and led to the selection of one strain (*Streptomyces* sp. WMMB272) that produced the novel natural product bottromycin D (**7**).[29] In another example, 30 termite-associated *Streptomyces* spp. were analyzed by LCMS/PCA and led to the selection of one strain (*Streptomyces* sp. MspM5) that produced novel natural products microtermolides A (**8**) and B (**9**).[30] Interestingly, the compound that caused the variance in PCA was the known antibiotic vinylamycin[31] which, after isolation and structure elucidation, was determined to be different than the original published structure (**10**); after careful analysis of NMR and MS data, the structure was revised (**11**).

In addition to natural products drug discovery, metabolomics tools can be used to investigate biochemical pathways. For example, 2D NMR-based metabolomics were used by Schroeder and co-workers to study metabolites produced by the model organism *C. elegans*.[32] Long-chain ascarosyl ethanolamides (**12-13**) were identified as being produced by *daf-22* mutant worms but not the wild-type. The *daf-22* gene has homology to mammalian 3-ketoacyl-CoA thiolases that may play a role in peroxisomal lipid β-oxidation. Crude extracts of the mutant and wild-type metabolmes were analyzed by dqfCOSY NMR and compared using principal component analysis. Several structural features, including methyl ketones and methyl α-branched fatty acids, were identified by COSY and HMBC NMR, and additional purification confirmed the presence of the ethanolamides. Therefore, differences between extracts were rapidly determined by 2D NMR metabolomics with minimal sample preparation, allowing for biochemical pathways to be studied.

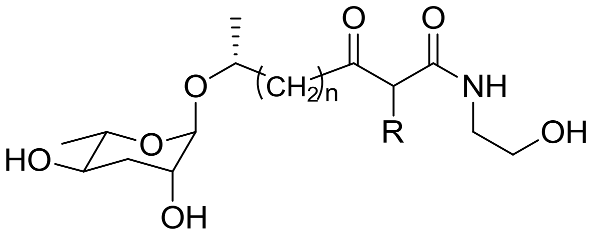

12: R = CH_3, n = 20
13: R = H, n = 22

Schroeder and co-workers continued to demonstrate the use of 2D-NMR metabolomics to better understand biochemical pathways by identifying several metabolites involved with development and behavior in *C. elegans.*[33] Secondary metabolites produced by wild-type *C. elegans* and a signaling-deficient mutant (*daf-22*) were analyzed by dqfCOSY 2D NMR. Minimal processing of the extracts allowed for an efficient method and observance of the entire metabolome; the wild-type and mutant metabolomes were compared using differential analysis by 2D NMR spectroscopy (DANS) and identified the 4 new ascarosides (**14-17**) in only the wild-type spectrum. Thus, 2D NMR metabolomics was used to rapidly identify the ascarosides, which are components of sex pheromones in *C. elegans*.

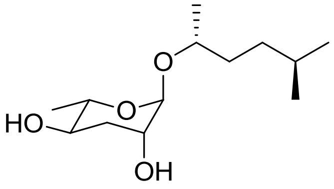

14

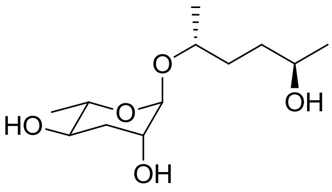

15

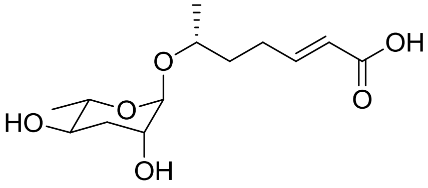

16

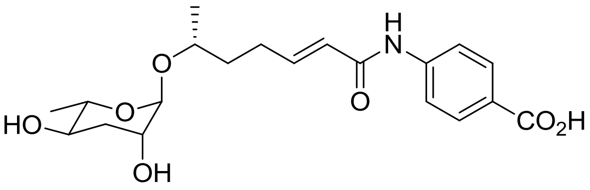

17

Metabolomics tools have also been used to investigate the co-culture of microorganisms. The culture of two different microorganisms together presents the possibility of inducing production of natural products (potentially by gene activation) that are not present in either mono-culture.[34] Two of the major challenges with co-culture are reproducibility and identifying whether there is different chemistry than the mono-cultures. Metabolomics tools have been used to deal with these challenges and evaluate the chemistry produced, as exemplified by the co-culture of two fungi, *Trichophyton rubrum* and *Bionectria ochroleuca*.[35] Extracts from each mono-culture and the co-culture were analyzed by UHPLC-HRMS, and a 2D ion map was constructed to compare the compounds produced in each extract. Five compounds were rapidly identified as being produced exclusively in co-culture, including 4"-hydroxysulfoxy-2,2"-dimethylthielavin P (**18**). Additionally, reproducibility of the production of these compounds in co-culture was confirmed by LCMS-based metabolomics. While there have been only a few examples of LCMS-based metabolomics as a tool for investigating the co-culture of microorganisms, continued interest in the field should spur additional publications in the near future.

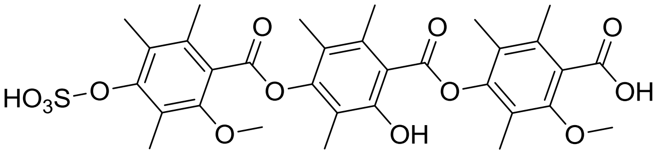

18

The field of phytochemicals, compounds that are produced by plants, has also begun using NMR and MS metabolomics tools. Chemical extracts from plants are composed of large numbers of metabolites, as is the case with most natural product extracts. Purification of these extracts can be time-consuming and challenging, and in some applications, it may not be feasible. For example, the hairy roots of *Phanax ginseng*, a medicinal herb, contain ginseng, the quality of which is determined by the plant’s age.[36] However, a method for determining the plant’s age was lacking. Using ultra-performance liquid chromatography/quadrupole time-of-flight mass spectrometry (UPLC-QTOFMS), a non-targeted metabolomics approach was able to determine certain influential metabolites, or biomarkers, of age in *Phanax ginseng*. The compounds' identities, including several ginsenoside derivatives (**19**-**21**), were confirmed by tandem MS.[36]

Additionally, NMR-based metabolomics can be used in phytochemical research. *Cannabis sativa* has been shown to have therapeutic potential in several areas, but differentiating between variations of the species – which is determined by location, among other factors – can be challenging. NMR metabolomics analysis of ^{1}H NMR spectra of *Cannabis sativa* extracts was used to differentiate variations of the species by the chemistry, such as Δ^9-tetrahydrocannabinolic acid (**22**), produced.[37] ^{1}H NMR spectra of crude extracts are complicated and often times difficult to interpret, but this method allowed rapid identification of chemical differences between the extracts with minimal purification.

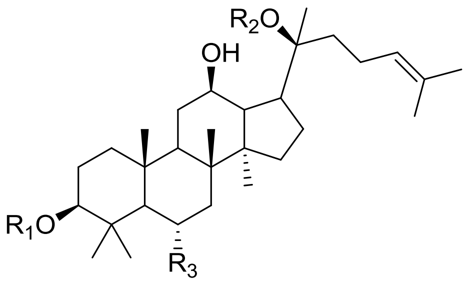

19: R_1 = H, R_2 = Glc, R_3 = OGlc^2-Rha
20: R_1 = Glc^2-Glc, R_2 = Glc, R_3 = H
21: R_1 = H, R_2 = H, R_3 = O-Glc^2-Rha

(Glc: β-D-glucose, Rha: α-L-rhanmose)

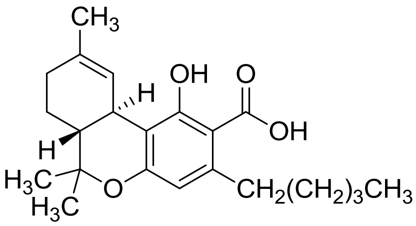

22

Similarly, NMR-based metabolomics enabled Verpoorte and co-workers to study tobacco plants infected with the tobacco mosaic virus (TMV).[38] Tobacco plants infected with TMV provide a defense known as systemic acquired resistance (SAR) to ensure that nearby tobacco leaves are not infected with the virus. For the first time, the metabolites associated with this defense system were characterized. Crude extracts from infected tobacco plants were subjected to multivariate data analysis of 2D *J*-resolved NMR spectra. This analysis rapidly identified 5-caffeoylquinic acid (**23**), an α-linolenic acid analog (**24**), and sesqui- and diterpenoids (**25**, **26**) in infected plants.

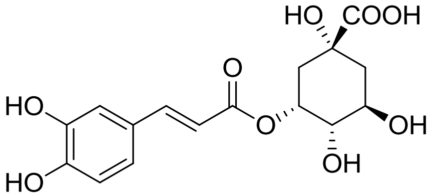

23

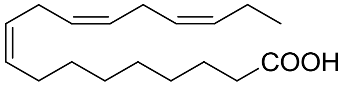

24

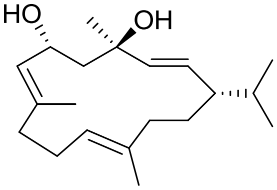

25

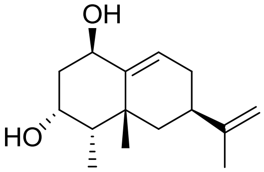

26

Therefore, metabolomics tools have been used to help make the drug discovery process more efficient. At the same time, metabolomics has been used in other areas of natural products research, including investigating biochemical pathways and phytochemicals. However, finding new and therapeutically relevant chemistry in an efficient manner is only part of the natural products bottleneck for drug discovery. Determining the complex structures can be just as – if not more – challenging. Specifically, determining the absolute configuration of these natural products can be the most difficult part of structure elucidation and has led to the development of new methods.

1.3. Absolute Configuration

Traditional methods for determining absolute configuration of natural products, in general, have utilized synthetic derivatization and NMR. Marfey's method[39] (and the updated Advanced Marfey's method[40]) has been a staple for determining the absolute configuration of amino acids, and Mosher's method[41] has been used for many years for the absolute configuration of secondary alcohols. Methodology similar to Mosher's method has now been applied to amines, polyols, and carboxylic acids, and those methods have been reviewed by Riguera and coworkers.[42-45] The *J*-based configurational analysis[46] has been used to solve the relative configuration, and further enabling the determination of the absolute configuration, of many complex natural products. While these methods for determining the absolute configuration are applicable to many natural products, there remain many instances where these methods are unsuccessful or cannot be applied to complex natural products.

To combat the challenge of determining the absolute configuration of natural products, new methods have been recently developed, taking advantage of technological advancements in areas such as mass spectrometry and NMR. These technological advancements have allowed for methods on the microscale. Rychnovsky and co-workers, for example, have developed a handful of methods targeted at diols and polyols. Williams and co-workers have used marine natural products as inspiration for developing new methodology for unique natural product structural features, such as statine units. Following the trend of microscale methodology enabled by technological advancements, density functional theory (DFT) calculations have allowed for the prediction of NMR shifts, which is useful for not only elucidation of the planar structure of natural products but also the absolute configuration. Increased computing power has ushered in *ab initio* calculations as a readily attainable tool for many laboratories.

Combining this increased computing power and advancements in NMR is residual dipolar coupling (RDC), another analytical method for determining the absolute configuration of natural products.

A variety of other methods have been recently developed that fit into this category. Molinski, for example, has developed methods in circular dichroism (CD)[47-52] for determining the absolute configuration of natural products, and Kishi has developed a database for determining the absolute configuration of polyols.[53] Many of these new methods address the shortcomings of previous methods in that they are applicable to a variety of natural product structural types, including complex structures with multiple stereocenters and hindered secondary alcohols. Although each method can be useful for determining the absolute configuration of natural products, often times multiple methods – both classic and newly developed – are necessary. The unique, complex scaffolds of natural products prevent a standard, streamlined approach for determination of absolute configuration. Therefore, a combination of these methods is required in order to complete the final – and often most challenging – step of structure elucidation: absolute configuration.

Rychnovsky and co-workers developed a method using kinetic resolution catalysts for determining the absolute configuration of secondary alcohols and potentially other structural types.[54] Mosher’s method has been the standard technique for determining the absolute configuration of secondary alcohols, but the method is limited to secondary alcohols that are not sterically hindered and in which the ester product is stable and can be purified. Rychnovsky’s kinetic resolution catalyst method, which is similar to Horeau’s method,[55] involves the derivatization of an optically active compound with each enantiomer of a chiral catalyst (Figure 1.2A). A set of empirical rules was developed for each catalyst using the rate of each reaction, which was monitored by ^{1}H NMR, to assign the absolute configuration. Birman's homobenzotetramisole (HBTM),[56] which has good selectivity and can be readily synthesized, was used by Rychnvosky to catalyze the acylation of a secondary alcohol. The *R*-HBTM catalyzed the reaction 13.5 times faster than the *S*-HBTM allowing for the assignment of *S*, based on previously determined empirical rules, for the absolute configuration of the secondary alcohol (**27**). The method is advantageous in that the ester product does not need to be stable, and it can potentially be extended to other molecular types. Thus, Rychnovsky has developed several microscale methods focused on determining the configuration of diols and polyols.

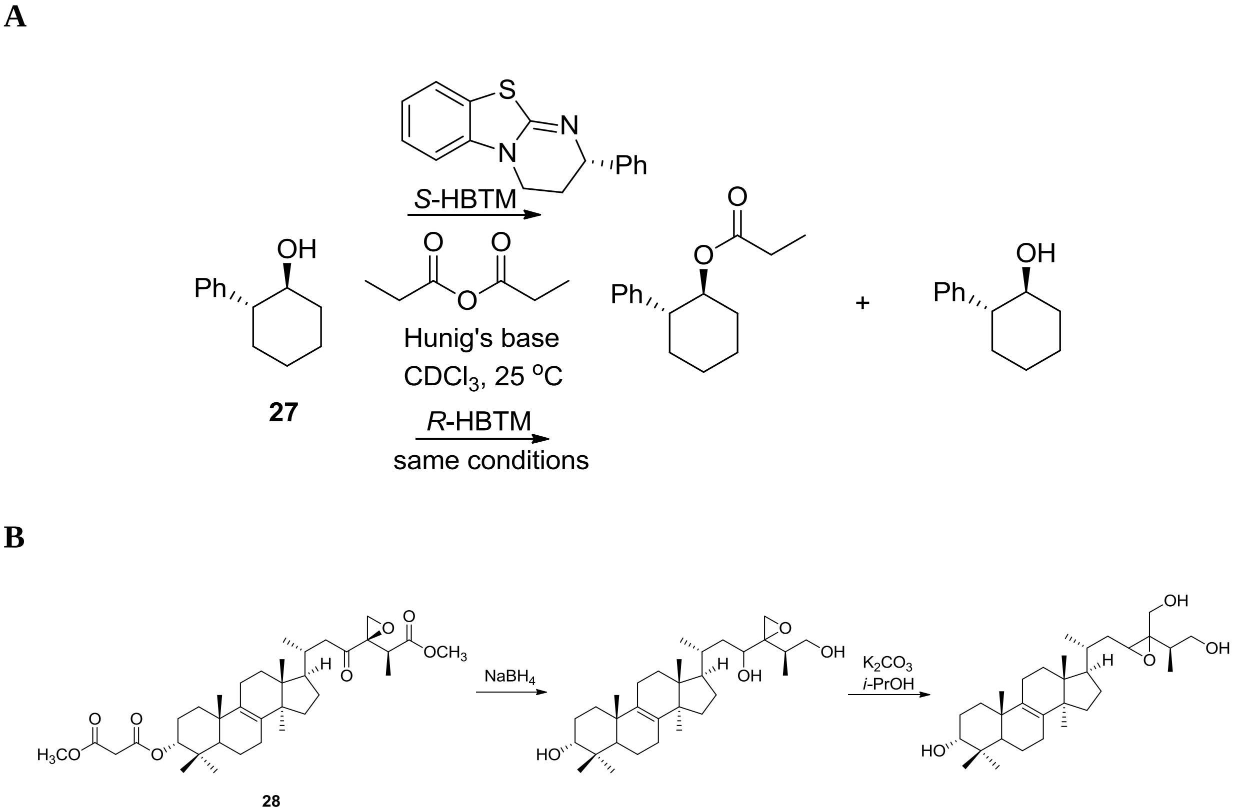

Figure 1.2. (A) Kinetic Resolution Catalysts. The absolute configuration of alcohol **27** was determined comparing the rate of formation of the ester product using *S*-HBTM and *R*-HBTM as catalysts. The rate of reaction was monitored by NMR. (B) Payne Rearrangement. Williams and co-workers demonstrated that the Payne rearrangement could be used to determine the relative configuration of an epoxide in daedalol C (**28**). The absolute configuration was later determined from NOE correlations and $^{3}J_{HH}$ values.

Williams and co-workers have developed several small scale synthetic methods to determine the configuration of natural products. A particularly difficult problem can be the relative configuration around epoxides. Primarily, little data in the literature surrounding heteronuclear coupling constant information precludes the use of methods such as the *J*-based method. To address this challenge in the structure elucidation of daedalol C (**28**), Williams used a Payne rearrangement (Figure 1.2B).[57] The Payne rearrangement, a stereoselective 1,2-epoxide migration, converted a terminal epoxide to a trisubsituted epoxide and allowed for determination of the absolute configuration from NOE correlations and $^3J_{HH}$ values.

Another problem that Williams and co-workers solved was the configuration of statine units, which are γ-amino-β-hydroxy acids.[58] Previous methods relied on hydrolysis and comparison to synthetic standards. Alternatively, conversion to oxazolidine derivatives followed by analysis of vicinal proton-proton coupling constants was used. Statine units have been found in a number of bioactive natural products, have use as bioisosteres, and have recently been identified as a key pharmacophore for inhibiting aspartic proteases such as BACE-1, a potential target to treat neurodegenerative disease caused by the accumulation of αβ-plaques. After demonstrating application of the method to seventy-three known compounds, Williams applied the method for assigning the configuration of γ-amino-β-hydroxy acid containing stictamides A-C (**29-31**).[59] Marfey's method was not successful in determining the absolute configuration of the statine related 4-amino-3-hydroxy-5-phenylpentanoic acid subunit (Ahppa); instead, simple derivatization of stictamide A (**29**) allowed for application of the statine NMR database and determination of the configuration. Microscale methods and methods that rely on non-destructive methods will continue to contribute to successful determination of configuration.

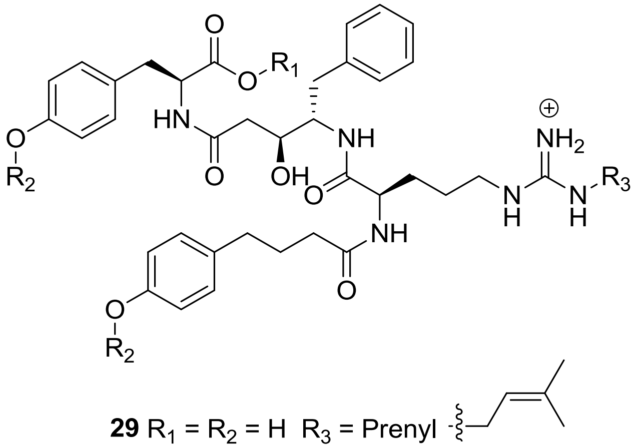

29 $R_1 = R_2 = H$ R_3 = Prenyl

30 $R_1 = R_2 = R_3 = H$

31 R_1 = Me $R_2 = H$ R_3 = Prenyl

While small scale methodology has played an important role in determining the absolute configuration of natural products, these methods cannot be applied to all natural products, and therefore, DFT calculations for calculating theoretical NMR shifts has emerged as a valuable tool for determining the absolute configuration of natural products. DFT methods, first used by Kohn, Hohenberg, and Sham,[60,61] are based in quantum chemistry and can allow for the calculation of theoretical properties of organic compounds. Most relevant to determining absolute configuration is the calculation of NMR shifts and CD spectra; we will focus on NMR in this section. While the calculation of theoretical NMR shifts has been used for many years to aid in elucidation of the planar structure of natural products, the development of methods to analyze this data and improved accuracy for calculations has enabled DFT methods to be used to assign the absolute configuration of natural products. DFT calculations are advantageous in that they do not require any compound, no reference shifts are necessary, and can provide a wealth of information (^{1}H and ^{13}C NMR shifts, coupling constants, NOE correlations) useful for stereochemical determination. However, several disadvantages to DFT methods exist, which will be discussed later in this section, but progress has been made to minimize these disadvantages.

Over the past two decades, advancements in software and methods for DFT calculations have provided an additional tool for natural product chemists to assign absolute configuration. Several software programs, such as Spartan,[62] Gaussian,[63] HyperChem,[64] Gamess,[65] and Jaguar,[66] are available for molecular modeling and DFT calculations. Each of these programs includes various calculation methods, such Hartree-Fock (HF), Molecular Mechanics, Møller-Plesset (MP), and DFT. DFT calculations, for example, are more accurate than HF because DFT takes into account the effects of electron correlations.[67] Each of these methods requires a functional and basis set. Among functionals, the B3LYP has found considerable use.[68-70]

While the magnetic shielding tensors calculated by these methods are generally accurate, several methods have been introduced to improve accuracy. The multi-standard approach (MSTD)[71] references the magnetic shielding tensors to two reference compounds, benzene and methanol, for sp^2-sp and sp^3 hybridized carbon atoms, respectively. Smith and Goodman developed the DP4 probability method,[72] which uses a mathematical algorithm to compare experimental and calculated NMR shifts in order to analyze the calculated NMR shifts and assign a structure that best fits the experimental data. For convenience, the authors have provided an online applet where one can compare calculated NMR shifts to experimentally measured values and analysis of those data by the DP4 probability. This method has been successfully used several times in natural products[68,70,73] since the original publication of the DP4 method in 2010.

While molecular modeling has been used in many instances in natural products chemistry, the recent technology for DFT calculations and methods for analyzing the data enabled absolute configuration determination in laboratories to become more commonplace. A key example in using DFT calculations for assigning absolute configuration is leiodermatolide

(**32**), a potent antimitotic macrolide from the marine sponge *Leiodermatium* sp., which was recently isolated by Paterson *et al.*.[68] Leiodermatolide (**32**) has nine stereocenters, resulting in 32 diastereomers for the macrocyclic core and 4 diastereomers for the δ–lactone. While Paterson *et al*. used NOE experiments and coupling constants to propose the absolute configuration, they used molecular modeling and DFT calculations to confirm this assignment. Molecular modeling using a Monte Carlo search (10,000 steps) and MMFF force field followed by ^{13}C and ^{1}H GIAO NMR shielding tensors at the B3LYP/6-31G(d,p) level resulted in 622 conformers for the macrolactone and 99 conformers for the δ-lactone. The calculated and experimental NMR shifts were then compared with the DP4 probability method; one diastereomer each for both the macrolactone and δ-lactone resulted in >99% probability using the DP4 method. This calculated diastereomer matched the originally assigned absolute configuration, demonstrating the ability of DFT calculations for assigning or confirming absolute configuration. Other molecules with challenging structural features, such as the thiochondrillines (Chapter 2)[70] and artarborol (**33**)[74] have demonstrated that DFT calculations can play an important role in assigning absolute configuration for natural products.

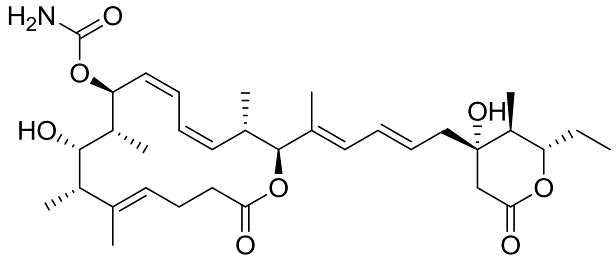

32

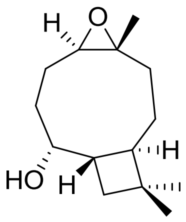

33

Despite the success of DFT calculations for assigning the absolute configuration of natural products, several challenges still remain. DFT calculations are computationally expensive, making it challenging to set up a system capable of such calculations. In addition, DFT calculations require an appropriate geometry optimized molecule, which can be difficult to obtain for some compounds that have conformational flexibility. Finally, DFT calculations for halogens, especially chlorines, have historically resulted in inaccurate calculated chemical shifts. Kaupp *et al.* determined that these accuracies are due to Spin-Orbit (SO) coupling,[75] and several groups have investigated methods to correct for these inaccuracies.[76] Li *et al*. demonstrated that the WC04 functional is effective at calculating ^{13}C NMR shifts of chlorinated organic compounds.[77,78] Therefore, progress has been made to improve the calculated shifts of halogenated organic compounds, as well as other challenges, and therefore, DFT methods have demonstrated recent success for determining the absolute configuration of natural products.

In addition to DFT calculations, residual dipolar coupling (RDC) has emerged as a key analytical tool for determining the absolute configuration of natural products. The basic principles of RDCs rely on the dipolar coupling between two nuclei; this coupling is dependent on the internuclear distance and the angle between the internuclear vector and external magnetic field. In solution, molecular motion is fast and therefore dipolar interactions are averaged to zero. Various alignment media are used to introduce a small amount of order/alignment to the sample. This makes dipolar couplings observable but still small compared to those observed in solid-state NMR. While NOE correlations and *J*-coupling are useful for molecules with many proton-proton interactions, these methods cannot be applied to molecules where protons are not linked in a spin system; instead, RDC analysis is advantageous in that it can determine the absolute configuration of distant stereogenic centers. The pioneering work on RDCs was conducted by Saupe,[79] but for many years RDCs were used much more frequently for proteins rather than small molecules. Mangoni[80] and Yan[81] were among the first to apply RDCs to organic small molecules, and since then, many methods have been developed to improve the accuracy and broaden the scope for RDC calculations.

One of the major areas of work in RDCs has been the development of alignment media for small molecules. Alignment media have been developed in a variety of forms: from liquid crystals[82] to polymer gels.[83,84] However, alignment media were not compatible with organic solvents until 2004 with the development of methods by Luy *et al*.[85,86] The numerous types of alignment media are a result of an attempt to apply RDCs to expand the scope for the use of more natural products. For example, alignment media have been developed to be compatible with DMSO[87,88] for molecules that are only DMSO-soluble. In addition to improvement in alignment media, a number of NMR experiments[89,90] have been developed to improve the accuracy of RDC methodology. Many of the early experiments focused on one bond dipolar coupling $^1D_{CH}$. However, this one bond coupling is limited; consequently Bax *et al*. developed NMR methodology for determining two- and three-bond dipolar coupling ($^2D_{CH}$ and $^3D_{CH}$).[91]

The development of new methods for RDCs has enabled the determination of the absolute configuration of several natural products. The absolute configuration of small molecules, such as archazolide A (**34**),[92] mefloquine HCl (**35**),[93] and sagittamide A (**36**),[94] have been determined by RDC methodology. R*ac*-*eythro*-Mefloquine HCl, the antimarlaria drug Lariam®, was developed in the 1970's, but the absolute configuration of the enantiomers, which cause adverse side effects, had not been irrefutably determined. Using RDC methodology, along with other analytical methods, the absolute configuration was conclusively determined, demonstrating the utility of RDCs. However, much of the work with RDCs in natural products has been completed on known structures in order to confirm the validity of a particular method. Given the recent success for determining the absolute configuration of known natural products using RDCs, these methods should soon become an important tool for determining the absolute configuration of novel structures.

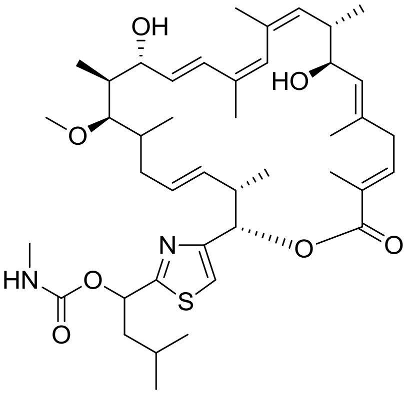

34

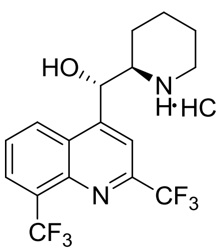

35

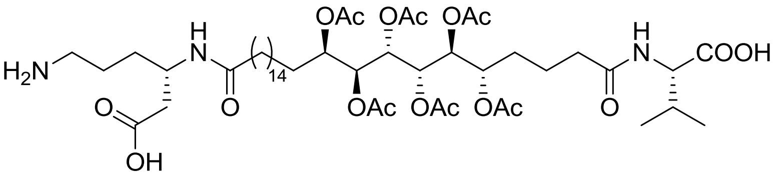

36

Despite the recent success of RDC methodology for determining the absolute configuration of natural products, several challenges still remain. Many examples of RDCs in natural products have been completed on rigid molecules due to the ease of modeling the compound and calculating RDC values. However, RDCs are much more challenging to apply to conformationally flexible natural products.[95] Thiele *et al.* developed methodology for determining the absolute configuration of a conformationally flexible α-methylene-γ-butyrolactone.[95] The method provides two approaches: using a single effective order tensor or using the individual order tensor from a population of conformers. The absolute configuration of the molecule was correctly assigned using this method, but Thiele *et al.* suggest that this method "is not guaranteed to be possible for other compounds, and even wrong assignments are not a priori ruled out." Other methods have been developed to improve computational methods for calculating RDCs,[96] but conformational flexibility still remains a major challenge in the application of RDCs to complex natural products. Despite these challenges, RDC methodology, utilizing the improved analytical technology, has demonstrated its ability to determine the absolute configuration of natural products, and with continued development, can have an even greater impact on the field of natural products.

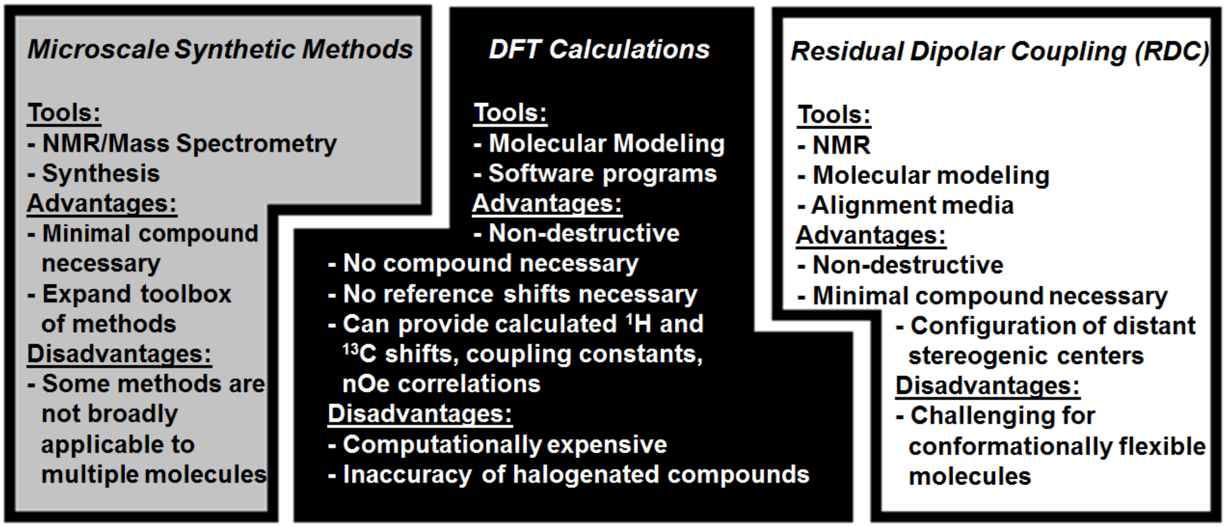

Figure 1.3. Absolute configuration: piecing together the puzzle.

1.4. Summation

Therefore, new methodologies, in both determining absolute configuration and selecting bacterial strains, have emerged to help shorten the natural product drug discovery process. LCMS-based metabolomics has been used as a tool for bacterial strain selection, media optimization, and optimizing other important processes. These methods have led to the discovery of several new compounds with therapeutic potential, such as bottromycin D (**7**). Metabolomics tools have seen expanded use in natural products to better understand biochemical pathways and phytochemicals, both of which could play a role in therapeutics. For determining absolute configuration, small scale synthetic methodology by Rychnovsky, Williams, and others has added to the toolbox of natural product chemists alongside mainstay methods such as Marfey's and Mosher's. DFT calculations have provided a way to predict NMR shifts of natural products that, in comparison to experimental data, can allow for assignment of the absolute configuration. Finally, RDC methodology has provided a means to determine the absolute configuration of all stereocenters in a natural product in "one shot." Despite the power of these methods individually, the combination of the methods increases their impact and ability for assigning absolute configuration (Figure 1.3). Riveira *et al*. demonstrated the use of multiple methods to confirm the absolute configuration of natural product-inspired cyclopenta(*b*)benzofuran synthetic derivatives.[73] Experimental NMR shifts of the synthesized derivative did not match as expected, leading them to determine the absolute configuration of the compound out of four possible diastereomers. Using molecular modeling and DFT calculations, Riveira *et al*. calculated the magnetic shielding tensors for the four diastereomers and used the DP4 probability method to compare the NMR shifts. Additionally, they used the RDC methodology with a biodegradable poly(methyl methacrylate) (PMMA) gel for alignment and analyzed the *singular value decomposition* (SVD) fitting for each diastereomer. Each method predicted the same diastereomer, allowing for greater confidence in assigning the absolute configuration. Therefore, innovative metabolomics methods for bacterial selection and methods for determining the absolute configuration of natural products have emerged to solve some of the most challenging aspects of the drug discovery process, but ultimately, the combination of these methods increases their overall potential. Likewise, the power of these methods, which have been spurred by technological advances, increases when paired with other emerging techniques in metagenomics and proteomics.

1.5. Thesis Overview

This thesis will investigate marine-derived bacteria for bioactive natural products and in doing so, will use several innovative tools for bacterial strain selection and structure elucidation. LCMS-based metabolomics was used for selection of two marine-derived bacterial strains, which in total produced twelve novel bioactive compounds (peptidolipins B-F, halomadurones A-D, forazoline A and B, and ecteinamycin). Additionally, five novel thiocoraline analogs will be described. The structures of these 17 novel natural products were rapidly elucidated using a variety of analytical techniques, including NMR, mass spectrometry, molecular modeling, and DFT calculations. The use of U^{13}C-glucose in the fermentation medium allowed for the production of ^{13}C-labeled halomadurone A, forazoline A, and ecteinamycin. Acquisition of a ^{13}C-^{13}C COSY on these labeled compounds allowed for rapid determination of the carbon backbone. The absolute configuration of the complex novel natural products described herein was determined by a variety of methods, including DFT calculations, advanced Marfey's method, ROE correlations, and NOE distance calculations. Thus, it was the combination of metabolomics methods for strain selection and analytical methods for structure elucidation that enabled the rapid discovery of these novel compounds.

Importantly, the 17 novel natural products demonstrated therapeutic potential in a variety of areas, including antibacterial (peptidolipins B-F and ecteinamycin), cytotoxic (thiocoraline and analogs), anti-neurodegenerative (halomadurones A-D), and antifungal (forazoline A and B) activity. Additional work is necessary for these compounds to continue down the drug development pipeline, but overall, they provide an example for the utility of methods, such as LCMS-based metabolomics and ^{13}C-labeling of bacterial-derived natural products, for improving the efficiency of the hit-to-lead process. Ultimately, the novel structures presented in this dissertation reinforce the potential of the marine environment as a source for therapeutics and therapeutic leads.

1.6. References

1. Cragg, G.M.; Newman, D.J. Biodiversity: A continuing source of novel drug leads. *Pure Appl. Chem*. **2005**, *77*, 7-24.

2. Dias, D.A.; Urban, S.; Roessner, U. A historical overview of natural products in drug discovery. *Metabolites* **2012**, *2*, 303-336.

3. McLafferty, F.W. A century of progress in molecular mass spectrometry. *Annu. Rev. Anal. Chem*. **2011**, *4*, 1-22.

4. Rigden, J.S. Quantum states and precession: the two discoveries of NMR. *Rev. Mod. Phys*. **1986**, *58*, 433-448.

5. Bloch, F.; Hansen, W.W.; Packard, M. Nuclear induction. *Phys. Rev*. **1946**, *69*, 127.

6. Purcell, E.M.; Torrey, H.C.; Pound, R.V. Resonance absorption by nuclar magnetic moments in solid. *Phys. Rev*. **1946**, *69*, 37.

7. McIntosh, M.; Cruz, L.J.; Hunkapiller, M.W.; Gray, W.R.; Olivera, B.M. Isolation and structure of a peptide toxin from the marine snail Conus magus. *Arch. Biochem. Biophys*. **1982**, *218*, 329-334.

8. Molinski, T.F.; Dailsay, D.S.; Lievens, S.L.; Saludes, J.P. Drug development from marine natural products. *Nat. Rev. Drug. Discov*. **2009**, *8*, 69-85.

9. Yu M.J.; Kishi Y.; Littlefield B.A. Discovery of E7389, a fully synthetic macrocyclic ketone analogue of halichondrin B. In Newman D.J.; Kingston, D.G.; Cragg; G.M. *Anticancer agents from natural products*. Washington, DC: Taylor & Francis 2005.

10. Rinehart, K.L. Antitumor compounds from tunicates. *Med. Res. Rev*. **2000**, *20*, 1-27

11. Koehn, F.E.; Carter, G.T. Rediscovering natural products as a source of new drugs. *Discov. Med*. **2005**, *26*, 159-164.

12. Zäehner, H.; Fiedler, H. P. The Need for New Antibiotics. In Fifty Years of Antimicrobials; Hunter, P. A., Darby, G. K., Russel, N. J., Eds.; Cambridge University Press: Cambridge, England, 1995; pp 67-84.

13. Suyama, T.L.; Gerwick, W.H.; McPhail, K.L. Survey of marine natural product structure revisions: a synergy of spectroscopy and chemical analysis. *Bioorg. Med. Chem.* **2011**, *19*, 6675-6701.

14. Hou, Y.; Braun, D.R.; Michel, C.R.; Klassen, J.L.; Adnani, N.; Wyche, T.P.; Bugni, T.S. Microbial strain prioritization using metabolomics tools for the discovery of natural products. *Anal. Chem*. **2012**, *84*, 4277-4283.

15. Larsen, T.O.; Petersen, B. O.; Duus, J. O.; Sorensen, D.; Frisvad, J. C.; Hansen, M. E. Discovery of new natural products by application of X-hitting, a novel algorithm for automated comparison of full UV spectra, combined with structural determination by NMR spectroscopy. *J. Nat. Prod.* **2005**, *68*, 871–874.

16. Williamson, R. T.; Chapin, E.L.; Carr, A.W.; Gilbert, J.R.; Graupner, P.R.; Lewer, P.; McKamey, P.; Carney, J.R.; Gerwick, W.H. New diffusion-edited NMR experiments to expedite the dereplication of known compounds from natural product mixtures. *Org. Lett*. **2000**, *2*, 289-292.

17. Lang, G.; Mayhudin, N.A.; Mitova, M.I.; Sun, L.; van der Sar, S.; Blunt, J.W.; Cole, A. L.; Ellis, G.; Laattsch, H.; Munro, M. H. Evolving trends in the dereplication of natural product extracts: new methodology for rapid, small-scale investigation of natural product extracts. *J. Nat. Prod*. **2008**, *71*, 1595-1599.

18. Fredenhagen, A.; Derrien, C.; Gassmann, E. An MS/MS library on an ion-trap instrument for efficient dereplication of natural products. Different fragmentation patterns for $[M+H]^+$ and $[M+Na]^+$ ions. *J. Nat. Prod.* **2005**, *68*, 385–391.

19. Konishi, Y.; Kiyota, T.; Draghici, C.; Gao, J.-M.; Yeboah, F.; Acoca, S.; Jarussophon, S.; Purisima, E. Molecular formula analysis by an MS/MS/MS technique to expedite dereplication of natural products. *Anal. Chem.* **2007**, *79*, 1187–97.

20. Nielsen, K.F.; Månsson, M.; Rank, C.; Frisvad, J.C.; Larsen, T.O. Dereplication of microbial natural products by LC-DAD-TOFMS. *J. Nat. Prod*. **2011**, *74*, 2338-2348.

21. Motti, C.A.; Freckelton, M.L.; Tapiolas, D.M.; Willis, R.H. FTICR-MS and LC-UV/MS-SPE-NMR applications for the rapid dereplication of a crude extract from the sponge lanthella flabelliformis. *J. Nat. Prod*. **2009**, *72*, 290-294.

22. Smith, C.A.; Want, E.J.; O'Maille, G.; Abagyan, R.; Siuzdak, G. XCMS: processing mass spectrometry data for metabolite profiling using nonlinear peak alignment, matching, and identification. *Anal Chem* **2006**, *78*, 779-787.

23. Pluskal, T.; Castillo, S.; Villar-Briones, A.; Oresic, M. MZmine 2: modular framework for processing, visualizing, and analyzing mass spectrometry-based molecular profile data. *BMC Bioinformatics* **2010**, *11*, 395-405.

24. Laatsch, H. *AntiBase, A Data Base for Rapid Dereplication and Structure Determination of Microbial Natural Products*; Wiley-VCH: Weinheim, Germany, 2012.

25. MarinLit, Marine Literature Database, version 14.3; Marine Chemistry Group, Department of Chemistry, University of Canterbury, Christchurch, New Zealand, 2009.

26. Loub, W.D.; Farnsworth, N.R.; Soejarto, D.D.; Quinn, M.L. NAPRALERT: Computer handling of natural product research data. *J. Chem. Inf. Comput. Sci*. **1985**, *25*, 99-103.

27. Krug, D.; Zurek, G.; Schneider, B.; Garcia, R.; Müller, R. Efficient mining of myxobacterial metabolite profiles enabled by liquid chromatography-electrospray ionisation-time-of-flight mass spectrometry and compound-based principal component analysis. *Anal. Chim. Acta* **2008**, *624*, 97−106.

28. Krug, D.; Zurek, G.; Revermann, O.; Vos, M.; Velicer, G. J.; Müller, R. Discovering the hidden secondary metabolome of Myxococcus xanthus: study of intraspecific diversity. *Appl. Environ. Microbiol*. **2008**, *74*, 3058−3068.

29. Hou, Y.; Tianero, M.D.; Kwan, J.C.; Wyche, T.P.; Michel, C.R.; Ellis, G.A.; Vazquez-Rivera E.; Braun, D.R.; Rose, W.E.; Schmidt, E.W.; Bugni, T.S. Structure and biosynthesis of the antibiotic bottromycin D. *Org. Lett.* **2012**, *14*, 5050-5053.

30. Carr, G.; Poulsen, M.; Klassen, J.L.; Hou, Y.; Wyche, T.P.; Bugni, T.S.; Currie, C.R.; Clardy, J. Microtermolides A and B from termite-associated Streptomyces sp. and structural revision of vinylamycin. *Org. Lett.* **2012**, *14*, 2822-2825.

31. Igarashi, M.; Shida, T.; Sasaki, Y.; Kinoshita, N. Vinlyamycin, a new depsipeptide antibiotic from Streptomyces sp. *J. Antibiot*. **1999**, *52*, 873-879.

32. Izrayelit, Y.; Robinette, S.L.; Bose, N.; von Reuss, S.H.; Schroeder, F.C. 2D NMR-based metabolomics uncovers interaction between conserved biochemical pathways in the model organism Caenorhabditis elegans. *ACS Chem. Biol*. **2013**, *8*, 314-319.

33. Pungaliya, C.; Srinivasan, J.; Fox, B.W.; Malik, R.U.; Ludewig, A.H.; Sternberg, P.W.; Schroeder, F.C. A shortcut to identifying small molecule signal that regulate behavior and development in Caenorhabditis elegans. *Proc Natl Acad Sci USA*. **2009**, *106*, 7708-7713.

34. Onaka, H.; Mori, Y.; Igarashi, Y.; Furumai, T. Mycolic acid-containing bacteria induce natural-product biosynthesis in Streptomyces species. *Appl. Environ. Microbiol*. **2011**, *77*, 400-406.

35. Bertrand, S.; Schumpp, O.; Bohni, N.; Monod, M.; Gindro, K.; Wolfender, J.-L. De novo production of metabolites by fungal co-culture of Trichophyton rubrum and Bionectria ochroleuca. *J. Nat. Prod*. **2013**, *76*, 1157-1165.

36. Kim, N.; Kim, K.; Lee, D.; Shin, Y.-S.; Bang, K.-H.; Cha, S.-W.; Lee, J.W.; Choi, H.-K.; Hwang, B.Y.; Lee, D. Nontargeted metabolomics approach for age differentiation and structure interpretation of age-dependent key constituents in hairy roots of *Panax ginseng*. *J. Nat. Prod*. **2012**, *75*, 1777-1784.

37. Choi, Y.H.; Kim, H.K.; Hazekamp, A.; Erkelens, C.; Lefeber, A.W.; Verpoorte, R. Metabolomic differentiation of *Cannabis sativa* cultivars using ^{1}H NMR spectroscopy and principal component analysis. *J. Nat. Prod*. **2004**, *67*, 953-957.

38. Choi, Y.H.; Kim, H.K.; Linthorst, J.M.; Hollander, J.G.; Lefeber, A.W.; Erkelens, C.; Nuzillard, J.; Verpoorte, R. NMR metabolomics to revisit the tobacco mosaic virus infection in *Nicotiana tabacum* leaves. *J. Nat. Prod*. **2006**, *69*, 742-748.

39. Marfey, P. Determination of D-Amino Acids .2. Use of a Bifunctional Reagent, 1,5-Difluoro-2,4-Dinitrobenzene. *Carlsberg Res. Comm.* **1984**, *49*, 591-596.\

40. Fujii, K.; Ikai, Y.; Mayumi, T.; Oka, H.; Suzuki, M.; Harada, K. A nonempirical method using LC/MS for determination of the absolute configuration of constituent amino acids in a peptide: Elucidation of limitations of Marfey's method and of its separation mechanism. *Anal. Chem.* **1997**, *69*, 3346-3352.

41. Dale, J.A.; Mosher, H.S. Nuclear Magnetic-Resonance Enantiomer Reagents - Configurational Correlations Via Nuclear Magnetic-Resonance Chemical-Shifts of Diastereomeric Mandelate, O-Methylmandelate, and Alpha-Methoxy-Alpha-Trifluoromethylphenylacetate (Mtpa) Esters. *J. Am. Chem. Soc.* **1973**, *95*, 512-519.

42. Louzao, I.; Seco, J.M.; Quinoa, E.; Riguera, R. ^{13}C NMR as a general tool for the assignment of absolute configuration. *Chem. Commun.* **2010**, *46*, 7903-7905.

43. Seco, J.M.; Quinoa, E.; Riguera, R. A practical guide for the assignment of the absolute configuration of alcohols, amines and carboxylic acids by NMR. *Tetrahedron-Asymmetry*, **2001**, *12*, 2915-2925.

44. Seco, J.M.; Quinoa, E.; Riguera, R. The assignment of absolute configuration by NMR. *Chem. Rev.* **2004**, *104*, 17-117.

45. Seco, J.M.; Quinoa, E.; Riguera, R. Assignment of the absolute configuration of polyfunctional compounds by NMR using chiral derivatizing agents. *Chem. Rev.* **2012**, *112*, 4603-4641.

46. Matsumori, N.; Kaneno, D.; Murata, M.; Nakamura, H.; Tachibana, K.. Stereochemical determination of acyclic structures based on carbon-proton spin-coupling constants. A method of configuration analysis for natural products. *J. Org. Chem.* **1999**, *64,* 866-876.

47. Dalisay, D.S.; Quach, T.; Nicholas, G.N.; Molinski, T.F. Amplification of the Cotton effect of a single chromophore through liposomal ordering-stereochemical assignment of plakinic acids I and J. *Angew. Chem.* **2009**, *48*, 4367-4371.

48. Skepper, C.K.; Macmillan, J.B.; Zhou, G.X.; Masuno, M.N.; Molinski, T.F. Chlorocyclopropane macrolides from the marine sponge Phorbas sp. assignment of the configurations of phorbasides A and B by quantitative CD. *J. Am. Chem. Soc.* **2007**, *129*, 4150-4151.

49. Morinaka, B.I.; Skepper, C.K.; Molinski, T.F. Ene-yne tetrahydrofurans from the sponge Xestospongia muta. exploiting a weak CD effect for assignment of configuration. *Org. Lett.* **2007**, *9*, 1975-1978.

50. Lievens, S.C.; Molinski, T.F. Progressive-convergent elucidation of stereochemistry in complex polyols. The absolute configuration of (-)-sagittamide A. *J. Am. Chem. Soc.* **2006**, *128*, 11764-11765.

51. MacMillan, J.B.; Molinski, T.F. Long-range stereo-relay: relative and absolute configuration of 1,n-glycols from circular dichroism of liposomal porphyrin esters. *J. Am. Chem. Soc.* **2004**, *126,* 9944-9945.

52. Macmillan, J.B.; Linington, R.G.; Andersen, R.J.; Molinski, T.F. Stereochemical assignment in acyclic lipids across long distance by circular dichroism: absolute stereochemistry of the aglycone of caminoside A. *Angew. Chem.* **2004** ,*43*, 5946-5951.

53. Higashibayashi, S.; Czechtizky, W.; Kobayashi, Y.; Kishi, Y. Universal NMR databases for contiguous polyols. *J. Am. Chem. Soc.* **2003**, *125,* 14379-14393.

54. Wagner, A.J.; David, J.G.; Rychnovsky, S.D. Determination of absolute configuration using kinetic resolution catalysts. *Org. Lett.* **2011**, *13*, 4470-4473.

55. Horeau, A. Principe et applications d'une nouvelle methode de determination des configurations dite “par dedoublement partiel”. *Tetrahedron Lett.* **1961**, *2*, 506-512.

56. Birman, V.B.; Li, X. Homobenzotetramisole: an effective catalyst for kinetic resolution of aryl-cycloalkanols. *Org. Lett.* **2008**, *10,* 1115-1118.

57. Sorribas, A.; Jimenez, J.I.; Yoshida, W.Y.; Williams, P.G. Daedalols A-C, fungal-derived BACE1 inhibitors. *Bioorgan. Med. Chem.* **2011**, *19,* 6581-6586.

58. Preciado, A.; Williams, P.G. A simple microscale method for determining the relative stereochemistry of statine units. *J. Org. Chem.* **2008**, *73,* 9228-9234.

59. Liang, Z.; Sorribas, A.; Sulzmaier, F.J.; Jimenez, J.I.; Wang, X.; Sauvage, T.; Yoshida, W.Y.; Wang, G.; Ramos, J.W.; Williams, P.G. Stictamides A-C, MMP12 inhibitors containing 4-amino-3-hydroxy-5-phenylpentanoic acid subunits. *J. Org. Chem.* **2011**, *76*, 3635-3643.

60. Hohenberg, P.; Kohn, W. Inhomogenous Electron Gas. *Phys. Rev.* **1964**, *136*, B864.

61. Kohn, W.; Sham, L.J. Self-Consistent Equations Including Exchange and Correlation Effects. *Phys. Rev.* **1965**, *140*, A1133.

62. Deppmeier, B.J.D., A.J.; Hehre, T.S.; Hehre, W.J.; Johnson, J.A.; Klunzinger, P.E.; Leonard, J.M.; Ohlinger, W.S.; Pham, I.N.; Pietro, W.J.; Yu, J. *Spartan 10*, v. 1.0.2; Wavefunction Inc.: Irvine, CA, 2011.

63. Frisch, M.J.T., G.W.; Schlegel, H.B.; Scuseria, G.E.; Robb, M.A.; Cheeseman, J.R.; Scalmani, G.; Barone, V.; Mennucci, B.; Petersson, G. A.; Nakatsuji, H.; Caricato, M.; Li, X.; Hratchian, H. P.; Izmaylov, A. F.; Bloino, J.; Zheng, G.; Sonnenberg, J.L.; Hada, M.; Ehara, M.; Toyota, K.; Fukuda, R.; Hasegawa, J.; Ishida, M.; Nakajima, T.; Honda, Y.; Kitao, O.; Nakai, H.; Vreven, T.; Montgomery, Jr., J.A.; Peralta, J.E.; Ogliaro, F.; Bearpark, M.; Heyd, J. J.; Brothers, E.; Kudin, K. N.; Staroverov, V. N.; Kobayashi, R.; Normand, J.; Raghavachari, K.; Rendell, A.; Burant, J.C.; Iyengar, S.S.; Tomasi, J.; Cossi, M.; Rega, N.; Millam, J.M.; Klene, M.; Knox, J. E.; Cross, J. B.; Bakken, V.; Adamo, C.; Jaramillo, J.; Gomperts, R.; Stratmann, R. E.; Yazyev, O.; Austin, A. J.; Cammi, R.; Pomelli, C.; Ochterski, J.W.; Martin, R. L.; Morokuma, K.; Zakrzewski, V. G.; Voth, G.A.; Salvador, P.; Dannenberg, J. J.; Dapprich, S.; Daniels, A. D.; Farkas, Ö.; Foresman, J.B.; Ortiz, J.V.; Cioslowski, J.; Fox, D.J. *Gaussian 09*, Revision A.1; Gaussian, Inc.: Wallingford, CT, 2009.

64. *HyperChem Professional*, v. 7.51; Hypercube, Inc.: Gainesville, FL, 2002.

65. Schmidt, M.W., Baldridge, K.K., Boatz, J.A., Elbert, S.T., Gordon, M.S., Jensen, J.J., Koseki, S., Matsunaga, N., Nguyen, K.A., Su, S., Windus, T. L., Dupuis, M., and Montgomery, J.A. General atomic and molecular electronic structure system. *Journal of Computational Chemistry*, **1993**, *14*, 1347-1363.

66. *Jaguar*, v. 7.0; Schrodinger, LLC.: New York, NY, 2007.

67. Foresman, J.B.; Frisch, A. *Exploring Chemistry with Electronic Structure Methods*, 2nd ed.; Gaussian, Inc.: Pittsburgh, PA, 1996.

68. Paterson, I.; Dalby, S. M.; Roberts, J. C.; Naylor, G. J.; Guzman, E. A.; Isbrucker, R.; Pitts, T. P.; Linley, P.; Divlianska, D.; Reed, J. K.; Wright, A. E. Leiodermatolide, a potent antimitotic macrolide from the marine sponge Leiodermatium sp. *Angew. Chem.* **2011**, *50*, 3219-3223.

69. Smith, S.G.; Paton, R.S.; Burton, J.W.; Goodman, J.M. Stereostructure assignment of flexible five-membered rings by GIAO ^{13}C NMR calculations: prediction of the stereochemistry of elatenyne. *J. Org. Chem.* **2008**, *73*, 4053-4062.

70. Wyche, T.P.; Hou, Y.; Braun, D.; Cohen, H.C.; Xiong, M.P.; Bugni, T.S. First natural analogs of the cytotoxic thiodepsipeptide thiocoraline A from a marine Verrucosispora sp. *J. Org. Chem.* **2011**, *76*, 6542-6547.

71. Sarotti, A.M.; Pellegrinet, S.C. A multi-standard approach for GIAO ^{13}C NMR calculations. *J. Org. Chem.* **2009**, *74*, 7254-7260.

72. Smith, S.G.; Goodman, J.M. Assigning stereochemistry to single diastereoisomers by GIAO NMR calculation: the DP4 probability. *J. Am. Chem. Soc.* **2010**, *132*, 12946-12959.

73. Riveira, M.J.; Gayathri, C.; Navarro-Vazquez, A.; Tsarevsky, N.V.; Gil, R.R.; Mischne, M.P. Unprecedented stereoselective synthesis of cyclopenta[b]benzofuran derivatives and their characterisation assisted by aligned media NMR and ^{13}C chemical shift ab initio predictions. *Org. Biomol. Chem.* **2011**, *9*, 3170-3175.

74. Fattorusso, C.; Stendardo, E.; Appendino, G.; Fattorusso, E.; Luciano, P.; Romano, A.; Taglialatela-Scafati, O. Artarborol, a nor-caryophyllane sesquiterpene alcohol from Artemisia arborescens. stereostructure assignment through concurrence of NMR data and computational analysis. *Org. Lett.* **2007**, *9*, 2377-2380.

75. Kaupp, M.; Malkina, O.L.; Malkin, V.G. Interpretation of C-13 NMR chemical shifts in halomethyl cations. On the importance of spin-orbit coupling and electron correlation. *Chem. Phys. Lett.* **1997**, *265*, 55-59.

76. Bagno, A.; Rastrelli, F.; Saielli, G. Predicting C-13 NMR spectra by DFT calculations. *J. Phys. Chem. A,* **2003**, *107*, 9964-9973.

77. Li, S. Q.; Zhou, W.F.; Gao, H.X.; Zhou, Z.Q. Density functional theory study of 13C NMR chemical shift of chlorinated compounds. *Magn. Reson. Chem.* **2012**, *50*, 106-113.

78. d'Antuono, P.; Botek, E.; Champagne, B.; Wieme, J.; Reyniers, M.F.; Marin, G.B.; Adriaensens, P.J.; Gelan, J.M. A joined theoretical-experimental investigation on the H-1 and C-13 NMR chemical shifts of chloro-alkenes. *Chem. Phys. Lett.* **2007**, *436*, 388-393.

79. Saupe, A.; Englert, G. High-Resolution Nuclear Magnetic Resonance spectra of orientated molecules. *Phys. Rev. Lett.* **1963**, *11*, 462-464.

80. Mangoni, A.; Esposito, V.; Randazzo, A. Configuration assignment in small organic molecules via residual dipolar couplings. *Chem. Commun.* **2003** ,154-155.

81. Yan, J.; Kline, A.D.; Mo, H.; Shapiro, M.J.; Zartler, E.R. A novel method for the determination of stereochemistry in six-membered chairlike rings using residual dipolar couplings. *J. Org. Chem.* **2003**, *68*, 1786-1795.

82. Thiele, C.M. Simultaneous assignment of all diastereotopic protons in strychnine using RDCs: PELG as alignment medium for organic molecules. *J. Org. Chem.* **2004**, *69*, 7403-7413.

83. Freudenberger, J.C.; Spiteller, P.; Bauer, R.; Kessler, H.; Luy, B. Stretched poly(dimethylsiloxane) gels as NMR alignment media for apolar and weakly polar organic solvents: an ideal tool for measuring RDCs at low molecular concentrations. *J. Am. Chem. Soc.* **2004**, *126*, 14690-14691.

84. Freudenberger, J.C.; Knor, S.; Kobzar, K.; Heckmann, D.; Paululat, T.; Kessler, H.; Luy, B. Stretched poly(vinyl acetate) gels as NMR alignment media for the measurement of residual dipolar couplings in polar organic solvents. *Angew. Chem.* **2005**, *44*, 423-426.

85. Luy, B.; Kobzar, K.; Kessler, H. An easy and scalable method for the partial alignment of organic molecules for measuring residual dipolar couplings. *Angew. Chem.* **2004**, *43*, 1092-1094.

86. Luy, B.; Kobzar, K.; Knor, S.; Furrer, J.; Heckmann, D.; Kessler, H. Orientational properties of stretched polystyrene gels in organic solvents and the suppression of their residual 1H NMR signals. *J. Am. Chem. Soc.* **2005**, *127*, 6459-6465.

87. Haberz, P.; Farjon, J.; Griesinger, C. A DMSO-compatible orienting medium: towards the investigation of the stereochemistry of natural products. *Angew. Chem.* **2005**, *44*, 427-429.

88. Kummerlowe, G.; Auernheimer, J.; Lendlein, A.; Luy, B. Stretched poly(acrylonitrile) as a scalable alignment medium for DMSO. *J. Am. Chem. Soc.* **2007**, *129*, 6080-6081.

89. Yu, B.; van Ingen, H.; Vivekanandan, S.; Rademacher, C.; Norris, S.E.; Freedberg, D. I. More accurate 1J(CH) coupling measurement in the presence of 3J(HH) strong coupling in natural abundance. *J. Magn. Reson.* **2012**, *215*, 10-22.

90. Giraudeau, P.; Montag, T.; Charrier, B.; Thiele, C. M. Fast access to residual dipolar couplings by single-scan 2D NMR in oriented media. *Magn. Reson. Chem.* **2012**, *50*, 553-557.

91. Trigo-Mourino, P.; Navarro-Vazquez, A.; Ying, J.; Gil, R.R.; Bax, A. Structural discrimination in small molecules by accurate measurement of long-range proton-carbon NMR residual dipolar couplings. *Angew. Chem.* **2011**, *50*, 7576-7580.

92. Fares, C.; Hassfeld, J.; Menche, D.; Carlomagno, T. Simultaneous determination of the conformation and relative configuration of archazolide a by using nuclear overhauser effects, J couplings, and residual dipolar couplings. *Angew. Chem.* **2008**, *47*, 3722-3726.

93. Schmidt, M.; Sun, H.; Rogne, P.; Scriba, G.K.; Griesinger, C.; Kuhn, L. T.; Reinscheid, U. M. Determining the absolute configuration of (+)-mefloquine HCl, the side-effect-reducing enantiomer of the antimalaria drug Lariam. *J. Am. Chem. Soc.* **2012**, *134*, 3080-3083.

94. Schuetz, A.; Junker, J.; Leonov, A.; Lange, O.F.; Molinski, T.F.; Griesinger, C. Stereochemistry of sagittamide A from residual dipolar coupling enhanced NMR. *J. Am. Chem. Soc.* **2007**, *129*, 15114-15115.

95. Thiele, C.M.; Schmidts, V.; Bottcher, B.; Louzao, I.; Berger, R.; Maliniak, A.; Stevensson, B. On the treatment of conformational flexibility when using residual dipolar couplings for structure determination. *Angew. Chem.* **2009**, *48*, 6708-6712.

96. Berlin, K.; O'Leary, D.P.; Fushman, D. Improvement and analysis of computational methods for prediction of residual dipolar couplings. *J. Magn. Reson.* **2009**, *201*, 25-33.

Chapter 2:

First Natural Analogs of the Cytotoxic Thiodepsipeptide Thiocoraline from a Marine *Verrucosispora* sp.

Portions of this chapter have been previously published as:

Wyche, T.P., Hou, Y., Braun, D., Cohen, H.C., Xiong, M.P., Bugni, T.S. First Natural Analogs of the Cytotoxic Thiodepsipeptide Thiocoraline from a Marine *Verrucosispora* sp. *J. Org. Chem.* **76**, 6542-6547 (2011).

2.1. Introduction

As discussed in Chapter 1, natural products isolated from terrestrial bacteria have historically contributed to the development of therapeutics.[1] However, the high rate of rediscovery[2] (99.5%) from terrestrial bacteria has necessitated a change in focus for drug discovery sources. The marine environment, which harbors over twenty million microbes,[3] has provided several microbial-derived compounds, such as salinosporamide A,[4] TZT-1027,[5] and ILX-651,[6] that are currently in clinical trials.[7] Among the list of microbial-derived marine natural products with therapeutic relevance is thiocoraline (**37**), a potential candidate for clinical trials.[8] First isolated in 1997 from the mycelia of *Micromonospora marina,*[9,10] thiocoraline (**37**), a bisintercalator, has shown potent cytotoxicity in lung, breast, colon, renal, and melanoma cancer cells,[10-12] and *in vivo* efficacy against human carcinoma xenografts.[8] As a result of the *in vivo* efficacy, thiocoraline has been the subject of several synthetic[13-17] and biosynthetic[18-22] studies. The 3-OH-quinaldic system, which has been proposed to stabilize the complex with DNA,[12] provides thiocoraline (**37**) with a unique mechanism of action and sequence specificity over other bisintercalators, such as echinomycin and triostin A, which contain a quinoxaline ring system.[23] While bisintercalators containing the quinoxaline ring result in DNA damage and inhibition of topoisomerase II, thiocoraline (**37**) inhibits DNA elongation by DNA polymerase α.[11] The synthesis of several thiocoraline analogs,[14-17] has provided insight into the SAR of thiocoraline. Synthetic analogs from the Boger group[14,15] demonstrated that the 3-OH-quinaldic system is a key contributor to the bioactivity of thiocoraline, and the synthesis of *N*-Me-azathiocoraline[17] demonstrated an increase in potency over thiocoraline.

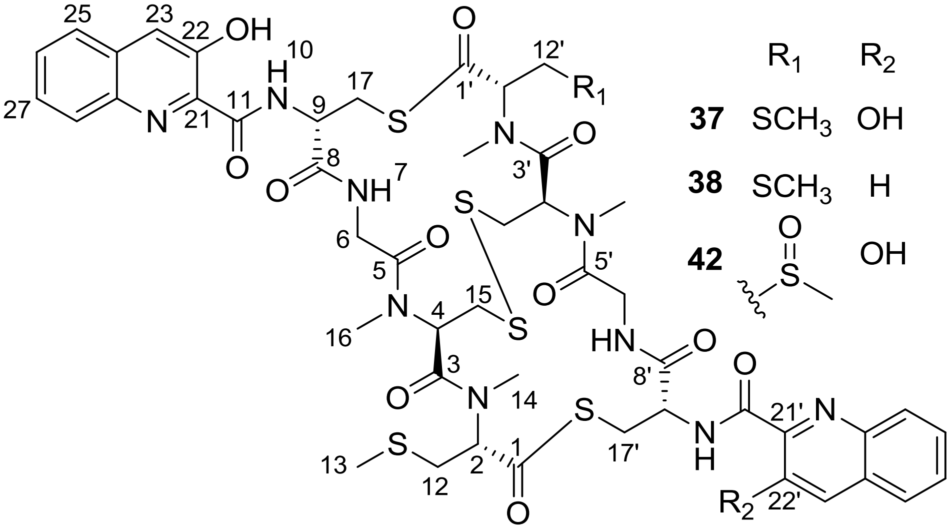

This chapter reports the first isolation of thiocoraline analogs. Five analogs, including three monomers we named the thiochondrillines, were isolated from a marine *Verrucosispora* sp. (Strain WMMA107), cultivated from the sponge *Chondrilla caribensis f. caribensis* (Rützler, Duran & Piantoni, 2007; order Chondrosida, family Chondrillidae). *Verrucosispora* is a gram-positive, spore-forming actinomycete genus,[24] and only three classes of compounds, the antibiotic abyssomicins,[25] proximicins,[26] and gifhornenolones[27] are known to be produced by *Verrucosispora*. Several *Verrucosispora* spp. have previously been cultivated from sponges.[28,29]

No natural products have been previously reported from the sponge *Chondrilla caribensis f. caribensis*, but natural products have been reported from other *Chondrilla* spp.[30,31] This chapter reports the first isolation of thiocoraline from a *Verrucosispora* sp. Spectroscopic methods, supported by mass spectrometry and molecular modeling, led to the elucidation of the structures. Cytotoxicity against the A549 human cancer cell line was determined for each compound. The new analogs provide insight into the biosynthesis of thiocoraline (**37**) and a better understanding of the SAR of thiocoraline (**37**).

2.2. Results and Discussion

Extracts from five *Verrucosispora* strains (WMMA102, WMMA105, WMMA107, WMMA110, and WMMA111) were screened in an antibacterial disc diffusion assay, and despite antibacterial activity from the extracts, no abyssomicins, proximicins, or gifhornenolones were identified. The source of the antibacterial activity was identified as thiocoraline (**37**), produced by strain WMMA107. Five analogs of thiocoraline were also isolated; NMR, MS, and molecular modeling provided the necessary data for determining the structures.

HRMS supported the molecular formula of $C_{48}H_{56}O_{11}N_{10}S_6$ for 22'-deoxythiocoraline (**38**). Integration of the ^1H spectrum and coupling between H-22' and H-23' (Table 2.1) indicated a difference of one phenol group. HMBC and COSY data confirmed that the rest of the aromatic ring moiety remained the same as thiocoraline (**37**). 22'-Deoxythiocoraline (**38**) is assumed to have the same biosynthetic machinery as thiocoraline (**37**) and consequently, will have the same absolute configuration as thiocoraline (**37**). Therefore, the absolute configuration of 22'-deoxythiocoraline (**38**) was assumed to be the same as thiocoraline (**37**) on the basis of biosynthetic precedent,[18] as well as a comparison of NMR shifts of thiocoraline.[9]

Table 2.1. ^{1}H and ^{13}C NMR data for **38**, **42** (600 MHz for ^{1}H, 150 MHz for ^{13}C, $CDCl_3$)

	38		**42**	
Position	δ_C, mult.	δ_H (J in Hz)	δ_C, mult.	δ_H (J in Hz)
1	199.6, C		199.7, C	
2	61.0, CH	5.79, dd (3.7, 11.5)	61.1, CH	5.78, dd (11.4, 4.0)
3	170.1, C		170.4, C	
4	56.6, CH	6.39, m (6.0)	56.0, CH	6.41, br t (6.0)
5	168.3, C		168.9, C	
6a	40.3, CH_2	3.62, m	40.5, CH_2	3.63, m (3.2)
6b		4.59, m (8.0)		4.55, m (6.0)
7-NH		6.77, m (10.5)		6.76, m
8	169.5, C		169.5, C	
9	54.2, CH	4.89, m	54.0, CH	4.91, m
10-NH		8.80, d (5.5)		8.80, d (6.3)
11	169.1, C		169.4, C	
12a	32.1, CH_2	2.84, m	32.1, CH_2	2.82, m
12b		3.23, m (4.1)		3.18, m
13	15.1, CH_3	2.12, s	15.3, CH_3	2.11, s
14	30.7, CH_3	3.04, s	31.0, CH_3	3.07, s
15a	41.6, CH_2	2.79, m	40.6, CH_2	2.88, m
15b		3.54, m		3.42, m
16	30.6, CH_3	2.99, s	30.8, CH_3	2.96, s
17a	30.2, CH_2	3.50, m	30.6, CH_2	3.50, dd (3.1, 14.4)
17b		3.73, m (5.4)		3.68, m (2.8)
21	133.6, C		134.0, C	
22	153.5, C		153.9, C	
22-OH		11.26, s		11.27, s
23	120.5, CH	7.59, s	121.2, CH	7.60, s
24	132.1, C		132.4, C	
25	128.6, CH	7.74, m	131.1, CH	7.76, m
26	127.7, CH	7.48, m	128.1, CH	7.47, m
27	129.7, CH	7.47, m	129.1, CH	7.46, m
28	126.2, CH	7.65, m (7.7)	126.9,CH	7.67, m
29	141.3, C		141.5, C	
1'	199.6, C		198.7, C	
2'	61.0, CH	5.80, dd (3.7, 11.5)	60.1, CH	6.06, dd (3.2, 11.5)
3'	169.8, C		170.3, C	
4'	56.6, CH	6.40, m (6.0)	56.0, CH	6.41, br t (6.0)
5'	168.3, C		168.6, C	
6a'	40.3, CH_2	3.58, m	40.5, CH_2	3.65, m (3.2)
6b'		4.62, m (8.0)		4.58, m (6.0)
7'-NH		6.77, m (10.5)		6.76, m
8'	169.5, C		169.7, C	
9'	54.3, CH	4.95, m	53.6, CH	4.98, m
10'-NH		8.66, d (5.5)		8.76, d (6.3)
11'	170.1, C		169.4, C	
12a'	32.1, CH_2	2.84, m	53.4, CH_2	3.15, m
12b'		3.23, m (4.1)		3.33, dd (3.7, 13.8)
13'	15.1, CH_3	2.12, s	40.2, CH_3	2.64, s
14'	30.7, CH_3	3.09, s	32.1, CH_3	3.21, s
15a'	41.6, CH_2	2.79, m	40.6, CH_2	2.90, m
15b'		3.54, m		3.46, m
16'	30.6, CH_3	2.99, s	30.8, CH_3	3.00, s
17a'	30.2, CH_2	3.50, m	30.6, CH_2	3.55, dd (3.1, 14.4)
17b'		3.73, m (5.4)		3.70, m
21'	148.4, C		134.0, C	
22'	119.2, CH	8.20, d (8.5)	153.9, CH	
22' -OH				11.27, s
23'	138.4, CH	8.27, d (8.5)	121.3, CH	7.59, s
24'	129.5, C		132.4, C	
25'	128.9, CH	7.84, m (8.4)	131.1, CH	7.72, m
26'	128.9, CH	7.59, m	127.9, CH	7.54, m
27'	131.2, CH	7.73, m	129.2, CH	7.52, m
28'	129.7, CH	7.87, m (8.4)	126.9, CH	7.70, m
29'	146.3, C		141.7, C	

Thiochondrilline A (**39**) and B (**40**), isolated in a 3:1 ratio, were inseparable despite extensive HPLC work. HRMS of the mixture helped support the molecular formula of $C_{27}H_{37}O_{7}N_{5}S_{3}$ for both compounds. ^{1}H NMR (Table 2.2) showed that the two compounds had nearly identical chemical shifts with the exception of H-2 and H-14. Extensive 1D and 2D NMR in comparison to thiocoraline (**37**) led to the initial structural assignments of thiochondrilline A (**39**) and B (**40**), though ambiguity remained about the conformation around the amide bond at C-3. The 2D ROESY spectrum showed a correlation between H-2 and H-4 for thiochondrilline B (**40**) and led to the proposal that thiochondrilline A (**39**) was *trans* and thiochondrilline B (**40**) was *cis* around the amide bond at C-3. Therefore, an *ab initio* study was performed in order to determine the conformation around the amide bond at C-3.

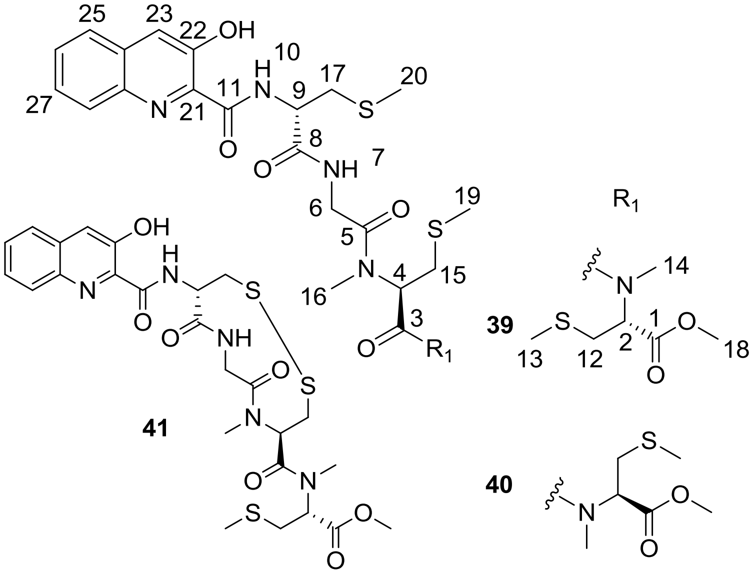

Thiochondrilline A (**39**) and B (**40**) were modeled with molecular modeling software, and *ab initio* calculations were analyzed with the DP4 probability method[32] to determine the conformation around the amide bond at C-3 and the absolute configuration at C-2. Spartan 10[33] was used to find the lowest energy conformer through a Monte Carlo conformer search (MMFF), and Gaussian 09[34] was used for geometry optimization and NMR calculations (B3LYP/6-

31G(d,p)).[35] NMR shifts were referenced to TMS and benzene using the multi-standard (MSTD) approach,[36] and the DP4 probability method[32] was used to compare the calculated NMR shifts for the two proposed structures with the observed chemical shifts. The recently published DP4 method was developed by testing 117 molecules, including 21 natural products that were originally published with misassigned stereochemistry.[32] Calculated and observed chemical shifts for thiochondrilline A (**39**) and B (**40**) were uploaded to the DP4 method online applet (http://www-jmg.ch.cam.ac.uk/tools/nmr/DP4), which uses a mathematical algorithm to quantify the probability of the correct assignment of each structure. The DP4 method calculated a 72.2% probability that thiochondrilline A (**39**) was *trans* around the amide bond at C-5 and a 94.3% probability that thiochondrilline B (**40**) was the *cis* isomer (See Figure A1.9 and A1.10 for all calculated NMR shifts). Absolute configurations at C-2, C-4, and C-9 were assumed to be the same as thiocoraline (**37**), and the configuration at C-2 was confirmed by *ab initio* calculations. Each configuration, *R* and *S*, at C-2 was modeled for thiochondrilline A (**39**) and B (**40**), and the DP4 probability method[32] calculated a 100% probability of the *R* configuration for both thiochondrilline A (**39**) and B (**40**) using calculated ^{1}H and ^{13}C NMR shifts. After determining the conformational relationship between thiochondrilline A (**39**) and B (**40**), variable temperature ^{1}H NMR experiments (500 MHz, $CDCl_3$) at 5 °C and 45 °C resulted in no change, indicating that the compounds were stable. The insolubility of thiochondrilline A (**39**) and B (**40**) in most solvents prevented variable temperature experiments at higher temperatures.

HRMS supported the molecular formula of $C_{25}H_{31}O_7N_5S_3$ for thiochondrilline C (**41**). ^{1}H NMR shifts (Table 2.2) closely resembled thiochondrilline A (**39**) and B (**40**) but with the absence of two *S*-methyl groups. The *S*-methyl at C-13 was present as evidenced by an HMBC correlation from H-13 to C-12. The absence of two *S*-methyl groups led to the initial proposal of

Table 2.2. ^{1}H and ^{13}C NMR data for **39-41** (600 MHz for ^{1}H, 150 MHz for ^{13}C, $CDCl_3$)

	39			**40**			**41**		
Position	δ_C, mult.	δ_H (J in Hz)	HMBC	δ_C, mult.	δ_H (J in Hz)	HMBC	δ_C, mult.	δ_H (J in Hz)	HMBC
1	169.8, C			169.8, C			170.1, C		
2	56.4, CH	5.11, dd (4.4, 11.5)		58.8, CH	4.76, dd (4.0, 10.5)		58.0, CH	5.04, dd (4.4, 11.2)	
3	169.7, C			169.6, C			169.0, C		
4	52.1, CH	5.62, m	3, 16	51.7, CH	5.63, m	3, 15, 16	58.1, CH	5.13, dd (3.5, 10.0)	3
5	167.9, C			167.9, C			168.8, C		
6a	41.5, CH_2	4.16, m (4.3)	5	41.3, CH_2	4.06, m (3.7)	5	44.6, CH_2	5.20 , dd (10.3, 15.6)	5, 8
6b		4.20, m (4.3)			4.12, m (3.7)			3.79, dd (2.6, 15.6)	
7-NH		7.27, t (2.7)			7.20, m			7.01, br d (9.7)	
8	169.4, C			169.4, C			169.2, C		
9	52.1, CH	4.84, m (7.7)	8, 11	52.2, CH	4.81, m (7.3)	8, 11	54.4, CH	4.80, br t (9.0)	
10-NH		9.09, d (8.1)			9.07, d (8.1)			8.86, d (8.5)	
11	169.2, C			169.2, C			168.1, C		
12a	32.6, CH_2	3.08, m	2, 13	33.3, CH_2	2.99, m		33.9, CH_2	2.92, dd (5.0, 9.4)	2, 13
12b		2.88, m			2.84, m			3.12 , m	
13	15.2, CH_3	2.10, s	12	15.4, CH_3	2.05, s	12	15.9, CH_3	2.12, s	12
14	32.5, CH_3	2.93, s	2, 3	29.3, CH_3	2.78, s	2, 3	33.2, CH_3	3.20, s	2, 3
15a	33.2, CH_2	2.91, m	19	33.2, CH_2	2.91, m	19	43.2, CH_2	4.00, br s	
15b		2.83, m			2.83, m			2.70, br s	
16	29.1, CH_3	2.87, s	4, 5	29.0, CH_3	2.80 ,s	4, 5	30.7, CH_3	2.86, s	5, 4
17a	36.2, CH_2	3.08, m	8, 20	36.2, CH_2	3.08, m	8, 20	43.6. CH_2	3.66, dd (9.7, 14.4)	8, 9
17b		3.04, m			3.03, m			3.13, m	
18	52.7, CH_3	3.72, s	1	52.7, CH_3	3.71, s	1	52.9, CH_3	3.75, s	1
19	15.6, CH_3	2.08, s	15	15.8, CH_3	2.14, s	15			
20	15.9, CH_3	2.23, s	17	15.9, CH_3	2.22, s	17			
21	134.0, C			134.0, C			134.0, C		
22	153.5, C			153.5, C			153.7, C		
22-OH		11.55, s	21, 23		11.53, s	21, 23		11.31, s	21, 23
23	120.5, CH	7.64, s	21, 22, 28, 29	120.5, CH	7.64, s	21, 22, 28, 29	120.9, CH	7.64, s	21, 22, 28, 29
24	132.1, C			132.1, C			132.4, C		
25	126.1, CH	7.70, m	27	126.1, CH	7.70, m	27	126.6, CH	7.70, d (7.9)	24, 27
26	128.7, CH	7.52, m	28	128.7, CH	7.52, m	28	129.1, CH	7.54 , m	28, 29
27	127.3, CH	7.54, m	25	127.3, CH	7.54, m	25	129.1, CH	7.56, m	24, 25
28	129.7, CH	8.01, d (8.3)	26	129.7, CH	8.01, d (8.3)	26	129.8, CH	7.97, d (8.2)	26, 29
29	141.4, C			141.4, C			141.7, C		

a disulfide bond linking the two side chains. Without direct evidence of HMBC correlations across the disulfide bond, several measures were taken to confirm the proposed structure. With the possibility that (+)ESI MS created the disulfide bond by the oxidation of two thiol groups, (-)ESI was conducted (608.1274 *m/z*) and supported the same molecular formula as calculated from (+)ESI MS. Thiochondrilline C (**41**) and the possible thiol analog were optimized with Spartan 10 and Gaussian 09, and *ab initio* NMR calculations were compared to observed chemical shifts. Using the DP4 probability method,[32] a comparison of all ^{13}C chemical shifts for thiochondrilline C (**41**) and the thiol analog produced a 97.5% probability of the correct structure being thiochondrilline C (**41**) rather than the thiol analog. An examination of the calculated chemical shifts at C-15 and C-17 especially supported the assignment of thiochondrilline C (**41**) (See Figure A1.11). The absolute configurations of thiochondrilline C (**41**) at C-2, C-4, and C-9 were assumed to be the same as thiocoraline (**37**) based on biosynthetic precedent.[18]

HRMS and isotopic distribution[37] supported the molecular formula of $C_{48}H_{56}O_{13}N_{10}S_6$ for 12'-sulfoxythiocoraline (**42**), one more oxygen atom than thiocoraline (**37**). H-13' (2.64 ppm), H-12' (3.13, 3.33 ppm), and H-2' (6.06 ppm) (Table 2.1) indicated the existence of an *S*-methyl-containing sulfoxide. The COSY and HMBC spectra confirmed the structural difference between thiocoraline (**37**) and 12'-sulfoxythiocoraline (**42**). The absolute configuration of 12'-sulfoxythiocoraline (**41**) was assumed to be the same as thiocoraline (**37**) due to the near identical ^{1}H and ^{13}C shifts. Currently, we cannot conclusively state whether 12'-sulfoxythiocoraline (**42**) originated as a natural product or an oxidized product of thiocoraline (**37**) as a result of our isolation process.

Table 2.3. A549 Cancer Cell Line Cytotoxicity Data

Compound	EC_{50}, µM
37	0.0095
38	0.13
39&40	>10
41	2.86
42	1.26

Each of the five analogs was screened against the A549 human cancer cell line in comparison to thiocoraline (**37**) (Table 2.3, Figure 2.1), and the cytoxicity of 22'-deoxythiocoraline (**38**) helped provide a better understanding of the SAR of thiocoraline (**37**).

Figure 2.1. A549 Cancer Cell Line Cytotoxicity

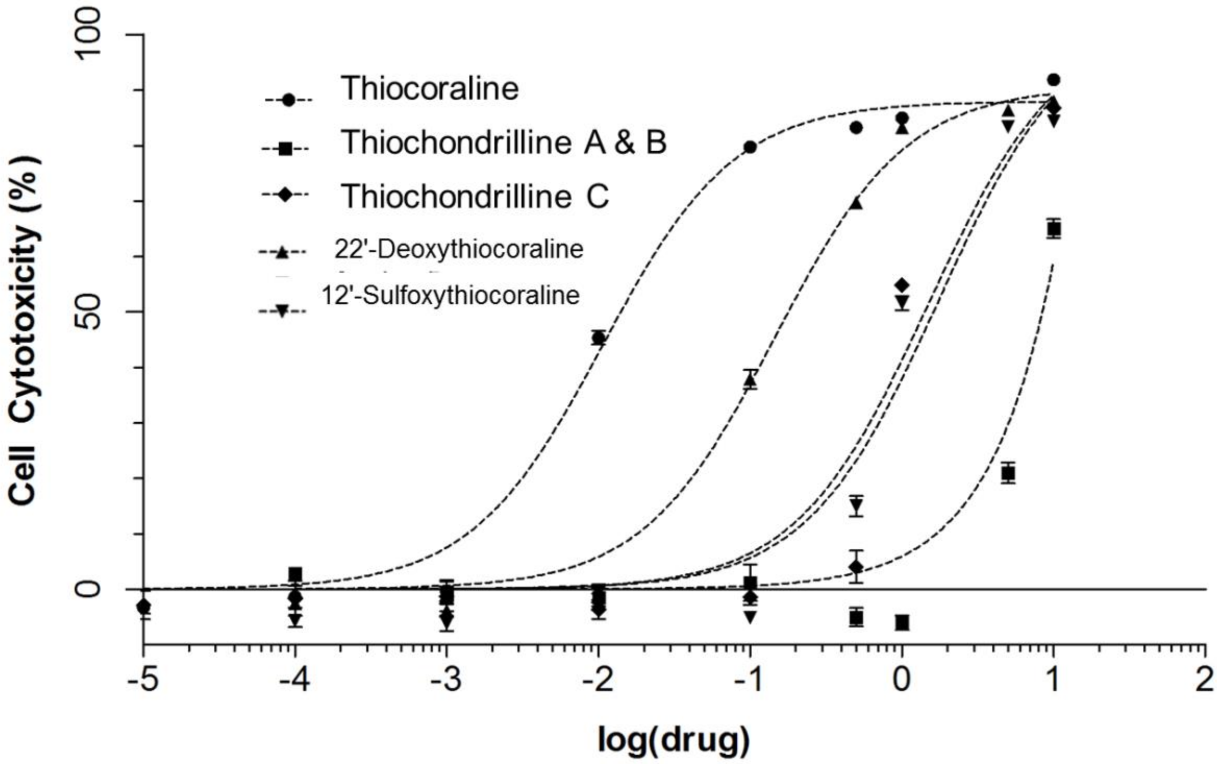

Related analogs synthesized by the Boger group[14-15] demonstrated that the absence of both phenol groups reduced the compound's cytotoxicity. [*N*-(2-quinoline carboxyl)-D-Cys-Gly-*N*Me-L-Cys-*N*Me-L-Cys-(Me)]$_2$ (cysteine thiol) dilactone), identical to thiocoraline (**37**) except the absence of both phenol groups, was one hundred times less potent than thiocoraline (**37**). 22'-deoxythiocoraline (**38**) was fourteen times less potent than thiocoraline (**37**) against the A549 cell line. Hence, the potency of 22'-deoxythiocoraline (**38**) lies between the potency of thiocoraline (**37**) and Boger's synthetic analog, emphasizing the importance of each phenol group to thiocoraline's activity. The 3-OH-quinaldic system provides a tricyclic hydrogen-bonded conformation that is proposed to stabilize the complex with DNA.[12] One phenol group, in the case of 22'-deoxythiocoraline (**38**), helps stabilize the complex with DNA, though to a lesser extent than the two phenol groups in thiocoraline (**37**). Consequently, 22'-

deoxythiocoraline (**38**) reinforces the role of the phenol group in interactions with DNA and effects on the potency.

22'-Deoxythiocoraline (**38**), thiochondrilline A (**39**), and thiochondrilline B (**40**) also provided insight into the biosynthetic pathway of thiocoraline. 22'-Deoxythiocoraline (**38**) suggested that the putative loading module, consisting of the TioJ and TioO proteins, can be promiscuous with respect to the starter unit. In the biosynthesis of thiocoraline (**37**), TioJ and TioO are proposed to load 3-OH-quinaldic acid as the starter unit.[18] However, the absence of one phenol group in 22'-deoxythiocoraline (**38**) suggested that TioJ and TioO also have the ability to load quinaldic acid as the starter unit.

As open chain monomers of thiocoraline (**37**), thiochondrilline A (**39**) and B (**40**) provided insight into the mechanisms by which thiocoraline (**37**) is cyclized. Thiochondrilline A (**39**) and B (**40**) revealed that cyclization of thiocoraline most likely occurs before methylation of the thiol groups. In thiocoraline, only the C-12 thiol groups are methylated. However, all three thiol groups are methylated in thiochondrilline A (**39**) and B (**40**), suggesting that the putative methylation protein, TioN,[38] has the ability to methylate multiple thiol groups and potentially carboxylic acids. Alternatively, if methylation were to occur prior, the expected product would contain C-15 *S*-Me Cys and not a disulfide bridge. Hence, cyclization most likely occurs before methylation in the biosynthesis of thiocoraline (**37**).

2.3. Conclusion

22'-deoxythiocoraline (**38**) reinforced the importance of both phenol groups in contributing to the bioactivity of thiocoraline (**37**) and, along with thiochondrilline A (**39**) and B (**40**), provided additional insight into the biosynthesis of thiocoraline (**37**). This study also demonstrated the utility of the DP4 probability method for analyzing *ab initio* NMR calculations to solve stereochemical problems in an efficient manner.

2.4. Materials and Methods

General Experimental Procedures

Optical rotations were measured on a Perkin–Elmer 241 Polarimeter. UV spectra were recorded on an Aminco/OLIS UV-Vis Spectrophotometer. IR spectra were measured with a Bruker Equinox 55/S FT–IR Spectrophotometer. NMR spectra were obtained in $CDCl_3$ with a Bruker Avance 600 MHz spectrometer equipped with a 1.7 mm $^{1}H\{^{13}C/^{15}N\}$ cryoprobe and a Bruker Avance 500 MHz spectrometer equipped with a $^{13}C/^{15}N\{^{1}H\}$ cryoprobe. HRMS data were acquired with a Bruker MaXis 4G QTOF mass spectrometer. RP HPLC was performed using a Shimadzu Prominence HPLC system and a Phenomenex Luna C18 column (250 × 10 mm, 5 µm).

Biological Material. Sponge specimens were collected on February 10, 2010, in the Florida Keys (24° 39’ 17.90”, 81° 17’ 51.09”). A voucher specimen for *Chondrilla caribensis f. caribensis* (FLK-10-4-24), identified by Mary Kay Harper-Ireland (University of Utah), is housed at the University of Wisconsin-Madison. For cultivation, a sample of sponge (1 cm^3) was rinsed with sterile seawater, macerated using a sterile pestle in a micro-centrifuge tube, and dilutions were made in sterile seawater, with vortexing between steps to separate bacteria from heavier tissues. Dilutions were separately plated on two distinct media that have yielded diverse actinomycetes from both marine sponges and sediment: M1 and M4.[39] M1 was made using artificial seawater. Both were supplemented with 50 µg/mL cycloheximide and 25 µg/mL nalidixic acid. Plates were incubated at 31 °C for 28 days.

Fermentation, Extraction, and Isolation. Strain WMMA107 was fermented in 25 × 150 mm culture tubes (4 × 10 mL) in medium ASW-A (20g soluble starch, 10g glucose, 10g peptone, 5g yeast extract, 5g $CaCO_3$ per liter of artificial seawater) for one week at 28 °C. 250 mL baffled flasks (16 × 50 mL) were inoculated with 2 mL from the culture tube and shaken at 200 RPM at 28 °C for seven days. 2 L flasks (32 × 500 mL) containing medium ASW-A with Diaion HP20 (4% by weight) were inoculated with 25 mL and shaken at 200 RPM at 28 °C for seven days. Filtered HP20 was washed with water and extracted with acetone. The acetone extract (35 g) was subjected to a liquid-liquid partitioning using 30% aqueous methanol and chloroform (1:1). The chloroform soluble partition (10 g) was subjected to silica gel (SiO_2) column chromatography (350 g, 40-60 µm particle size) with hexanes and ethyl acetate (0-100%). Fractions containing **37-42** were combined and subjected to RP HPLC (10-100% CH_3CN-H_2O, 30 min) using a Phenomenex Luna C18 column (250 × 10 mm, 5 µm), yielding **41** (2.0 mg, RT 23.2 min), **42** (1.6 mg, RT 23.6 min), **39** and **40** (1.5mg, RT 24.2 min), **38** (0.5 mg, RT 25.6 min), and **37** (80 mg, RT 27.5 min), respectively. Fraction 8, containing thiochondrilline A (**39**) and B (**40**), was subjected to 11 isocratic and gradient methods of HPLC separation testing different solvents and solvent compositions. Insufficient separation was achieved. The inability to separate amide rotamers chromatographically is consistent with past literature,[40,41] though amide rotamers have been chromatographically separated in some cases.[42]

Sequencing. Genomic DNA was extracted using the UltraClean Microbial DNA Isolation kit (Mo Bio Laboratories, Inc.). 16S rDNA genes were amplified using 100-200 ng genomic DNA template with the primers 8-27F (5' to 3' GAGTTTGATCCTGGCTCAG) and 1492R (5' to 3' GGTTACCTTGTTACGACTT). The following PCR conditions were used: 94 °C for 5 min, followed by 30 cycles of 94 °C for 30 s, 55 °C for 1 min, 72 °C for 1.5 min, with a final step of

72 °C for 5 min. The PCR bands were excised from the gel and purified using the QIAquick Gel Extraction kit (QIAGEN). One µL purified product was sequenced. Sequencing reactions were performed by the UW Biotechnology Center and reactions were sequenced with an ABI 3730xl DNA Analyzer. WMMA107, WMMA102, WMMA105, WMMA110, and WMMA111 were identified as a *Verrucosispora* sp. by 16S sequencing, and WMMA107 demonstrated 99% sequence similarity to *Verrucosispora* sp. CNP-852 SD01 (accession number EU 214938.1). The 16S sequence was deposited in GenBank (accession number JF520832-JF520836).

Cytotoxicity. Human lung adenocarcinoma A549 cells were obtained from the American Tissue Culture Collection (CCL-185) and were cultured in Dulbecco's Modified Eagle's Medium supplemented with 10% (v/v) FBS and 1% (v/v) penicillin/streptomycin (Cellgro) at 37 °C in a humidified atmosphere containing 5% CO_2. Cytoxicity of the compounds was determined using the resazurin assay.[43] The EC_{50} was calculated using GraphPad Prism Version 5.0.

Molecular Modeling Calculations. Molecular modeling calculations were performed on a Dell Precision T5500 Linux workstation with a Xeon processor (3.3 GHz, 6-core). Low energy conformers were obtained using Spartan 10 software (MMFF). The low energy conformer for each compound was analyzed by Gaussian 09 for geometry optimization and NMR calculations (B3LYP/6-31G(d,p)). Molecules were modeled in gas phase.

22'-Deoxythiocoraline (38): white solid; $[\alpha]^{25}_{D}$ -98 (c 0.0005, $CHCl_3$); UV (MeOH) λ_{max} (log ε) 210 (4.96), 230 (4.57), 299 (3.72), 360 (3.62) nm; IR (ATR) υ_{max} 3355, 1657, 1519, 1225, 772 cm^{-1}; ^1H and ^{13}C NMR (See Table 2.1); HRMS $[M+H]^+$ *m/z* 1141.2533 (calcd for $C_{48}H_{57}O_{11}N_{10}S_6$, 1141.2527).

Thiochondrilline A & B (39,40): white solid; $[\alpha]^{25}_{D}$ -128 (c 0.0013, $CHCl_3$); UV (MeOH) λ_{max}

(log ε) 210 (4.87), 230 (4.46), 298 (3.57), 360 (3.24) nm; IR (ATR) υ_{max} 3344, 1651, 1519, 757 cm^{-1}; ^1H and ^{13}C NMR (See Table 2.2); HRMS $[M+Na]^+$ *m/z* 662.1745 (calcd for $C_{27}H_{37}O_7N_5S_3Na$, 662.1747).

Thiochondrilline C (41): white solid; $[\alpha]^{25}_D$ -77 (c 0.0011, $CHCl_3$); UV (MeOH) λ_{max} (log ε) 209 (4.84), 230 (4.43), 298 (3.47), 360 (3.43) nm; IR (ATR) υ_{max} 3354, 1656, 1519, 1229, 782 cm^{-1}; ^1H and ^{13}C NMR (See Table 2.2); HRMS $[M+Na]^+$ *m/z* 632.1297 (calcd for $C_{25}H_{31}O_7N_5S_3Na$, 632.1278).

12'-Sulfoxythiocoraline (42): white solid; $[\alpha]^{25}_D$ -96 (c 0.0013, $CHCl_3$); UV (MeOH) λ_{max} (log ε) 209 (5.07), 230 (4.65), 299 (3.76), 360 (3.69) nm; IR (ATR) υ_{max} 3359, 1656, 1519, 747 cm^{-1}; ^1H and ^{13}C NMR (See Table 2.1); HRMS $[M+H]^+$ *m/z* 1173.2424 (calcd for $C_{48}H_{57}O_{13}N_{10}S_6$, 1173.2425).

2.5. References

1. Berdy, J. Bioactive Microbial Metabolites. *J. Antibiot*. **2005**, *58,* 1-26.

2. Zäehner, H.; Fiedler, H.P. The Need for New Antiobiotics. In *Fifty Years of Antimicrobials*. Hunter, P.A.; Darby, G.K.; Russel, N.J., Eds.; Cambridge University Press: Cambridge, England, 1995; 67-84.

3. Qui, J. Nature News. http://www.nature.com/news/2010/100418/full/news.2010.190.html, 18 Apr 2010 (DOI: 10.1038/news.2010.190).

4. Feling, R.H.; Buchanan, G.O.; Mincer, T.J.; Kaufmann, C.A.; Jensen, P.R.; Fenical, W. Salinosporamide A: a highly cytotoxic proteasome inhibitor from a novel microbial source, a marine bacterium of the new genus Salinospora. *Angew. Chem. Int. Ed*. **2003**, *42,* 355-357.

5. Kobayashi, M.; Natsume, T.; Tamaoki, S.; Watanabe, J.; Asano, H.; Mikami, T.; Miyasaka, K.; Miyazaki, K.; Gondo, M.; Sakakibara, K.; Tsukagoshi, S. Antitumor activity of TZT-1027, a novel dolastatin 10 derivative. *Jpn. J. Cancer Res*. **1997**, 88, 316-327.

6. Mita, A.C.; Hammond, L.A.; Bonate, P.L.; Weiss, G.; McCreery, H.; Syed, S.; Garrison, M.; Chu, Q.S.; DeBono, J.S.; Jones, C.B.; Weitman, S.; Rowinski, E.K. Phase I and pharmacokinetic study of tasidotin hydrochloride (ILX651), a third generation dolastatin-15 analogue, administered weekly for 3 weeks every 28 days in patients with advanced solid tumors. *Clin. Cancer Res*. **2006**, *12*, 5207-5215.

7. Mayer, A.M.; Glaser, K.B.; Cuevas, C.; Jacobs, R.S.; Kem, W.; Little, R.D.; McIntosh, J.M.; Newman, D.J.; Potts, B.C.; Shuster, D.E. The odyssey of marine pharmaceuticals: a current pipeline perspective. *Trends Pharmacol. Sci.* **2010**, *31*, 255-265.

8. Faircloth, G; Jimeno, J. D'lncalci, M. Biological activity of thiocoraline, a novel marine depsipeptide. *Eur. J. Cancer* **1997**, *33*, S175.

9. Pérez Baz, J.; Cañedo, L.M.; Fernández-Puentes, J.L.; Silva Elipe, M.V. Thiocoraline, a novel depsipeptide with antitumor activity produced by a marine Micromonospora. II. Physico-chemical properties and structure elucidation. *J. Antibiot*. **1997**, *50*, 738-741.

10. Romero, F.; Espliego, F.; Pérez Baz, J.; García de Quesada, T.; Grávalos, D.; De la Calle, F.; Fernández-Puentes, J.L. Thiocoraline, a new depsipeptide with antitumor activity produced by a marine Micromonospora. I. Taxonomy, fermentation, isolation, and biological activities. *J. Antibiot*. **1997**, *50*, 734-737.

11. Erba, E.; Bergamashi, D.; Ronzoni, S.; Faretta, M.; Taverna, S.; Bonfanti, M.; Catapano, C.V.; Faircloth, G.; Jimeno, J.; D'Incalci, M. Mode of action of thiocoraline, a natural marine compound with anti-tumour activity. *Br. J. Cancer*. **1999**, *80*, 971.

12. Negri, A.; Marco, E.; García-Hernández, V.; Domingo, A.; Llamas-Saiz, A.L.; Porto-Sandá, S.; Riguera, R.; Laine, W.; David-Cordonnier, M.H.; Bailly, C.; García-Fernández, L.F.; Vaquero, J.J.; Gago, F. Antitumor activity, X-ray crystal structure, and DNA binding properties of thiocoraline A, a natural bisintercalating thiodepsipeptide. *J. Med. Chem*. **2007**, *50*, 3322-3333.

13. Boger, D. L.; Ichikawa, S. Total Syntheses of Thiocoraline and BE-22179: Establishment of Relative and Absolute Stereochemistry. *J. Am. Chem. Soc*. **2000**, *122*, 2956-2957.

14. Boger, D.L.; Ichikawa, S.; Tse, W.C.; Hedrick, M.P.; Jin, Q. Total syntheses of thiocoraline and BE-22179 and assessment of their DNA binding and biological properties. *J. Am. Chem. Soc*. **2001**, *123*, 561-568.

15. Boger, D. L. Analogues of Thiocoraline and BE-22179. U.S. Patent Application 20040072738, April, 15, 2004. URL: http://ip.com/patapp/US20040072738.

16. Tulla-Puche, J.; Bayó-Puxan, N.; Moreno, J.A.; Francesch, A.M.; Cuevas, C.; Álvarez, M.; Albericio, F. Solid-phase synthesis of oxathiocoraline by a key intermolecular disulfide dimer. *J. Am. Chem. Soc.*, **2007**, *129*, 5322-5323.

17. Tulla-Puche, J.; Marcucci, E.; Prats-Alfonso, E.; Bayó-Puxan, N.; Albericio, F. *N*Me Amide as a Synthetic Surrogate for the Thioester Moiety in Thiocoraline. *J. Med. Chem*. **2009**, *52*, 834–839.

18. Lombó, F.; Velasco, A.; Castro, A.; de la Calle, F.; Braña, A.F.; Sánchez-Puelles, J.M.; Méndez, C.; Salas, J.A. Deciphering the biosynthesis pathway of the antitumor thiocoraling from a marine actinomycete and its expression in two *Streptomyces* species. *Chembiochem*. **2006**, *7*, 366-376.

19. Sheoran, A.; King, A.; Velasco, A.; Pero, J.M.; Garneau-Tsodikova, S. Characterization of TioF, a tryptophan 2,3-dioxygenase involved in 3-hydroxyquinaldic acid formation during thiocoraline biosynthesis. *Mol. Biosyst*. **2008**, *4*, 622-628.

20. Robbel, L.; Hoyer, K.M.; Marahiel, M.A. TioS T-TE – a prototypical thioesterase responsible for cyclodimerization of the quinoline- and quinoxaline-type class of chromodepsipeptides. *FEBS J*. **2009**, *276*, 1641-1653.

21. Biswas, T.; Zolova, O.E.; Lombó, F.; de la Calle, F.; Salas, J.A.; Tsodikov, O.V.; Garneau-Tsodikova, S. A new scaffold of an old protein fold ensures binding to the bisinteracalator thiocoraline. *J. Mol. Biol*. **2010**, *397*, 495-507.

22. Mady, A.S.; Zolova, O.E.; San Millán, M.A.; Villamizar, G.; De la Calle, F.; Lombó, F.; Garneau-Tsodikova, S. Characterization of TioQ, a type II thioesterase from the thiocoraline biosynthetic cluster. *Mol. BioSyst*. **2011**, *7*, 1999-2011.

23. Waring, M.J. Echinomycin and Related Quinoxaline Antibiotics. In *Molecular Aspects of Anticancer Drug-DNA Interactions*; Neidle, S., Waring, M.J., Eds.; Macmillan & Co.: London, 1993; Vol. 1, pp. 213-242.

24. Rheims, H.; Schumann, P.; Rohde, M.; Stackebrandt, E. Verrucosispora gifhornensis gen. nov., sp. nov., a new member of the actinobacterial family Micromonosporaceae. *Int. J. Syst. Bacteriol.* **1998**, *48*, 1119-1127.

25. Bister, B.; Bischoff, D.; Ströbele, M.; Riedlinger, J.; Reicke, A.; Wolter, F.; Bull, A.T.; Zäehner, H.; Fiedler, H.P.; Süssmuth, R.D. *Angew. Chem. Int. Ed*. **2004**, *43*, 2574-2576.

26. Fiedler, H.P.; Bruntner, C.; Riedlinger, J.; Bull, A.T.; Knutsen, G.; Goodfellow, M.; Jones, A.; Maldonado, L.; Pathom-aree, W.; Beil, W.; Schneider, K.; Keller, S.; Sussmuth, R.D. *J. Antibiot*. **2008**, *61*, 158–163.

27. Shirai, M.; Okuda, M.; Motohashi, K.; Imoto, M.; Furihata, K.; Matsuo, Y.; Katsuta, A.; Shizuri, Y.; Seto, H. Terpenoids produced by actinomycetes: isolation, structural elucidation and biosynthesis of new diterpenes, gifhornenolones A and B from Verrucosispora gifhornensis YM28-088. *J. Antibiot*. **2010**, *63*, 245-250.

28. Jiang, S.; Sun, W.; Chen, M.; Dai, S.; Zhang, L.; Liu, Y.; Lee, K.J.; Li, X. Diversity of

culturable actinobacteria isolated from marine sponge *Haliclona* sp. *Antonie Van Leeuwenhoek* **2007**, *92*, 405-416.

29. Yi-lei, N.; Ru, L.; Yong-biao, Z.; Hui, Z.; Yuan-rong, C.; Wei, Z.; Hong, J. 2'-Deoxyuridine produced by Verrucosispora sp. FIM06031 from marine sponge. *Chin. J. Antibiot*. **2010**, 6, 426-430.

30. Schmitz, F.J.; McDonald, F.J. Isolation and identification of cerebrosides from the marine sponge Chondrilla nucula. *J. Lipid Res*. **1974**, *15*, 158-164.

31. Zierer, M.S.; Mourão, P.A. A wide diversity of sulfated polysaccharides are synthesized by different species of marine sponges. *Carbohydr. Res*. **2000**, *328*, 209-216.

32. Smith, S.G.; Goodman, J.M. Assigning stereochemistry to single diastereoisomers by GIAO NMR calculation: the DP4 probability. *J. Am. Chem. Soc*. **2010**, *132*, 12946-12959.

33. Spartan 10, v. 1.0.2. Wavefunction Inc. 2011.

34. Gaussian 09, Revision A.1, Frisch, M. J.; Trucks, G. W.; Schlegel, H. B.; Scuseria, G. E.; Robb, M. A.; Cheeseman, J. R.; Scalmani, G.; Barone, V.; Mennucci, B.; Petersson, G. A.; Nakatsuji, H.; Caricato, M.; Li, X.; Hratchian, H. P.; Izmaylov, A. F.; Bloino, J.; Zheng, G.; Sonnenberg, J. L.; Hada, M.; Ehara, M.; Toyota, K.; Fukuda, R.; Hasegawa, J.; Ishida, M.; Nakajima, T.; Honda, Y.; Kitao, O.; Nakai, H.; Vreven, T.; Montgomery, Jr., J. A.; Peralta, J. E.; Ogliaro, F.; Bearpark, M.; Heyd, J. J.; Brothers, E.; Kudin, K. N.; Staroverov, V. N.; Kobayashi, R.; Normand, J.; Raghavachari, K.; Rendell, A.; Burant, J. C.; Iyengar, S. S.; Tomasi, J.; Cossi, M.; Rega, N.; Millam, N. J.; Klene, M.; Knox, J. E.; Cross, J. B.; Bakken, V.; Adamo, C.; Jaramillo, J.; Gomperts, R.; Stratmann, R. E.; Yazyev, O.; Austin, A. J.; Cammi, R.; Pomelli, C.; Ochterski, J. W.; Martin, R. L.; Morokuma, K.; Zakrzewski, V. G.; Voth, G. A.; Salvador, P.; Dannenberg, J. J.; Dapprich, S.; Daniels, A. D.; Farkas, Ö.; Foresman, J. B.; Ortiz, J. V.; Cioslowski, J.; Fox, D. J. Gaussian, Inc., Wallingford CT, 2009.

35. Stappen, I.; Buchbauer, G.; Robien, W.;Wolschann, P. ^{13}C NMR spectra of santalol derivatives: a comparison of DFT-based calculations and database-oriented prediction techniques. *Magn. Reson. Chem.* **2009**, *47*, 720-726.

36. Sarotti, A.M.; Pellegrinet, S.C. A multi-standard approach for GIAO ^{13}C NMR calculations. *J. Org. Chem*. **2009**, *74*, 7254-7260.

37. Ojanperä, S.; Pelander, A.; Pelzing, M.; Krebs, I.; Vuori, E.; Ojanperä, I. Isotopic pattern and accurate mass determination in urine drug screening by liquid chromatography/time-of-flight mass spectrometry. *Rapid Commun. Mass Spectrom*. **2006**, *20*, 1161-1167.

38. Zolova, O.E.; Mady, A.S.; Garneau-Tsodikova, S. Recent developments in bisintercalator natural products. *Biopolymers* **2010**, *93*, 777-790.

39. Maldonado, L.A.; Fragoso-Yáñez, D.; Pérez-García, A.; Rosellón-Druker, J.; Quintana, E.T. Actinobacterial diversity from marine sediments collected in Mexico. *Antonie Van Leeuwenhoek* **2009**, *95*, 111-120.

40. Yang, J.; Wu, H.; Shen, L.; Qin, Y. Total synthesis of (±)-communesin F. *J. Am. Chem. Soc*. **2007**, *129*, 13794-13795.

41. Seong, C.M.; Park, C.M.; Choi, J.; Park, N.S. An efficient base-mediated intermolecular condensation of 2-(disubstituted amino)-benzonitriles to 3-aminoindoles. *Tetrahedron Lett*. **2009**, *50*, 1029-1031.

42. McCombie, S.W.; Tagat, J.R.; Vice, S.F. Lin, S.; Steensma, R.; Palani, A.; Neustadt, B.R.; Baroudy, B.M.; Strizki, J.M. Endres, M.; Cox, K.; Dan, N.; Chou, C. Piperazine-based CCR5 antagonists as HIV-1 inhibitors. III: synthesis, antiviral and pharmacokinetic profiles of symmetrical heteroaryl carboxamides. *Bioorg. Med. Chem. Lett*. **2003**, *13*, 567-571.

43. O’Brien, J.; Wilson, I.; Orton, T.; Pognan, F. Investigation of the Alamar Blue (resazurin) fluorescent dye for the assessment of the mammalian cell cytotoxicity. *Eur. J. Biochem*. **2000**, *267*, 5421-5426

Chapter 3:

Thiocoraline Activates the Notch Pathway in Carcinoids and Reduces Tumor Progression *in vivo*

Portions of this chapter have been submitted for publication as:

Wyche, T.P., Dammalapati, A., Cho, H., Harrison, A.D., Kwon, G.S., Chen, H., Bugni, T.S., Jaskula-Sztul, R. Thiocoraline activates the Notch pathway in carcinoids and reduces tumor progression *in vivo*. *Endocr.-relat. Cancer* (2014) submitted.

2.3. Introduction

Carcinoids are slow-growing neuroendocrine tumors (NETs) that are characterized by hormone overproduction.[1-4] Carcinoids, which make up about 0.5% of all malignant tumors,[5,6] are most commonly found in the small intestine but can also be present in the lungs, rectum, appendix, and stomach, among other locations. Symptoms from carcinoids are often absent but when left untreated can lead to carcinoid syndrome, which includes effects such as diarrhea, bronchospasm, and right-sided valvular heart lesions.[1-4] Treatment of carcinoids remains an ever-present issue as they are resistant to current therapeutics: the single agent chemotherapy response rate is only 20%.[4] Responses to chemotherapy are typically short-lived and not correlated with prolonged survival. Consequently, surgery remains the only curative option for treatment. Therefore, further studies are necessary to find more viable options for treatment of carcinoid disease.

Activation of Notch1 signaling in carcinoids has been shown to have a role in tumor suppression.[7] Notch isoforms (1-4) are transmembrane receptors that are activated by proteolytic cleavage following ligand binding.[8-10] The Notch intracellular domain (NICD) translocates into the nucleus where it forms a complex with centromere binding factor 1 (CBF1) and other proteins to activate gene transcription (HES and HEY genes). The Notch1 signaling pathway is not active in carcinoid tumors.[7] As a result of studies implicating Notch as a tumor suppressor in carcinoid tumors, therapeutic leads that activate this signaling pathway represent promising strategies for treatment of carcinoids.

Thiocoraline (**37**) was originally isolated from a marine *Micromonospora* sp.[11-12] and has demonstrated potent cytotoxicity against lung, breast, colon, renal, and melanoma cancer cells and *in vivo* efficacy against human carcinoma xenografts.[12-15] Thiocoraline (**37**) is a bisintercalator and does not damage DNA or inhibit topoisomerase II; however, it does inhibit DNA elongation by DNA polymerase α.[16] More recently, we isolated thiocoraline (**37**) and new analogs from an ascidian-derived *Verrucosispora* sp..[17] We also demonstrated that thiocoraline altered the neuroendocrine phenotype and activated the Notch pathway in medullary thyroid cancer (MTC).[18] Due to the need for additional therapeutic options for neuroendocrine cancers we aimed to investigate the effect of thiocoraline on carcinoids.

In this study, we investigated thiocoraline's effect on cell proliferation in human pancreatic carcinoid tumor cells (BON) and human bronchopulmonary carcinoid cells (H727). Additionally, we determined thiocoraline's ability to alter the neuroendocrine phenotype of carcinoids. Moreover, we have shown that thiocoraline (**37**) transcriptionally activates the Notch pathway. To better understand the mechanism of action of thiocoraline's antiproliferative effects, we performed cell cycle analysis by flow cytometry and validated protein expression of cell cycle markers by western blot. Finally, a formulation for thiocoraline (**37**) was developed to overcome solubility problems using nanoparticle polymeric micelles in order to improve the solubility for *in vivo* studies. Thiocoraline (**37**) slowed the progression of carcinoid tumor growth in mice. Altogether, the results from this study provided evidence for the therapeutic potential of thiocoraline (**37**) against carcinoid tumors.

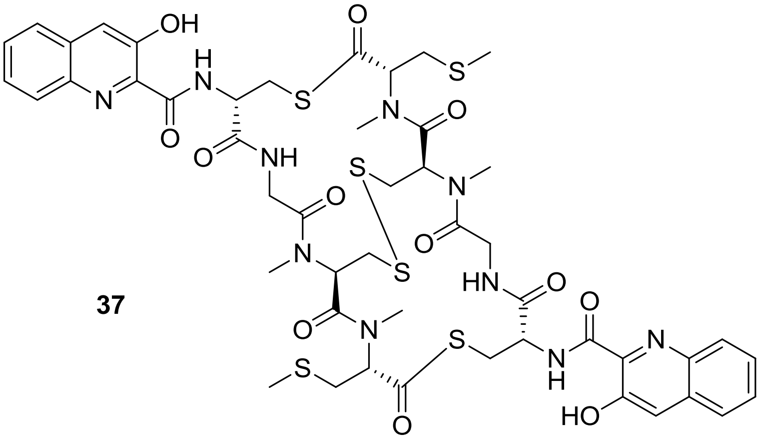

37

3.2. Results and Discussion

Thiocoraline inhibits BON and H727 cell proliferation *in vitro*

Thiocoraline (**37**) has previously been shown to decrease cell proliferation in MTC-TT cells at nanomolar concentrations,[18] and consequently, the survival of BON and H727 cells treated with thiocoraline was investigated. Thiocoraline (**37**) exhibited low nanomolar potency against BON (Figure 3.1A) and H727 cells (Figure 3.1B). Additionally, cell survival over the course of eight days was monitored after treatment with thiocoraline (0-40 nM; Figure 3.1C-D). For both BON and H727 cells, treatment of thiocoraline (**37**) at concentrations between 20-40 nM resulted in a steady decrease in cell proliferation over the course of eight days. Treatment of thiocoraline at 5 and 10 nM resulted in a decrease in cell proliferation through six days of treatment in H727 cells.

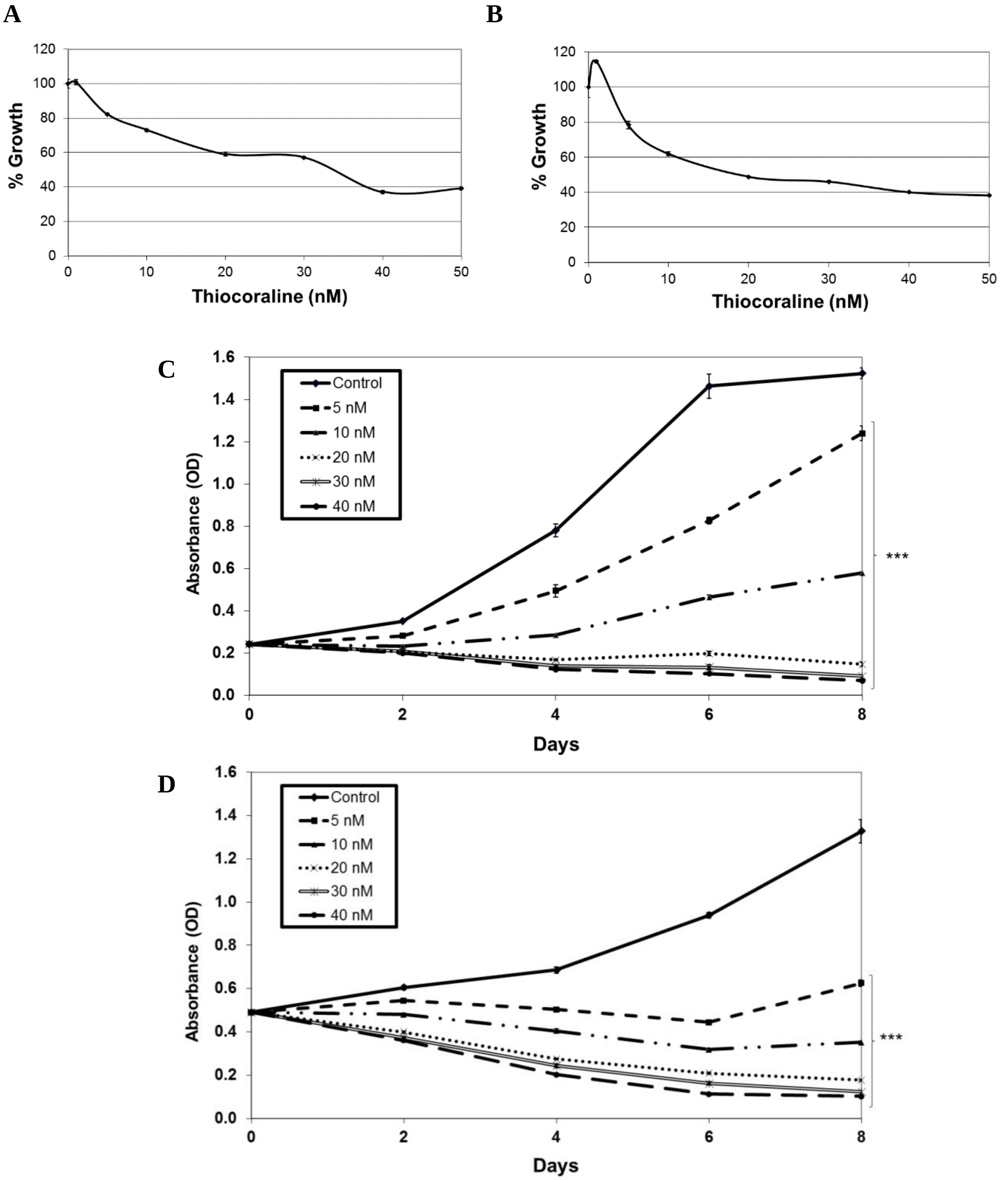

Figure 3.1. Thiocoraline inhibits BON and H727 cell proliferation *in vitro*. The IC_{50} was determined for BON (A) and H727 (B) cells treated with thiocoraline for 48 hours using the MTT assay. Using the MTT assay, two-day treatment of thiocoraline for BON (C) and H727 (D) cells over the course of 8 days demonstrated a decrease in cell proliferation at concentrations as low as 20 nM. Experiments were done in quadruplicate, and data are plotted as mean ± SEM. ***, P<0.001.

Thiocoraline induces cell cycle arrest in BON and H727 cells

After determining the ability of thiocoraline (**37**) to reduce cell proliferation in BON and H727 cells, the mechanism of action of thiocoraline (**37**) was investigated by western blot and flow cytometry (Figure 3.2). Cell cycle marker proteins (p21, p27, cyclin B1, and cyclin D1) were monitored by western blot and suggested arrest in the G2/M phase induced by thiocoraline (**37**) in BON and H727 cells. An increase in expression of p21, a cyclin dependent kinase (Cdk) inhibitor that promotes cell cycle suppression, was demonstrated by western blot after treatment of BON and H727 cells with thiocoraline (**37**). Additionally, flow cytometry analyses of BON and H727 cells treated with thiocoraline (0-40 nM) suggested that thiocoraline (**37**) causes cell cycle arrest in the G2/M phase (Figure 3.2). An increase in cell population in the G2/M phase and with concomitant decrease in cell population in the G1 phase was displayed with increasing concentrations of thiocoraline (**37**) in the BON and H727 cell lines. The percentage of cells in the S phase showed variable change in both cell lines.

Thiocoraline decreases neuroendocrine tumor markers *in vitro*

Achaete-scute complex like-1 (ASCL-1), chromogranin A (CgA), and neurospecific enolase (NSE) have been characterized as markers of NETs.[19,20] Treatment of thiocoraline (0-40 nM) in BON and H727 cells effectively changed their neuroendocrine phenotype and resulted in a dose-dependent decrease in expression of ASCL-1, CgA, and NSE as demonstrated by western blot analysis (Figure 3.3).

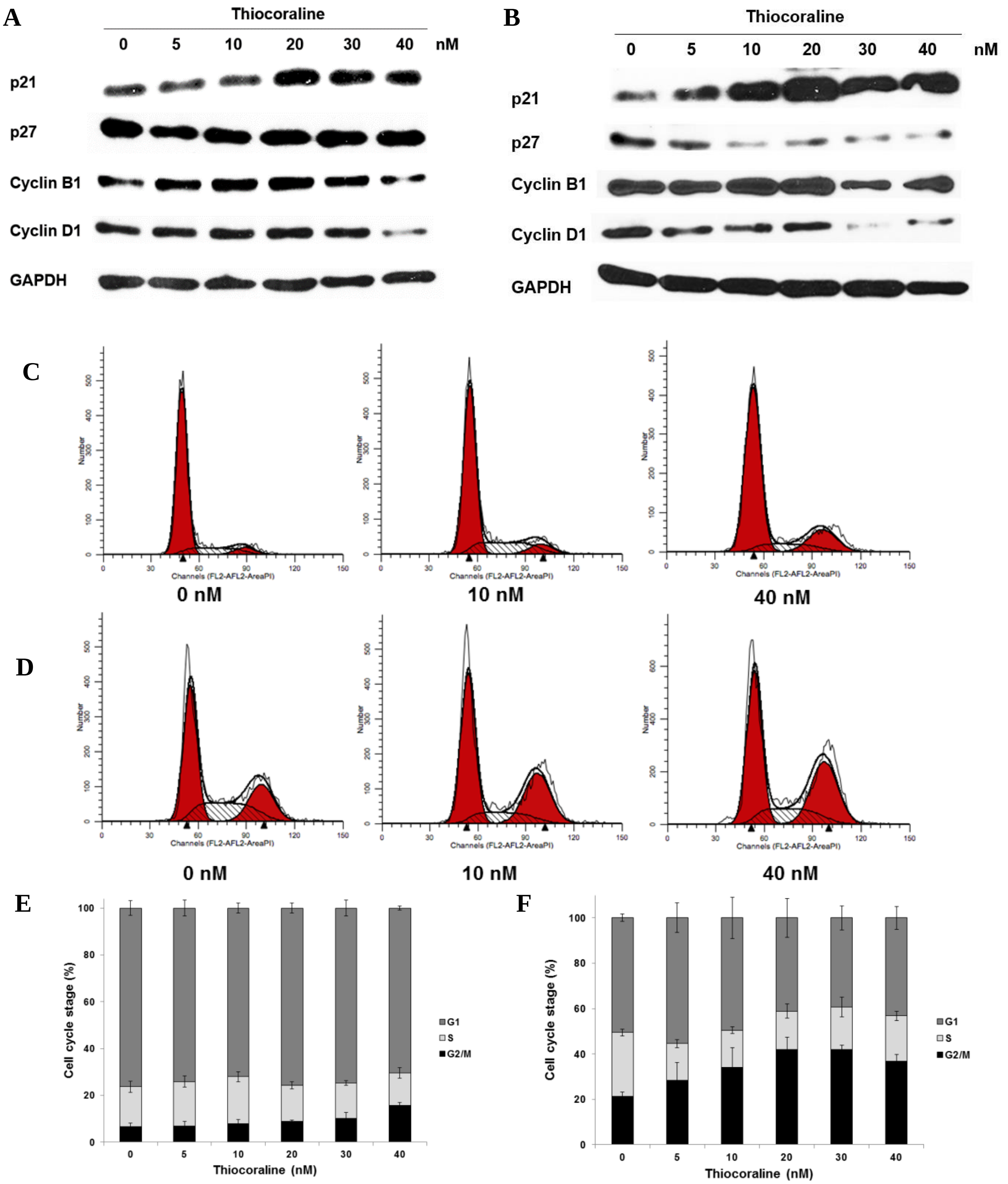

Figure 3.2. Thiocoraline suppresses cell proliferation through cell cycle arrest. Western blot analysis of cell cycle markers of BON (A) and H727 (B) cells treated with thiocoraline demonstrated cell cycle arrest. Equal loading was confirmed with GAPDH. Flow cytometry analysis of BON (C, E) and H727 (D, F) cells treated with thiocoraline confirmed cell cycle arrest in the G2/M phase.

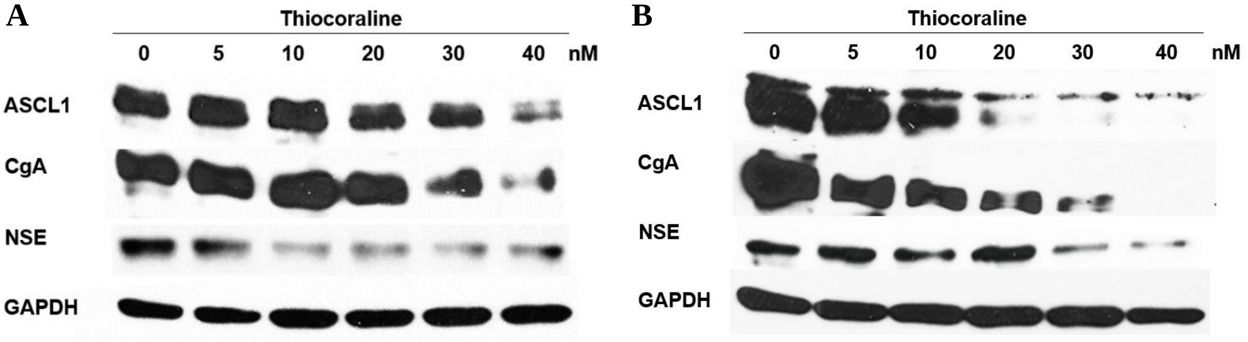

Figure 3.3. Thiocoraline reduces neuroendocrine tumor markers in *vitro*. Western blot analysis of BON (A) and H727 (B) cells treated with thiocoraline demonstrated a dose-dependent decrease of neuroendocrine tumor markers expression: ASL1, CgA, and NSE. Equal loading was confirmed with GAPDH.

Thiocoraline induces Notch isoforms expression in BON cells

After demonstrating the ability of thiocoraline (**37**) to cause cell cycle arrest in BON and H727 cells, western blot analysis and qRT-PCR were used to further investigate thiocoraline's mechanism of action. Clinical studies have shown that clinical efficacy was correlated with activation of the Notch pathway in NETs;[21] therefore, Notch activation was investigated. The expression of Notch1 was monitored by western blot and quantitative real-time PCR (qRT-PCR) in BON cells treated with thiocoraline (0-40 nM). A dose-dependent increase of Notch1 expression in BON cells was apparent by western blot analysis and qRT-PCR (Figure 3.4). qRT-PCR showed a four-fold increase in expression of Notch1 between the control (0 nM) and treatment with 40 nM thiocoraline. H727 cells treated with thiocoraline did not demonstrate a statistically significant increase in expression of Notch1 at the protein or mRNA level. To further determine whether thiocoraline functionally activated the Notch pathway, a luciferase reporter assay incorporating four CBF1-binding sites was used. Thiocoraline treatment of BON cells resulted in a nearly 3-fold induction of luciferase activity indicating that this increase was caused by Notch activation followed by Notch-CBF1 binding. Additionally, activation of

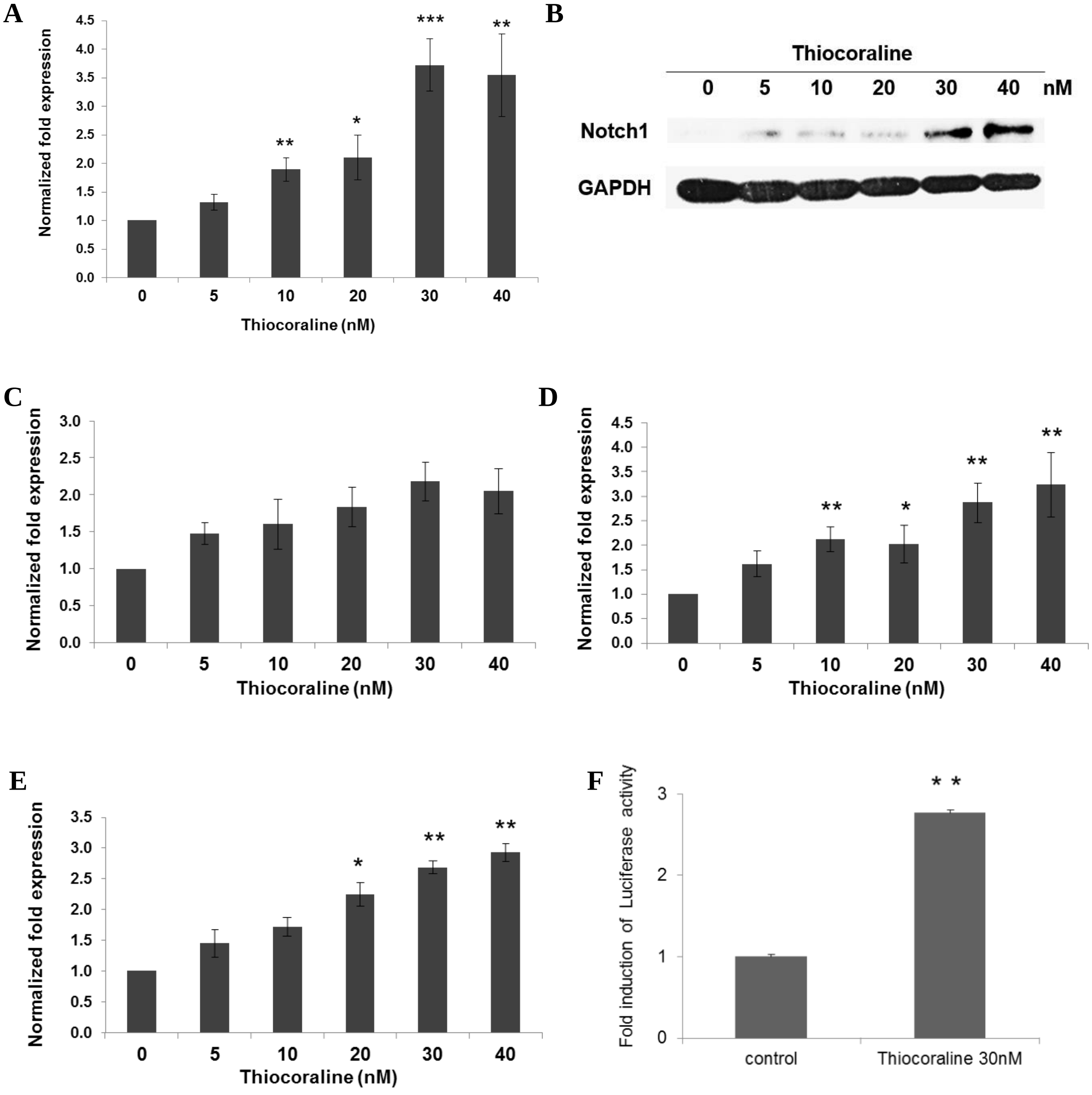

Figure 3.4. Activation of Notch1 and downstream targets by thiocoraline. (A) Quantitative RT PCR showed dose-dependent activation of Notch1 at the mRNA level in BON cells treated with thiocoraline; data were plotted relative to control cells without thiocoraline treatment. *, P<0.05, **, P<0.01,***, P<0.001. (B) Western blot analysis showed dose-dependent activation of Notch1 at the protein level in BON cells treated with thiocoraline. Equal loading was confirmed with GAPDH. Thiocoraline dose-dependently induced mRNA levels of downstream targets of Notch (HES1 (C), HES5 (D), and HEY2 (E)) monitored by qRT-PCR. *, P<0.05, **, P<0.01, ***, P<0.001. (F) BON cells treated with thiocoraline induced CBF1 luciferase activity. **, P<0.01.

downstream targets of Notch were apparent by qRT-PCR. A dose dependent increase in the mRNA levels of HES1, HES5, and HEY2 was detected in BON cells treated with thiocoraline. These results suggest that thiocoraline (**37**) functionally activates Notch signaling in carcinoids.

Thiocoraline reduced tumor progression *in vivo*

After investigating thiocoraline's *in vitro* effect against carcinoid cell lines, an *in vivo* study was pursued. Thiocoraline (**37**) has poor solubility in DMSO and aqueous solutions,

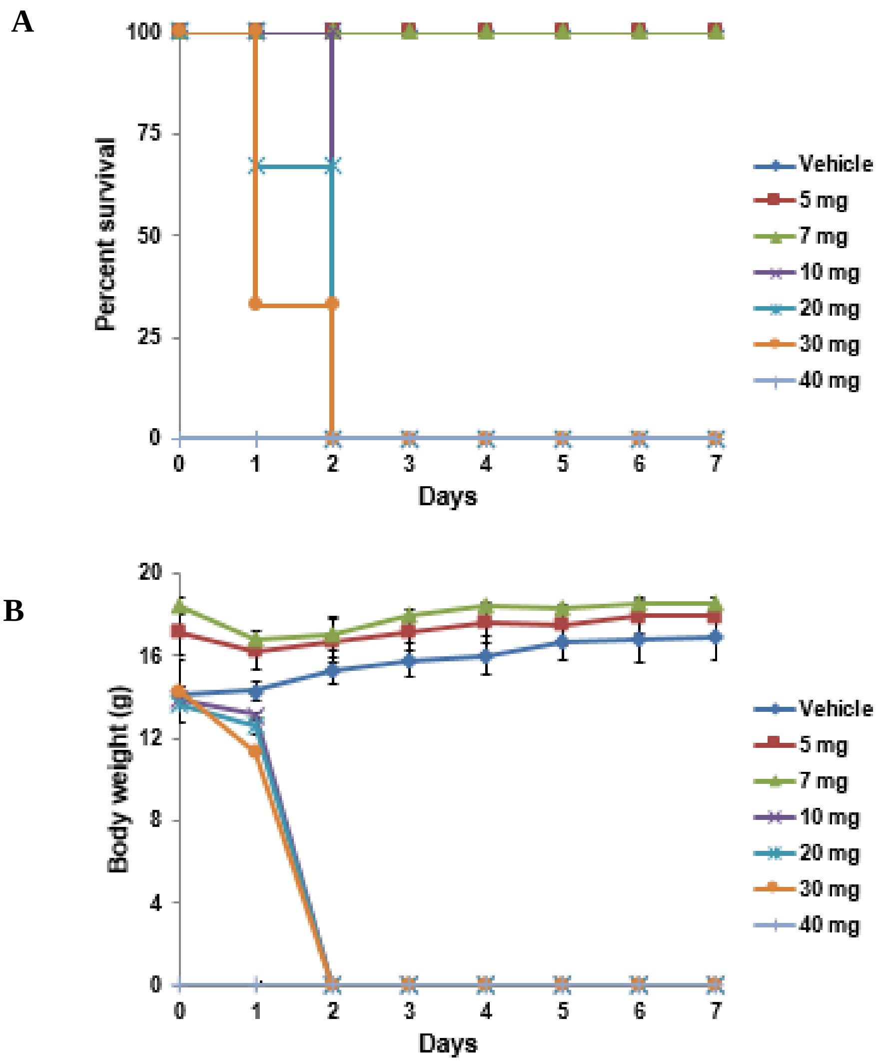

Figure 3.5. Maximum tolerated dose (MTD) study. (A) Animal survival proportions. Thiocoraline-incorporated PEG-*b*-PLA micelles were intravenously injected to mice and demonstrated that the maximum tolerated dose was 7 mg/kg. (B) Animal body weight changes for MTD study.

which initially prevented *in vivo* experiments, but formulation using nanoparticle polymeric micelles (PEG-*b*-PLA) increased the aqueous solubility to 4.23 ± 1.15 mg/mL. This formulation enabled a maximum tolerated dose (MTD) study in mice; the MTD was determined to be 7 mg/kg (Figure 3.5). At 7 mg/kg, there was 100% survival of mice and no loss in body weight.

After determining the MTD, an *in vivo* study investigated the therapeutic potential of thiocoraline (**37**). Mice were inoculated with BON cells stably transfected with luciferase-expressing plasmid *luc2*, and tumors were allowed to grow for 14 days. Thiocoraline formulated in polymeric micelles was dosed to 6 mice on days 15, 22, and 29 at 5 mg/kg. Likewise, empty micelles were dosed to 6 additional mice at the same time points. Thiocoraline slowed the progression of tumor growth compared to the vehicle control (Figure 3.6). There was a 62.6% reduction in tumor volume between mice treated with thiocoraline and vehicle. Moreover, validation of tumor growth by bioluminescence imaging (73.4% reduction in tumor growth) confirmed that thiocoraline formulated in polymeric micelles has significant antitumor activity. Western blot analysis of proteins from the tumor tissue and qRT-PCR demonstrated increased expression of Notch1 in only mice treated with thiocoraline.

The only current treatment for carcinoid tumors is surgery, and therefore, there is a need for additional therapeutic options. This study demonstrated that thiocoraline (**37**) causes a decrease in cell proliferation in BON and H727 cells, acting by cell cycle arrest. Additionally, a decrease in NET markers and an increase in Notch1 protein and mRNA levels suggested that thiocoraline (**37**) functionally activates the Notch pathway in BON cells. In general, these results parallel recent work investigating the potential for thiocoraline (**37**) as a treatment for MTC (TT cells).[18]

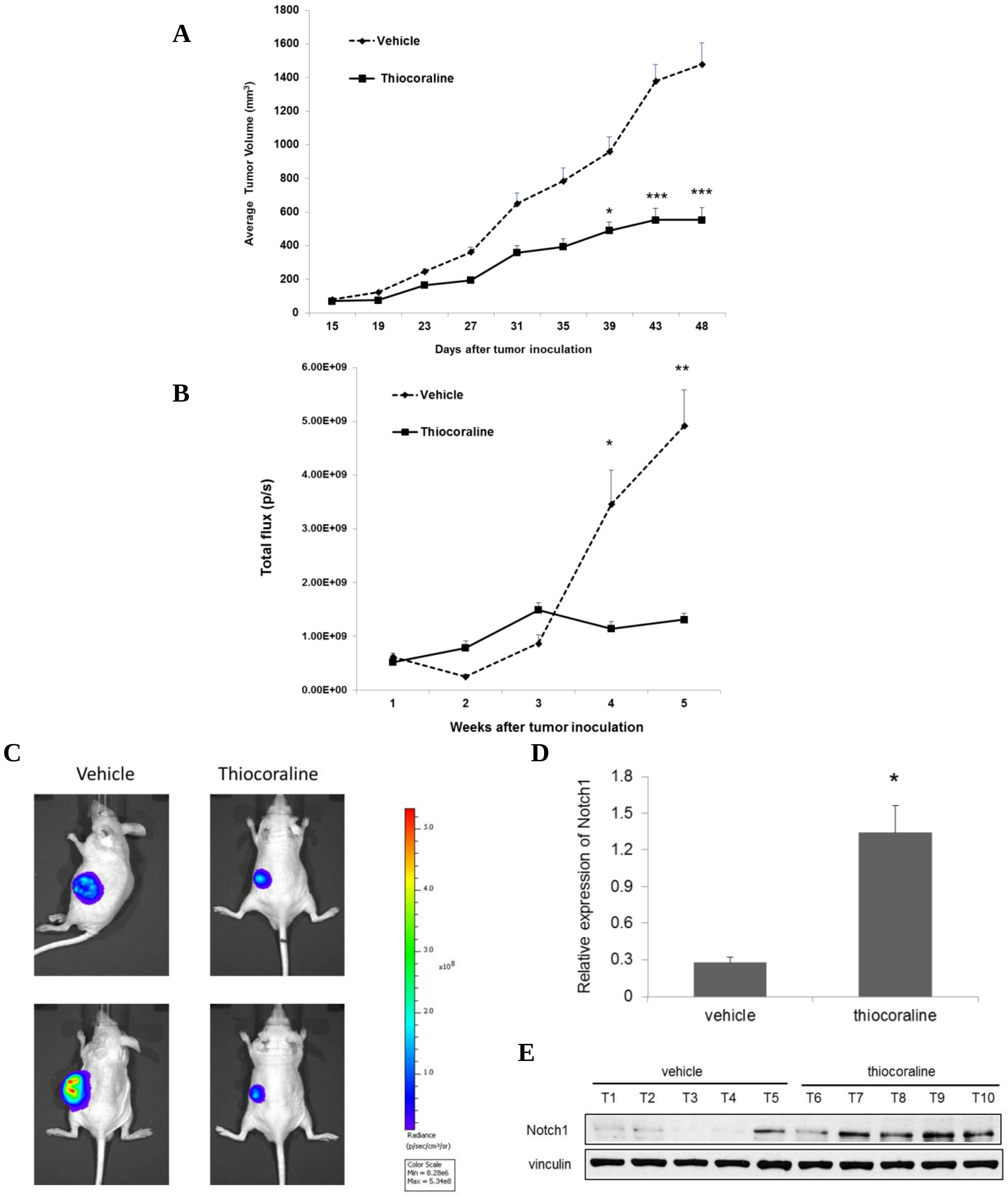

Figure 3.6. (A) Average tumor volume measured by caliper for mice treated with thiocoraline and vehicle. *, $P<0.05$, ***, $P<0.001$ (B) The bioluminescence values as a total flux (photons/sec/cm^2/steradian) of the tumor region were quantified for each group of mice and mean values ± SD are plotted over time. (C) Representative comparison of mice treated with vehicle and thiocoraline after four weeks of tumor growth. Expression of Notch1 in tumor tissue samples was determined by qRT-PCR (D) and western blot analysis (E) for mice treated with thiocoraline and vehicle. *, $P<0.05$. BON tumor bearing animals are represented by five tumor lysates from each treatment group. ±SD.

However, one major difference between the BON, H727, and TT cells treated with thiocoraline (**37**), was the stage of cell cycle arrest. MTC-TT cells treated with thiocoraline (**37**) resulted in G1 phase arrest. Additionally, previous work has shown that thiocoraline (**37**) induced G1 phase arrest in LoVo and SW620 colon cancer cells.[16] However, our results demonstrated that thiocoraline (**37**) induced G2/M phase arrest in BON and H727 cells. The difference in phase for cell cycle arrest could suggest a difference in mechanism of action for thiocoraline in carcinoids compared to other cell lines. Further work is necessary to better understand this difference in cell cycle inhibition.

Another difference between the BON, H727, and TT cells was the considerable increase in expression of Notch2 signaling in TT cells. While BON cells showed no apparent increase in Notch2 expression, TT cells demonstrated a nearly 30-fold increase in expression of Notch2 at the mRNA level. Despite this difference, thiocoraline (**37**) reduces cell proliferation and NET tumor markers in a similar fashion in all three NET cell lines.

The ability of thiocoraline (**37**) to activate Notch signaling and cause a decrease in cell proliferation in carcinoids, as well as MTC cells, is a promising step towards finding alternative forms of treatment for NETs. Importantly, the *in vivo* study presented here demonstrated that thiocoraline (**37**) can slow progression of carcinoid tumors. This work complements other recent work on thiocoraline (**37**) as a potential therapeutic. Considerable progress has been made for the total synthesis of thiocoraline (**37**), which could make it more amenable to pharmaceutical development. Thiocoraline was originally synthesized by Boger and co-workers,[22,23] and work has been done more recently by Albericio and co-workers to complete an efficient solid-phase synthesis of thiocoraline (**37**) using enzyme-labile protecting groups.[24] Another issue for thiocoraline (**37**) is its poor aqueous solubility, which hinders its ability to be delivered *in vivo*.

Our formulation using polymeric micelles helps alleviate this problem. Additionally, recent work has been done with liposomes to improve the ability to deliver thiocoraline (**37**).[25,26] Overall, considerable work is still necessary, but many of the pieces are in place for thiocoraline (**37**) as a potential therapeutic.

3.3. Conclusion

Thiocoraline activates the Notch signaling pathway and reduces cell proliferation in carcinoids. Treatment of BON and H727 cells with thiocoraline at nanomolar concentrations resulted in a decrease in NET markers (ASCL-1, CgA, and NSE). Cell cycle analyses by flow cytometry and western blot demonstrated arrest in the G2/M phase induced by thiocoraline in BON and H727 cells. A dose-dependent increase of Notch1 on the protein and mRNA levels in BON cells treated with thiocoraline, as well as an increase of downstream targets of Notch, points towards the tumor suppression role of thiocoraline in carcinoids. While further work is necessary to better understand thiocoraline's mechanism of action, these results suggest that thiocoraline could be a potential treatment for NETs.

3.4. Materials and Methods

Cell Culture

BON human pancreatic carcinoid tumor cells,[27] and H727 human bronchopulmonary carcinoid cells (ATCC #CRL-5815) (ATCC, Manassas, VA, USA) were maintained as previously described.[28,29] The BON cell line was authenticated in May 2012 at Genetica DNA laboratories.[30] For the purpose of *in vivo* study, BON cells were stably transfected with luciferase–expressing plasmid *luc2* (pGL4.50[*luc2*/CMV/Hygro], Promega, Madison, WI) using lipofectamine 2000 (Invitrogen, Carlsbad, CA). Twenty-four hours after transfection, cells were cultured in the BON cells medium additionally containing selective antibiotic - 100μg/mL of hygromycin B (Invitrogen) - for 3 weeks to obtain hygromycin-resistant clones. Selected clones were then tested for luciferase expression using a luciferase assay system kit (Promega), and the clone with the highest activity was chosen for the *in vivo* experiments.

Thiocoraline

Chondrilla caribensis f. caribensis sponge specimens were collected in the Florida Keys on February 10, 2010 as was previously described.[17] Thiocoraline (**37**) was isolated and purified from the marine bacterium *Verrucosispora* sp., as was previously described.[17] Thiocoraline (**37**) was dissolved in dimethyl sulfoxide (DMSO) and diluted in standard media to achieve desired concentrations.

Cell Proliferation Assay and IC_{50} determination

Cell proliferation was measured via 3-(4,5-dimethylthiazol-2yl)-2,5 diphenyltetrazolium bromide (MTT) assay as previously described.[29,31] Cells were plated in quadruplicates in 24-well plates under standard conditions and allowed to attach overnight. The following day, cells were treated with thiocoraline (0-40 nM) and incubated for up to 8 days. Control treated cells (0 nM) received DMSO at 0.005% final concentration. Cell proliferation was assessed after 2, 4, 6, and 8 days. Following two days of thiocoraline (**37**) treatment, the dose effect curve was plotted to determine the IC_{50} value. The MTT assay was performed by replacing the standard media with 250 μL of serum-free RMPI 1640 containing 0.5 mg/mL MTT and incubated for 3.5 hours at 37 °C. After incubation, 750 μL of DMSO was added per well. Plates were shaken for 5 minutes to enhance dissolution. Absorbance at 540 nM was measured via a spectrophotometer (μQuant; Bio-Tek Instruments, Winooski, VT).

Flow Cytometry

To analyze the cell cycle progression of BON and H727 cells, the DNA content was quantified via flow cytometry. BON and H727 cells were treated for two days with thiocoraline (0-40 nM). After treatment, cells were washed with cold 1X PBS pH 7.2 (Life Technologies) and harvested with trypsin (Life Technologies) to enhance dissociation. Cells were then centrifuged at 1200 RPM at 4 °C and washed twice with cold 1X PBS before fixed with cold 70% ethanol and kept at -20 °C before staining. Prior to staining, cells were again washed twice with cold 1X PBS with centrifugation after each wash. The pellet was suspended in a propidium iodide (PI) staining solution containing 20 mg/mL RNAse-A (Sigma) and 330 µg/mL propidium iodide dissolved in 1X PBS. Cells were stained in the dark overnight at 4 °C. Samples were filtered prior to analysis. FACS analysis was performed on a flow cytometer at 488 nM (FACSCalibur flow cytometer; BD Biosciences), and results were analyzed with ModFit LT 3.2 software (Verity, Topsham, ME).

Western Blot Analysis

Cell lysates. BON and H727 cells were treated for two days with thiocoraline (0-40 nM) and protein extracts were harvested and quantified as previously described.[28,32] Denatured cellular extracts (30-40 µg) were subjected to gel electrophoresis on 7.5% or 10% SDS-PAGE (Invitrogen), transferred onto nitrocellulose membranes (Bio-Rad Laboratories, Hercules, CA), and blocked in milk solution.[33] Membranes were incubated overnight at 4°C with the appropriate primary antibody. The following primary antibodies were used at the following concentrations: anti-NOTCH1 (1:2000); anti-MASH1 (mammalian ASH1) to detect ASCL1 (1:2000; Pharmingen, San Diego, CA, USA); anti-CgA (1:1000; Zymed Laboratories Inc., San Francisco, CA, USA); anti-p21 (1:2000); anti-p27 (1:2000); anti-cyclin B1 (1:1000), anti-cyclin

D1 (1:1000), anti-NSE (1:2000), anti-glyceraldehyde-3 phosphate (GAPDH) (1:10,000; Trevigen Inc., Gaithersburg, MD, USA) and vinculin (1:2000; Cell Signaling, Danvers, MA, USA). Following primary antibody incubation, membranes were washed as previously described and incubated with secondary antibody.[33] The following secondary antibodies at the indicated dilutions were used: goat anti-rabbit (Notch1 1:4000, Cyclin D1 1:2000, p27 1:6000, CgA 1:4000, GAPDH 1:3000); goat anti-mouse (Cyclin B1 1:3000, p21 1:6000, ASCL1 1:5000, NSE 1:6000, and vinculin 1:2000). Following secondary antibody incubation, the membranes were washed as previously described.[32,33] Proteins were visualized using SuperSignal West Femto, West Dura, West Pico (Pierce), or Immunstar (Bio-Rad Laboratories) chemiluminescent substrate according to manufacturers' directions. The detection of GAPDH was used as a loading control.

Tumor Extracts. Tumor tissue (2 mm^3) was pulverized in the Cryoprep tissue homogenizer (Covaris, Woburn, MA) and the tissue powder was used for protein lysates preparation as described previously.[34] Briefly, the tissue powder was dissolved in 500 μL of lysis buffer containing 50 mM Tris, pH 7.5, 150 mM NaCl, 1% Igepal CA-630, 0.1% sodium dodecyl sulfate, 0.1 μM phenylmethylsulfonyl fluoride, 5 mM ethylene diaminetetraacetic acid, 12 μL/mL protease inhibitor cocktail (Sigma, St Louis, Missouri, USA); incubated on ice for 45 minutes; and centrifuged at 13,000 RPM for 30 minutes at 4 ^{o}C. The supernatants were collected, and protein concentration was determined by the bicinchoninic acid protein assay kit (Pierce, Rockford, Illinois, USA). Western blot analysis for Notch1 expression was performed as described above.

Quantitative Real-time PCR (qRT-PCR)

Following two-day thiocoraline (**37**) treatment, RNA was isolated using RNeasy Mini-kit (Qiagen, Valencia, CA) and reverse transcribed with the iScript cDNA synthesis kit (Bio-Rad). Quantitative real-time PCR was performed by the iCycler IQ detection system (Bio-Rad). A 25 µL volume reaction containing 2 µL cDNA sample (200 ng/µL), 200 nM forward and reverse primers, and 12.5 µL SYBR Green Supermix (Bio-Rad) was used. The following PCR forward and reverse primer pairs were used: Notch1 (5'-GTCAACGCCGTAGATGACCT-3' and 5'-TTGTTAGCCCCGTTCTTCAG-3'), HES1 (5'-TTGGAGGCTTCCAGGTGGTA-3' and 5'-GGCCCCGTTGGGAATG-3'), HES2 (5'-CTCATTTCGGACCTCGGTT-3' and 5'-TTCGAGCAGTTGGAGTTCT-3'), HES5 (5'-ACCGCATCAACAGCAGCATT -3' and 5'-AGGCTTTGCTGTGCTTCAGGT-3') and s27 (5'-TCTTTAGCCATGCACAAACG-3' and 5'-TTTCAGTGCTGCTTCCTCCT-3'), as a loading control. The RT-PCR reactions were performed in duplicate under previously described conditions.[34] Results were normalized to s27 mRNA levels and expression was plotted as average ± standard error of the mean (SEM).

Luciferase reporter assay

Notch1 functional activity was measured, by the degree of CBF1-binding, utilizing a luciferase construct containing four CBF1-binding sites (4xCBF1-Luc). BON cells were transiently transfected with CBF1-luciferase reporter construct and then treated with 0 or 30 nM of thiocoraline for 48 hours. To normalize for transfection efficiency, 0.5 μg of cytomegalovirus β-galactosidase (CMV-β-gal) was cotransfected as previously described.[32]

Statistical Analysis

Statistical analyses were performed using a one-way analysis of variance (ANOVA) and the Kruskal-Wallis rank sum test or by repeated measures ANOVA. A value of $p \leq 0.05$ was considered statistically significant.

Preparation of thiocoraline-incorporated polymeric micelle

Poly(ethylene glycol)-*block*-poly($_{D,\ L}$-lactide) (PEG-*b*-PLA; 7.4k-*b*-2.3k) was purchased from Advanced Polymer Materials Inc. (Montreal, Canada). The solvent evaporation method[35] was used for the preparation of thiocoraline-loaded PEG-*b*-PLA micelles. Briefly, 1, 3, or 5 mg of thiocoraline and 10, 30, or 50 mg of the polymer were completely dissolved in acetone and transferred into round bottom flasks. Acetone was evaporated under low pressure by rotary evaporation in a 60 ^{o}C water bath until a clear thin-layered film was formed. This film was rehydrated by adding 1 mL of 0.9% sodium chloride solution in 60 ^{o}C water bath. The rehydrated thiocoraline-incorporated PEG-*b*-PLA solution was centrifuged for 5 min at 10,000 g and filtered with 0.22 μm regenerated cellulose filter to remove unloaded thiocoraline and obtain a sterilized polymeric micelle solution. Thiocoraline (**37**) acquired aqueous solubility of 4.23 ± 1.15 mg/mL in water by forming polymeric micelles with PEG-*b*-PLA.

Quantification of thiocoraline encapsulated in polymeric micelle

The thiocoraline encapsulated in polymeric micelle was detected and quantified by UV Cary 100 Bio UV-visible spectrophotometer (Varian, Palo Alto, CA) at 360 nm.

Size distribution

Particle size distributions of PEG-*b*-PLA micelles containing thiocoraline (**37**) were determined by dynamic light scattering measurement using a Zetasizer Nano-ZS (Malvern Instruments, UK).

Maximum tolerate dose (MTD) study

Female 6-8 week-old balb/c mice were purchased from National Cancer Institute (Rockville, MD) and randomized into 6 groups. Empty vehicle, 5, 7, 10, 20, 30, and 40 mg/kg thiocoraline-incorporated PEG-*b*-PLA micelles were intravenously injected to mice and animal body weight changes were monitored for 8 consecutive days. Institutional guidelines were followed for maintenance of animals and end point of animal studies.

Xenograft study

Four-week-old male athymic nude mice were obtained from Charles Rivers (Wilmington, Maryland, USA). Before beginning the experiment, the mice were allowed to acclimate one week in the animal facility to reduce stress after arrival. Mice were maintained under specific pathogen-free conditions. BON cells stably transfected with the vector encoding the luciferase reporter gene *luc2* were subcutaneously inoculated into the left flank of mouse (5×10^6 cells/animal) in 100 µL of Hanks Balanced Salt Solution (Mediatech, Inc, Manassas, Virginia, USA). Fifteen days after inoculation, mice with palpable tumors were randomized into two groups (n=6), and intravenously (IV) injected with 5 mg/kg body weight (BW) thiocoraline-incorporated micelles and vehicle (empty PEG-*b*-PLA micelles), respectively. The treatment was repeated at day 22 and 29. Tumor volumes were measured from day 15 by external caliper every four days and then were calculated by the modified ellipsoidal formula: Tumor volume = ½ (length x width^2). Additionally, mice were imaged weekly using a cooled CCD camera (Xenogen IVIS) to validate the dynamics of tumor growth. In brief, 250 µL (3.75mg) of substrate D-Luciferin (Caliper Life Science, Hopkinton, MA) in PBS was injected intraperitoneally in each mouse 12 minutes prior to the whole-body imaging. The image acquisition and tumor size analysis based on the total photon counts of bioluminescence were done by using Live Imaging software (Caliper Life Science, Hopkinton, MA). At the end of the experiment, mice were sacrificed and the tumors were dissected from the surrounding tissues and flash frozen in liquid nitrogen for storage in -80 ^{o}C. Postmortem examination of the lungs, liver, kidneys, and spleen were performed to confirm that there was no evidence of metastases or tumor growth outside of the inoculation site. All experimental procedures were performed in compliance with our animal care protocol approved by the University of Wisconsin-Madison Research Animal Resources Committee in accordance with the NIH Guideline for the Care and Use of Laboratory Mice.

3.5. References

1. Pinchot, S.N.; Holen, K.; Sippel, R.S.; Chen, H. Carcinoid tumors. *Oncologist* **2008**, *13*, 1255-1269.

2. Sippel, R.S.; Chen, H. Carcinoid tumors. *Surg. Oncol. Clin. N. Am*. **2006**, *15*, 463-478.

3. Kulke, M.H.; Mayer, R.J. Carcinoid tumors. *N. Engl. J. Med*. **1999**, *340*, 858-868.

4. Schnirer, I.I.; Yao, J.C.; Ajani, J.A. Carcoinoid—a comprehensive review. *Acta Oncol*. **2003**, *42*, 672-692.

5. Taal, B.G.; Visser, O. Epidemiology of neuroendocrine tumours. *Neuroendocrinology* **2004**, *80 (Suppl 1)*, 3-7.

6. Modlin, I.M.; Lye, K.D.; Kidd, M. A 5-decade analysis of 13,715 carcinoid tumors. *Cancer* **2003**, *97*, 934-59.

7. Kunnimalaiyaan, M.; Chen, H. Tumor suppressor role of Notch-1 signaling in neuroendocrine tumors. *Oncologist* **2007**, *12*, 535-542.

8. Allenspach, E.J.; Maillard, I.; Aster, J.C.; Pear, W.S. Notch signaling in cancer. *Cancer Biol. Ther*. **2002**, *1*, 466-476.

9. Artavanis-Tsakonas, S.; Rand, M.D.; Lake, R.J. Notch signaling: Cell fate control and signal integration in development. *Science* **1999**, *284*, 770-776.

10. Bray, S.J. Notch signalling: A simple pathway becomes complex. *Nat. Rev. Mol. Cell. Biol*. **2006**, *7*, 678-689.

11. Pérez Baz, J.; Cañedo, L.M.; Fernández-Puentes, J.L.; Silva Elipe, M.V. Thiocoraline, a novel depsipeptide with antitumor activity produced by a marine *Micromonospora*. II. Physico-chemical properties and structure elucidation. *J. Antibiot*. **1997**, *50*, 738-741.

12. Romero, F.; Espliego, F.; Pérez Baz, J.; García de Quesada, T.; Grávalos, D.; De la Calle, F.; Fernández-Puentes, J.L. Thiocoraline, a new depsipeptide with antitumor activity produced by a marine *Micromonospora*. I. Taxonomy, fermentation, isolation, and biological activities. *J. Antibiot*. **1997**, *50*, 734-737.

13. Erba, E.; Bergamashi, D.; Ronzoni, S.; Faretta, M.; Taverna, S.; Bonfanti, M.; Catapano, C.V.; Faircloth, G.; Jimeno, J.; D'Incalci, M. Mode of action of thiocoraline, a natural marine compound with anti-tumour activity. *Br. J. Cancer*. **1999**, *80*, 971.

14. Negri, A.; Marco, E.; García-Hernández, V.; Domingo, A.; Llamas-Saiz, A.L.; Porto-Sandá, S.; Riguera, R.; Laine, W.; David-Cordonnier, M.H.; Bailly, C.; García-Fernández, L.F.; Vaquero, J.J.; Gago, F. Antitumore activity, X-ray crystal structure, and DNA binding properties of thiocoraline A, a natural bisintercalating thiodepsipeptide. *J. Med. Chem*. **2007**, *50*, 3322-3333.

15. Faircloth, G; Jimeno, J. D'lncalci, M. Biological activity of thiocoraline, a novel marine depsipeptide. *Eur. J. Cancer* **1997**, *33*, S175.

16. Erba, E.; Bergamashi, D.; Ronzoni, S.; Faretta, M.; Taverna, S.; Bonfanti, M.; Catapano, C.V.; Faircloth, G.; Jimeno, J.; D'Incalci, M. Mode of action of thiocoraline, a natural marine compound with anti-tumour activity. *Br. J. Cancer*. **1999**, *80*, 971.

17. Wyche, T.P.; Hou, Y.; Braun, D.; Cohen, H.C.; Xiong, M.P.; Bugni, T. S. First natural analogs of the cytotoxic thiodepsipeptide thiocoraline A from a marine *Verrucosispora* sp. *J. Org. Chem*. **2011**, *76*, 6542–6547.

18. Tesfazghi, S.; Eide, J.; Dammalapati, A.; Korlesky, C.; Wyche, T.P.; Bugni, T.S.; Chen, H.; Jaskula-Sztul, R. Thiocoraline alters neuroendocrine phenotype and activates the Notch pathway in MTC-TT cell line. *Cancer Med*. **2013**, *2*, 734-743.

19. Chen, H.; Udelsman, R.; Zeiger, M.; Ball, D. Human achaete-scute homolog-1 is highly expressed in a subset of neuroendocrine tumors. *Oncol. Rep.* **1997**, *4*, 775-778.

20. Oberg, K.; Janson, E.T.; Eriksson, B. Tumor markers in neuroendocrine tumours. *Ital. J. Gastroenterol. Hepatol.* **1999**, *31*, S160-S162 suppl 2.

21. Mohammed, T.A.; Holen, K.D.; Jaskula-Sztul, R.; Mulkerin, D.; Lubner, S.J.; Schelman, W.R.; Eickhoff, J.; Chen, H.; LoConte, N.K. A pilot Phast II study of valproic acid for treatment of low-grade neuroendocrine carcinoma. *Oncologist* **2011**, *16*, 835-843.

22. Boger, D.L.; Ichikawa, S. Total syntheses of thiocoraline and BE-22179: Establishment of relative and absolute stereochemistry. *J. Am. Chem. Soc.* **2000**, *122,* 2956-2957.

23. Boger, D.L.; Ichikawa, S.; Tse, W.C.; Hedrick, M.P.; Jin, Q. Total syntheses of thiocoraline and BE-22179 and assessment of their DNA binding and biological properties. *J. Am. Chem. Soc.* **2001**, *123* 561-568.

24. Tulla-Puche, J.; Góngora-Benítez, M.; Bayó-Puxan, N.; Francesch, A.M.; Cuevas, C.; Albericio, F. Enzyme-labile protecting groups for the synthesis of natural products: solid-phase synthesis of thiocoraline. *Angew. Chem. Int. Ed.* **2013**, *52*, 5726-5730.

25. Van der Westen, R.; Hosta-Rigau, L.; Sutherland, D.S.; Goldie, K.N.; Albericio, F.; Postma, A.; Städler, B. Myoblast cell interaction with polydopamine coated liposomes *Biointerphases* **2012**, *7***,** 1-9.

26. Lynge M.E.; Laursen, M.B.; Hosta-Rigau, L.; Jensen, B.E.; Ogaki, R.; Smith, A.A.; Zelikin, A.N.; Städler, B. Liposomes as drug deposits in multilayered polymer films. *ACS Appl. Mater. Interfaces* **2013**, *5* 2967-2975.

27. Parkekh D.; Ishizuka, J.; Townsend, C.M. Jr.; Haber, B.; Beauchamp, R.D.; Karp, G.; Kim S.W.; Rajaraman, S.; Greeley, G. Jr.; Thompson, J.C. Characterization of a human pancreatic carcinoid in vitro: morphology, amine and peptide storage, and secretion. *Pancreas* **1994**, *9*, 83-90.

28. Zarebczan, B.; Pinchot, S.N.; Kunnimalaiyaan, M.; Chen, H. Hesperetin, a potential therapy for carcinoid cancer. *Am. J. Surg*. **2011**, *201*, 329-332.

29. Kunnimalaiyaan, M.; Yan, S.; Wong, F.; Zhang, Y.; Chen, H. Hairy enhancer of split-1 (HES-1), a Notch1 effector, inhibits the growth of carcinoid tumor cells. *Surgery* **2005**, *138*, 1137-1142.

30. Valentino J.D.; Li, J.; Zaytseva, Y.Y.; Mustain, W.C.; Elliot, V.A.; Kim, J.T.; Harris, J.W.; Campbell, K.; Weiss, H.; Wang, C.; Song, J.; Anthony, L.; Townsend, C.M. Jr.; Evers, B.M. Cotargeting the PI3K and RAS pathways for the treatment of neuroendocrine tumors. *Clin. Cancer Res*. **2014**, *20*, 1212-1222.

31. Van Gompel, J.J.; Kunnimalaiyaan, M.; Holen, K.; Chen, H. ZM336372, a Raf-1 activator, suppresses growth and neuroendocrine hormone levels in carcinoid tumor cells. *Mol. Cancer Ther.* **2005**, *4*, 910-917.

32. Kunnimalaiyaan, M.; Vaccaro, A.M.; Ndiaye, M.A.; Chen, H. Overexpression of the NOTCH1 intracellular domain inhibits cell proliferation and alters the neuroendocrine phenotype of medullary thyroid cancer cells. *J. Biol. Chem.* **2006**, *281*, 39819-39830.

33. Jaskula-Sztul, R.; Pisarnturakit, P.; Landowski, M.; Chen, H.; Kunnimalaiyaan, M. Expression of the active Notch1 decreases MTC tumor growth in vivo. *J Surg Res.* **2011**, *171*, 23-27.

34. Vaccaro A.; Chen, H.; Kunnimalaiyaan, M. In-vivo activation of Raf-1 inhibits tumor growth and development in a xenograft model of human medullary thyroid cancer. *Anticancer Drugs* **2006**, *17*, 849-853.

35. Shin, H.-C.; Alani, A.W.; Cho, H.; Bae, Y.; Kolesar, J.M.; Kwon, G.S. A 3-in-1 polymeric micelle nanocontainer for poorly water-soluble drugs. *Mol. Pharmaceutics* **2011**, *8*, 1257-165.

Chapter 4:

Peptidolipins B-F, Antibacterial Lipopetides from an Ascidian-derived *Nocardia* sp.

Portions of this chapter have been previously published as:

Wyche, T.P., Hou, Y., Vazquez-Rivera, E., Braun, D., Bugni, T.S. Peptidolipins B-F, Antibacterial Lipopeptides from an Ascidian-Derived Nocardia sp. *J. Nat. Prod.* **75**, 735-740 (2012).

4.1. Introduction

Marine-derived actinomycetes have emerged as a rich source of secondary metabolites with therapeutic relevance,[1] as evidenced in Chapters 2 and 3. Marine *Nocardia* spp., while not investigated as extensively as other marine actinomycetes, have been a source of antibacterial compounds such as the nocathiacins,[2] nocardithiocin,[3] and chemomicin A.[4] Among the antibacterial compounds derived from terrestrial isolates of *Nocardia* spp. is the lipopeptide peptidolipin NA (**43**).[5] Peptidolipin NA belongs to a rare class of lipopeptides that are characterized by a peptide cyclized via an ester to a lipophilic tail; most lipopeptides, such as daptomycin,[6] do not cyclize through the lipophilic tail. Other members of this class of bacterial-derived compounds have been isolated from *Bacillus subtilis* and include surfactin,[7] iturin A,[8] and bacillomycin D.[9]

Originally isolated in 1966 from *Nocardia asteroides*,[5] peptidolipin NA (**43**) and its L-Val(6) analog (**44**) have demonstrated antibiotic activity and are known to form ion-conducting pores in lipid bilayers.[10] Small molecule interactions with lipid bilayers play an important role in several pharmacologically-relevant processes, such as the detection of specific signaling molecules such as inositol phosphates.[11] Additional studies[12,13] investigating the conformational and self-association properties of peptidolipin NA (**43**) and its L-Val(6) (**44**) analog have revealed considerable flexibility within the peptide backbone; the conformation of the peptide backbone depends on the solvent polarity.

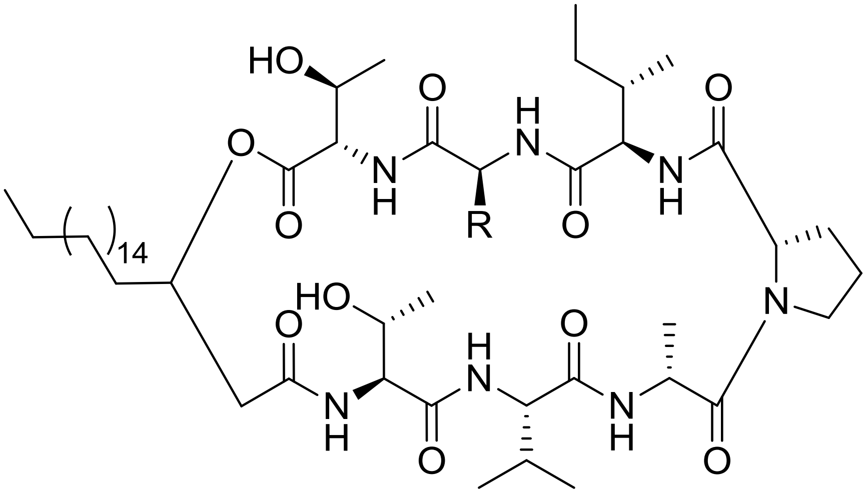

		R
43	Peptidolipin NA	Me
44	L-Val(6) Peptidolipin	*i*Pr

Five new lipopeptides, peptidolipins B-F (**45-49**) were isolated from a marine *Nocardia* sp. (Strain WMMB215), cultivated from the ascidian *Trididemnum orbiculatum* (Van Name, 1902). Peptidolipins B-F (**45-49**) were deemed similar to the L-Val(6) analog of peptidolipin NA (**44**). Each peptide contained a lipid chain; peptidolipin E (**48**) and F (**49**) contained an olefin and cyclopropyl group, respectively, within the lipid chain. A combination of NMR, mass spectrometry, synthetic modifications, and molecular modeling led to the elucidation of the structures.

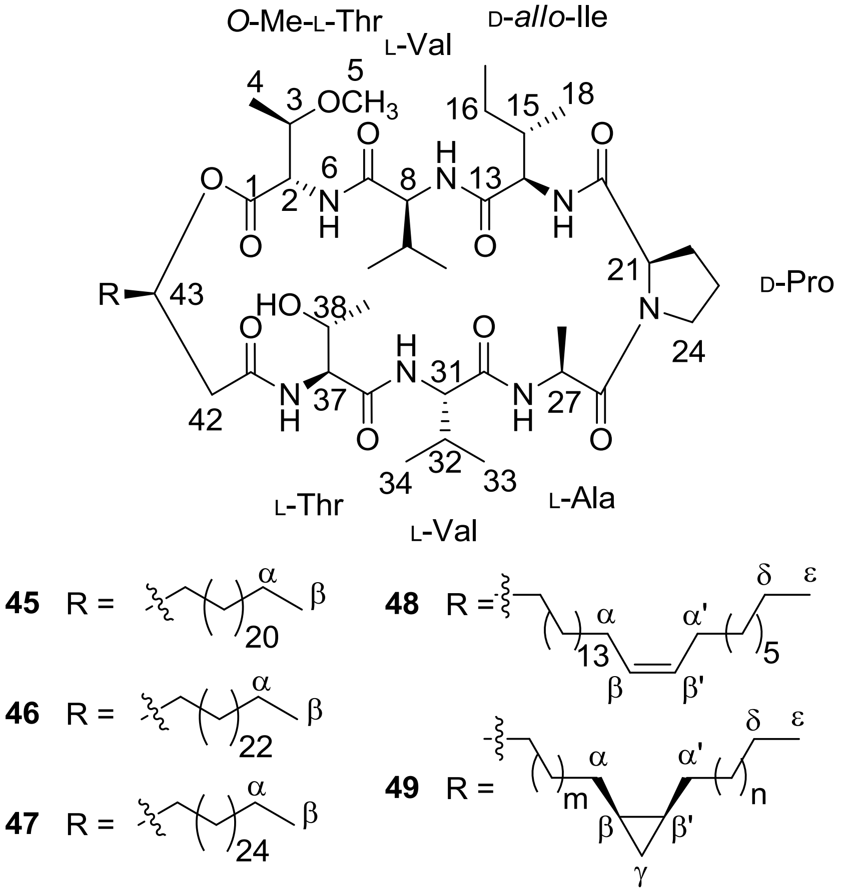

4.2. Results and Discussion

Strain WMMB215 was selected from 48 marine-derived bacterial extracts, which were analyzed by LCMS and PCA,[14] to investigate potentially new chemistry (Figure 4.1). The strains clustered into four major groups that were mainly segregated by genus. Strain WMMB215 was selected from the group of *Nocardia* spp. and was found to produce five new lipopeptides, which we named peptidolipins B-F (**45**-**49**).

HRMS supported the molecular formula of $C_{59}H_{107}N_7O_{11}$ for peptidolipin B (**45**). Extensive 1D and 2D NMR data (Table 4.1) were analyzed to establish the peptide backbone and the lactone. In particular, 2D ROESY, COSY, and HMBC NMR data were used to confirm the amino acid sequence (Figure 4.2). The presence of an *O*-Me threonine at C-5 (δ_H 3.38) in peptidolipin B (**45**) was the only difference in the peptide chain when compared to the L-Val(6) analog of peptidolipin NA (**44**). The Pro residue was assigned as *trans* based on the ^{13}C NMR

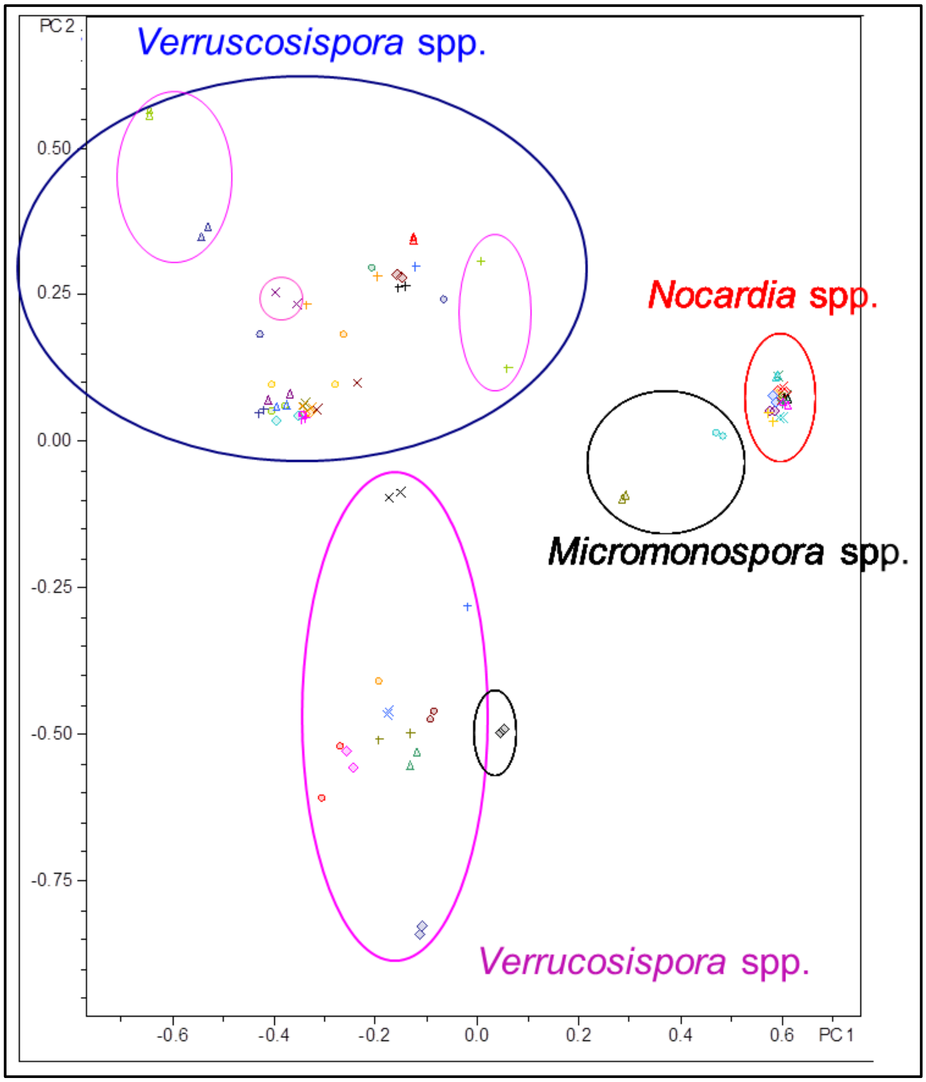

Figure 4.1. PCA analysis. The scores plot, in which each point signifies one bacterial strain, showed that strains grouped by genus. Rather than investigating every strain – a time-consuming procedure – one strain from each group was selected to represent the chemistry from each group as a whole. Strain WMMB215 was selected from the group of *Nocardia* spp. (upper right). While this example demonstrates one potential use of PCA for strain selection, Chapters 5-7 will highlight a different utility of the method.

shifts of the β- and γ-carbon atoms ($\Delta\delta_{\beta\gamma}$). $\Delta\delta_{\beta\gamma}$ for *trans*-Pro is regularly less than 5 ppm while $\Delta\delta_{\beta\gamma}$ for *cis*-Pro is regularly between 5 and 10 ppm.[15] $\Delta\delta_{\beta\gamma}$ for the proline residue in **45** was 0.1 ppm, supporting the assignment as *trans*. After determining the peptide portion of peptidolipin B (**45**), the lipid chain length was confirmed from analysis of the HRMS data.

Figure 4.2. Key ROESY and COSY correlations for **45**

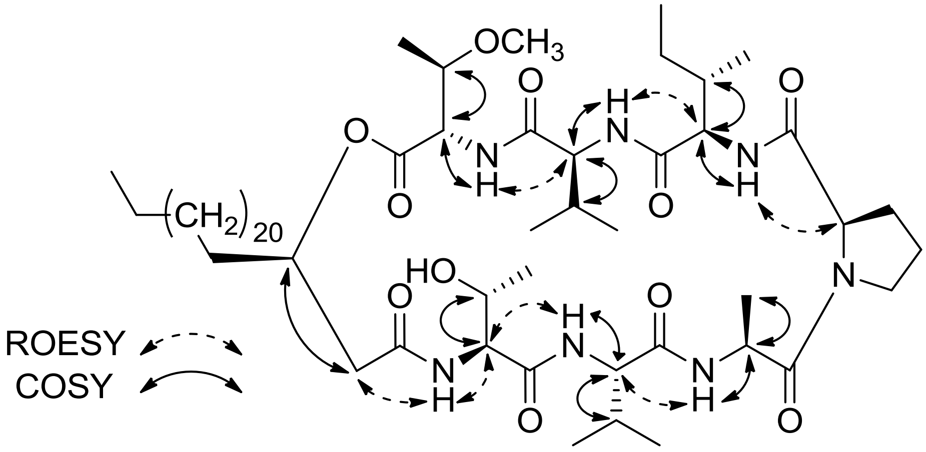

The advanced Marfey's method[16] was used to determine the absolute configuration of each amino acid. L-FDLA and DL-FDLA were synthesized from 1,5-difluoro-2,4-dinitrobenzene (DFDNB) and L- and DL-leucineamide hydrochloride, respectively.[17] The acid hydrolysate of peptidolipin B (**45**) was split into two equal portions and derivatized with L-FDLA and DL-FDLA, respectively. LCMS analysis of the L-FDLA and DL-FDLA products supported the assignment of L-Ala, L-Val(2), L-Val(6), and D-Pro. Amino acid standards derivatized with L-FDLA were used for the assignment of L-Thr, *O*Me-L-Thr, and D-*allo*-Ile. The absolute configurations of L-Ala and D-Pro in peptidolipin B (**45**) differed from the corresponding amino acids in L-Val(6) peptidolipin NA (**44**). Minor differences in the ^{1}H chemical shifts between L-Val(6) peptidolipin

Table 4.1. ^{1}H and ^{13}C NMR Data for **45** (600 MHz for ^{1}H, 150 MHz for ^{13}C, pyridine-d$_5$)

Position	δ_C, mult.	δ_H (J in Hz)	COSY	HMBC
1	170.9, C			
2	57.2, CH	5.35, m	3, 6	1
3	79.7, CH	4.16, m	2, 4	
4	14.3, CH$_3$	1.09, d (6.0)	3	
5	56.7, CH$_3$	3.38, s		
6- NH		9.46, d (10.2)	2	7
7	172.1, C			
8	59.0, CH	5.55, t (8.7)	12, 9	7, 9, 10, 11
9	32.8, CH	2.48, m	8, 10, 11	
10	19.83, CH$_3$	1.31, m	9	8
11	19.80, CH$_3$	1.28, m	9	8
12-NH		9.31, d (8.7)	8	13
13	173.4, C			
14	57.3, CH	5.07, m	15, 19	18
15	37.6, CH	2.13, m	14,18	
16	27.5, CH$_2$	1.54, m	17	14, 15
		1.31, m		
17	11.8, CH$_3$	0.80, t (7.5)	16	15, 16
18	14.5, CH$_3$	1.15, d (6.8)	15	14, 15, 16
19-NH		8.31, d (9.0)	18	
20	172.4, C			
21	58.9, CH	5.05, m		20 ,22, 24
22	24.7, CH$_2$	2.52, m	23	24
		1.54, m		
23	24.8, CH$_2$	2.01, m	22, 24	
		1.70, m		
24	46.2, CH$_2$	3.45, m	23	23
		3.40, m		
26	172.17, C			
27	48.3, CH	5.04, m	28, 29	26, 28
28	17.0, CH$_3$	1.68, d (6.4)	27	26, 27
29-NH		8.85, d (6.4)	27	27, 30
30	172.19, C			
31	59.2, CH	5.25, t (9.0)	32, 35	30, 32, 33
32	32.2, CH	2.31, m	31, 33, 34	31, 33
33	19.6, CH$_3$	1.19, d (6.8)	32	31, 32, 3
34	20.1, CH$_3$	1.24, m	32	31, 32, 33
35-NH		10.15, d (9.4)	31	36
36	171.9, C			
37	59.5, CH	5.38, m	38, 40	36, 38, 39
38	68.2, CH	4.45, m	37, 39	
38-OH		6.79, d (5.3)	38	
39	20.4, CH$_3$	1.46, d (6.0)	38	37, 38
40-NH		7.72, d (8.7)	37	41
41	169.6, C			
42	41.4, CH$_2$	2.89, dd (13.6, 3.8)	43	41, 43, 44
		2.59, dd (13.6, 3.8)		
43	72.6, CH	5.40, m	42, 44	
44	32.5, CH$_2$	1.87, m	43, 45	43
		1.82, m		
45	32.1, CH$_2$	1.23, m	44	
46-64	30.0-30.4, CH$_2$	1.2-1.4, m		
α	23.1, CH$_2$	1.25, m		β
β	14.4, CH$_3$	0.88, t (6.4)		α

NA and peptidolipin B (**45**) were observed and prevented us from making any additional conclusions regarding the differences in absolute configuration.

For the known peptidolipins, the absolute configuration at C-43 had not been assigned and prevented any comparisons. Several options were considered for determining the absolute configuration of C-43 in peptidolipin B (**45**). In theory, hydrolysis of the lactone and subsequent esterification using a chiral auxiliary would be sufficient. However, methanolysis of peptidolipin B (**45**) resulted in a complicated ^{1}H spectrum with significant peak broadening indicating multiple conformations. The conformational flexibility would preclude the use of a Mosher type method.[18] Complete hydrolysis would provide a secondary alcohol with little distinction among the adjacent methylene proton shifts and would likely not be amenable to a modified Mosher approach. Instead, the chiral BINOL borate method,[19] which compares the chemical shift of the methine hydrogen bonded to the stereogenic carbon, was attempted on the β–hydroxy acid hydrolysate of peptidolipin B (**45**). No change was observed in the ^{1}H chemical shifts of H-43 in the *R*- and *S*-BINOL borate derivatives (See Section 4.4), and consequently, another chemical derivatization method was pursued. Lipase B from *Candida antarctica* has been shown to selectively catalyze the hydrolysis of *R*-secondary acetates.[20,21] Methanolysis of peptidolipin B (**45**) followed by acetylation with acetic anhydride in pyridine,[21] resulted in a diacetylated derivative of peptidolipin B (**45**) (See Section 4.4). Addition of lipase B resulted in no reaction of either acetate. The lipophilicity of the diacetate derivative could limit availability of the diacetate derivative to enzymatic hydrolysis. Therefore, several chemical derivatization methods were inconclusive, and a density functional theory (DFT) study was used to assign the absolute configuration of C-43.

Ptak *et al*. demonstrated that multiple conformations were observed for peptidolipin NA (**43**) dependent on solvent polarity.[13] The NMR studies on peptidolipin NA (**43**) demonstrated that peptidolipin NA (**43**) adopted a stable conformation in pyridine and undergoes self-association in $CDCl_3$. Similarly, different conformations were observed for peptidolipins B-F (**45-49**) in pyridine-d_5 and $CDCl_3$, evidenced by considerable chemical shift differences for amide proton resonances. In pyridine-d_5, the amide proton resonances showed increased dispersion and were well resolved compared to $CDCl_3$ indicating stable hydrogen bonding. These results were in agreement with NMR studies performed on peptidolipin NA (**43**) and its L-Val(6) analog (**44**).[13] Careful analysis of the ROESY spectrum identified key transannular ROEs that would aid with analysis of results from molecular modeling to help confirm that the molecular modeling provided a conformation similar to that observed in pyridine-d_5.

Models for C-43 *R*- and *S*-peptidolipin B (**45**) were constructed with the lipid chain of peptidolipin B (**45**) truncated to a propyl group to limit conformational flexibility due to the lipid chain. Spartan 10[22] was used to identify the 20 lowest energy conformers for each stereoisomer using a Monte Carlo conformer search with the MMFF force field. For C-43 *R*-peptidolipin B, the three lowest energy conformers accounted for 99.9% of the room temperature populations based on the Boltzmann distribution. The Boltzmann population distribution was 93.9, 3.8, and 2.2%, with energies of 395.4, 403.2, and 404.5 kJ/mol, respectively. Likewise, Boltzmann distribution for the three lowest energy conformers for C-43 *S*-peptidolipin B was 60.2, 22.3, and 8.8%, with energies of 405.0, 407.5, and 409.8 kJ/mol, respectively. The calculated distributions suggested that one major conformer should be observed by ^1H NMR, paralleled our observation of a stable structure in pyridine, and suggested that a gas phase calculated structure could potentially mimic that observed in pyridine. In parallel with trying to identify the diastereomer that best matched the experimental NMR data, key ROE correlations and coupling constants were used to help confirm that the gas phase model was consistent with the solution structure in pyridine.

Figure 4.3. Molecular modeling of peptidolipin B (**45**)

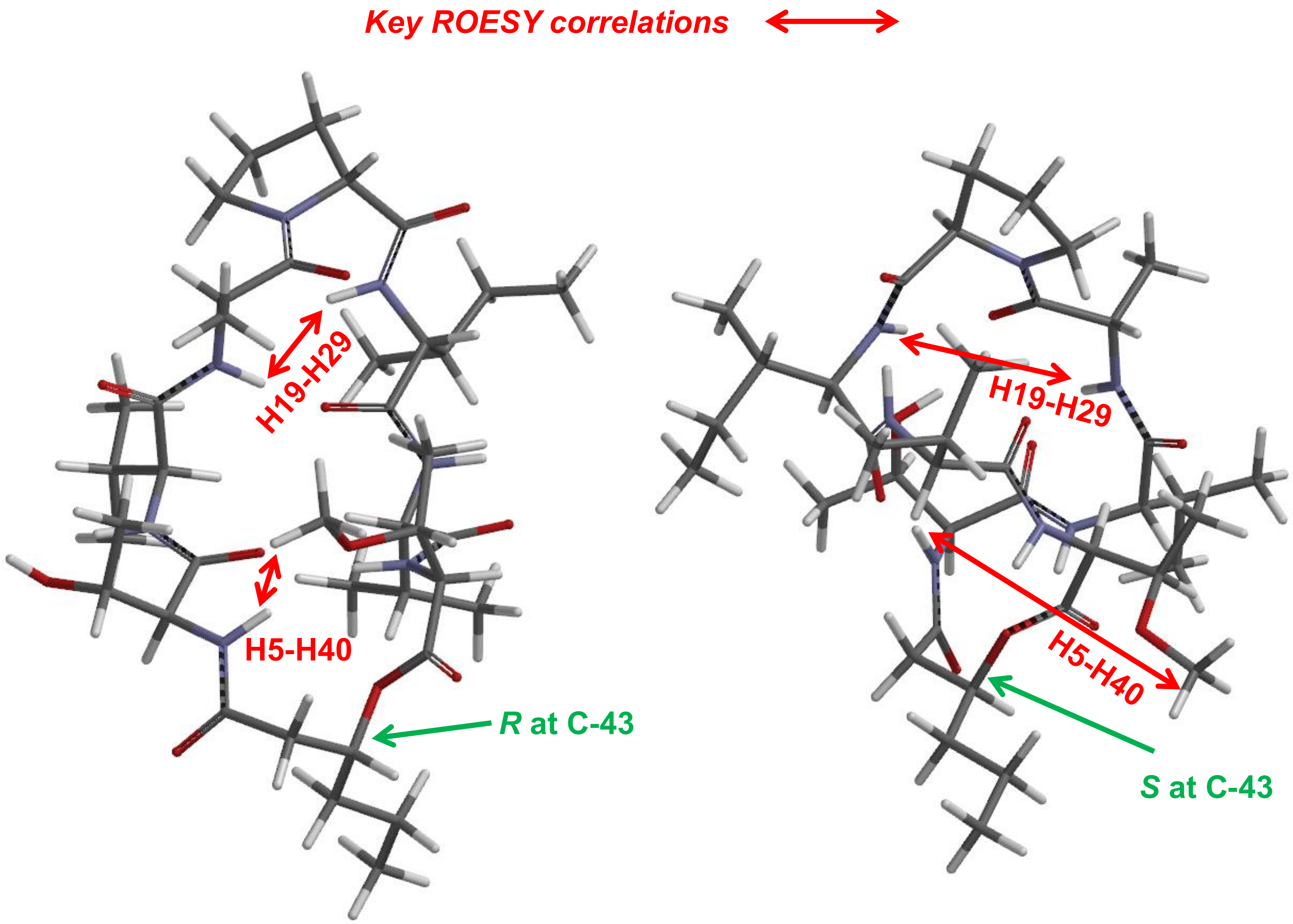

Correlation	*R*	*S*
H5-H40	2.897 Å	8.137 Å
H19-H29	2.737 Å	4.214 Å

The DP4 probability method[23] was used to compare the calculated NMR shifts for the two structures with the observed chemical shifts of peptidolipin B (**45**). For the low energy conformer of each epimer, Gaussian 09[24] was used for geometry optimization and NMR calculations (B3LYP/6-31G(d,p)).[25] A comparison of the experimental and calculated ^{13}C NMR shifts with the DP4 probability yielded a 100.0% probability for the *R* configuration compared to the *S* configuration (Figure A2.11). Additionally, key transannular ROE correlations between H-5 and H-40 as well as H-29 and H-19 were examined in each calculated structure (Figure 4.3).

The model of peptidolipin B (**45**) with the *R* configuration at C-43 fit both of these ROE correlations, but the model for the *S* C-43 did not fit with the correlation between H-5 and H-40. In addition to the ROE correlations, both H-42a and H-42b showed small vicinal $^{3}J_{\mathrm{H}}$ coupling constants of 3.8 Hz to H-43 which is consistent only with the model for C-43 *R*-peptidolipin B (**45**). The model for C-43 *R*-peptidolipin B (**45**) had a dihedral angle of 60.60°, consistent with a small coupling constant, while the model for C-43 *S*-peptidolipin B (**45**) had a dihedral angle of 156.28°, consistent with a large coupling constant.[26] Therefore, the absolute configuration of peptidolipin B (**45**) at C-43 was assigned *R* based on the calculated NMR shifts, ROE correlations, and a vicinal coupling constant.

HRMS supported the molecular formula of $C_{61}H_{111}N_7O_{11}$ for peptidolipin C (**46**) and $C_{63}H_{115}N_7O_{11}$ for peptidolipin D (**47**). Extensive analysis of 1D and 2D NMR data (Table 4.2) confirmed that **46** and **47** had the same cyclic peptide structure as peptidolipin B (**45**), and analysis of the HRMS data confirmed that the lipid chain contained two and four additional methylene groups for **46** and **47**, respectively. The absolute configurations in **46** and **47** were assigned the same as **45** due to a shared biogenesis and the identical chemical shifts.

Table 4.2. ^{1}H and ^{13}C NMR Data for **46** and **47** (600 MHz for ^{1}H, 150 MHz for ^{13}C, pyridine-d_5)

	46		**47**	
Position	δ_C, mult.	δ_H (J in Hz)	δ_C, mult.	δ_H (J in Hz)
1	170.9, C		170.9, C	
2	57.2, CH	5.35, m	57.2, CH	5.35, m
3	79.7, CH	4.15, m	79.7, CH	4.15, m
4	14.5, CH_3	1.08, d (6.0)	14.3, CH_3	1.08, d (6.4)
5	56.6, CH_3	3.38, s	56.7, CH	3.38, s
6- NH		9.45, d (10.2)		9.45, d (9.8)
7	172.1, C		172.1, C	
8	59.0, CH	5.55, t (8.3)	59.0, CH	5.56, t (8.7)
9	32.8, CH	2.47, m	32.9, CH	2.49, m
10	19.70, CH_3	1.31, m	19.83, CH_3	1.31, m
11	19.68, CH_3	1.28, m	19.80, CH_3	1.28, m
12-NH		9.29, d (8.3)		9.30, d (8.3)
13	173.4, C		173.4, C	
14	57.2, CH	5.06, m	57.2, CH	5.07, m
15	37.7, CH	2.12, m	37.7, CH	2.12, m
16	27.7, CH_2	1.53, m	27.4, CH_2	1.56, m
		1.31, m		1.33, m
17	12.1, CH_3	0.80, t (7.2)	11.8, CH_3	0.80, t (7.5)
18	14.8, CH_3	1.14, d (6.8)	14.6, CH_3	1.15, d (6.8)
19-NH		8.30, d (9.0)		8.31, d (9.4)
20	172.4, C		172.4, C	
21	58.9, CH	5.04, m	59.0, CH	5.05, m
22	24.8, CH_2	2.52, m	24.9, CH_2	2.53, m
		1.54, m		1.56, m
23	25.0, CH_2	1.99, m	24.9, CH_2	2.00, m
		1.68, m		1.70, m
24	46.2, CH_2	3.43, m	46.2, CH_2	3.45, m
		3.39, m		3.40, m
26	172.16, C		172.17, C	
27	48.3, CH	5.01, m	48.3, CH	5.03, m
28	17.3, CH_3	1.67, d (6.0)	17.0, CH_3	1.68, d (6.4)
29-NH		8.84, d (6.4)		8.85, d (6.4)
30	172.18, C		172.19, C	
31	59.2, CH	5.23, t (9.2)	59.2, CH	5.25, t (9.0)
32	32.2, CH	2.29, m	32.3, CH	2.31, m
33	20.0, CH_3	1.19, d (6.8)	19.6, CH_3	1.20, d (6.8)
34	20.2, CH_3	1.24, m	19.9, CH_3	1.24, m
35-NH		10.15, d (9.4)		10.15, d (10.2)
36	171.9, C		171.9, C	
37	59.4, CH	5.37, m	59.5, CH	5.39, m
38	68.2, CH	4.44, m	68.2, CH	4.44, m
38-OH		6.78, d (4.9)		6.77, d (4.1)
39	20.6, CH_3	1.45, d (6.0)	20.2, CH_3	1.46, d (6.4)
40-NH		7.72, d (8.7)		7.72, d (9.0)
41	169.6, C		169.6, C	
42	41.3, CH_2	2.88, dd (13.6, 3.4)	41.3, CH_2	2.88, dd (13.6, 3.8)
		2.58, m		2.57, dd (13.6, 2.6)
43	72.5, CH	5.39, m	72.5, CH	5.40, m
44	32.5, CH_2	1.86, m	32.6, CH_2	1.88, m
		1.81, m		1.83, m
45	32.5, CH_2	1.22, m	32.1, CH_2	1.22, m
46-64	30.0-30.4, CH_2	1.2-1.4, m	30.0-30.4, CH_2	1.2-1.4, m
α	23.2, CH_2	1.25, m	23.0, CH_2	1.26, m
β	14.6, CH_3	0.87, t (6.8)	14.6, CH_3	0.88, t (6.8)

HRMS supported the molecular formula of $C_{61}H_{109}N_7O_{11}$ for peptidolipin E (**48**) and $C_{64}H_{115}N_7O_{11}$ for peptidolipin F (**49**). On the basis of 1D and 2D NMR data the same cyclic peptide structure as peptidolipins B-D (**45-47**) was confirmed for **48** and **49**. The molecular formula for peptidolipin E (**48**) showed that **48** had an additional degree of unsaturation compared to peptidolipin B (**45**). As supported by chemical shifts of δ_H 5.52 (H-52, H-53) and δ_C 130.0 (C-52, C-53), peptidolipin E (**48**) had an olefin within the lipid chain. The olefin was assigned as *Z* based on the ^{13}C NMR chemical shifts of the allylic carbons.[27] Oxidative cleavage of the double bond in peptidolipin E (**48**) with sodium periodate and osmium tetroxide in aqueous THF formed aldehyde **50 (**Figure 4.4).[28] HRMS supported the molecular formula of $C_{52}H_{91}N_7O_{12}$ for aldehyde **50** with high mass accuracy (0.1 ppm error), indicating that the double bond was located at C-59 and C-60.

Figure 4.4. Oxidation of **48**

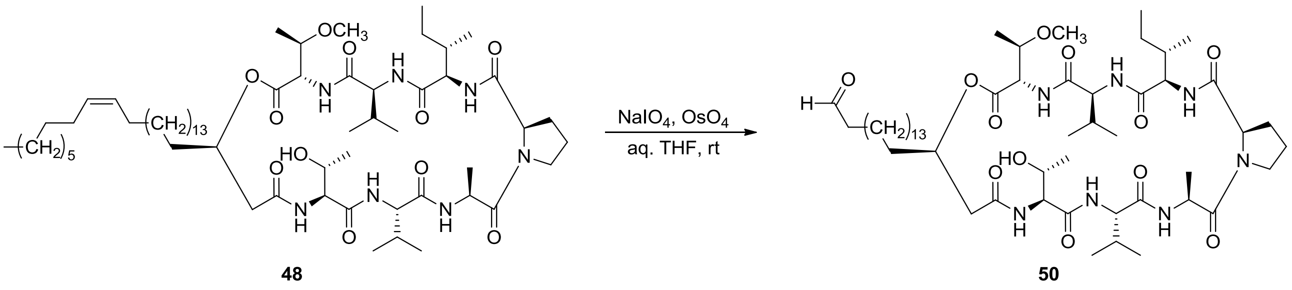

The molecular formula for peptidolipin F (**49**) indicated an additional carbon compared to peptidolipin D (**47**). The 1D NMR spectrum showed a multiplet at -0.19 ppm, characteristic of a diastereotopic hydrogen in a *cis* cyclopropyl group.[29] The geminal diastereotopic hydrogen at 0.68 ppm and adjacent methine protons at 0.75 ppm confirmed the presence of a cyclopropyl group. Previously, the location of cyclopropyl groups in lipid chains was determined by GCMS

Table 4.3. ^{1}H and ^{13}C NMR Data for **48** and **49** (600 MHz for ^{1}H, 150 MHz for ^{13}C, pyridine-d$_5$)

	48		**49**	
Position	δ_C, mult.	δ_H (J in Hz)	δ_C, mult.	δ_H (J in Hz)
1	170.9, C		170.9, C	
2	57.2, CH	5.35, m	57.2, CH	5.35, m
3	79.7, CH	4.16, m	79.7, CH	4.15, m
4	14.2, CH$_3$	1.09, d (5.7)	14.2, CH$_3$	1.08, d (6.4)
5	56.7, CH$_3$	3.38, s	56.7, CH	3.38, s
6- NH		9.46, d (10.0)		9.45, d (9.8)
7	172.1, C		172.1, C	
8	59.0, CH	5.55, t (8.6)	59.0, CH	5.55, t (8.7)
9	32.8, CH	2.48, m	32.9, CH	2.49, m
10	19.13, CH$_3$	1.31, m	19.82, CH$_3$	1.31, m
11	19.10, CH$_3$	1.28, m	19.79, CH$_3$	1.28, m
12-NH		9.30, d (8.1)		9.30, d (8.3)
13	173.4, C		173.4, C	
14	57.2, CH	5.07, m	57.3, CH	5.07, m
15	37.6, CH	2.13, m	37.7, CH	2.12, m
16	27.5, CH$_2$	1.54, m	27.5, CH$_2$	1.56, m
		1.31, m		1.33, m
17	12.1, CH$_3$	0.80, t (7.1)	11.9, CH$_3$	0.80, t (7.2)
18	14.5, CH$_3$	1.15, d (6.7)	14.7, CH$_3$	1.15, d (6.8)
19-NH		8.31, d (9.5)		8.31, d (9.4)
20	172.4, C		172.4, C	
21	59.0, CH	5.05, m	59.0, CH	5.05, m
22	24.8, CH$_2$	2.51, m	24.9, CH$_2$	2.53, m
		1.54, m		1.56, m
23	24.6, CH$_2$	2.00, m	24.8, CH$_2$	2.00, m
		1.70, m		
24	46.2, CH$_2$	3.44, m	46.2, CH$_2$	3.45, m
		3.39, m		3.40, m
26	172.18, C		172.18, C	
27	48.2, CH	5.04, m	48.3, CH	5.04, m
28	17.0, CH$_3$	1.68, d (6.0)	17.1, CH$_3$	1.68, d (6.4)
29-NH		8.85, d (6.4)		8.85, d (6.4)
30	172.20, C		172.20, C	
31	59.2, CH	5.24, t (9.3)	59.2, CH	5.25, t (9.0)
32	32.1, CH	2.31, m	32.3, CH	2.31, m
33	19.6, CH$_3$	1.20, d (6.7)	19.6, CH$_3$	1.20, d (6.8)
34	20.1, CH$_3$	1.24, m	20.1, CH$_3$	1.24, m
35-NH		10.15, d (9.3)		10.15, d (9.4)
36	171.9, C		171.9, C	
37	59.5, CH	5.38, m	59.5, CH	5.38, m
38	68.2, CH	4.45, m	68.2, CH	4.44, m
38-OH		6.79, d (4.0)		6.79, d (5.3)
39	20.4, CH$_3$	1.46, d (6.0)	20.4, CH$_3$	1.46, d (6.4)
40-NH		7.72, d (8.6)		7.72, d (8.7)
41	169.6, C		169.6, C	
42	41.4, CH$_2$	2.89, dd (13.4, 3.1)	41.4, CH$_2$	2.88, dd (13.6, 3.8)
		2.58, dd (13.4, 3.1)		2.58, dd (13.9, 2.6)
43	72.5, CH	5.40, m	72.6, CH	5.40, m
44	32.5, CH$_2$	1.88, m	32.6, CH$_2$	1.88, m
		1.82, m		1.82, m
45	32.2, CH$_2$	1.22, m	32.1, CH$_2$	1.23, m
46-62	30.0-30.4, CH$_2$	1.2-1.4, m	30.0-30.4, CH$_2$	1.2-1.4, m
α, α’	27.6, CH$_2$	2.13, m	29.5, CH$_2$	1.47, m
β, β’	130.0 CH	5.52, m	16.7, CH	0.75, m
γ			11.8, CH$_2$	0.68, m
				-0.19, m
			31.0, CH$_2$	1.46, m
δ	23.1, CH$_2$	1.26, m	23.1, CH$_2$	1.26, m
ε	14.4, CH$_3$	0.88, t (6.7)	14.5, CH$_3$	0.88, t (6.9)

of picolinyl ester derivatives of cyclopropyl-containing fatty acids.[30,31] Picolinyl esters of cyclopropyl-containing fatty acids showed defined fragmentation patterns when analyzed by GCMS and thus, provided important information for structure determination[30,31] while fragmentation of methyl ester lipids resulted in spectra that were difficult to interpret.[32] An attempt was made to use a similar approach to determine the location of the cyclopropyl group in peptidolipin F (**49**). Hydrolysis of **49** with 6 N HCl at 110 °C for 4 h[33] and extraction with $CHCl_3$ provided fatty acid **51**. Esterification of fatty acid **51** with 3-hydroxymethylpyridine under anhydrous conditions formed picolinyl ester **52** (Figure 4.5). Ester **52** was subjected to GCMS, but was not detected, potentially due to the large molecular weight of the compound. Ester **52** was observed by MALDI, but MALDI MSMS provided complicated fragmentation that was not useful to identify the location of the cyclopropyl group. In the end, the location of the cyclopropyl group was not determined.

Figure 4.5. Hydrolysis and Esterification of **49**

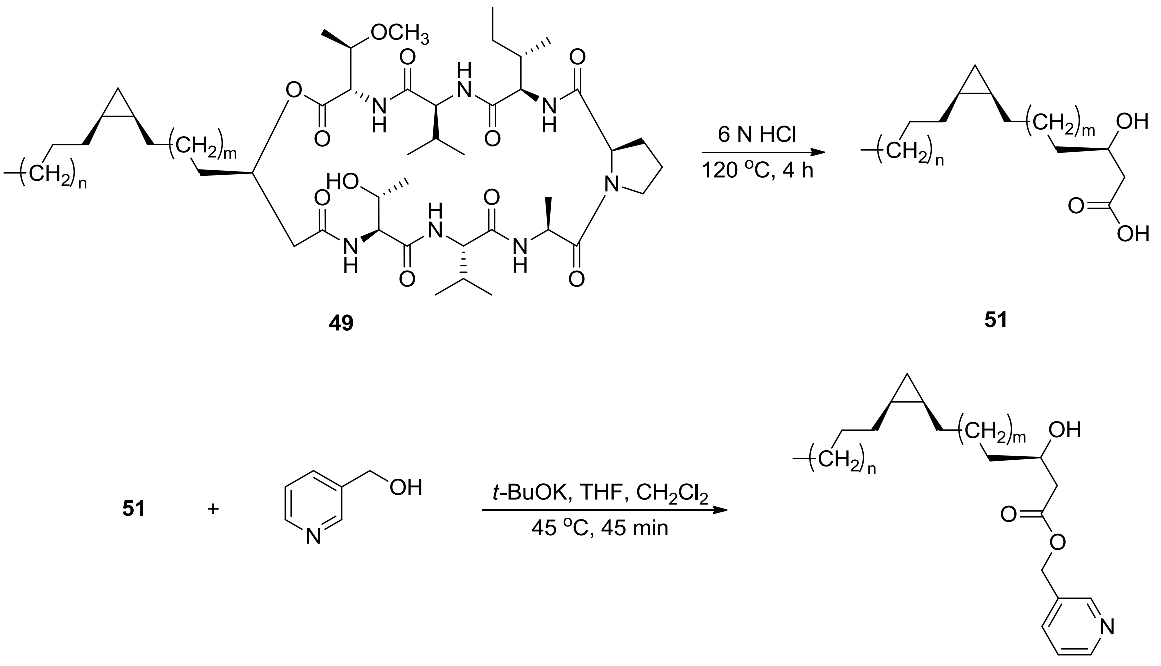

49

51

52

Peptidolipins B-F (**45**-**49**) were tested for antibacterial activity against methicillin-sensitive *Staphylococcus aureus* (MSSA) and methicillin-resistant *Staphylococcus aureus* (MRSA), and the minimum inhibitory concentration (MIC) was determined for each compound. Peptidolipins B (**45**) and E (**48**) were determined to have an MIC of 64 µg/mL against MSSA and MRSA. Peptidolipins C (**46**), D (**47**), and F (**49**) were determined to have an MIC of greater than 64 µg/mL against MSSA and MRSA. The bioactivity of peptidolipins B (**45**) and E (**48**) was similar to the moderate antibacterial activity reported for peptidolipin NA (**43**) and its L-Val(6) analog (**44**).[13] In order to identify if peptidolipins B (**45**) and E (**48**) were bactericidal or bacteriostatic, a sterile swab was dipped into each well that showed inhibition of bacterial growth and was inoculated on an LB plate. A bactericidal agent would show no growth on the LB plate while a bacteriostatic agent would show bacterial growth.[34] Therefore, bacterial growth of each sample on the LB plate suggested that peptidolipin B (**45**) and E (**48**) are bacteriostatic agents.

4.3. Conclusion

Peptidolipins B-F (**45**-**49**) were isolated from a marine *Nocardia* sp. and demonstrated conformational flexibility similar to peptidolipin NA (**43**) and its L-Val(6) analog (**44**). Peptidolipins B (**45**) and E (**48**) exhibited antibacterial activity against MRSA and MSSA and bacteriostatic action. The long lipophilic tail, containing between 23 and 27 carbons, in peptidolipins B-F (**45-49**) is unique among lipopeptides. Peptidolipin C (**46**) was subjected to a SciFinder similarity search to identify known compounds with similar structural features.[35] Of the 8268 compounds identified as having 65-99% similarity to peptidolipin C (**46**), no compound contained a lipophilic tail with greater than 17 carbons, demonstrating the unique structural features of the isolated compounds.

4.4. Materials and Methods

General Experimental Procedures

Optical rotations were measured on a Perkin–Elmer 241 Polarimeter. UV spectra were recorded on an Aminco/OLIS UV-Vis Spectrophotometer. IR spectra were measured with a Bruker Equinox 55/S FT–IR Spectrophotometer. NMR spectra were obtained in pyridine-d_5 with a Bruker Avance 600 MHz spectrometer equipped with a 1.7 mm $^1H\{^{13}C/^{15}N\}$ cryoprobe and a Bruker Avance 500 MHz spectrometer equipped with a $^{13}C/^{15}N\{^1H\}$ cryoprobe. HRMS data were acquired with a Bruker MaXis 4G QTOF mass spectrometer. RP HPLC was performed using a Shimadzu Prominence HPLC system and a Phenomenex Luna C18 column (250 × 10 mm, 5 µm). The Advanced Marfey's method utilized a Waters Acquity UPLC coupled with a Bruker MaXis 4G mass spectrometer.

Biological Material. Ascidian specimens were collected on October 11, 2010, in the Florida Keys (24° 37.487′, 81° 27.443′). Identification was confirmed by Shirley Parker-Nance. A voucher specimen (FLK10-5-1) for *Trididemnum orbiculatum* (Van Name, 1902) is housed at the University of Wisconsin-Madison. For cultivation, a sample of ascidian (1 cm^3) was rinsed with sterile seawater, macerated using a sterile pestle in a micro-centrifuge tube, and dilutions were made in sterile seawater, with vortexing between steps to separate bacteria from heavier tissues. Dilutions were separately plated on three media: ISP2, R2A, and M4. Each medium was supplemented with 50 µg/mL cycloheximide and 25 µg/mL nalidixic acid. Plates were incubated at 28 °C for at least 28 days.

Sequencing. 16S rDNA sequencing was conducted as previously described.[36] WMMB215 was identified as a *Nocardia* sp. and demonstrated 99% sequence similarity to *Nocardia araeonsis* W

9705 (accession number GQ376160.1). The 16S sequence for WMMB215 was deposited in GenBank (accession number JN638997).

Fermentation, Extraction, and Isolation. Two 10 mL seed cultures (25 × 150 mm tubes) in medium ASW-A (20 g soluble starch, 10 g glucose, 5 g peptone, 5 g yeast extract, 5 g $CaCO_3$ per liter of artificial seawater) were inoculated with strain WMMB215 and shaken (200 RPM, 28 °C) for seven days. Two hundred fifty mL baffled flasks (12 × 50 mL) containing ASW-A were inoculated with 1 mL seed culture and were incubated (200 RPM, 28 °C) for seven days. Two-liter flasks (24 × 500 mL) containing medium ASW-A with Diaion HP20 (4% by weight) were inoculated with 25 mL from the 50 mL culture and shaken (200 RPM, 28 °C) for seven days. Filtered HP20 and cells were washed with H_2O and extracted with acetone. The acetone extract (13.0 g) was subjected to liquid-liquid partitioning using 30% aqueous MeOH and $CHCl_3$ (1:1). The $CHCl_3$-soluble partition (2.2 g) was fractionated by Sephadex LH20 column chromatography ($CHCl_3$: MeOH, 1:1). Further separation was achieved by silica gel (SiO_2) column chromatography (10 g, 40-60 µm particle size) with hexanes and isopropanol (0-100%). Fractions containing **45-49**, eluted with 40% isopropanol, were combined and subjected to RP HPLC (2-50% CH_3CN-CH_2Cl_2, 30 min) using a Phenomenex Luna C18 column (250 × 10 mm, 5 µm), yielding **48** (2.0 mg, RT 25.5 min), **45** (1.8 mg, RT 26.4 min), **46** (5.5 mg, RT 28.0 min), **49** (1.1 mg, RT 28.7 min), and **47** (1.2 mg, RT 29.3 min).

Peptidolipin B (45): white solid; $[\alpha]^{25}_{D}$ +19 (c 0.1, $CHCl_3$); UV (MeOH) λ_{max} (log ε) 213 (4.64) nm; IR (ATR) υ_{max} 3279, 2926, 1742, 1641, 1546, 1458 cm^{-1}; ^1H and ^{13}C NMR (See Table 4.1); HRMS $[M+H]^+$ m/z 1090.8087 (calcd for $C_{59}H_{108}N_7O_{11}$, 1090.8101).

Peptidolipin C (46): white solid; $[\alpha]^{25}_{D}$ +21 (*c* 0.5, $CHCl_3$); UV (MeOH) λ_{max} (log ε) 210 (4.43) nm; IR (ATR) υ_{max} 3284, 2926, 1738, 1646, 1544, 1462 cm^{-1}; ^{1}H and ^{13}C NMR (See Table 4.2); HRMS $[M+H]^+$ *m/z* 1118.8407 (calcd for $C_{61}H_{112}N_7O_{11}$, 1118.8414).

Peptidolipin D (47): white solid; $[\alpha]^{25}_{D}$ +4.4 (*c* 0.1, $CHCl_3$); UV (MeOH) λ_{max} (log ε) 212 (4.83) nm; IR (ATR) υ_{max} 3278, 2928, 1743, 1643, 1543, 1464 cm^{-1}; ^{1}H and ^{13}C NMR (See Table 4.2); HRMS $[M+H]^+$ *m/z* 1146.8702 (calcd for $C_{63}H_{116}N_7O_{11}$, 1146.8727).

Peptidolipin E (48): white solid; $[\alpha]^{25}_{D}$ +20 (*c* 0.2, $CHCl_3$); UV (MeOH) λ_{max} (log ε) 213 (4.60) nm; IR (ATR) υ_{max} 3283, 2928, 1742, 1639, 1541, 1460 cm^{-1}; ^{1}H and ^{13}C NMR (See Table 4.3); HRMS $[M+H]^+$ *m/z* 1116.8233 (calcd for $C_{61}H_{110}N_7O_{11}$, 1116.8258).

Peptidolipin F (49): white solid; $[\alpha]^{25}_{D}$ +6.4 (*c* 0.09, $CHCl_3$); UV (MeOH) λ_{max} (log ε) 211 (4.51) nm; IR (ATR) υ_{max} 3287, 2926, 1735, 1648, 1542, 1460 cm^{-1}; ^{1}H and ^{13}C NMR (See Table 4.3); HRMS $[M+H]^+$ *m/z* 1158.8707 (calcd for $C_{64}H_{116}N_7O_{11}$, 1158.8727).

Molecular Modeling Calculations. Molecular modeling calculations were performed on a Dell Precision T5500 Linux workstation with a Xeon processor (3.3 GHz, 6-core). Low energy conformers were obtained using Spartan 10 software (MMFF, 10000 conformers examined). The low energy conformer for each compound was analyzed using Gaussian 09 for geometry optimization and NMR calculations (B3LYP/6-31G(d,p)). NMR shifts were referenced to TMS and benzene using the multi-standard (MSTD) approach.[37] Molecules were modeled in the gas phase.

Determination of Amino Acid Configurations. L- and DL-FDLA were synthesized as previously reported.[17] Peptidolipin B (**45**) (0.3 mg) was hydrolyzed with 6 N HCl (1 mL) for 4 h at 110 °C and dried under vacuum. The acid hydrolysate was dissolved in 100 µL H_2O and split into two equal portions. Each portion was mixed with 1 N $NaHCO_3$ (20 µL), acetone (110 µL), and 20 µL of L- or DL-FDLA (10 mg/mL in acetone). Each solution was stirred for 1 h at 40 °C. The reaction was quenched with 1 N HCl (20 µL) and dried under vacuum. A portion of each product was dissolved in MeOH:H_2O (1:1) for LCMS analysis. Separation of the derivatives was achieved with a Phenomenex Kinetex C18 reversed-phase column (2.6 µm, 150 x 2.0 mm) at a flow rate of 0.2 mL/min and with a linear gradient of H_2O (containing 0.1% formic acid) and MeOH (90:10 to 3:97 over 29 min). The absolute configurations of the amino acids were determined by comparing the retention times of the L- and DL-FDLA derivatives, which were identified by MS. Retention times of the DL-FDLA amino acid derivatives were 13.7 and 19.0 min (Ala), 13.2 and 15.7 min (Val), and 9.6 and 12.7 min (Pro). The retention times of the L-FDLA amino acid derivatives were 13.8 (L-Ala), 13.2 (L-Val(2) and L-Val (6)), and 12.3 min (D-Pro). The absolute configurations of the remaining amino acids were assigned based on a comparison of retention time of amino acid standards (L-Thr, D-*allo*-Ile, and *O*Me-L-Thr) derivatized with L-FDLA. The retention times of L-FDLA derivatives of the acid hydrolysate and the amino acid standards were identified at 11.2 (L-Thr), 11.9 (*O*Me-L-Thr), and 16.5 min (D-*allo*-Ile). The amino acids were assigned as L-Thr, L-Val(2), L-Ala, D-Pro, D-*allo*-Ile, L-Val(6), and *O*Me-L-Thr.

Aldehyde 50. Compound **48** (500 µg) was dissolved in THF and H_2O (1:1 v/v, 2 mL). While stirring, 60 mg $NaIO_4$ was added to the solution. OsO_4 (0.84 mg in H_2O) was slowly added to the solution. The solution was stirred at room temperature (rt) for 1 h. THF was removed using rotary evaporation, and the remaining aqueous phase was extracted twice with CH_2Cl_2. The CH_2Cl_2 portions were dried using rotary evaporation to yield about 300 µg of crude product, containing aldehyde **50**. The crude product was analyzed by ^1H NMR and HRESIMS to determine the structure of **50**. **50**: HRMS *m/z* 1006.6797 $[M+H]^+$ (calcd for $C_{52}H_{92}N_7O_{12}$, 1006.6798).

Ester 52. Compound **49** (500 µg) was dissolved in 6 N HCl (2 mL) and stirred at 120 °C for 4 h. After 4 h, the solution was cooled to rt and extracted with $CHCl_3$. The $CHCl_3$ layer was dried in vacuo to yield acid **51**. Acid **51** was dissolved in dry CH_2Cl_2 (500 µL) and added to a solution containing potassium *t*-butoxide (1.0 M) in THF (50 µL) and 3-hydroxymethylpyridine (100 µL). The mixture was held at 45 °C for 45 min. After 45 min, the reaction mixture was cooled to rt. H_2O (0.5 mL) and hexanes (1 mL) were added and vortexed. The organic phase was collected and dried under argon to yield ester **52**.

Chiral BINOL borate reaction. Peptidolipin B (**45**) (0.3 mg) was hydrolyzed with 6 N HCl (1 mL) for 4 h at 110 °C, extracted with $CHCl_3$, and dried under vacuum to form hydrolysate **53**. Hydrolysate **53** was separated into 2 equal portions, and 600 µL $CDCl_3$ was added to each portion. $B(OMe)_3$ (1 mM) and *S*- or *R*-BINOL (1 mM) were added to each portion in the

Figure 4.6. Chiral BINOL borate reaction

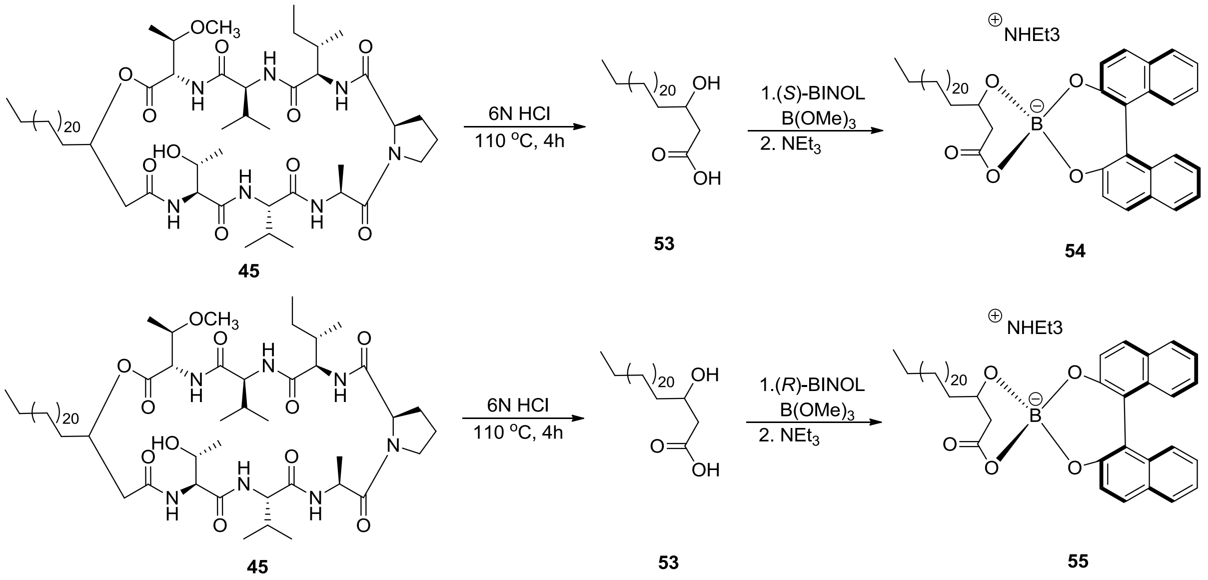

presence of 4 Å (8-12 mesh) molecular sieves. After gently mixing each solution for 10 min, NEt_3 (0.5 mM) was added, and the reaction solution was immediately transferred to an NMR tube for ^1H NMR acquisition. The chiral BINOL borate method was also attempted on L-(-)-3-phenyllactic acid and resulted in a downfield shift of the *S*-BINOL borate derivative, confirming that the reaction conditions were correct.

Lipase-catalyzed hydrolysis. Sodium methoxide (500 µL, 0.5 N) in methanol was added to peptidolipin B (**45**) (0.5 mg), and the solution was stirred for 14 h at rt to form alcohol **56**. Pyridine (100 µL) and acetic anhydride (50 µL) were added to alcohol **56** and stirred at rt for 24 h to form diacetate **57**. Diacetate **57** was dried under argon and dissolved in 30 µL isopropanol. Lipase B from *Candida antarctica* (1 mg, 9 units/mg) was dissolved in 900 µL 1X PBS. Lipase B solution (150 µL) was added to acetate **57** solution and stirred at 37 °C for 24 h. The solution was extracted with CH_2Cl_2 and resulted in no reaction. The absolute configuration at C-38 was previously determined to be *R* and therefore, should have resulted in hydrolysis of the secondary acetate. Thus, we can conclude that the reaction did not work with peptidolipin B (**45**).

Figure 4.7. Lipase-catalyzed hydrolysis

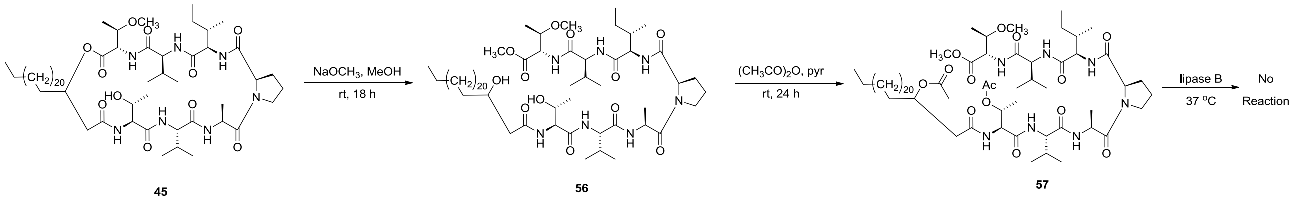

Antibacterial Assay. Peptidolipins B-F (**45-49**) were tested for antibacterial activity against MSSA (ATCC #29213) and MRSA (ATCC #33591), and MICs were determined using a dilution antimicrobial susceptibility test for aerobic bacteria.[38] Peptidolipins B-F (**45-49**) were dissolved in DMSO, serially diluted to 10 concentrations (0.125 – 64 µg/mL), and tested in a 96-well plate. Vancomycin was used as a control and exhibited an MIC of 1 µg/mL against MSSA and 1 µg/mL against MRSA. Peptidolipins B-F (**45-49**) were tested in triplicate, and vancomycin was tested in triplicate. Six untreated media controls were included on each plate. The plates were incubated at 33 °C for 18 h. The MIC was determined as the lowest concentration that inhibited visible growth of bacteria.

4.5. References

1. Fenical, W.; Jensen, P.R. Developing a new resource for drug discovery: marine actinomycete bacteria. *Nat. Chem. Biol*. **2006**, *2*, 666-673.

2. Li, W.; Leet, J.E.; Ax, H.A.; Gustavson, D.R.; Brown, D.M.; Turner, L.; Brown, K.; Clark, J.; Yang, H.; Fung-Tomc, J.; Lam, K.S. Nocathiacin, new thiazolyl peptide antibiotics from Nocardia sp. I. Taxonomy, fermentation and biological activities. *J. Antibiot*. **2003**, *56*, 226-231.

3. Mukai, A.; Fukai, T.; Hoshino, Y.; Yazawa, K.; Harada, K.; Mikami, Y. Nocardithiocin, a novel thiopeptide antibiotic, produced by pathogenic Nocardia pseudobrasiliensis IFM 0757. *J. Antibiot*. **2009**, *62*, 613-619.

4. Sun, C.; Wang, Y.; Wang, Z.; Zhou, J.; Jin, W.; You, X.; Gao, H.; Zhao, L.; Si, S.; Li, X. Chemomicin A, a new angucyclinone antibiotic produced by Nocardia mediterranei subsp. *kanglensis* 1747-64. *J. Antibiot*. **2007**, *60*, 211-215.

5. Guinand, M.; Michel, G. Structure of a peptidolipid isolated from Nocardia asteroides, peptidolipin NA. *Biochim Biophys Acta*. **1966**, *125*, 75-91.

6. Eliopoulos, G.M.; Willey, S.; Reiszner, E.; Spitzer, P.G.; Caputo, G.; Moellering, R.C. In vitro and in vivo activity of LY146032, a new cyclic lipopeptide antibiotic. *Antimicrob. Agents Chemother*. **1986**, *30*, 532-535.

7. Arima, K.; Kakinuma, A.; Tamura, G. Surfactin, a crystalline peptidelipid surfactant produced by Bacillus subtilis: isolation, characterization and its inhibition of fibrin clot formation. *Biochem. Biophys. Res. Commun.* **1968**, 31, 488-94.

8. Delcambe, L.; Peypoux, F.; Besson, F.; Guinand, M.; Michel, G. Structure of iturin and iturin-like substances. *Biochem. Soc. Trans*. **1977**, *5*, 1122-1124.

9. Peypoux, F.; Besson, F.; Michel, G.; Delcambe, L. Structure of bacillomycin D, a new antibiotic of the iturin group. *Eur. J. Biochem*. **1981**, *118*, 323-327.

10. Maget-Dana, R.; Heitz, F.; Ptak, M.; Peypoux, F.; Guinand, M. Bacterial lipopeptides induce ion-conducting pores in planar bilayers. *Biochem. Biophys. Res. Commun*. **1985**, *129*, 965-971.

11. Scheidt, H.A.; Huster, D. The interaction of small molecules with phospholipid membranes studied by ^{1}H NOESY NMR under magic-angle spinning. *Acta Pharmacol. Sin*. **2008**, *29*, 35-49.

12. Ptak, M.; Heitz, A.; Guinand, M.; Michel, G. A 400 MHz ^{1}H NMR study of peptidolipin NA, a natural cyclic lipopeptide. *Biochem. Biophys. Res. Commun*. **1980**, *94*, 1311-1318.

13. Ptak, M.; Heitz, A.; Guinand, M.; Michel, G. 400 MHz ^{1}H NMR study of the conformation and self-association of peptidolipin NA. *Int. J. Biol. Macromol*. **1982**, *4*, 79-90.

14. Hou, Y.; Braun, D.R.; Michel, C.R.; Klassen, J.L.; Adnani, N.; Wyche, T.P.; Bugni, T.S. Microbial strain prioritization using metabolomics tools for the discovery of the natural products. *Anal. Chem*. **2012**, *84*, 4277-4283.

15. Siemion, I.Z.; Wieland, T.; Pook, K.H. Influence of the distance of the proline carbonyl from the beta and gamma carbon on the ^{13}C chemical shifts. *Angew. Chem. Int. Ed*. **1975**, *14*, 702-703.

16. Fujii, K.; Ikai, Y.; Oka, H.; Suzuki, M.; Harada, K. A nonempirical method using LC/MS for determination of the absolute configuration of constituent amino acids in a peptide: Combination of Marfey’s method with mass spectrometry and its practical application. *Anal. Chem.* **1997**, *69*, 5146–5151.

17. Marfey, P. Determination of D-amino acids. II. Use of a bifunctional reagent, 1,5-difluoro-2,4-dinitrobenzene. *Carlsberg Res. Commun*. **1984**, *49*, 591-596.

18. Dale, J.A.; Mosher, H.S. Nuclear magnetic resonance enantiomer reagents. Configurational correlations via nuclear magnetic resonance chemical shifts of diastereomeric mandelate, O-methylmandelate, and α-methoxy-α-trifluoromethylphenylacetate (MTPA) esters. *J. Am. Chem. Soc*. **1973**, *95*, 512-519.

19. Freire, F.; Quiñoá, E.; Riguera, R. In tube determination of the absolute configuration of alpha- and beta-hydroxy acids by NMR via chiral BINOL borates. *Chem. Commun*. **2008**, 4147-4149.

20. Ohtanib, T.; Nakatsukasaa, H.; Kamezawab, M.; Tachibanab, H.; Naoshimaa, Y. Enantioselectivity of Candida antarctica lipase for some synthetic substrates including aliphatic secondary alcohols. *J. Mol. Catal. B: Enzym.* **1998**, *4*, 53-60.

21. Whitson, E.L.; Ratnayake, A.S.; Bugni, T.S.; Harper, M.K.; Ireland, C.M. Isolation, structure elucidation, and synthesis of eudistomides A and B, lipopeptides from a Fijian ascidian Eudistoma sp. *J. Org. Chem.* **2009**, *74*, 1156-1162.

22. Deppmeier, B.J.; Driessen, A.J.; Hehre, T.S.; Hehre, W.J.; Johnson, J.A.; Klunzinger, P.E.; Leonard, J.M.; Ohlinger, W.S.; Pham, I.N.; Pietro, W.J.; Yu, J. *Spartan 10*, v. 1.0.2.; Wavefunction Inc.: Irvine, CA, 2011.

23. Smith, S.G.; Goodman, J.M. Assigning stereochemistry to single diastereoisomers by GIAO NMR calculation: the DP4 probability. *J. Am. Chem. Soc.* **2010**, *132*, 12946-12959.

24. Gaussian 09, Revision A.1, Frisch, M. J.; Trucks, G. W.; Schlegel, H. B.; Scuseria, G. E.; Robb, M. A.; Cheeseman, J. R.; Scalmani, G.; Barone, V.; Mennucci, B.; Petersson, G. A.; Nakatsuji, H.; Caricato, M.; Li, X.; Hratchian, H. P.; Izmaylov, A. F.; Bloino, J.; Zheng, G.; Sonnenberg, J. L.; Hada, M.; Ehara, M.; Toyota, K.; Fukuda, R.; Hasegawa, J.; Ishida, M.; Nakajima, T.; Honda, Y.; Kitao, O.; Nakai, H.; Vreven, T.; Montgomery, Jr., J. A.; Peralta, J. E.; Ogliaro, F.; Bearpark, M.; Heyd, J. J.; Brothers, E.; Kudin, K. N.; Staroverov, V. N.; Kobayashi, R.; Normand, J.; Raghavachari, K.; Rendell, A.; Burant, J. C.; Iyengar, S. S.; Tomasi, J.; Cossi, M.; Rega, N.; Millam, N. J.; Klene, M.; Knox, J. E.; Cross, J. B.; Bakken, V.; Adamo, C.; Jaramillo, J.; Gomperts, R.; Stratmann, R. E.; Yazyev, O.; Austin, A. J.; Cammi, R.; Pomelli, C.; Ochterski, J. W.; Martin, R. L.; Morokuma, K.; Zakrzewski, V. G.; Voth, G. A.; Salvador, P.; Dannenberg, J. J.; Dapprich, S.; Daniels, A. D.; Farkas, Ö.; Foresman, J. B.; Ortiz, J. V.; Cioslowski, J.; Fox, D. J. Gaussian, Inc., Wallingford CT, 2009.

25. Stappen, I.; Buchbauer, G.; Robien, W.; Wolschann, P. ^{13}C NMR spectra of santalol derivatives: a comparison of DFT-based calculations and database-oriented prediction techniques. *Magn. Reson. Chem.* **2009**, *47*, 720-726.

26. Karplus, M. Vicinal proton coupling in nuclear magnetic resonance. *J. Am. Chem. Soc.* **1963**, *85*, 2870–2871.

27. Carpita, A.; Quirici, M. G.; Veracini, C. A. Insect pheromone components: Use of ^{13}C NMR spectroscopy for assigning the configuration of C-C double bonds of monoenic or dienic pheromone components and for quantitative determination of *Z*/*E* mixtures. *Tetrahedron* **1982**, *38*, 639-644.

28. Rappo, R.; Allen, D.S., Jr.; Lemieux, U.; Johnson, W.S. Osmium tetroxide-catalyzed periodate oxidation of olefinic bonds. *J. Org. Chem.* **1956**, *21*, 478-479.

29. Knothe, G. NMR characterization of dihydrosterculic acid and its methyl ester. *Lipids* **2006**, *41*, 393-396.

30. Destaillats, F.; Angers, P. One-step methodology for the synthesis of FA picolinyl esters from intact lipids. *J. Am. Oil Chem. Soc*. **2002**, *79*, 253-256.

31. Harvey, D.J. Picolinyl esters as derivatives for the structural determination of long chain branched and unsaturated fatty acids. *Biomed. Mass Spectrom*. **1984**, *11*, 187-192.

32. Hanus, L.O.; Goldshlag, P.; Dembitsky, V.M. Identification of cyclopropyl fatty acids in walnut (Juglans regia L.) oil. *Biomed. Pap. Med. Fac. Univ. Palacky. Olomouc Czech Repub*. **2008**, *152*, 41-45.

33. Laird, D.W.; LaBarbera, D.V.; Feng, X.; Bugni, T.S.; Harper, M.K.; Ireland, C.M. Halogenated cyclic peptides isolated from the sponge Corticium sp. *J. Nat. Prod*. **2007**, *70*, 743-746.

34. Pankey, G.A.; Sabath, L.D. Clinical relevance of bacteriostatic versus bactericidal mechanisms of action in the treatment of gram-positive bacterial infections. *Clin. Infect. Dis*. **2004**, *38*, 864-870.

35. *SciFinder,* version 2011.1; Chemical Abstracts Service: Columbus, OH, 2011; (accessed 04 Jan 2012).

36. Wyche, T. P.; Hou, Y.; Braun, D.; Cohen, H. C.; Xiong, M. P.; Bugni, T. S. First natural analogs of the cytotoxic thiodepsipeptide thiocoraline A from a marine Verrucosispora sp. *J. Org. Chem*. **2011**, *76*, 6542–6547.

37. Sarotti, A.M.; Pellegrinet, S.C. A multi-standard approach for GIAO ^{13}C NMR calculations. *J. Org. Chem*. **2009**, *74*, 7254-7260.

38. National Committee for Clinical Laboratory Standards. *Methods for Dilution Antimicrobial Susceptibility Tests for Bacteria that Grow Aerobically*, 7th ed.; NCCLS: Villanova, PA, 2006; Approved standard M7-A7.

Chapter 5:

Activation of the Nuclear Factor E2-related Factor 2 Pathway by Novel Natural Products Halomadurones A-D and a Synthetic Analog

Portions of this chapter have been previously published as:

Wyche, T.P., Standiford, M., Hou, Y., Braun, D., Johnson, D.A., Johnson, J.A., Bugni, T.S. Activation of the nuclear factor E2-related factor 2 pathway by novel natural products halomadurones A-D and a synthetic analogue. *Marine Drugs*. **11**, 5089-5099 (2013).

5.1. Introduction

The prevalence of neurodegenerative diseases, such as Alzheimer's disease (AD), Parkinson's disease, Huntington's disease, and amyotrophic lateral sclerosis (ALS) is on the rise worldwide;[1-3] cases of AD, the most common neurodegenerative disease, are projected to reach 115 million by the year 2050.[3] Meanwhile, only a handful of therapeutics are available that target these diseases, most of which only treat the symptoms not the underlying cause. Many neurodegenerative diseases are caused by mitochondrial DNA mutation or oxidative stress damage.[4] Therefore, determining methods of minimizing oxidative stress is a potential strategy towards preventing many neurodegenerative diseases.[5-6]

The transcription factor Nrf2 (nuclear factor E2-related factor) activates the antioxidant response element (ARE), which is located in the promoter region of genes that encode cytoprotective and antioxidant enzymes including many phase II detoxification enzymes.[7-9] Therefore, activation of Nrf2 represents a promising therapeutic strategy for combatting neurodegenerative diseases. In order to identify activators of this pathway in conjunction with having an *in vivo* model for evaluating therapeutics for neurodegenerative diseases, a transgenic mouse model was created that contained a human placental alkaline phosphatase reporter under the control of the ARE. For *in vitro* testing, primary neuronal cells from ARE-hPAP transgenic reporter were used to test for Nrf2/ARE activation.[10-11] The use of primary neuronal cells has provided an *in vitro* model that most closely resembles the *in vivo* pathology, albeit without the blood brain barrier. In parallel, the 3-(4,5)-dimethylthiazol-2-yl)-5-(3-carboxymethoxyphenyl)-2-(4-sulfophenyl) 2H tetrazolium inner salt (MTS) assay can be used to test toxicity of the compounds. There have been only limited reports on natural product pharmacophores that activate the Nrf2/ARE pathway. The vast majority have been electrophiles, such as Michael acceptors.[12-16] More recently, activation of the Nrf2-ARE pathway with small molecules was also investigated by Luesch and co-workers leading to the discovery of Nrf2-ARE activators from seaweed extracts[17] and an electrophile ARE activator with *in vivo* activity.[16]

In our pursuit of Nrf2/ARE activators, this chapter reports the isolation of four novel halogenated polyketides that were named halomadurones A-D (**58-61**), from a marine *Actinomadura* sp. (Strain WMMB499) cultivated from the ascidian *Ecteinascidia turbinata* (Herdman, 1880). Halomadurones C (**60**) and D (**61**) demonstrated potent nuclear factor E2-related factor antioxidant response element (Nrf2-ARE) activation in the ARE-hPAP assay. The cytotoxicity studies and activity in the ARE-hPAP assay indicated a narrow therapeutic window. Synthesis of a non-halogenated pyrone (**62**) demonstrated that bromination was a key feature of the pharmacophore.

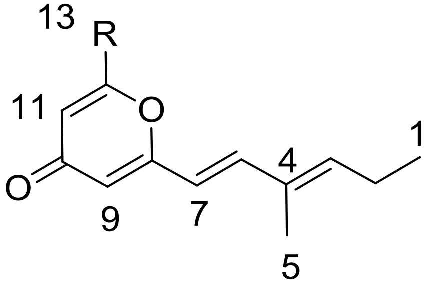

	R
58	$-CCl_3$
59	$-CHCl_2$
60	$-CHBrCl$
61	$-CHBr_2$
62	$-CH_3$

In addition to the promising *in vitro* activity, halomadurones A–D (**58**–**61**) represent a new carbon skeleton due to the position of the methyl group. Additionally, halomadurone A (**58**) contains a trichloromethyl group, which is a rare moiety in natural products. Most natural products that contain a trichloromethyl group, such as barbamide A[18] and dysidenamide,[19] were isolated from cyanobacteria and also contain a thiazole ring. However, cytotoxic trichlorinated polyenones neocarzilin A (**63**) and B (**64**)[20] were produced by the soil-derived bacterium *Streptomyces carzinostaticus* and do not contain a thiazole ring. Consequently, neocarzilins A (**63**) and B (**64**), which have been the target for various synthetic[21] and biosynthetic studies,[22] are now joined by halomadurone A (**58**) as the sole members of actinomycete-derived trichlorinated natural products. The role of the trichloromethyl group in bioactivity was investigated with halomadurones A-D (**58-61**) and a non-halogenated analog, 2-methyl-6-((*E*)-3-methyl-1,3-hexadiene)-γ-pyrone (**62**), which we synthesized.

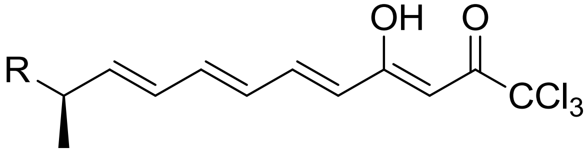

	R
63	CH_2CH_3
64	CH_3

Finally, the halomadurones were used as a proof of concept to test the application of a ^{13}C-^{13}C gCOSY for structure determination. While the gCOSY requires isotopic enrichment, ^{13}C-optimized cryoprobes drastically reduce the amount of compound needed and the amount of U-^{13}C glucose required, thereby making the route economically feasible. To support this proof of concept, the ^{13}C-^{13}C gCOSY was compared to the more commonly known 2D

INADEQUATE; the minimum amount of ^{13}C-labeled compound necessary to acquire the ^{13}C-^{13}C gCOSY was determined.

5.2. Results and discussion

Bacterial strain selection and structure elucidation

Our attention was drawn to strain WMMB499 after analysis of thirty-four marine-derived bacterial extracts using LCMS-based metabolomics relying on principal component analysis (PCA).[23] When compared to the other 33 LCMS chromatograms using PCA, WMMB499 was identified as having unique chemical signatures and putative novel natural products (Figure 5.1); after saline fermentation and isolation, WMMB499 was found to produce halomadurones A (**58**) and B (**59**). Halomadurones C (**60**) and D (**61**) were produced by WMMB499 by increasing the ratio KBr/NaCl. Previous studies have demonstrated that many halogenases are promiscuous with respect to using Br and Cl.[24,25]

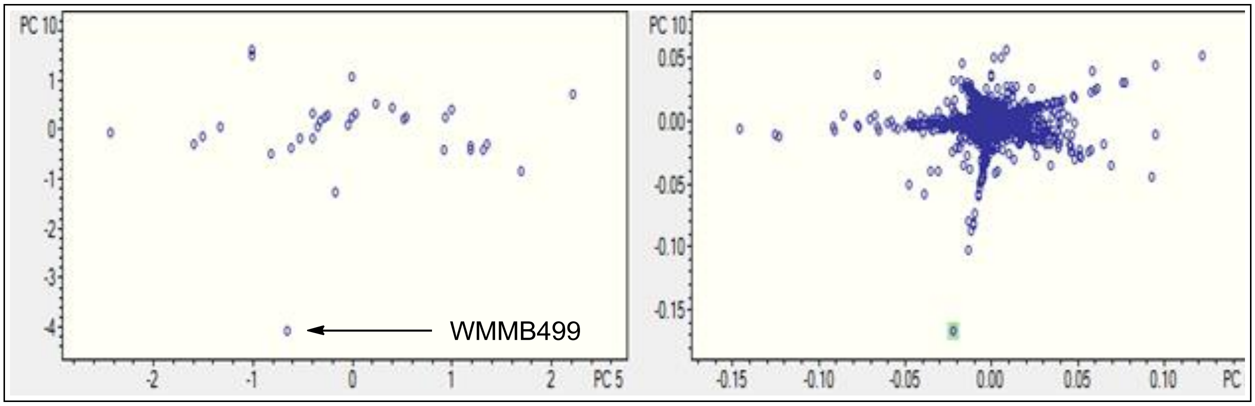

Figure 5.1. PCA analysis. The scores plot (left), in which each point signifies one bacterial strain, showed that strain WMMB499 separated from the other 33 bacterial strains (in PC10). In the loadings plot (right), each point signifies a metabolite produced by a bacterial strain. Although halomadurones A-D (**58**-**61**) were not seen in the loadings plot, strain WMMB499 appeared to produce several other new compounds (Chapters 6 and 7), which warranted its investigation.

HRMS supported the molecular formula of $C_{13}H_{13}Cl_3O_2$ and $C_{13}H_{14}Cl_2O_2$ for halomadurone A (**58**) and B (**59**), respectively. Analysis of ^{1}H and ^{13}C NMR data (Table 5.1) allowed for determination of the structures of halomadurones A (**58**) and B (**59**). The ^{1}H and ^{13}C NMR data for halomadurone A (**58**) supported the conclusion that C-13 was connected to only one carbon, and in combination with the ^{13}C chemical shift at C-13 (90.3 ppm) and molecular formula, allowed for the assignment of the trichloromethyl group. A large vicinal coupling constant (^3J_H 15.6) for H-6 and H-7 supported the assignment of the *E* conformation.[26] ROESY NMR data allowed for the assignment of the *E* olefin at C-3 and C-4 (Figure 5.2). A comparison of ^{1}H and ^{13}C NMR shifts between halomadurones A (**58**) and B (**59**) showed that the only difference between the two structures was at C-13. C-13 in halomadurone B (**59**) contained two chlorine atoms and one hydrogen as evidenced by the upfield shift of C-13 to 65.8 ppm and a

Table 5.1. ^{1}H and ^{13}C NMR data for **58 - 61** (600 MHz for ^{1}H, 150 MHz for ^{13}C, $CDCl_3$)

	58		**59**		**60**		**61**	
No.	δ_C, mult.	δ_H (*J* in Hz)	δ_C, mult.	δ_H (*J* in Hz)	δ_C, mult.	δ_H (*J* in Hz)	δ_C, mult.	δ_H (*J* in Hz)
1	13.8, CH_3	1.04, t (7.3)	13.8, CH_3	1.04, t (7.3)	13.8, CH_3	1.04, t (7.5)	13.8, CH_3	1.05, t (7.5)
2	22.4, CH_2	2.24, qn (7.3)	22.4, CH_2	2.24, qn (7.3)	22.4, CH_2	2.24, qn (7.5)	22.5, CH_2	2.24, qn (7.5)
3	144.3, CH	5.93, t (7.3)	144.0, CH	5.92, t (7.3)	144.0, CH	5.93, t (7.2)	144.0, CH	5.94, t (7.5)
4	132.6, C		132.6, C		132.7, C		132.7, C	
5	12.2, CH_3	1.82, s	12.2, CH_3	1.82, s	12.2, CH_3	1.82, s	12.2, CH_3	1.82, s
6	143.3, CH	7.14, d (15.6)	142.9, CH	7.14, d (15.6)	142.9, CH	7.14, d (15.8)	142.9, CH	7.17, d (15.8)
7	115.8, CH	6.07, d (15.6)	116.1, CH	6.07, d (15.6)	116.2, CH	6.04, d (15.8)	116.3, CH	6.05, d (15.8)
8	163.2, C		162.9, C		163.4, C		163.4, C	
9	112.3, CH	6.17, d (1.8)	112.7, CH	6.17, d (2.0)	112.2, CH	6.14, d (2.3)	113.1, CH	6.13, d (2.3)
10	179.5, C		179.5, C		179.6, C		179.5, C	
11	111.8, CH	6.85, d (1.8)	112.7, CH	6.42, d (2.0)	112.1, CH	6.39, d (2.3)	111.4, CH	6.32, d (2.3)
12	160.5, C		160.2, C		160.7, C		160.8, C	
13	90.3, C		65.8, CH	6.35, s	50.1, CH	6.35, s	32.5, CH	6.24, s

methine proton at 6.35 ppm. The relative configuration of the two olefins was assigned the same as halomadurone A (**58**) on the basis of vicinal coupling constants and ROESY NMR data.

Figure 5.2. Key ROESY correlations

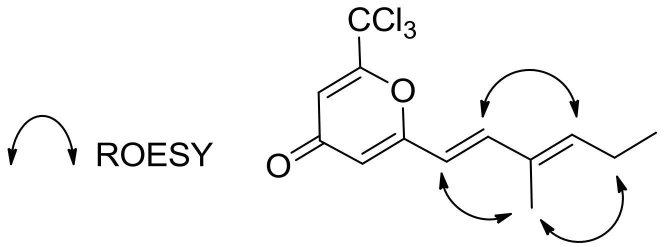

After the structural elucidation of halomadurones A (**58**) and B (**59**), the amount of KBr was increased from 0.1 g/L to 10 g/L and NaCl was reduced from 20 g/L to 0 g/L in fermentation medium ASW-A, resulting in the production of brominated analogs. Many halogenases have low specificity for the halide substrate, and the incorporation of a specific halogen often depends on the relative concentration of each halogen anion in the fermentation medium.[27,28] HRMS of the two brominated analogs, halomadurones C (**60**) and D (**61**), supported the molecular formulas of $C_{13}H_{14}BrClO_2$ and $C_{13}H_{14}Br_2O_2$, respectively. A comparison of the ^1H and ^{13}C NMR shifts (Table 5.1) of halomadurones C (**60**) and D (**61**) with halomadurone B (**59**) confirmed that the only difference in the structures was the halogenated atoms at C-13. The relative configuration of the two olefins for halomadurones C (**60**) and D (**61**) was assigned the same as halomadurone A (**58**) on the basis of vicinal coupling constants and ROESY NMR data. The lack of optical rotation by halomadurone C (**60**) suggested that a racemic mixture of both enantiomers existed.

Synthetic analog

After isolation and structure elucidation of halomadurones A-D (**58-61**), a non-halogenated analog, 2-methyl-6-((*E*)-3-methyl-1,3-hexadiene)-γ-pyrone (**62**) was synthesized to compare the bioactivity of the novel structures (Figure 5.3). In particular, the effect of substitution on the pyrone methyl could be investigated. 2-6-dimethyl-γ-pyrone in sodium ethoxide was added to 2-methyl-2-pentenal and stirred at room temperature for 5 hours.[29] Purification of the product (Section 5.4) resulted in 4.0 mg 2-methyl-6-((*E*)-3-methyl-1,3-hexadiene)-γ-pyrone (**62**).

Figure 5.3. Synthesis of **62**

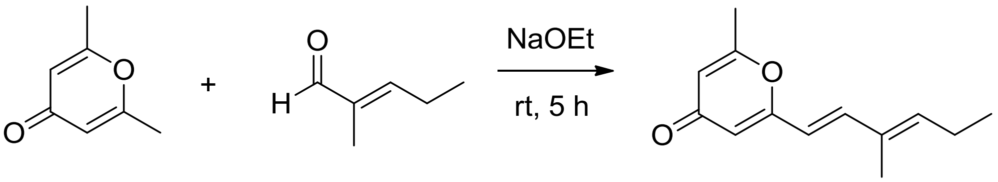

62

The structure was confirmed by analysis of ^{1}H and ^{13}C NMR (Table 5.2) and MS data. ROESY NMR data and vicinal coupling constants confirmed the assignment of the *E* olefin at C-3 and C-4. Although sufficient compound yield was achieved for initial *in vitro* studies, the overall yield was low (~2 %) as expected.

Table 5.2. ^{1}H and ^{13}C NMR data for **62** (600 MHz for ^{1}H, 150 MHz for ^{13}C, $CDCl_3$)

δ_C, mult.	δ_H (J in Hz)	COSY	HMBC
13.8, CH_3	1.02, t (7.6)	2	2, 3
22.2, CH_2	2.22, qn (7.6)	1, 3	1, 3, 4
142.6, CH	5.84, t (7.3)	2	1, 2, 5, 6
132.6, C			
12.1, CH_3	1.80, s		3, 4, 6
141.3, CH	7.02, d (15.9)	7	3, 4, 5, 7, 8
116.8, CH	6.00, d (15.9)	6	3, 4, 8, 9
163.2, C			
114.0, CH	6.07, d (2.2)	11	7, 8, 10, 11
180.9, C			
112.4, CH	6.12, d (2.2)	9	9, 10, 12, 13
165.3, C			
20.8, CH	2.28, s		11, 12

Biological Activity

On the basis of structural motifs that were present in other natural product activators, we hypothesized that the halomadurones could be activators and would contribute further knowledge surrounding SAR. Therefore, halomadurones A–D (**58**–**61**) and 2-methyl-6-((*E*)-3-methyl-1,3-hexadiene)-γ-pyrone (**62**) were evaluated for Nrf2-ARE activation (Figure 5.4). *Tert*-butylhydroquinone (*t*BHQ) was used as a positive control. Halomadurones C (**60**) and D (**61**) demonstrated potent Nrf2-ARE activation in the hPAP assay, but toxicity was apparent at higher concentrations (Figure 5.4B). Nrf2 activation did not increase in a dose-dependent manner with increasing concentrations of halomadurones C (**60**) and D (**61**) due to cytotoxicity. For example, treatment with concentrations of 7.5 and 15 µM resulted in greater Nrf2 activation than treatment with 30 µM. This decrease in activation at higher concentrations of halomadurones C (**60**) and D (**61**) correlated with an increase in cytotoxicity indicative of a narrow therapeutic window. More specifically, halomadurone D (**61**) had a dramatic decrease in hPAP activity at 30 µM in comparison to halomadurone C (**60**); yet, halomadurone D (**61**) had greater hPAP activity than halomadurone C (**60**) at 15 and 7.5 µM. Halomadurones A (**58**) and B (**59**) and 2-methyl-6-((*E*)-3-methyl-1,3-hexadiene)-γ-pyrone (**62**) demonstrated less than a ten-fold increase in Nrf2-ARE activation, considerably less than *t*BHQ. The four halogenated pyrones (**58**–**61**) demonstrated greater Nrf2 activation than the non-halogenated pyrone (**62**), suggesting the importance of the halogen atoms in their activity. Among the halogenated pyrones, brominated halomadurones C (**60**) and D (**61**) demonstrated a considerable increase in activation compared to chlorinated halomadurones A (**58**) and B (**59**), potentially due to the increased electrophilicity from the bromine atoms. However, at higher concentrations, electrophiles sometimes react with thiol

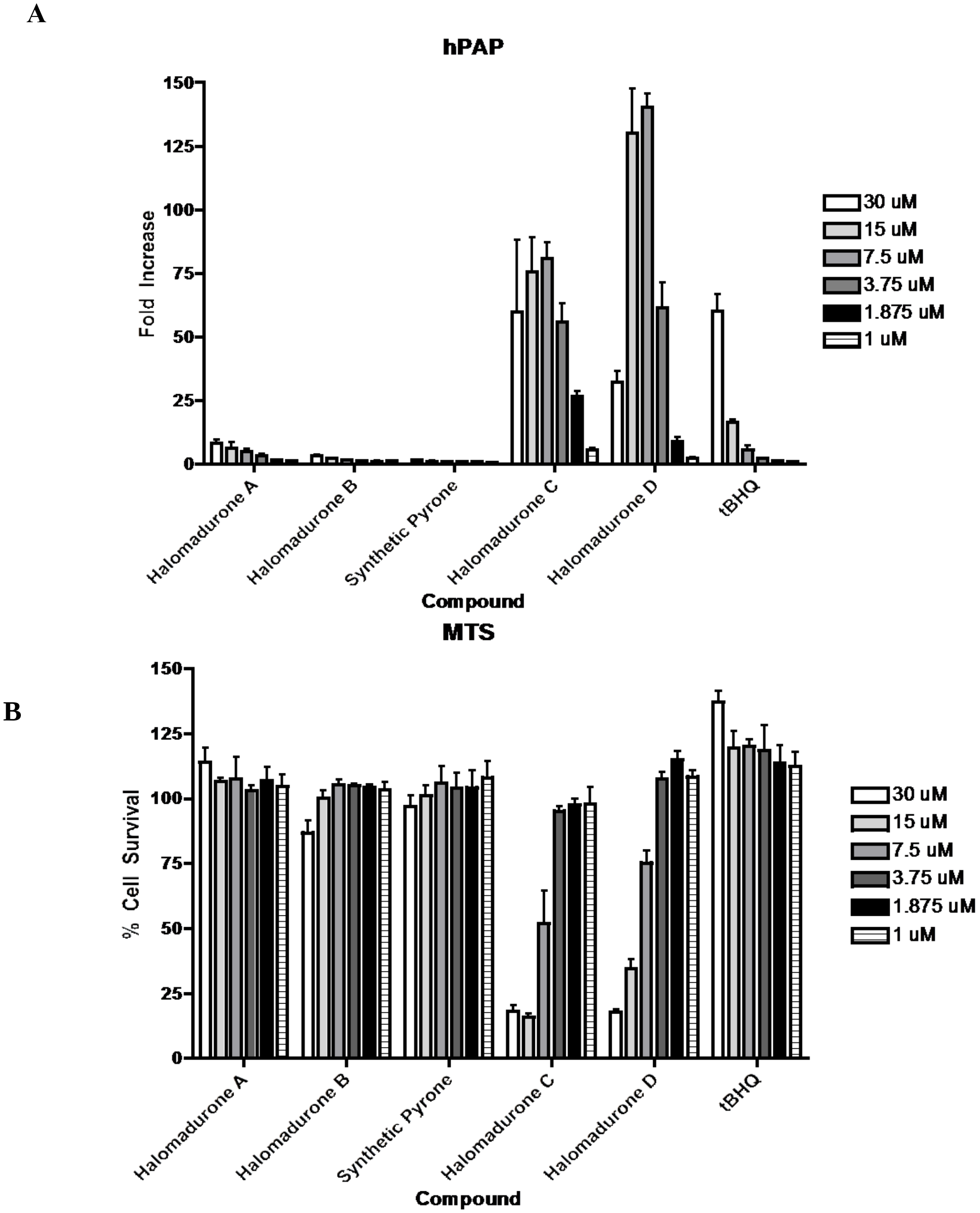

Figure 5.4. Nrf2 activation and cytotoxicity of **58-62**. Primary cortical cultures were prepared and treated with vehicle or compounds at increasing concentrations for 48 h. (A) hPAP activity was measured. All values are standardized to the vehicle treated value and presented as fold change. Mean ± SEM (B) Cell viability was assessed using MTS assay. All values are standardized to the vehicle treated value and presented as percent of Mean ± SEM.

groups, which can lead to toxicity.[30] Neuroprotection assays were conducted for halomadurone C (**60**) and D (**61**) at 3 µM, but neither compound demonstrated neuroprotection.

Isotopic enrichment and ^{13}C-^{13}C gCOSY studies

In addition to halomadurones A-D (**58-61**), WMMB499 was found to produce two other novel classes of polyketide natural products (Chapter 6 and 7). The additional two classes contained highly complex and novel carbon skeletons, which led us to pursue a method to determine carbon-carbon connectivity by using a ^{13}C-^{13}C gCOSY for rapid structure elucidation of microbial-derived natural products. Halomadurones A-D (**58-61**) were produced in high yield, which assisted the COSY proof of concept, and therefore, halomadurones A-D (**58-61**) were used to investigate the feasibility of using a ^{13}C-^{13}C gCOSY.

NMR experiments, such as the 2D INADEQUATE, have been used to establish carbon-carbon connectivity within natural products.[31,32] However, we decided to evaluate a ^{13}C-^{13}C gCOSY, which would require a shorter minimum phase cycle, could be easily implemented, and could be easily interpreted. In particular, calculations suggested that the standard two-pulse gCOSY implemented on NMR spectrometers for ^{1}H experiments could be used for ^{13}C-^{13}C with no modifications to the pulse program. In fact, after adjusting for frequency of ^{13}C and spectral widths, a theoretical sampling of coupling constants in the range 30 to 60 Hz would produce maximum polarization transfer at 33 to 17 ms, respectively. Additionally, S/N for J_{CC} = 60 Hz would be maximized with 450 increments, resulting in the 2D resolution of 0.55 ppm (see Figure A3.13). The combination of easily optimizing for a range of ^{13}C-^{13}C coupling constants combined with the fact that the gCOSY does not require ^{13}C inversion pulses and that the experiment could be immediately implemented by others with no requirement for pulse programming, made the simple gCOSY an encouraging prospect. The only drawback was that the ^{13}C-^{13}C COSY type experiment requires isotopic enrichment. To address this problem, we tested the feasibility of ^{13}C incorporation of microbial-derived natural products in conjunction with evaluating the feasibility of the ^{13}C-^{13}C gCOSY, both in terms of economics and ease of implementation.

Figure 5.5. ^{13}C-labeled NMR. **(**A) 1D ^{13}C spectrum (downfield region) of halomadurone A (**58**) (B) ^{13}C-^{13}C gCOSY of ^{13}C-labeled halomadurone A (**58**)

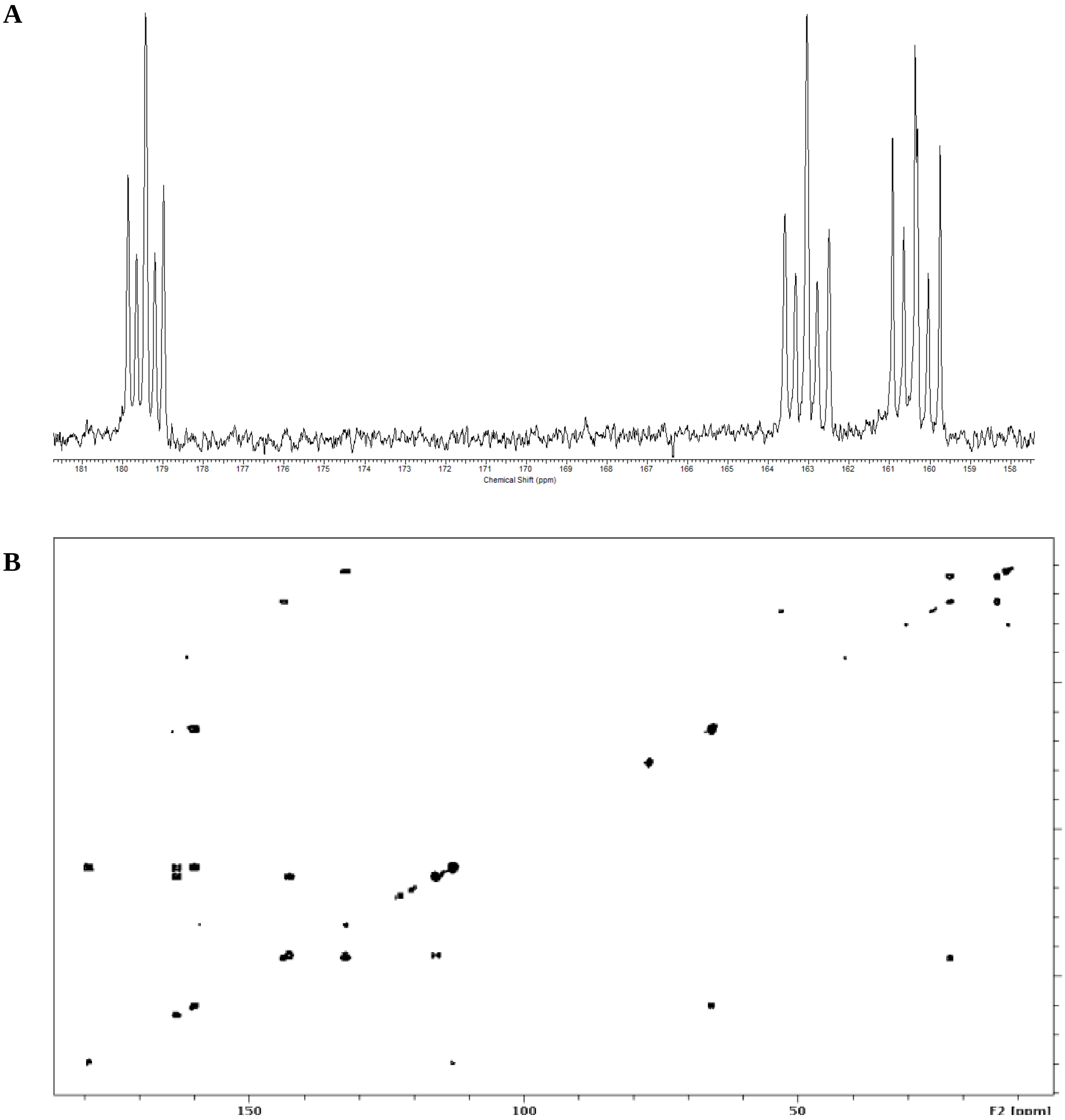

To increase the ^{13}C abundance, fermentation of WMMB499 in 1 L ASW-A using uniformly ^{13}C-labeled glucose (10 g/L ASW-A) and subsequent purification (Section 5.4) yielded halomadurone A (**58**) and B (**59**) with nearly 75% ^{13}C incorporation (as evidenced by MS isotopic distribution). The ^{13}C-^{13}C gCOSY (Figure 5.5) was acquired in two hours on 16 µmoles (96 µM) halomadurone A (**58**) and allowed for complete assignment of the carbon backbone.

After successfully acquiring a ^{13}C-^{13}C gCOSY on halomadurone A (**58**) and B (**59**), we investigated the minimum amount of ^{13}C-labeled compound necessary to acquire the ^{13}C-^{13}C gCOSY by acquiring data on varying concentrations of ^{13}C-labeled halomadurone A (**58**). A ^{13}C-^{13}C gCOSY spectrum was acquired in 18 hours (132 scans, 256 increments) on 200 µg (650 nmoles; 3.7 mM) using a Bruker Avance 500 MHz spectrometer equipped with a ^{13}C/^{15}N{^{1}H} cryoprobe (Figure A3.15). Considering the production of halomadurone A (**58**) was about 5 mg/L ASW-A, a 25 mL culture of WMMB499 in ASW-A (with U^{13}C-glucose) would produce enough ^{13}C-labeled halomadurone A (**58**) to acquire a ^{13}C-^{13}C COSY in an overnight NMR experiment. The cost of U^{13}C-glucose (250 mg) for a 25 mL culture of ASW-A would be about \$59, making this a very cost and time effective method.

While these data were acquired using a ^{13}C-optimized cryoprobe, this technology was not yet a commonly available tool for laboratories. Thus, in parallel, we acquired a ^{13}C-^{13}C gCOSY of halomadurone B (1.9 mg; 7.0 µmoles; 35 mM) using a 500 MHz spectrometer with a 5 mm room temperature probe to demonstrate the capabilities of the ^{13}C-^{13}C gCOSY with labeled compound (Figure A3.20). The spectrum showed adequate signal-to-noise and all of the expected correlations, demonstrating the feasibility of this method on a room temperature probe.

Table 5.3. Summary of NMR Experiments

Sample	Spectrometer	NMR Experiment	Hours of acquisition	Amount (mg)	(moles)	(mM)
^{13}C-labeled **58**	a	^{13}C-^{13}C gCOSY	18	0.20	0.65	37
^{13}C-labeled **59**	b	^{13}C-^{13}C gCOSY	12	1.9	7.0	35
Unlabeled **59**	a	^{13}C-^{13}C gCOSY[c]	14	5.3	19	110
^{13}C-labeled **59**	a	^{13}C-^{13}C gCOSY	7	1.1	4.0	6.7
^{13}C-labeled **59**	a	2D INADEQUATE	7	1.1	4.0	6.7
^{13}C-labeled **59**	a	^{13}C-^{13}C gCOSY	2	1.1	4.0	6.7

[a] Bruker Avance 500 MHz spectrometer with ^{13}C/^{15}N{^{1}H} cryoprobe. [b] Varian Unity-Inova 500 MHz spectrometer (room temperature quad-nucleus probe). [c] Experiment resulted in no crosspeaks

After determining the minimum amount of compound necessary to acquire a ^{13}C-^{13}C gCOSY on ^{13}C-labeled compound, we aimed to demonstrate the importance of using labeled compound for acquiring a ^{13}C-^{13}C gCOSY. A 1D ^{13}C NMR spectrum (NS=32, D1=4) was acquired on 5.3 mg (19 µmoles) of unlabeled halomadurone B (**59**) in 175 µL $CDCl_3$ (0.11 M) on a Bruker Avance 500 MHz spectrometer equipped with a ^{13}C/^{15}N{^{1}H} cryoprobe and appeared to have adequate signal-to-noise after the two minute experiment (Figure A3.16). However, when the same sample (0.11 M unlabeled halomadurone B) was used to acquire a ^{13}C-^{13}C COSY (96 scans, 256 increments, 14 hour experiment time), no cross-peaks were observed in the ^{13}C-^{13}C COSY. This experiment demonstrated that acquisition of a ^{13}C-^{13}C COSY with unlabeled compound is not possible within a reasonable amount of time, and therefore, ^{13}C-labeling of natural products can save significant time and resources. ^{13}C-^{13}C COSY spectra were successfully acquired with much lower concentrations of ^{13}C-labeled sample with much shorter experimental times.

In addition to the ^{13}C-^{13}C gCOSY, we attempted a ^{13}C-^{13}C dqfCOSY experiment using ^{13}C-labeled halomadurone B (**59**). However, the ^{13}C-^{13}C dqfCOSY did not appear to be as sensitive as the ^{13}C-^{13}C gCOSY, and therefore, we did not pursue further experiments with the dqfCOSY.

Instead, we turned our focus to a comparison of the 2D INADEQUATE with the ^{13}C-^{13}C gCOSY. A 2D INADEQUATE (NS=32) was acquired on 1.1 mg ^{13}C-labeled halomadurone B (4.0 µmoles; 6.7 mM) (**59**), and while all the expected ^{13}C-^{13}C correlations were present, a number of artifacts were interspersed throughout the spectrum (Figure A3.17). Additionally, one of the limitations of the 2D INADEQUATE is the long minimum phase cycle. The minimum phase cycle for this standard 2D INADEQUATE pulse program was 32 scans, resulting in a 7 hour total experiment time. Attempting to run the experiment with less than 32 scans resulted in considerable artifacts and difficulty in interpreting the data. While using less than 32 scans would not be feasible with an unlabeled sample, an adequate amount of labeled sample should not require 32 scans. In contrast, the ^{13}C-^{13}C gCOSY does not have a minimum phase cycle so it is theoretically possible to run the experiment with only one scan if enough labeled compound is used. To demonstrate this point, we acquired a ^{13}C-^{13}C COSY (NS=32) on the same sample of ^{13}C-labeled halomadurone B (**59**) with a total experiment time of about 7 hours (Figure A3.18). A ^{13}C-^{13}C gCOSY with NS=4 and a total experiment time of less than 2 hours was also acquired and appeared the same as the 7 hour ^{13}C-^{13}C gCOSY spectrum (Figure A3.19). Thus, about 5 hours of experiment time was saved due to the shorter minimum phase cycle for the ^{13}C-^{13}C COSY compared to the 2D INADEQUATE. As a whole, our studies demonstrated both economic advantages and the ease of implementation for using ^{13}C-labeled compounds to acquire a ^{13}C-^{13}C gCOSY.

5.3. Conclusion

This chapter reported the isolation and structure elucidation of halomadurones A-D (**58**-**61**), novel halogenated electrophilic pyrones from an *Actinomadura* sp. and the synthesis of a non-halogenated analog, 2-methyl-6-((*E*)-3-methyl-1,3-hexadiene)-γ-pyrone (**62**). Halomadurones C (**60**) and D (**61**) demonstrated potent Nrf2-ARE activation. Therefore, halomadurones A-D (**58**-**61**) could play an important role in the discovery of new therapeutics, especially considering the ever-present need for therapeutics for neurodegenerative diseases. Halomadurones A (**58**) and B (**59**) were enriched with ^{13}C-labeled glucose that allowed for the acquisition of a ^{13}C-^{13}C COSY and determination of the carbon backbone of the structures. In particular, this method could be valuable for molecules with multiple quaternary centers, which make structure elucidation by standard NMR experiments more challenging. Hence, ^{13}C incorporation and subsequent acquisition of a ^{13}C-^{13}C COSY could be a useful method for the rapid structure elucidation of microbial-derived natural products. While this example demonstrated ^{13}C incorporation of microbial-derived polyketides, ^{13}C incorporation of other natural product structural types, such as terpenoids and peptides, is currently being investigated; initial results indicated successful ^{13}C-labeling of two novel peptides. With increasing sensitivity of NMR spectrometers, the COSY represents a feasible method to drastically reduce the time for structure determination.

5.4. Materials and Methods

General Experimental Procedures

Optical rotations were measured on a Perkin–Elmer 241 Polarimeter. UV spectra were recorded on an Aminco/OLIS UV-Vis spectrophotometer. IR spectra were measured with a Bruker

Equinox 55/S FT–IR spectrophotometer. NMR spectra were obtained in $CDCl_3$ with a Bruker Avance 600 MHz spectrometer equipped with a 1.7 mm $^{1}H\{^{13}C/^{15}N\}$ cryoprobe, a Bruker Avance 500 MHz spectrometer equipped with a $^{13}C/^{15}N\{^{1}H\}$ cryoprobe, and a Varian Unity-Inova 500 MHz spectrometer. HRMS data were acquired with a Bruker MaXis 4G QTOF mass spectrometer. RP HPLC was performed using a Shimadzu Prominence HPLC system and a Phenomenex Onyx Monolithic C18 column (100 × 4.6 mm).

Biological Material

Ascidian specimens were collected on August 10, 2011, in the Florida Keys (24° 39.591′, 81° 25.217′). A voucher specimen (FLK10-5-6) for *Ecteinascidia turbinata* (Herdman, 1880) is housed at the University of Wisconsin-Madison. For cultivation, a sample of ascidian (1 cm^3) was rinsed with sterile seawater, macerated using a sterile pestle in a micro-centrifuge tube, and dilutions were made in sterile seawater, with vortexing between steps to separate bacteria from heavier tissues. Dilutions were separately plated on three media: ISP2, R2A, and M4. Each medium was supplemented with 50 μg/mL cycloheximide and 25 μg/mL nalidixic acid. Plates were incubated at 28 °C for at least 28 days, and strain WMMB499 was purified from an ISP2 isolation plate.

Sequencing

16S rDNA sequencing was conducted as previously described.[33] WMMB499 was identified as an *Actinomadura* sp. and demonstrated 99% sequence similarity to *Actinomadura* sp. 13679C (accession number EU741239). The 16S sequence for WMMB499 was deposited in GenBank (accession number JX101467).

Fermentation, Extraction, and Isolation

Two 10 mL seed cultures (25 × 150 mm tubes) in medium ASW-A (20 g soluble starch, 10 g glucose, 5 g peptone, 5 g yeast extract, 5 g $CaCO_3$ per liter of artificial seawater) were inoculated with strain WMMB499 and shaken (200 RPM, 28 °C) for seven days. Two hundred fifty mL baffled flasks (12 × 50 mL) containing ASW-A were inoculated with 1 mL seed culture and were incubated (200 RPM, 28 °C) for seven days. Two-liter flasks (6 × 500 mL) containing medium ASW-A with Diaion HP20 (4% by weight) were inoculated with 25 mL from the 50 mL culture and shaken (200 RPM, 28 °C) for seven days. Filtered HP20 and cells were washed with H_2O and extracted with acetone. The acetone extract (3.5 g) was subjected to liquid-liquid partitioning using 30% aqueous MeOH and $CHCl_3$ (1:1). The $CHCl_3$-soluble partition (2.5 g) was fractionated by Sephadex LH20 column chromatography ($CHCl_3$:MeOH, 1:1). Fractions containing **58** and **59** were subjected to RP HPLC (55/45% to 75/25% MeOH/H_2O, 15 min, 3 mL/min) using a Phenomenex Onyx Monolithic C18 column (100 × 4.6 mm), yielding **59** (3.0 mg, RT 7.1 min) and **58** (3.2 mg, RT 11.0 min). For production of **60** and **61**, the amount of KBr in medium ASW-A was increased from 0.1 g/L to 10 g/L, and no NaCl was included. After fermentation of 500 mL ASW-A (with KBr), the same isolation procedure was used. One additional purification step by RP HPLC (70/30% to 76/24% ACN/H_2O, 11 min, 4 mL/min) using a Phenomenex Luna C18 column (250 × 10 mm, 5 µm) yielded **60** (1.3 mg, RT 8.8 min) and **61** (1.2 mg, RT 9.1 min). For ^{13}C incorporation, the same procedure was used with two-liter flasks (2 × 500 mL) containing medium ASW-A (U^{13}C-glucose substituted for unlabeled glucose).

Bioassay hPAP and MTS

Primary cortical neuronal cultures were derived from ARE-hPAP reporter mice as previously described.[10-11] Compounds were dissolved in 100% DMSO and administered to cells for 48 h.

Tert-butylhydroquinone (tBHQ) was used as a control. After 48 h, Nrf2 activation was determined by measuring for hPAP activity as previously described.[34] Using one-second integration luminescence was measured on a Berthold Orionmicroplate luminometer (Berthold Technologies GmbH & Co., Bad Wildbad, Germany). Baseline signals from hPAP negative control culture samples were subtracted from all values. Cell viability was assayed using the MTS assay following the manufacturer's suggested protocol (Promega, Madison, Wisconsin, USA). All hPAP and MTS data are represented as mean ± SEM ($n = 4$). Results of hPAP assays are expressed as the fold increase in hPAP activity over basal levels. Statistical analysis was performed using one-way ANOVA followed by Newman–Keuls multiple comparison (GraphPad Prism, version 4). A $p<0.05$ was considered statistically significant.

Halomadurone A (58). White solid; UV (MeOH) λ_{max} (log ε) 204 (3.96), 223 (3.99), 255 (3.90), 315 (3.92) nm; IR (ATR) υ_{max} 1644, 1635, 1394, 1215 cm^{-1}; ^{1}H and ^{13}C NMR (See Table 5.1); HRMS $[M+H]^+$ *m/z* 307.0044 (calcd for $C_{13}H_{14}Cl_3O_2$, 307.0054).

Halomadurone B (59). White solid; UV (MeOH) λ_{max} (log ε) 204 (4.04), 222 (3.94), 253 (3.79), 315 (3.83) nm; IR (ATR) υ_{max} 1641, 1632, 1602, 1369, 932 cm^{-1}; ^{1}H and ^{13}C NMR (See Table 5.1); HRMS $[M+H]^+$ *m/z* 273.0453 (calcd for $C_{13}H_{15}Cl_2O_2$, 273.0444).

Halomadurone C (60). White solid; UV (MeOH) λ_{max} (log ε) 206 (4.02), 253 (3.40), 324 (3.50) nm; IR (ATR) υ_{max} 1650, 1601, 1396, 1215, 934 cm^{-1}; ^{1}H and ^{13}C NMR (See Table 5.1); HRMS $[M+H]^+$ *m/z* 316.9937 (calcd for $C_{13}H_{15}BrClO_2$, 316.9938).

Halomadurone D (61). White solid; $[\alpha]^{25}_{D}$ ±0 (*c* 0.12, MeOH); UV (MeOH) λ_{max} (log ε) 206 (4.30), 255 (3.42), 324 (3.42) nm; IR (ATR) υ_{max} 1651, 1601, 1396, 1215, 934 cm^{-1}; ^{1}H and ^{13}C NMR (See Table 5.1); HRMS $[M+H]^+$ *m/z* 360.9433 (calcd for $C_{13}H_{15}Br_2O_2$, 360.9433).

2-methyl-6-((*E*)-3-methyl-1,3-hexadiene)-γ-pyrone (62). To a solution of 2-6-dimethyl-γ-pyrone (1.24 g) in 15 mL ethanol was added 2-methyl-2-pentenal (2.28 mL) and sodium ethoxide (680 mg) in 7.5 mL ethanol. The reaction mixture was stirred for 5 h at rt. After 5 h, dilute HCl was added to the mixture and dried under vacuum. The reaction mixture was subjected to RP HPLC (40%/60% to 100%/0% MeOH/H_2O containing 0.1% acetic acid, 20 mins) using a Phenomenex Gemini C18 column (100 × 30 mm, 5 μm). Additional purification of the fraction containing **62** was conducted by Normal Phase HPLC (60%/40% to 100%/0% ethyl acetate/hexanes, 30 mins) using a Phenomenex Luna Silica column (250 × 10 mm, 5 μm), yielding **62** (4.0 mg, 2.0% yield, t_R 25.5 min) as a white solid; UV (MeOH) λ_{max} (log ε) 208 (3.99), 227 (4.00), 314 (4.17) nm; IR (ATR) υ_{max} 1655, 1597, 1398, 1217, 925 cm^{-1}; ^1H and ^{13}C NMR (See Table 5.2); HRMS $[M+H]^+$ *m/z* 205.1230 (calcd for $C_{13}H_{17}O_2$, 205.1223).

5.5. References

1. Menken, M.; Munsat, T.L.; Toole, J.F. The global burden of disease study: implications for neurology. *Arch. Neurol*. **2000**, *57*, 418-420.

2. Hebert, L.E.; Weuve, J.; Scherr, P.A.; Evans, D.A. Alzheimer disease in the United States (2010-2050) estimated during the 2010 census. *Neurology*. **2013**, *80*, 1778-1783.

3. Alzheimer's Disease International. World Alzheimer Report 2009. London: Alzheimer's Disease International, 2009.

4. Uttara, B.; Singh, A.V.; Zamboni, P.; Mahajan, R.T. Oxidative Stress and Neurodegenerative Diseases: A Review of Upstream and Downstream Antioxidant Therapeutic Options. *Curr. Neuropharmacol*. **2009**, *7*, 65-74.

5. de Vries, H.E.; Witte, M.; Hondius, D.; Rozemuller, A.J.M.; Drukarch, B.; Hoozemans, J.; van Horssen, J. Nrf2-induced antioxidant protection: a promising target to conteract ROS-mediated damage neurodegenerative disease? *Free Radical Biol. Med*. **2008**, *45*, 1375-1383.

6. Calkins, M.J.; Johnson, D.A.; Townsend, J.A.; Vargas, M.R.; Dowell, J.A.; Williamson, T.P.; Kraft, A.D.; Lee, J.-M.; Li, J.; Johnson, J.A. The Nrf2/ARE pathway as a potential

therapeutic target in neurodegenerative disease. *Antioxid. Redox Signal*. **2009**, *11*, 497-508.

7. Vanugopal, R.; Jaiswal, A.K. Nrf1 and Nrf2 positively and c-Fos and Fra1 negatively regulate the human antioxidant response element-mediated expression of NAD(P)H:quinone oxidoreductase$_1$ gene. *Proc. Natl. Acad. Sci. USA* **1996**, *93,* 14960-14965.

8. Itoh, K.; Ishii, T.; Wakabayashi, N.; Yamamoto, M. Regulatory mechanism of cellular response to oxidative stress. *Free Radical Res.* **1999**, *31,* 319-324.

9. Wild, A.C.; Moinova, H.R.; Mulcahy, R.T. Regulation of γ-glutamylcysteine synthetase subunit gene expression by the transription factor Nrf2. *J. Biol. Chem*. **1999**, *274,* 33627-33636.

10. Kraft, A.D.; Johnson, D.A.; Johnson, J.A. Nuclear factor E2-related factor 2-dependent antioxidant response element activation by tert-butylhydroquinone and sulforaphane occurring preferentially in astrocytes conditions neurons against oxidative insult. *J. Neurosci*. **2004**, *24*, 1101-1112.

11. Johnson, D.A.; Andrews, G.K.; Xu, W.; Johnson, J.A. Activation of the antioxidant response element in primary cortical neuronal cultures derived from transgenic reporter mice *J. Neurochem*. **2002**, *81*, 1233-1241.

12. Balogun E.; Hoque, M.; Gong, P.; Killeen, E.; Green, C.J.; Foresti, R.; Alam, J.; Motterlini, R. Curcumin activates the haem oxygenase-1 gene via regulation of Nrf2 and the antioxidant-responsive element. *Biochem. J*. **2003**, *371*, 887–895.

13. Haridas, V.; Hanausek, M.; Nishimura, G.; Soehnge, H.; Gaikwad, A.; Narog, M.; Spears, E.; Zoltaszek, R.; Walaszek, Z.; Gutterman, J.U. Triterpenoid electrophiles (avicins) activate the innate stress response by redox regulation of a gene battery. *J. Clin. Invest.* **2004**, *113*, 65–73.

14. Shibuya, A.; Onda, K.; Kawahara, H.; Uchiyama, Y.; Nakayama, H.; Omi, T.; Nagaoka, M.; Matsui, H.; Hirano, T. Sofalcone, a gastric mucosa protective agent, increases vascular endothelial growth factor via the Nrf2-heme-oxygenase-1 dependent pathway in gastric epithelial cells. *Biochem. Biophys. Res. Commun*. **2010**, *398,* 581–584.

15. Lee, Y.M.; Jeong, G.S.; Lim, H.D.; An, R.B.; Kim, Y.C.; Kim, E.C. Isoliquiritigenin 2′-methyl ether induces growth inhibition and apoptosis in oral cancer cells via heme oxygenase-1. *Toxicol. in Vitro* **2010**, *24*, 776–782.

16. Wang, R.; Paul, V.; Luesch, H. Seaweed extracts and unsaturated fatty acid constituents from the green alga Ulva lactuca as activators of the cytoprotective Nrf2-ARE pathway. *Free Radical Bio. Med*. **2013**, *57,* 141-153.

17. Wang, R.; Mason, D.E.; Choe, K.P.; Lewin, A.S.; Peters, E.C.; Luesch, H. In vitro and in vivo characterization of a tunable dual-reactivity probe of the Nrf2-ARE Pathway. *ACS Chem. Biol*. **2013**, *8*, 1764-1774.

18. Orjala, J.; Gerwick, W.H. Barbamide, a chlorinated metabolite with molluscicidal activity from the Caribbean cyanobacterium Lyngbya majuscula. *J. Nat. Prod*. **1996**, *59*, 427-430.

19. Jiménez, J.I.; Scheuer, P.J. New lipopeptides from the Caribbean cyanobacterium Lyngbya majuscula. *J. Nat. Prod*. **2001**, *64*, 200-203.

20. Nozoe, S.; Ishii, N.; Kusano, G.; Kikuchi, K.; Ohta, T. Neocarzilins A and B, novel polyenones from Streptomyces carzinostaticus. *Tetrahedron Lett*. **1992**, *33*, 7547-7550.

21. Nozoe, S.; Kikuchi, K.; Ishii, N.; Ohta, T. Synthesis of neocarzilin A: An absolute sterochemistry. *Tetrahedron Lett*. **1992**, *33*, 7551-7552.

22. Otsuka, M.; Ichinose, K.; Fujii, I.; Ebizuka, Y. Cloning, sequencing, and functional analysis of an iterative type I polyketide synthase gene cluster for biosynthesis of the antitumor chlorinated polyenone neocarzilin in “Streptomyces carzinostaticus”. *Antimicrob. Agents Chemother*. **2004**, *48*, 3468-3476.

23. Hou, Y.; Braun, D.R.; Michel, C.R.; Klassen, J.L.; Adnani, N.; Wyche, T.P.; Bugni, T.S. Microbial strain prioritization using metabolomics tools for the discovery of the natural products. *Anal. Chem*. **2012**, *84*, 4277-4283.

24. Zeng, J.; Zhan, J. A novel fungal flavin-dependent halogenase for natural product biosynthesis. *ChemBioChem* **2010**, *11*, 2119–2123.

25. Vaillancourt, F.H.; Vosburg, D.A.; Walsh, C.T. Dichlorination and bromination of a Threonyl-*S*-carrier protein by the non-heme FeII halogenase SYRB2. *Chembiochem* **2006**, *7*, 748–752.

26. Williams, D.H.; Fleming, I. *Spectroscopic Methods in Organic Chemistry*, 4th edition, McGraw-Hill Book Company Limited: London, 1989, Table 3.27.

27. Eustaquio, A.S.; Pojer, F.; Noel, J.P.; Moore, B.S. Discovery and characterization of a marine bacterial SAM-dependent chlorinase. *Nat. Chem. Biol*. **2008**, *4*, 69–74.

28. Wagner, C.; El Omari, M.; König, G.M. Biohalogenation: Nature’s way to synthesize halogenated metabolites. *J. Nat. Prod*. **2009**, *72*, 540–553.

29. Ghandi, M.; Bayat, Y.; Teimuri-mofrad, R. A novel method for the synthesis of formyl and hydroxymethyl derivatives of 4H-pyran-4-one. *Org. Prep. Proced. Int*. **2002**, *34*, 525-530.

30. Satoh, T.; McKercher, S.R.; Lipton, S.A. Nrf2/ARE-mediated antioxidant actions of pro-electrophilic drugs. *Free Radical Biol. Med.* **2013**, *65*, 645–657.

31. Bugni, T.S.; Bernan, V.S.; Greenstein, M.; Janso, J.E.; Maiese, W.M.; Mayne, C.L.; Ireland, C.M. Brocaenols A-C: Novel polyketides from a marine-derived Penicillium brocae. *J. Org. Chem.* **2003**, *68*, 2014-2017.

32. Meyer, S.W.; Köck, M. NMR studies of phakellins and isophakellins. *J. Nat. Prod.* **2008**, *71*, 1524-1529.

33. Wyche, T.P.; Hou, Y.; Braun, D.; Cohen, H.C.; Xiong, M.P.; Bugni, T.S. First natural analogs of the cytotoxic thiodepsipeptide thiocoraline A from a marine *Verrucosispora* sp. *J. Org. Chem.* **2011**, *76*, 6542-6547.

34. Fischedick, J.T.; Standiford, M.; Johnson, D.A.; Johnson, J.A. Structure activity relationship of phenolic diterpenes from Salvia officinalis as activators of the nuclear factor E2-related factor 2 pathway. *Bioorg. Med. Chem.* **2013**, *21*, 2618-2622.

Chapter 6:

Ecteinamycin, a Novel Polyether Antibiotic from an Ascidian-derived *Actinomadura* sp.

5.1. Introduction

Antibiotic resistance continues to be a major threat worldwide: antibiotic-resistant pathogens sicken 2 million people and contribute to 23,000 deaths each year in the United States.[1] *Clostridium difficile*, Carbapenem-resistant Enterobacteriaceae, and drug-resistant *Neisseria gonorrhoaea* are among the most dangerous infectious diseases and consequently, were recently elevated to the "Urgent" hazard level for infections by the CDC.[1]

Clostridium difficile, a rod-shaped, spore-forming, gram-positive anaerobic bacterium, is among the top three hospital-acquired infections in the United States, resulting in about 500,000 cases per year.[2] *C. difficile* is the most common infectious disease of nosocomial diarrhea but also results in many other effects, including death in some cases.[2-6] Vancomycin and metronidazole are the most common antibiotics used for treatment; the recently-approved fidaxomicin has also been used to treat *C. difficile*.[6] Despite these options for treatment, the prevalence of *C. difficile* has increased dramatically worldwide since the early 2000s, in part due to the rise of a new hypervirulent strain, ribotype 027.[5] This new strain, which has been seen across the United States and Europe, has resulted in increased mortality: about 14,000 people die each year in the United States from *C. difficile*.[1] Additionally, *C. difficile* spreads very quickly as it is resistant to a wide range of antibiotics used for other infections. Therefore, there is a growing need for additional antibiotics to treat *C. difficile*.

In our search for novel antibiotics, we isolated a novel polyether antibiotic, which we named ecteinamycin (**65**), from a marine *Actinomadura* sp. cultivated from the ascidian *Ecteinascidia turbinata* (Herdman, 1880). The structure of ecteinamycin was elucidated with a ^{13}C-^{13}C COSY with a ^{13}C-enriched sample and other spectroscopic methods. Ecteinamycin (**65**) demonstrated potent activity against gram positive bacteria, including selectivity for *Clostridium difficile* (MIC ≤ 31 ng/mL). Initial mechanism of action studies, including a chemical genomic approach, and the structure of ecteinamycin (**65**) suggested that it belongs to the class of polyether ionophore antibiotics. Ionophore antibiotics are characterized by the ability to transport ions (K^+, Na^+, Ca^+, Mg^{2+}) across the cell membrane.[7] Many of the early ionophore antibiotics, such as lasalocid (**66**), salinomycin (**67**), and monensin (**68**) have been used primarily as anticoccidials in poultry farming, but the investigation of new therapeutic targets in humans could spur a new source for antibiotics.[8] Several structural features of ecteinamycin, such as the acyltetronic acid moiety, are identical to other polyether ionophore antibiotics, such as tetronomycin[9] (**69**) and tetronasin (**70**).[10] However, as a whole, ecteinamycin represents a novel carbon skeleton, and its potent selectivity against *C. difficile* offers a potential antibiotic. A pharmacokinetic study in mice indicated that ecteinamycin (**65**) is orally bioavailable.

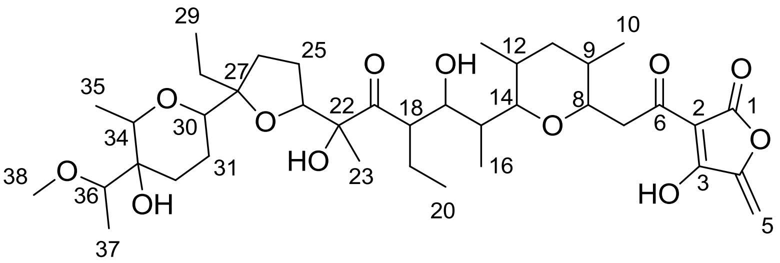

65

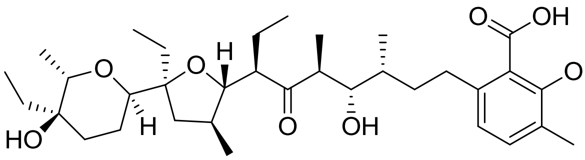

66

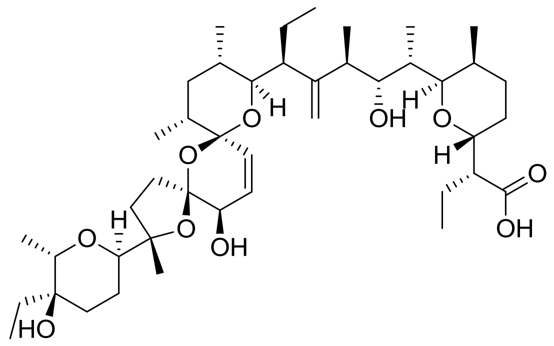

67

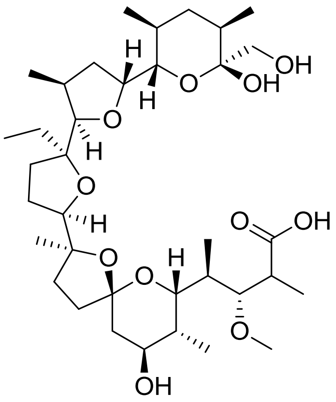

68

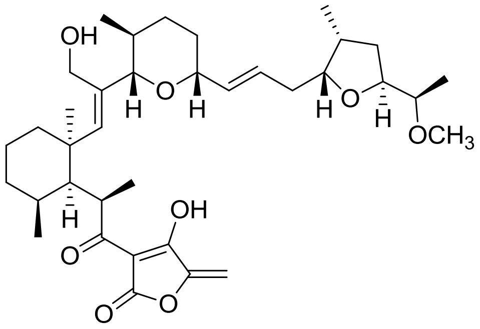

69

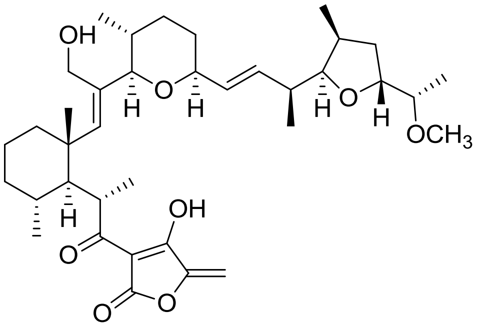

70

6.2. Results and Discussion

LCMS of 34 marine-derived bacterial extracts and subsequent multivariate analysis by principal component analysis (PCA)[11] led us to pursue strain WMMB499, which demonstrated unique chemistry compared to other strains by PCA (Figure 6.1). Strain WMMB499 was found to produce halomadurones A-D[12] (Chapter 5) and forazoline A (Chapter 7), as well as ecteinamycin (**65**), a novel polyether antibiotic.

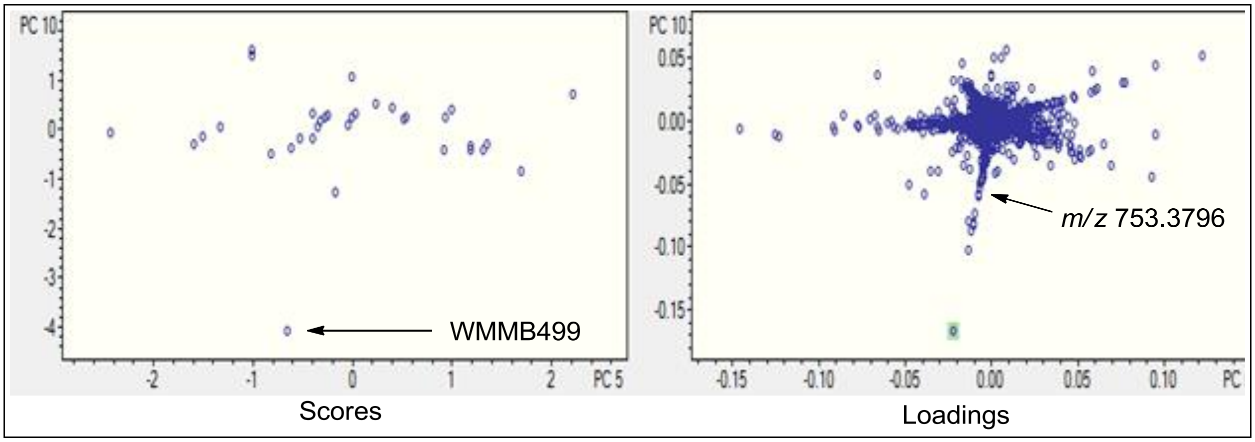

Figure 6.1. PCA analysis. The scores plot, in which each point signifies one bacterial strain, showed that strain WMMB499 separated from the other 33 bacterial strains (in PC10). In the loadings plot, in which each point signifies a metabolite produced by a bacterial strain, a metabolite with *m/z* 753.3796 showed separation from the large grouping of metabolites. That ion was only produced by WMMB499 and was later determined to be ecteinamycin (**50**).

HRMS supported the molecular formula of $C_{38}H_{60}O_{12}$ for ecteinamcyin (**65**). Extensive 1D and 2D NMR data (Table 6.1) allowed us to determine the majority of the planar structure, but to improve the efficiency of structure elucidation we used a method that we have previously published[13] and discussed in Chapter 5: U^{13}C-glucose was used to increase the incorporation of ^{13}C in the sample of ecteinamycin (**65**), and acquisition of a ^{13}C-^{13}C COSY provided the carbon backbone of the structure.

A combination of ROESY correlations, coupling constants, ^{13}C chemical shifts, molecular modeling, and other spectroscopic methods were used to determine the relative configuration of ecteinamycin (**65**). A ROESY correlation between H-9 and H-13 suggested the

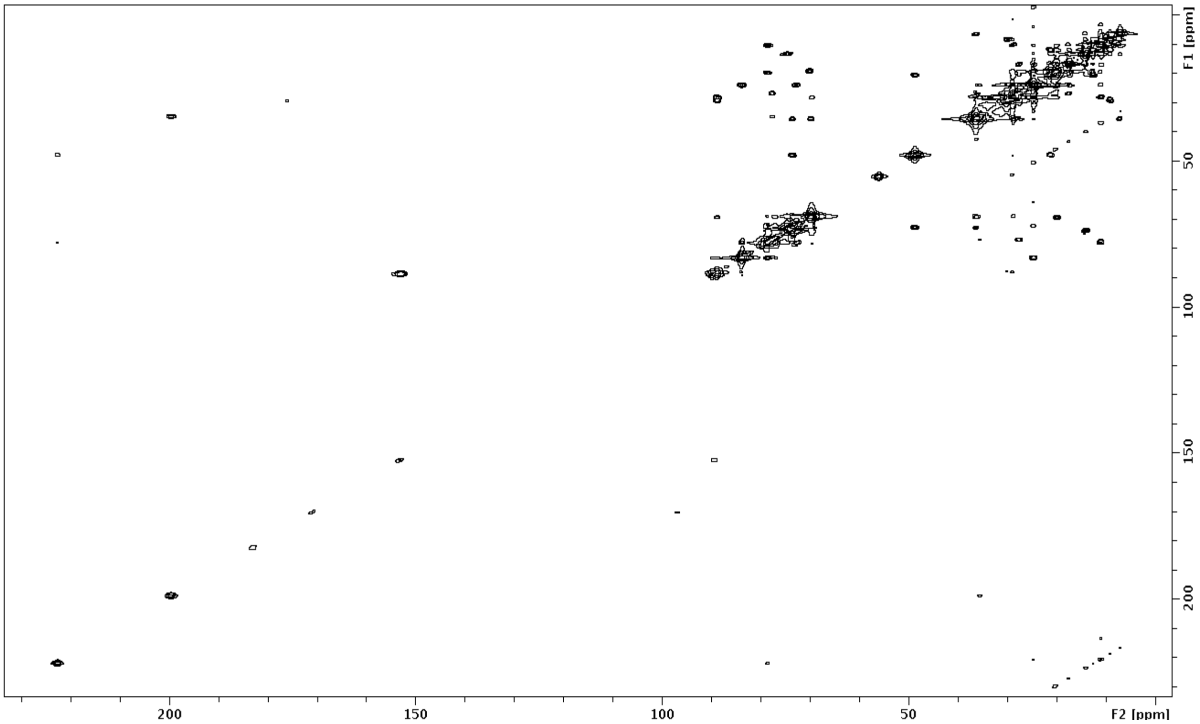

Figure 6.2. ^{13}C-^{13}C COSY of ecteinamycin (**65**)

C-10 and C-13 methyl groups were *anti*. C-10 and C-13 were assigned equatorial and axial, respectively, due to the ^{13}C chemical shifts. ^{13}C NMR shifts of equatorial carbons are further downfield (~17 ppm) than axial carbons (~11 ppm) in similar chemical systems.[14] A ROESY correlation between H-7 and H-14 suggested that H-8 and H-14 were *anti*. A small coupling constant (^3J_H 6.0 Hz) between H-8 and H-9 suggested that the two protons were *cis*.[15] This relative configuration of H-8, H-9, H-12, and H-14 was confirmed by molecular modeling with Spartan10 software.[15] The low energy conformer for each of the possible diastereomers for that cyclic system was modeled, and the proposed relative configuration matched best with the experimental ROESY correlations and coupling constants.

Table 6.1. ^{1}H and ^{13}C NMR data for **65** (600 MHz for ^{1}H, 150 MHz for ^{13}C, $CDCl_3$)

Position	δ_{C},[b] mult.	δ_{H}[a] (*J* in Hz)	COSY	HMBC
1	171.3, C			
2	97.1, C			
3	183.3, C			
4	153.3, C			
5	89.7, CH_2	5.16, s		2, 3, 4
		4.77, s		
6	199.8, C			
7	35.9, CH_2	3.46, d (11.6)		2, 3, 6, 8, 9
		2.41, t (11.6)		
8	77.9, CH	4.19, dd (11.6, 5.9)	7, 9	6, 7, 9, 14
9	27.9, CH	2.20, m	10, 11	8, 10, 11
10	17.8, CH_3	0.95, d (6.8)	9	8, 9, 11
11	36.5, CH_2	1.45, m	9, 12	
12	29.1, CH	1.76, m	11, 13, 14	
13	11.3, CH_3	0.89, d (6.8)	12	11, 12, 14
14	70.0, CH	3.60, m	12, 15	8, 11, 13, 17
15	36.7, CH	1.50, m	16	14, 16
16	7.5, CH_3	0.80, d (6.8)	15	14, 15, 17
17	73.9, CH	3.80, m	18	14, 16, 18, 19
17-OH		6.37, br s	17	17, 18
18	49.0, CH	3.60, m	17, 19	17, 21
19	21.5, CH_2	1.59, m	18, 20	21
		1.28, m		
20	12.9, CH_3	0.72, t (7.2)	19	18, 19
21	222.9, C			
22	78.9, C			
22-OH		5.91, s	23	21, 22, 23
23	20.7, CH_3	1.06, s	22-OH	21, 22, 24
24	84.1, CH	4.43, dd (11.2, 6.4)	25	22, 25, 26
25	25.0, CH_2	2.18, m	24, 26	
		1.84, m		
26	29.3, CH_2	1.74, m	25	27, 28, 30
27	89.1, C			
28	30.2, CH_2	1.64, m	29	26, 27, 29, 30
		1.40, m		
29	9.4, CH_3	0.77, t (7.5)	28	27, 28
30	70.3, CH	3.52, m	31	
31	20.2, CH_2	1.94, m	30	27
		1.57, m		
32	25.0, CH_2	1.68, m	33-OH	
		1.44, m		
33	73.2, C			
33-OH		4.39, s	32	32, 33
34	74.9, CH	3.98, q (6.4)	35	30, 32, 33, 35
35	14.4, CH_3	1.11, d (6.4)	34	33, 34
36	78.9, CH	3.04, q (6.2)	37	32, 34, 37, 38
37	11.3, CH_3	1.11, d (6.2)	36	36
38	56.5, CH_3	3.26, s		36

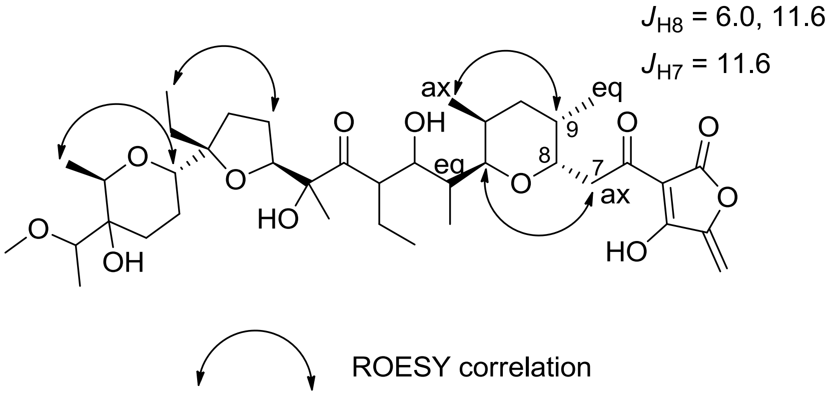

Figure 6.3. Key ROESY correlations

A ROESY correlation between H-30 and H-35 suggested that H-30 and H-34 were *anti*. Although several other ROESY correlations existed within the C-24 to C-38 region, additional experiments were necessary in order to confidently assign the configuration for the remaining stereocenters. Considerable overlap in the upfield region of the 2D ROESY initially prevented assignment of ROESY correlations in this region. In order to clearly distinguish these correlations, a 1D selective TOCSY-NOESY NMR experiment was acquired. H-24 (4.43 ppm) was selectively excited and showed TOCSY correlations to several protons, including H-25a (2.18 ppm) and H-25b (1.84 ppm). The 1D selective TOCSY allowed for the isolation of these signals away from interfering signals in other portions of the structure. A 1D selective NOESY experiment was then completed by selectively exciting H-25a (Figure 6.4). Signals for H-23, H-25b, H-26, H-28b, and H-29 were seen in the 1D selective NOESY, indicating these protons were within 5 Å of H-25b. Most important of these signals were H-28b (1.40 ppm) and H-29 (0.77 ppm), which were across the ether ring. This data was compared to molecular models of the two possible isomers at C-24 and C-27. Spartan10[16] was used to calculate the low energy conformer for a truncated ecteinamycin with C-22 and C-28 *syn* and *anti* to each other. In the *syn* model, H-25a and H-25b were less than 5 Å from H-28a, H-28b, and H-29, in agreement with the ROESY NMR data. However, when C-22 and C-28 were *anti* to each other, H-25a was greater than 5 Å away from H-29 and thus, not matching the NOESY NMR data. Consequently, C-22 and C-28 were assigned *syn* to each other in the ether ring. The same procedure was repeated for a 1D selective NOESY of H-25b (1.84 ppm) and resulted in similar correlations.

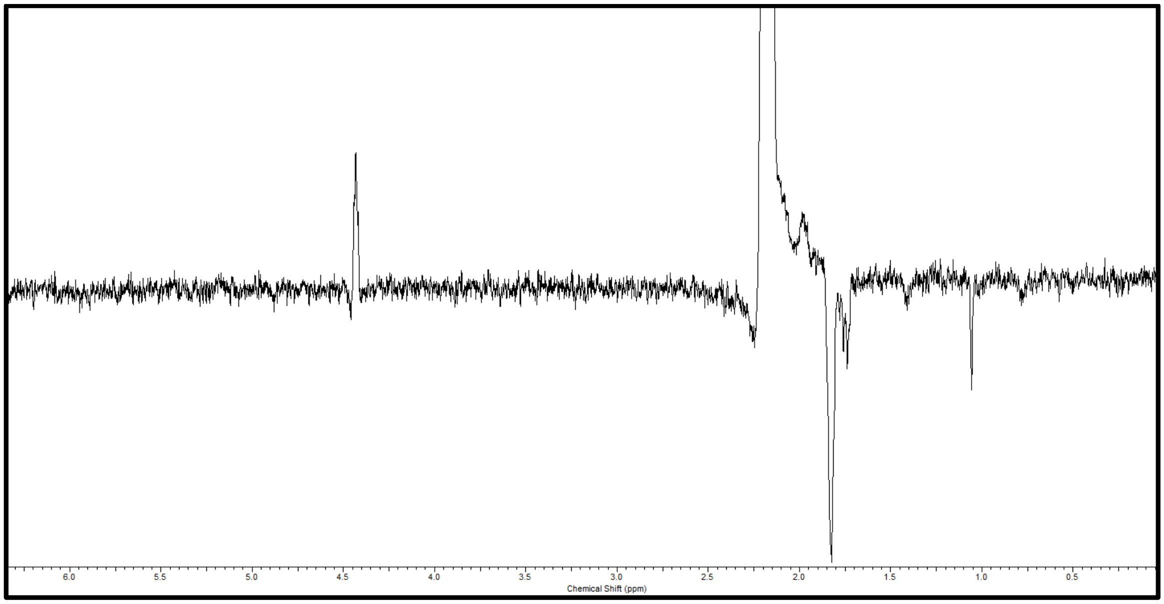

Figure 6.4. 1D selective TOCSY-NOESY NMR

After determining this relative configuration, considerable molecular modeling and DFT NMR calculations were undertaken in attempt to assign the configuration at the remaining stereocenters, but results were inconclusive. Modified Mosher's method[18,19] was attempted for the C-17 hydroxyl but did not form the expected product. Additionally, HSQMBC[20] data were acquired on ecteinamycin (**65**) in attempt to use the *J*-based configuration method[21] to assign the stereochemistry for C-15 to C-18 but was inconclusive. Ecteinamycin (**65**) was also compared to the structures of other polyether antibiotics. In particular, lasalocid (**66**) and salinomycin (**67**) have a very similar structural motif to ecteinamycin (**65**) in the C-24 to C-38 region. Cane *et al*. proposed a stereochemical model that relates the stereochemistry for many of the polyether antibiotics, based partially on biosynthetic considerations.[22] Many polyether antibiotics share certain similar structural features, and these compounds, in most cases, have the same stereochemistry in that region.[22] Lasalocid (**66**) and salinomycin (**67**) have the exact same stereochemistry in the terminal ether ring, and while the model proposed by Cane *et al*.[22] would suggest that ecteinamycin has the same stereochemistry, a comparison of ^{1}H and ^{13}C NMR data was inconclusive and prevented assigning the stereochemistry using this method.

Crystallization has been the primary method for determining the stereochemistry of polyether antibiotics.[23-25] After considerable literature searches, the only other method used for determination of the absolute configuration of the polyether antibiotics has been total synthesis.[26-28] Considerable efforts were undertaken to crystallize ecteinamycin, using a variety of solvents and conditions, but ultimately, no crystal was formed. Thus far, about half of the relative configuration of ecteinamycin (**65**) has been assigned by the aforementioned NMR methods, but additional work is necessary.

Ecteinamycin (**65**) was screened against a panel of gram-positive and gram-negative bacteria. The minimum inhibitory concentration (MIC) of ecteinamycin is reported in Table 6.2. Ecteinamycin was particularly potent against gram-positive bacteria, which is consistent with the activity of ionophore antibiotics. Among gram-positive bacteria, ecteinamycin demonstrated the highest potency against *C. difficile* with an MIC of $\leq$ 31 ng/mL. Nigericin, a polyether ionophore antibiotic, has also been reported to be selectively potent against *C. difficile* with an MIC of 2.5 ng/mL; monensin was not as potent with an MIC of 0.5 μg/mL against *C. difficile*.[29]

Flow cytometry was used to determine if ecteinamycin (**65**), like other polyether ionophore antibiotics, depolarizes cell membranes. DiOC$_2$(3) (3,3'-diethyloxacarbocyanine iodide) fluoresces green in bacterial cells but shifts to red when the cell membrane is depolarized.[30] Therefore, the ratio of red to green fluorescence is indicative of the membrane potential. *S. aureus* ATCC 92113 cells were treated with ecteinamycin (**65**) at concentrations of 6 and 32 μg/mL. Additionally, carbonyl cyanide m-chlorophenylhydrazone (CCCP), which has been demonstrated to depolarize cell membranes, was used as a positive control. All cells except the DMSO negative control were treated with DiOC$_2$(3) and analyzed by flow cytometry. Ecteinamycin demonstrated membrane depolarization of *S. aureus* cells at 6 μg/mL (Figure 6.2). CCCP demonstrated membrane depolarization to a greater extent than ecteinamycin. This mechanism of action therefore matches that of other ionophore antibiotics.

Table 6.2. Minimum inhibitory concentration (MIC) of ecteinamycin (**65**)

Organism	MIC (μg/mL)
E. coli	16
Methicillin-sensitive *Staphylococcus aureus*	0.125
Methicillin-resistant *Staphylococcus auerus*	0.125
Vancomycin-resistant *Enterococcus*	0.25
P. aeruginosa	8
S. cerevisiae	8
C. difficile	≤ 0.0313

In parallel, chemical genomic profiling with the yeast, *Saccharomyces cerevisiae*, was used to understand the the effects of ecteinamycin (**65**) on eukaryotic cells. This method has been used for determining the mechanism of action and molecular target for many bioactive compounds, including natural products.[31-34] Ecteinamcyin (**65**) was screened against over four thousand deletion mutant yeast strains, genomic DNA was extracted, and mutant-specific DNA barcodes were amplified and sequenced by Illumina sequencing. Ecteinamycin (**65**) sensitive and resistant mutants were determined by quantification of DNA-barcodes, providing a chemical genomic profile, which was used to evaluate the mechanism of action.

Ecteinamycin (**65**) gave a distinct chemical genomic profile at 250 µg/mL (Table 6.3). When we compared the chemical genomic profile of ecteinamycin (**65**) to our existing dataset of known compounds, we found the top two correlations to be with the polyether antibiotics

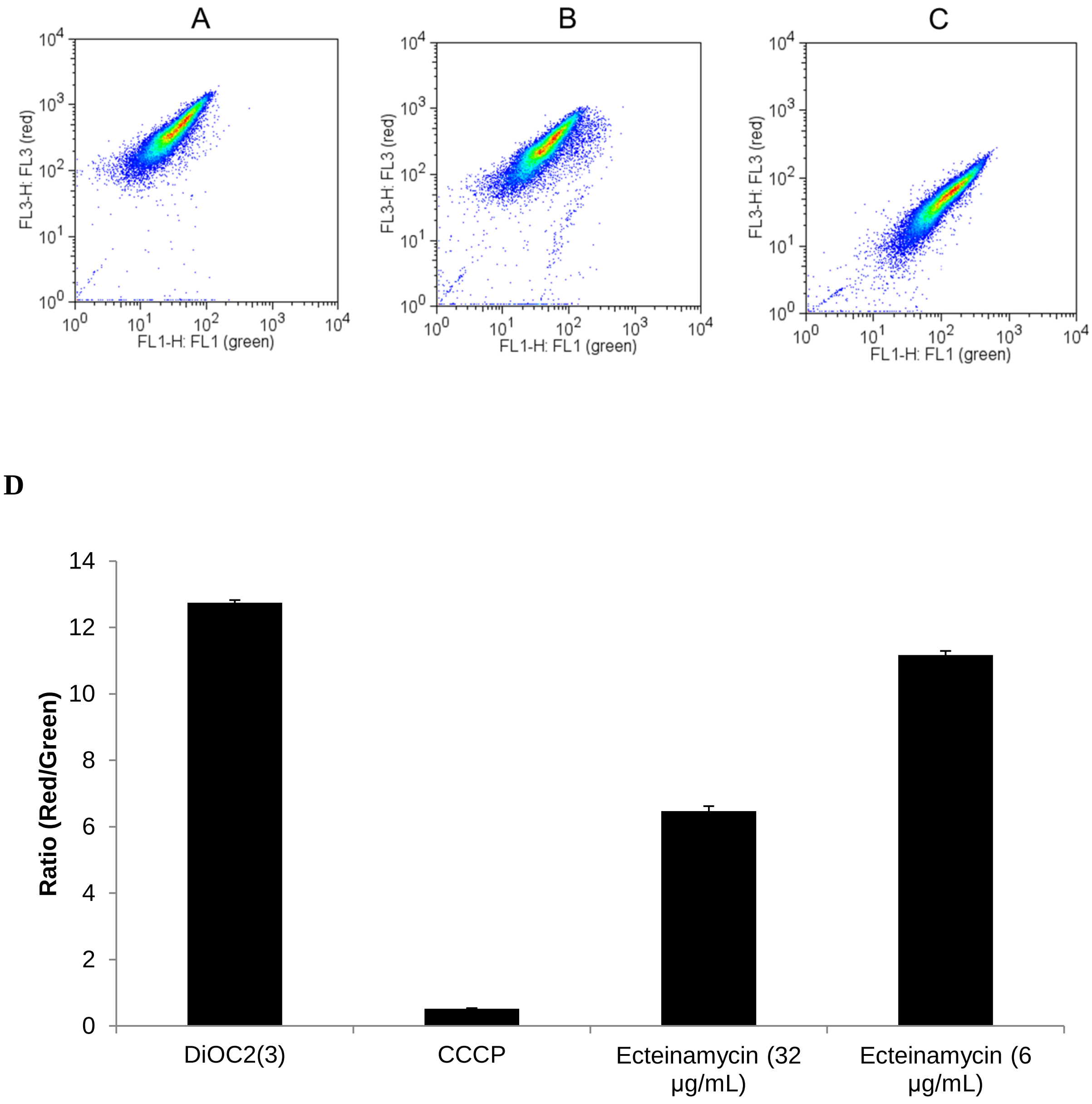

Figure 6.5. Membrane depolarization assay. Flow cytometry analysis of MSSA cells treated with DiOC$_2$(3) dye control (A), ecteinamycin (B), and CCCP (C). (D) The ratio of red to green fluorescence for MSSA cells treated with DiOC$_2$(3) dye and corresponding compound.

Table 6.3. Ecteinamycin responsive yeast deletion mutants. Fold change in abundance of the mutants relative to the solvent control was calculated with EdgeR. A fold change value <1 indicates sensitivity to ecteinamycin, while a value >1 indicates resistance.

	Disrupted gene	**Fold Change**	**Adj. P-value**	**Gene Function**
Sensitive	*PAR32*	0.017	$1.5e^{-39}$	Putative protein of unknown function
	YMR010W	0.122	$3.13e^{-22}$	Putative protein of unknown function
	YPT7	0.016	$4.28e^{-22}$	Rab family GTPase
	APL4	0.076	$1.65e^{-21}$	Gamma-adaptin; large subunit of the clathrin-associated protein (AP-1) complex
	APM2	0.037	$3.11e^{-21}$	homologous to the medium chain of mammalian clathrin-associated protein complex
	YOL162W	0.145	$8.75e^{-20}$	Member of the Dal5p subfamily of the major facilitator family
	YPR089W	0.110	$1.83e^{-18}$	Protein of unknown function; exhibits genetic interaction with ERG11
	VPS38	0.087	$8.25e^{-17}$	Part of a Vps34p phosphatidylinositol 3-kinase complex
	TRP4	0.136	$6.02e^{-16}$	Anthranilate phosphoribosyl transferase; transferase of the tryptophan biosynthetic pathway
	DRS2	0.040	$6.64e^{-16}$	Trans-golgi network aminophospholipid translocase (flippase)
Resistant	*PHO2*	5.974	$1.14e^{-22}$	Homeobox transcription factor; regulatory targets include genes involved in phosphate metabolism
	UME6	10.979	$2.56e^{-22}$	Component of the Rpd3L histone deacetylase complex
	YPL205C	4.953	$6.57e^{-13}$	Hypothetical protein; deletion of locus affects telomere length
	IRC25	3.732	$1.23e^{-11}$	Component of a heterodimeric Poc4p-Irc25p chaperone; involved in assembly of alpha subunits into the 20S proteasome
	MRH1	4.129	$9.71e^{-11}$	Protein that localizes primarily to the plasma membrane
	PRE9	5.995	$3.46e^{-10}$	Alpha 3 subunit of the 20S proteasome
	MSS11	2.585	$7.36e^{-10}$	Mitochondrial protein; forms a heterodimer complex with Mto1p that performs the 5- modification of the wobble uridine base in mitochondrial tRNAs
	EGT2	3.564	$9.12e^{-10}$	Glycosylphosphatidylinositol (GPI)-anchored cell wall endoglucanase
	PHO84	2.986	$4.57e^{-09}$	High-affinity inorganic phosphate (Pi) transporter
	HAL9	3.379	$3.03e^{-08}$	Putative transcription factor containing a zinc finger

duamycin and nigericin[35] (P<0.0001). Both of these compounds act by generating ion channels in cellular membranes and inhibit golgi function in eukaryotic cells. The top sensitive mutant strains (P<0.0001) were significantly enriched for genes involved in post-golgi mediated transport ($P=9.1e^{-5}$). This enrichment was driven by sensitive mutants with deletions of the genes *DRS2*, *APL4*, *APM2*, and *YPT7*. We found no functional enrichment among the top mutant strains resistant to ecteinamycin (**65**). The most sensitive protein complex to ecteinamycin based on the sum of Z-scores of mutants in the complex, was the AP-1 adaptor complex, a membrane coat adaptor complex in the trans-golgi network. We identified only one significantly sensitive DAmP mutant (P=0.03), a hypomorph of *SEC14*, a phosphatidylinositol/phosphatidylcholine transfer protein required for correct trans-golgi network dynamics.[36]

When we compared the chemical genomic profile to the genetic interaction network of *S. cerevisiae*, among the top 20 genetic mutant profiles we saw significant enrichment for genes involved in the GO processes “regulation of intracellular pH” (P=0.007) driven by correlation with the genetic profiles of mutants of *VMA8*, *VMA1*, and *VMA10*. There was also significant enrichment for genes involved in “intra-golgi vesicle-mediated transport” (P=0.007) driven by correlation with the genetic profile of deletion mutant of *COG6*, *COG8*, *COG5*. Combined with the structural similarity of ecteinamycin (**65**) and other polyether antibiotics, these data suggest ecteinamycin (**65**) works through a similar mechanism by forming ion channels and disruption of golgi dynamics in eukaryotes.

In addition, a pharmacokinetic study in mice was pursued to determine the oral bioavailability of ecteinamycin (**65**). A standard curve (Figure 6.6) using known concentrations of ecteinamycin was constructed to determine the amount of ecteinamycin in the mouse plasma. Mice were dosed orally with ecteinamycin (**65**) at 5 mg/kg, or by retro-orbital intravenous (IV) injection at 2.5 mg/kg. IV injection of ecteinamycin (**65**) at 5 mg/kg was lethal so IV injection was reduced to 2.5 mg/kg. Accounting for this difference in dosage, the oral bioavailability was determined to be 10.9% after 30 mins of treatment and 29.3% after 1 h of treatment. These results are somewhat similar to other polyether ionophore antibiotics, such as salinomycin (**67**) and monensin (**68**). Most animal studies for polyether ionophore antibiotics have focused on ruminant animals, such as cattle and chickens, which make up most of the market for anticoccidials. For example, oral bioavailability for monensin (**68**) in chickens was determined to be 30%.[37] Oral bioavailability of polyether ionophore antibiotics in ruminants does not usually exceed 50% as the compounds are rapidly metabolized in the liver.[38] Additionally, toxicity issues exist for many of the polyether antibiotics at higher concentrations,[39,40] similar to ecteinamycin (**65**).

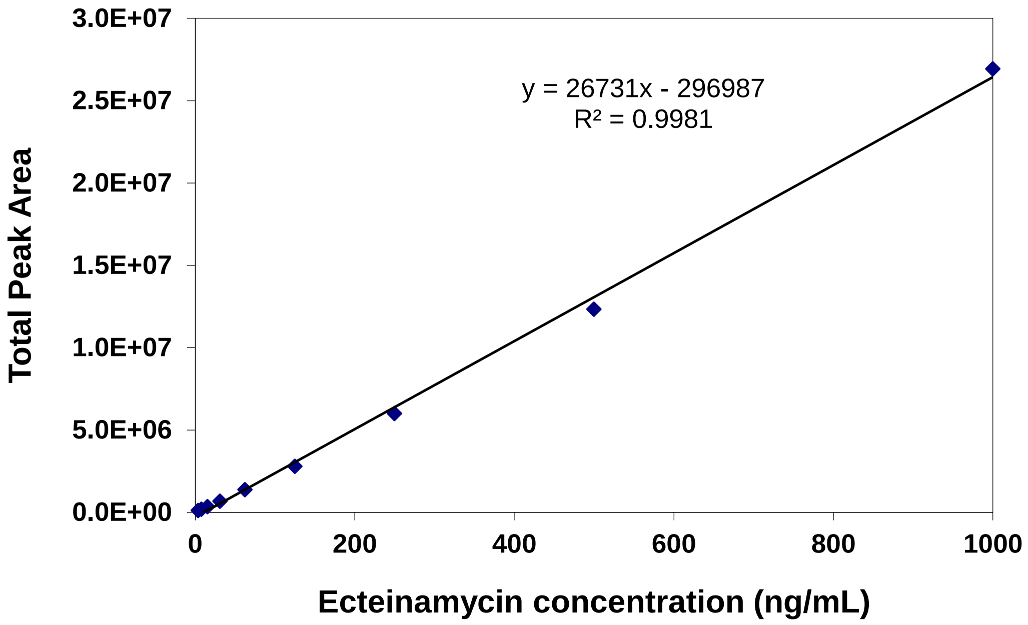

Figure 6.6. Standard curve for pharmacokinetic study

6.3. Conclusion

With the continued rise in antibiotic resistance, there is an immediate need for new antibiotics. In particular, *C. difficile* poses a major threat to human health. Ecteinamycin (**65**), a potent polyether antibiotic, was iolated from a marine-derived *Actinomadura* sp (Strain WMMB499). The *Actinomadura* sp. was targeted for investigation based on PCA of LCMS data of bacterial extracts that showed the *Actinomadura* sp. had a unique chemical signature and potentially novel chemistry. After isolation, the structure of ecteinamycin (**50**) was rapidly elucidated by ^{13}C-^{13}C COSY NMR of ^{13}C-labeled compound and other spectroscopic methods. Most importantly, ecteinamycin (**65**) demonstrated potent antibacterial activity, especially against gram-positive bacteria. In particular, ecteinamycin (**65**) showed selectivity towards *C. difficile*. Initial mechanism of action studies suggested that ecteinamycin (**65**) acts as an ionophore antibiotic. PK studies in mice demonstrated that ecteinamycin has oral bioavailability, albeit somewhat low; low bioavailability would allow the compound to remain in the gut for bioactivity and remain out of the bloodstream to limit toxicity.[41] While additional work is necessary to more thoroughly characterize the mechanism of action, the discovery of ecteinamycin (**65**) provides a promising therapeutic lead against *C. difficile*.

6.4. Materials and Methods

General Experimental Procedures

Optical rotations were measured on a Perkin–Elmer 241 Polarimeter. UV spectra were recorded on an Aminco/OLIS UV-Vis Spectrophotometer. IR spectra were measured with a Bruker Equinox 55/S FT–IR Spectrophotometer. NMR spectra were obtained in $CDCl_3$ with a Bruker Avance 600 MHz spectrometer equipped with a 1.7 mm $^{1}H\{^{13}C/^{15}N\}$ cryoprobe and a Bruker

Avance 500 MHz spectrometer equipped with a $^{13}C/^{15}N\{^1H\}$ cryoprobe. HRMS data were acquired with a Bruker MaXis 4G QTOF mass spectrometer. RP HPLC was performed using a Shimadzu Prominence HPLC system and a Phenomenex Luna C18 column (250 × 10 mm, 5 μm).

Biological Material. Ascidian specimens were collected on October 11, 2010, in the Florida Keys (24° 37.487′, 81° 27.443′). Identification was confirmed by Shirley Parker-Nance. A voucher specimen (FLK10-5-3) for *Ecteinascidia turbinata* (Herdman, 1880) is housed at the University of Wisconsin-Madison. For cultivation, a sample of ascidian (1 cm^3) was rinsed with sterile seawater, macerated using a sterile pestle in a micro-centrifuge tube, and dilutions were made in sterile seawater, with vortexing between steps to separate bacteria from heavier tissues. Dilutions were separately plated on three media: ISP2, R2A, and M4. Each medium was supplemented with 50 μg/mL cycloheximide and 25 μg/mL nalidixic acid. Plates were incubated at 28 °C for at least 28 days.

Sequencing. 16S rDNA sequencing was conducted as previously described.[42] WMMB499 was identified as an *Actinomadura* sp. and demonstrated 99% sequence similarity to *Actinomadura* sp. 13679C (accession number EU741239). The 16S sequence for WMMB499 was deposited in GenBank (accession number JX101467).

Fermentation, Extraction, and Isolation. Two 10 mL seed cultures (25 × 150 mm tubes) in medium ASW-A (20 g soluble starch, 10 g glucose, 5 g peptone, 5 g yeast extract, 5 g $CaCO_3$ per liter of artificial seawater) were inoculated with strain WMMB499 and shaken (200 RPM, 28 °C) for seven days. Two hundred fifty mL baffled flasks (12 × 50 mL) containing ASW-A were inoculated with 1 mL seed culture and were incubated (200 RPM, 28 °C) for seven days. Two-liter flasks (6 × 500 mL) containing medium ASW-A with Diaion HP20 (4% by weight) were inoculated with 25 mL from the 50 mL culture and shaken (200 RPM, 28 °C) for seven days. Filtered HP20 and cells were washed with H_2O and extracted with acetone. The acetone extract (3.2 g) was subjected to liquid-liquid partitioning using 30% aqueous MeOH and $CHCl_3$ (1:1). The $CHCl_3$-soluble partition (2.2 g) was fractionated by Sephadex LH20 column chromatography ($CHCl_3$: MeOH, 1:1). Fractions containing **65** were subjected to RP HPLC (75/25% to 100/0% MeOH-ammonium acetate 10 mM in 15 mins) using a Phenomenex Luna C18 column (250 × 10 mm, 5 μm) and yielded **65** (1.0 mg, RT 13.5 min). For ^{13}C incorporation, the same procedure was used with two-liter flasks (2 × 500 mL) containing medium ASW-A ($U^{13}C$-glucose substituted for unlabeled glucose).

Ecteinamycin (65): white solid; $[\alpha]^{25}_{D}$ +67 (*c* 0.08, MeOH); UV (MeOH) λ_{max} (log ε) 200 (3.91), 250 (4.16), 299 (3.89) nm; IR (ATR) υ_{max} 1735, 1635, 1538, 1457, 1215 cm^{-1}; ^1H and ^{13}C NMR (See Table 6.1); HRMS $[M+H]^+$ *m/z* 709.4141 (calcd for $C_{38}H_{61}O_{12}$, 709.4158).

***In vitro* Assay.** Ecteinamycin (**65**) was tested for antibacterial activity against *C. difficile* (ATCC BAA-1870), MRSA (ATCC #33591), MSSA (ATCC #29213), *E. coli* (ATCC #25922), *P. aeruginosa* (ATCC #27853), and VRE (ATCC), and MICs were determined using a dilution antimicrobial susceptibility test for aerobic[43] (MRSA, MSSA, *E. coli*, *P. aeruginosa*, and VRE) and anaerobic (*C. difficile*) bacteria.[44] Ecteinamycin (**65**) was dissolved in DMSO, serially diluted to 10 concentrations (0.0313 – 32 μg/mL), and tested in a 96-well plate. Vancomycin was used as a control and exhibited an MIC of 1 μg/mL against MSSA and 1 μg/mL against MRSA. Ecteinamycin (**65**) and vancomycin were tested in triplicate. Six untreated media controls were included on each plate. For MRSA, MSSA, *E. coli*, and *P. aeruginosa*, the plates were incubated at 33 °C for 18 h. For *C. difficile*, the plate was incubated at 36 °C for 48 h anaerobically and then read visually using a mirror apparatus. All manipulations to the plate were done inside the anaerobe chamber. The MIC was determined as the lowest concentration that inhibited visible growth.

Membrane Depolarization Assay. *S. aureus* (ATCC #29213) cells were grown to log phase (14 h) in Mueller Hinton Broth cation-adjusted (MHB_{50}) and were diluted to 0.07 OD_{600} with media. One mL aliquots were transferred to 1.5 mL centrifuge tubes and treated with the following in triplicate: 10 µL DMSO (control), 10 µL of 600 µg/mL ecteinamycin (**65**), 10 µL of 3.2 mg/mL ecteinamycin (**1**), and 10 µL of 500 µM carbonyl cyanide m-chlorophenylhydrazone (CCCP). Additionally, each tube received 10 µL of 3 mM $DiOC_2(3)$ (3,3'-diethyloxacarbocyanine iodide). The tubes were shaken for 15 minutes at room temperature. The cells were then analyzed with a FACSCalibur (BD Biosciences) flow cytometer and CellQuestPro software (BD Biosciences). Collected data represent the geometric means of fluorescence of 40,000 gated events.

Chemical genomic analysis. A chemical genomic analysis of ecteinamycin (**65**) was performed as described previously.[34,45] A concentration of 250 µg/mL of ecteinamycin (**65**) was used and inhibited by 70% compared to the solvent control. Two hundred µL cultures of a pooled, genome-wide collection of ~5000 *S. cerevisiae* non-essential deletion mutants and a collection of essential gene hypomorphs[46] with 250 µg/mL ecteinamycin (**65**) or a DMSO control in duplicate were grown for 48 h at 30 °C. Genomic DNA was extracted using the Epicentre MasterPure™ Yeast DNA purification kit. Mutant-specific molecular barcodes were amplified with specially designed multiplex primers containing adapters for Illumina sequencing.[47] The barcodes were sequenced using an Illumina HiSeq2500 Rapid Run platform, and replicates of each condition were sequenced (ecteinamycin vs. DMSO). The barcode counts for each yeast deletion mutant in the presence of ecteinamycin (**65**) were normalized against the DMSO control conditions to generate a Z-score to define sensitivity or resistance of individual strains (the chemical genomic profile). In addition, differential abundance analysis was calculated for each mutant's response to ecteinamycin versus DMSO using edgeR.[48] Mutants with very low counts (<5) were filtered out before using the edgeR package (version 3.4.2) to calculate an adjusted P-value and log fold change for each mutant. A Bonferroni corrected hypergeometric distribution test was used to search for significant enrichment of GO terms among the top sensitive and resistant deletion mutants with a P-value less than 0.0001.[49] The chemical genomic profile of ecteinamycin (**65**) was compared against our existing chemical genomic dataset (unpublished) by Pearson correlation.

Pharmacokinetic analysis

An Agilent 1100 LCMS system (ESI-MS positive mode) with a Phenomenex Kinetix C18 column (100 × 4.6 mm, 2.6 μm) at a flow rate of 0.5 mL/min was used for all analysis. The gradient was from 75% MeOH/25% 1 mM ammonium acetate in H_2O to 93% MeOH/7% 1 mM ammonium acetate in H_2O in 11 mins, then 93% MeOH/7% 1 mM ammonium acetate in H_2O to 100% MeOH for 0.1 min and holding 100% MeOH for 3.9 min.

Assay validation. A standard curve was constructed using known concentrations of ecteinamycin (1000, 500, 250, 125, 62.50, 31.25, 15.625, 7.8125, 3.90625 ng/mL) in blank human plasma. Linear regression analysis was performed on the peak areas, and the resulting linear equation was used to calculate the ecteinamycin concentrations of quality control (QC) standards of ecteinamycin in human plasma (800, 200, 25, 12.5 ng/mL). The limit of detection was determined to be 31.25 ng/mL, and the limit of quantification was determined to be 62.50 ng/mL.

Animals. Eight-to-nine-week-old FVB female mice weighing 20.5 to 25.6 g were used for all studies. Animals were maintained in accordance with the American Association for Accreditation of Laboratory Care criteria. Animal studies were approved by the University of Wisconsin Animal Care Committee.

Determination of ecteinamycin in plasma. Ecteinamycin was formulated with polyethylene glycol (PEG) 300, 25 mM Tris (1:1), pH 8.9. Mice were treated orally at 5 mg/kg or by retro-orbital intravenous injection at 2.5 mg/kg. Retro-orbital intravenous injection at 5 mg/kg was lethal. After 30 min and 1 h, approximately 400 μL of blood was collected from the chest cavity in BD microtainer tubes with lithium heparin. Blood was centrifuged at 10,000 rpm for 10 min. Fifty μL of supernatant was added to 200 μL of acetonitrile (containing 0.1% formic acid) in a new polypropylene tube, vortexed for 1 min, and centrifuged for 10 min at 14,000 RPM at 4 ˚C. One hundred μL was transferred to a 96 well polypropylene microplate, 100 μL of H_2O was added, and the plate was covered and shaken for 1 min and placed in the autosampler for analysis. Three replicates were completed for each time point for both oral and IV dosing (except 2 replicates for retro-orbital IV 1 h timepoint due to lethal injection of one mouse). Sample quantitation was determined by weighted (R^2) linear regression using a 9-point curve. Linear regression analysis was performed on the peak areas, and the resulting linear equation was used to calculate the ecteinamycin concentrations of the unknowns. The % oral bioavailability was calculated from the concentration of ecteinamycin (adjusted for dose) in plasma between oral and IV dose: $[\text{ecteinamycin}_{\text{oral}}]/[\text{ecteinamycin}_{\text{IV}}] \times 100$.

6.5. References

1. Center for Disease Control and Prevention. http://www.cdc.gov/drugresistance/threat-report-2013/ (accessed 24 Jan 2014)

2. Rupnik, M.; Wilcox, M.H.; Gerding, D.N. Clostridium difficile infection: new developments in epidemiology and pathogensis. *Nat. Rev. Microbiol.* **2009**, *7,* 526-536.

3. Kachrimanidou, M.; Malisiovas, N. Clostridium difficile infection: a comprehensive review. *Crit. Rev. Microbiol.* **2011**, *37,* 178-187.

4. Kevin, D.A.; Meujo, D.A.; Hamann, M.T. Polyether ionophores: broad-spectrum and promising biologically active molecules for the control of a drug-resistant bacteria and parasites. *Expert Opin. Drug. Discov.* **2009**, *4*, 109-146.

5. Freeman, J.; Bauer, M.P.; Baines, S.D.; Corver, J.; Fawley, W.N.; Goorhuis, B.; Kuijper, E.J.; Wilcox, M.H. The changing epidemiology of Clostridium difficile infections. *Clin. Microbiol. Rev.* **2010**, *23,* 529-549.

6. Chaparro, F.; Mullane, K.M. Emerging therapies for Clostridium difficile infection – focus on fidaxomicin. *Infect. Drug Resist.* **2013**, *6*, 41-53.

7. Dutton, C.J.; Banks, B.J.; Cooper, C.B. Polyether ionophores *Nat. Prod. Rep.* **1995**, *12*, 165-181.

8. Callaway, T.R.; Edrington, T.S.; Rychlik, J.L.; Genovese, K.J.; Poole, T.L.; Jung, Y.S.; Bischoff, K.M.; Anderson, R.C.; Nisbet, D.J. Ionophores: their use as ruminant growth promotants and impact on food safety. *Curr. Issues. Intest. Microbiol.* **2003**, *4*, 43-51.

9. Keller-Juslén, C.; King, H.D.; Kuhn, M.; Lossli, H.; Pache, W.; Petcher, T.J.; Weber, H.P.; Wartburg, A.V. Tetronomycin, a novel polyether of unusual structure. *J. Antibiot.* **1982**, *35*, 142-150.

10. Davies, D.H.; Snape, E.W.; Suter, P.J.; King, T.J.; Falshaw, C.P. Structure of antibiotic M139603; x-ray crystal structure of the 4-bromo-3,5-dinitrobenzoyl derivative. *J. Chem. Soc., Chem. Commun.* **1981**, 1073-1074.

11. Hou, Y.; Braun, D.R.; Michel, C.R.; Klassen, J.L.; Adnani, N.; Wyche, T.P.; Bugni, T.S. Microbial strain prioritization using metabolomics tools for the discovery of natural products. *Anal. Chem.* **2012**, *84*, 4277-4283.

12. Wyche, T.P.; Standiford, M.; Hou, Y.; Braun, D.; Johnson, D.A.; Johnson, J.A.; Bugni, T.S. Activation of the nuclear factor E2-related factor 2 pathway by novel natural products halomadurones A-D and a synthetic analogue. *Marine Drugs*, **2013**, *11,* 5089-5099.

13. Ellis, G.A.; Wyche, T.P.; Fry, C.G.; Braun, D.R.; Bugni, T.S. Solwaric acids A and B, antibacterial aromatic acids from a marine Solwaraspora sp. *Marine Drugs*, **2014**, *12*, 1013-1022.

14. Wang, F.; Xu, M.; Li, Q.; Sattler, I.; Lin, W. p-Aminoacetophenoic acids produced by a mangrove endophyte Streptomyces sp. (strain HK10552). *Molecules* **2010**, *15*, 2782-2790.

15. Crew, P.; Rodríguez, J.; Jaspars, M. *Organic Structure Analysis*, 2nd ed.; Oxford University Press: New York, 2010.

16. Spartan 10, v. 1.0.2. Wavefunction Inc. 2011.

17. Uhrín, D.; Barlow, P.N. Gradient-enhanced one-dimensional proton chemist-shift correlation with full sensitivity. *J. Magn. Reson*. **1997**, *126*, 248-255.

18. Seco, J. M.; Quinoa, E.; Riguera, R. A practical guide for the assignment of the absolute configuration of alcohols, amines and carboxylic acids by NMR. *Tetrahedron-Asymmetry*, **2001**, *12*, 2915-2925.

19. Seco, J. M.; Quinoa, E.; Riguera, R. The assignment of absolute configuration by NMR. *Chem. Rev.* **2004**, *104*, 17-117.

20. Williamson, R.T.; Márquez, B.L.; Gerwick, W.H.; Köver, K.E. One- and two-dimensional gradient-selected HSQMBC NMR experiments for the efficient analysis of long-range heteronuclear coupling constants. *Magn. Reson. Chem*. **2000**, *38*, 265-273.

21. Matsumori, N.; Kaneno, D.; Murata, M.; Nakamura, H.; Tachibana, K.. Stereochemical determination of acyclic structures based on carbon-proton spin-coupling constants. A method of configuration analysis for natural products. *J. Org. Chem.* **1999**, *64*, 866-876.

22. Cane, D.E.; Celmer, W.D.; Westley, J.W. Unified stereochemical model of polyether antibiotic structure and biogenesis. *J. Am. Chem Soc*. **1983**, *105*, 3594-3600.

23. Smith, G.D.; Duax, W.L. Crystal and molecular structure of the calcium ion complex of A23187. *J. Am. Chem Soc*. **1976**, *98*, 1578-1580.

24. Shiro, M.; Nakai, H.; Nagashima, K.; Tsuji, N. X-Ray determination of the structure of the polyether antibiotic K-41. *J. Chem. Soc., Chem. Commun*. **1978**, *16*, 682-683.

25. Suh, I.H.; Aoki, K.; Yamazaki, H. Crystal structure of a silver salt of the antibiotic lasalocid A: a dimer having an exact 2-fold symmetry. *Inorg. Chem*. **1989**, *28*, 358-362.

26. Evans, D.A.; Bender, S.L.; Morris, J. Total synthesis of the polyether antibiotic X-206. *J. Am. Chem. Soc.* **1988**, *110*, 2506-2526.

27. Horita, K.; Inoue, T.; Tanaka, K.; Yonemitsu, O. Total synthesis of the polyether antibiotic lysocellin. *Tetrahedron Lett*. **1992**, *33*, 5537-5540.

28. Evans, D.A.; Ratz, A.M.; Huff, B.E.; Sheppard, G.S. Total synthesis of the polyether antibiotic lonomycin A (emericid). *J. Am. Chem. Soc*. **1995**, *117*, 3448-3467.

29. Wu, X.; Charian, P.T.; Lee, R.E.; Hurdle, J.G. The membrane as a target for controlling hypervirulent Clostridium difficile infections. *J. Antimicrob. Chemother*. **2013**, *68*, 806-815.

30. Silverman, J.A.; Perlmutter, N.G.; Shapiro, H.M. Correlation of daptomycin bactericidal activity and membrane depolarization in Staphylococcus aureus. *Antimicrob. Agents Chemother*. **2003**, *47*, 2538-2544.

31. Ho, C.H.; Piotrowski, J.; Dixon, S.J.; Baryshnikova, A.; Costanzo, M.; Boone, C. Combining functional genomics and chemical biology to identify targets of bioactive compounds. *Curr. Opin. Chem. Biol*. **15**, *2011*, 66-78.

32. Parsons, A.B.; Brost, R.L.; Ding, H.; Li, Z.; Zhang, C.; Sheikh, B.; Brown, G.W.; Kane, P.M.; Hughes, T.R.; Boone, C. Integration of chemical-genetic and genetic interaction data links bioactive compounds to cellular target pathways. *Nat. Biotechnol*. **2004**, *22*, 62-69.

33. Costanzo, M.; Baryshnikova, A.; Bellay, J.; Kim, Y.; Spear, E.D.; Sevier, C.S.; Ding, H.; Koh, J.L.; Toufighi, K.; Mostafavi, S.; Prinz, J.; St Onge, R.P.; VanderSluis, B.; Makhnevych, T.; Vizeacoumar, F.J.; Alizadeh, S.; Bahr, S.; Brost, R.L.; Chen, Y.; Cokol, M.; Deshpande, R.; Li, Z.; Lin, Z.Y.; Liang, W.; Marback M.; Paw, J.; San Luis, B.J.; Shuteriqi, E.; Tong, A.H.; van Dyk, N.; Wallace, I.M.; Whitney, J.A.; Weirauch, M.T.; Zhong, G.; Zhu, H.; Houry, W.A.; Brudno, M.; Ragibizadeh, S.; Papp, B.; Pál, C.; Roth, F.P.; Giaever, G.; Nislow, C.; Troyanskaya, O.G.; Bussey, H.; Bader, G.D.; Gingras, A.C.; Morris, Q.D.; Kim, P.M.; Kaiser, C.A.; Myers, C.L.; Andrews, B.J.; Boone, C. The genetic landscape of a cell. *Science* **2010**, *327*, 425-431.

34. Fung, S.-Y.; Sofiyev, V.; Schneiderman, J.; Hirschfeld, A.F.; Victor, R.E.; Woods, K.; Piotrowski, J.S.; Deshpande, R.; Li, S.C.; de Voogd, N.J.; Myers, C.L.; Boone, C.; Andersen, R.J.; Turvey. S.E. Unbiased screening of marine sponge extracts for anti-inflammatory agents combined with chemical genomics identifies girolline as an inhibitor of protein synthesis. *ACS Chem. Biol*. **2014**, *9*, 247-257.

35. Steinrauf, L.K.; Pinkerton, M. The structure of nigericin. *Biochem. Biophys. Res. Commun.* **1968**, *33*, 29-31.

36. Mousley, C.J.; Tyeryar, K.; Ile, K.E.; Schaaf, G.; Brost, R.L.; Boone, C.; Guan, X.; Wenk, M.R.; Bankaitis, V.A. Trans-Golgi network and endosome dynamics connect ceramide homeostasis with regulation of the unfolded protein response and TOR signaling in yeast. *Mol. Biol. Cell* **2008**, *19*, 4785–4803.

37. Henri, J.; Maurice, R.; Postollec, G.; Dubreil-Cheneau, E.; Roudaut, B.; Laurentie, M.; Sanders, P. Comparison of the oral bioavailability and tissue disposition of monensin and salinomycin in chickens and turkeys. *J. Vet. Pharmacol. Therap*. **2011**, *35*, 73-81.

38. Bhavsar, S.K.; Thaker, A.M. (2012). Pharmacokinetics of Antimicrobials in Food Producing Animals. In Readings in Advanced Pharmacokinetics - Theory, Methods and Applications; Noreddin, A., Ed.; InTech: Rejeka, Croatia, 2012.

39. Rollinson, J.; Taylor, F.G.; Chesney, J. Salinomycin poisoning in horses. *Vet. Rec*. **1987**, *121*, 1955-1959.

40. Plumlee, K.H.; Johnson, B.; Galey, F.D. Acute salinomycin toxicosis of pigs. *J. Vet. Diagn. Investig*. **1995**, *7*, 419-420.

41. Van de Waterbeemd, H.; Smith, D.A.; Beaumont, K.; Walker, D.K. Property-based design: optimization of drug absorption and pharmacokinetics. *J. Med. Chem*. **2011**, *44*, 1313-1333.

42. Wyche, T.P.; Hou, Y.; Braun, D.; Cohen, H.C.; Xiong, M.P.; Bugni, T.S. First natural analogs of the cytotoxic thiodepsipeptide thiocoraline A from a marine Verrucosispora sp. *J. Org. Chem*. **2011**, *76*, 6542-6547.

43. National Committee for Clinical Laboratory Standards. *Methods for Dilution Antimicrobial Susceptibility Tests for Bacteria that Grow Aerobically*, 7th ed.; NCCLS: Villanova, PA, 2006; Approved standard M7-A7.

44. National Committee for Clinical Laboratory Standards. *Methods for Antimicrobial Susceptibility Testing of Anaerobic Bacteria*, 6th ed.; NCCLS: Wayne, PA, 2004; Approved standard M11-A6.

45. Parsons, A.B.; Lopez, A.; Givoni, I.E.; Williams, D.E.; Gray, C.A.; Porter, J.; Chua, G.; Sopko, R.; Brost, R.L.; Ho, C.H.; Wang, J.; Ketela, T.; Brenner, C.; Brill, J.A.; Fernandez, G.E.; Lorenz, T.C.; Payne, G.S.; Ishihara, S.; Ohya, Y.; Andrews, B.; Hughes, T.R.; Frey, B.J.; Graham, T.R.; Andersen, R.J.; Boone, C. Exploring the mode-of-action of bioactive compounds by chemical-genetic profiling in yeast. *Cell* **2006**, *126*, 611-625.

46. Yan, Z.; Costanzo, M.; Heisler, L.E.; Paw, J.; Kaper, F.; Andrews, B.J.; Boone, C.; Giaever, G.; Nislow, C. Yeast barcoders: a chemogenomic application of a universal donor-strain collection carrying bar-code identifiers. *Nat. Meth*. **2008**, *5*, 719–725.

47. Smith, A.M.; Heisler, L.E.; Mellor, J.; Kaper, F.; Thompson, M.J.; Chee, M.; Roth, F.P.; Giaever, F.; Nislow, C. Quantitative phenotypes via deep barcode sequencing. *Genome Res*. **2009**, *19*, 1836– 1842.

48. Robinson, M.D.; McCarthy, D.J.; Smyth, G.K. edgeR: a Bioconductor package for differential expression analysis of digital gene exptression data. *Bioinformatics* **2010**, *26*, 139–140.

49. Boyle, E.I.; Weng, S.; Gollub, J.; Jin, H.; Botstein, D.; Cherry, J.M.; Sherlock, G. GO::TermFinder – open source software for accessing Gene Ontology information and finding significantly enriched Gene Ontology terms associated with a list of genes. *Bioinformatics* **2004**, *20*, 3710– 3715.

Chapter 7:

Forazoline A, a Novel Marine-Derived Polyketide with Antifungal *In vivo* Efficacy

Portions of this chapter have been submitted for publication as:

Wyche, T.P., Piotrowski, J.S., Hou, Y., Braun, D., Deshpande, R., McIlwain, S.J., Ong, I.M., Myers, C.L., Westler, W.M., Andes, D.R., Bugni, T.S. Forazoline A, a novel marine-derived polyketide with antifungal *in vivo* efficacy. *Angew. Chem.* (2014) submitted.

7.1. Introduction

Fungal infections result in over 1.5 million deaths annually worldwide and cost $12 billion to treat.[1] *Candida* spp. are the most common fungal infections, especially in intensive care units, solid-organ transplantation, and blood and marrow transplantation patients.[2] Of the more than one hundred known *Candida* spp., *Candida albicans* is the most common cause of fungal-born human disease.[2] *C. albicans* causes various infections, including candidiasis, a bloodstream infection that affects about 400,000 people per year, with a mortality rate between 46 and 75%.[2]

To combat these infections, numerous therapeutics have been developed, ranging from azole-based antimycotic agents to inhibitors of glucan synthesis.[3] Amphotericin B (**71**) has remained the standard for treatment of severe systemic fungal infections.[4,5] Despite amphotericin's continued use, it suffers from low solubility, that complicates delivery and is associated with dose limiting toxicity.[4,5] The high mortality rate[2] combined with the continued rise in fungal resistance to many current therapeutics[6] demonstrates the ever-present need for therapeutics to combat fungal infections.

Natural products (and their derivatives), which have contributed to 74% of antimicrobial drugs in the past 30 years – including antifungal drugs such as amphotericin and caspofungin – offer a rich resource for finding new antifungal agents.[7] Metabolomics methodology holds great promise for streamlining the discovery of novel natural products[8] and overcoming historic barriers such as the high rate of rediscovery of known compounds.[9]

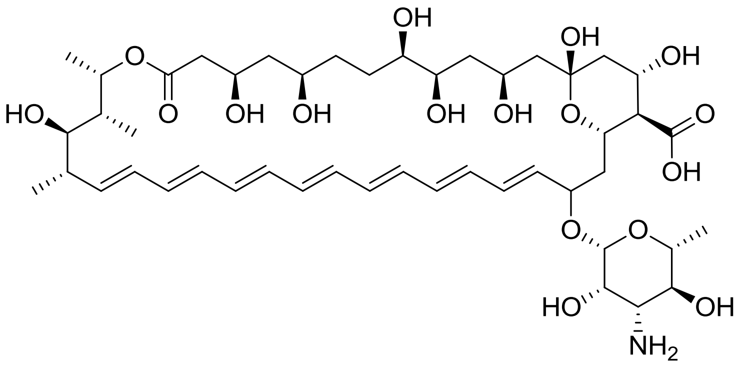

71

As reported in Chapters 5 and 6, LCMS profiles of 34 marine-derived bacterial extracts were analyzed by principal component analysis[8] and identified strain WMMB499, an *Actinomadura* sp. cultivated from the ascidian *Ecteinascidia turbinata* (Herdman, 1880), as a metabolic outlier. After fermentation in medium ASW-A and subsequent purification, WMMB499 was found to produce three distinct classes of novel compounds. The first class, halogenated electrophilic polyketides halomadurones A-D (**58-61**), was described in Chapter 5.[10] The second novel class (ecteinamycin) was described in Chapter 6, and the third class is described here. Forazoline A (**72**) was the lead compound and consisted of a complex and unprecedented polyketide-peptide structure. Forazoline A (**72**) demonstrated *in vivo* efficacy against the fungal pathogen *Candida albicans*. Forazoline B (**73**), a brominated analog, was also produced to aid in structure elucidation.

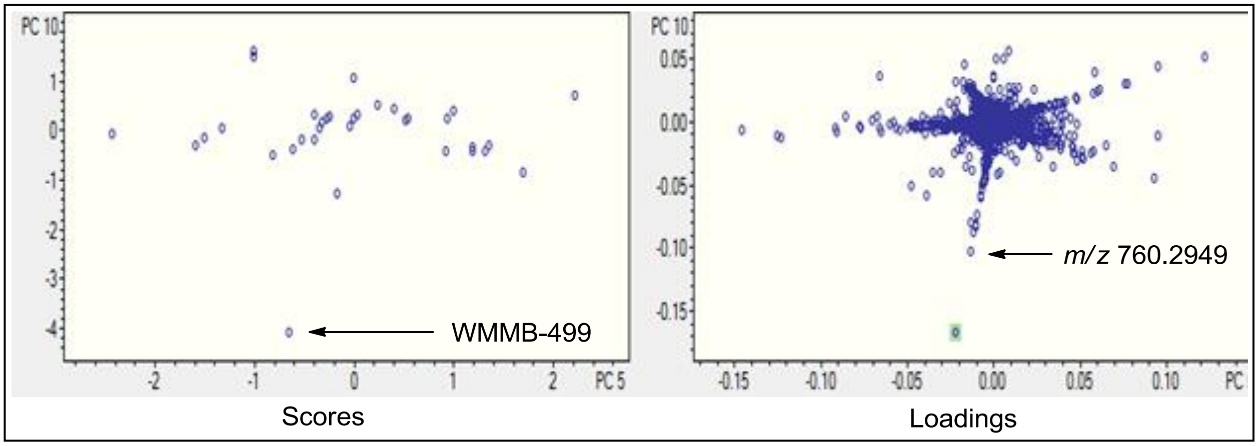

Scores

Loadings

Figure 7.1. PCA analysis. The scores plot, in which each point signifies one bacterial strain, showed that strain WMMB499 separated from the other 33 bacterial strains (in PC10). In the loadings plot, in which each point signifies a metabolite produced by a bacterial strain, a metabolite with *m/z* 760.2949 showed separation from the large grouping of metabolites. That ion was only produced by WMMB499 and was later determined to be a fragment (loss of one forosamine sugar) ion of forazoline A (**72**).

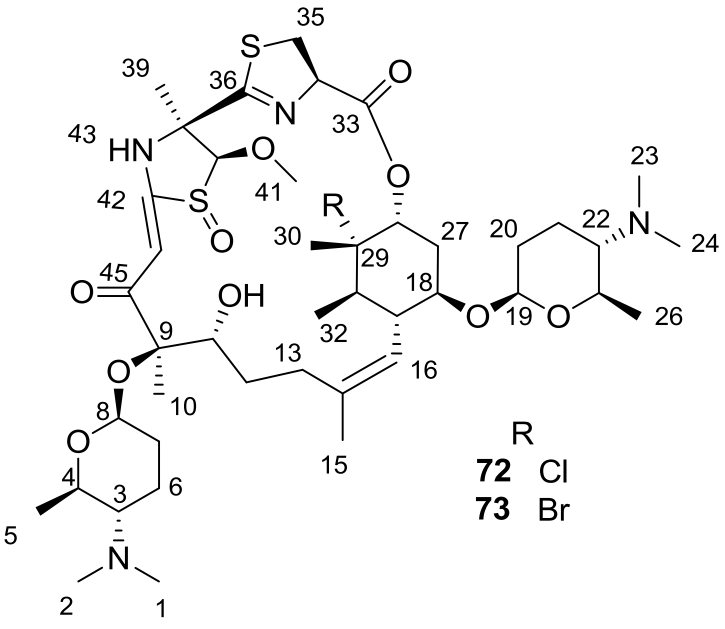

7.2. Results and Discussion

Analysis of forazoline A (**72**) by HRMS provided several potential molecular formulas, and additional data were required to confirm the molecular formula of $C_{43}H_{69}ClN_4O_{10}S_2$. Extensive 1D and 2D NMR data (Table 7.1) were analyzed to establish the majority of the planar structure, but the presence of several quaternary centers complicated structure elucidation. We sought to determine the carbon backbone of the structure by increasing the ^{13}C abundance with uniformly-labeled ^{13}C glucose and acquisition of a ^{13}C-^{13}C gCOSY, which we previously have demonstrated to be useful for rapidly determining the carbon-carbon connectivity of microbial-derived natural products[11] and was described in Chapter 5. Fermentation of WMMB499 in ASW-A with ^{13}C-labeled glucose and subsequent purification, yielded forazoline A (**72**) with approximately 75% ^{13}C incorporation. The ^{13}C-^{13}C gCOSY was acquired in 30 minutes on 7.0 mg forazoline A (**72**) and allowed for complete assignment of the carbon backbone.

Despite knowing the carbon backbone, elucidation was complicated due to the presence of two rings that contained multiple heteroatoms – oxygen, nitrogen, and sulfur. The ^{13}C chemical shifts of several carbon atoms did not conclusively indicate which heteroatoms were attached to each carbon. Therefore, a method was pursued to directly determine the ^{13}C-^{15}N connectivity, which has never been achieved for a natural product. Fermentation of only 250 mL of WMMB499 in a variation of ASW-A, containing $^{15}NH_4Cl$ and uniformly-labeled ^{13}C-glucose, provided ^{13}C- and ^{15}N-doubly labeled forazoline A (**72**). A ^{13}C-^{15}N HMQC ($^1J_{CN}$ 15 Hz) was then developed and acquired to determine the ^{13}C-^{15}N connectivity (Figure 7.2). The spectrum revealed that N-43 (δ 140.2 ppm) was attached to C-42 (δ 166.5) and C-38 (δ 76.2 ppm), and N-37 (δ 302.6 ppm) was attached to C-36 (δ 170.3 ppm) and C-34 (δ 76.3 ppm); the spectrum also confirmed the presence of two *N*-dimethyl groups. The downfield shift of N-37, combined with

Table 7.1. ^{1}H and ^{13}C NMR data for forazoline A (**72**) and B (**73**)(600 MHz for ^{1}H NMR, 150 MHz for ^{13}C, CDCl$_3$)

	1		**2**		COSY	HMBC
Position	δ_C, mult.	δ_H (J in Hz)	δ_C, mult.	δ_H (J in Hz)		
1	40.9, CH$_3$	2.22, s	40.9, CH$_3$	2.22, s		2, 3
2	40.9, CH$_3$	2.22, s	40.9, CH$_3$	2.22, s		1, 3
3	65.0, CH	2.26, m	65.0, CH	2.26, m	4, 6	5
4	74.2, CH	3.47, m	74.2, CH	3.46, m	3, 5	5, 8
5	19.4, CH$_3$	1.28, d (6.3)	19.4, CH$_3$	1.27, d (6.2)	4	3, 4
6	18.7, CH$_2$	1.48, m	18.7, CH$_2$	1.48, m	3, 7	3, 7, 8
		1.85, m		1.85, m		
7	32.6, CH$_2$	1.65, m	32.6, CH$_2$	1.65, m	6, 8	
		1.95, m		1.95, m		
8	97.9, CH	4.76, dd (1.9, 9.4)	97.9, CH	4.76, dd (1.9, 9.4)	7	7, 9
9	92.6, C		92.6, C			
10	22.8 CH$_3$	1.75. s	22.8 CH$_3$	1.75. s		9, 10, 44
11	78.8, CH	4.19, d (10.1)	78.8, CH	4.19, t (9.9)	12	12
12	27.3, CH$_2$	1.30, m	27.3, CH$_2$	1.30, m	11, 13	10, 14
		1.69, m		1.69, m		
13	32.1, CH$_2$	2.05, m	32.1, CH$_2$	2.05, m	12	11, 14, 16
		2.16, m		2.16, m		
14	136.0, C		136.0, C			
15	19.9, CH$_3$	1.63, s	19.9, CH$_3$	1.63, s	16	12, 14, 16
16	122.4, CH	5.08, d (9.4)	122.4, CH	5.07, d (9.3)	15, 17	13, 15
17	47.8, CH	2.33, q (9.8)	47.8, CH	2.33, q (9.8)	16, 18	14, 16, 18, 31, 32
18	73.4, CH	4.04, td (5.3, 9.8)	73.1, CH	4.04, m	17, 27	16, 19, 27
19	101.8, CH	4.91, dd (1.3, 9.1)	101.8, CH	4.90, dd (1.4, 9.1)	20	18, 20
20	31.7, CH$_2$	1.30, m	31.7, CH$_2$	1.30, m	19, 21	19, 21
21	18.7, CH$_2$	1.58, m	18.7, CH$_2$	1.58, m	20, 22	
		1.81, m		1.81, m		
22	65.4, CH	2.15, m	65.4, CH	2.10, m	21, 25	
23	40.9, CH$_3$	2.22, s	40.9, CH$_3$	2.22, s		22, 24
24	40.9, CH$_3$	2.22, s	40.9, CH$_3$	2.22, s		22, 23
25	74.3, CH	3.48, m	74.3, CH	3.49, m	22, 26	19, 26
26	19.3, CH$_3$	1.26, d (8.8)	19.3, CH$_3$	1.23, d (6.0)	25	22, 25
27	34.7. CH$_2$	1.90, m	34.7. CH$_2$	1.91, m	18, 28	17, 29
		2.08, m		2.02, m		
28	78.2, CH	5.33, t (2.7)	78.9, CH	5.41, t (2.7)	27	18, 29, 30, 31, 33
29	75.9, C		74.5, C			
30	22.8, CH$_3$	1.53, s	22.8, CH3	1.53, s		29, 31
31	41.4, CH	1.90, m	42.2, CH	2.00, m	32	16, 17, 29, 30, 32
32	13.4, CH$_3$	0.76, d (6.9)	13.4, CH3	0.83, d (7.0)	31	17, 29, 31
33	171.6, C		171.6, C			
34	76.3, CH	5.50, dd (4.1, 10.4)	76.3, CH	5.50, m	35	33, 35, 36, 38, 40
35	38.8, CH$_2$	3.80, t (11.2)	38.8, CH$_2$	3.84, t (11.1)	34	33, 34
		3.94, dd (4.1, 11.3)		3.92, dd (4.2,		
36	170.3, C		170.3, C			
37	76.2, C		76.2, C			
38	24.8, CH$_3$	1.59, s	24.8, CH$_3$	1.59, s		36, 37, 39
39	94.4, CH	5.04, s	94.4, CH	5.04 ,s	NH	37, 38, 41, 43
40	57.2, CH$_3$	3.40, s	57.2, CH$_3$	3.40, s		39
41	166.5, C		166.5, C			
42-NH		14.58, s		14.59, s	39	37, 39, 41, 43
43	106.4, CH	7.30, s	106.4, CH	7.29, s		39, 41
44	212.0, C		212.0, C			

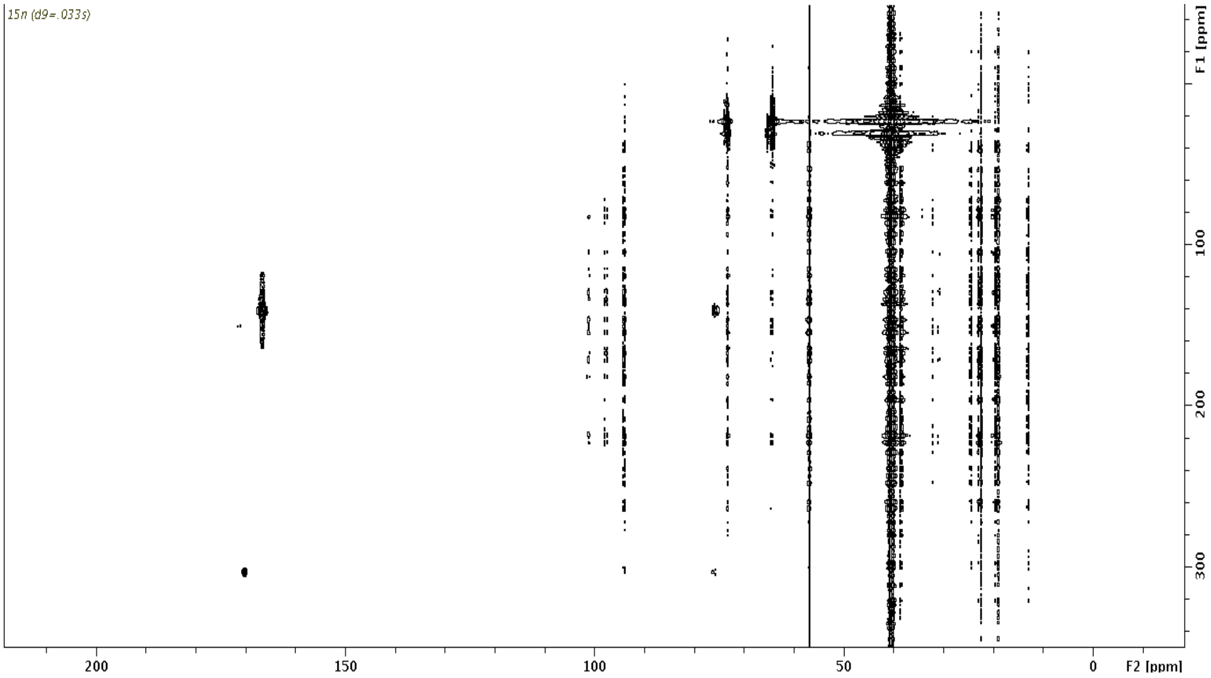

Figure 7.2. ^{13}C-^{15}N HMQC of forazoline A (**72**).

the knowledge that it was connected to only two carbons, suggested the presence of a thiazoline ring.

While analysis of the ^{13}C-^{13}C COSY and ^{13}C-^{15}N HMQC rapidly provided the majority of the planar structure, additional data was necessary to determine the complex structure. HRMS of forazoline A (**57**) in CD_3OD and D_2O revealed the presence of two exchangeables. Acquisition of a ^{1}H-^{15}N HSQC allowed us to conclude that one of the exchangeables was an amine (δ_H 14.58, δ_N 170.3). To determine the location of the other exchangeable proton, forazoline A (**72**) was acetylated (See Section 7.4). Two major products, with one and two acetyl units, were formed, and acquisition of 1D and 2D NMR determined that the other exchangeable proton was attached to a heteroatom at C-11. The chemical shift (δ_C 78.8) at C-11 suggested that the exchangeable was a hydroxyl.

The MS isotopic distribution and molecular formula suggested the presence of one chlorine atom. To determine the location of the chlorine atom, the amount of KBr in fermentation medium ASW-A was increased from 0.1 g/L to 10 g/L to produce a brominated analog, forazoline B (**72**). HRMS of forazoline B (**73**) supported the molecular formula of $C_{43}H_{69}BrO_{10}N_4S_2$. A comparison of the ^{1}H and ^{13}C NMR shifts of forazoline A (**72**) and B (**73**) showed that the chemical shifts of H-28, H-31, C-28, and C-31 shifted downfield, and C-29 shifted upfield in forazoline B (**73**). No other significant changes in chemical shifts between forazoline A (**72**) and B (**73**) existed. Combining this knowledge with the fact that C-29 was a methine attached to two carbons, allowed us to conclude that the halogen atom was located at C-29.

The presence of the sulfoxide was indicated by an absorption band in the IR spectrum at 1060 cm^{-1}, leaving two possibilities for the sulfoxide location. Apratoxin, isolated from the marine cyanobacterium *Lyngbya majuscula*,[12] has a thiazoline ring; more recently, apratoxin sulfoxide, which contains a thiazoline moiety with a sulfoxide, was isolated.[13] The ^{13}C NMR shift of the thiazoline methylene in apratoxin and apratoxin sulfoxide was 37.6 ppm and 58.3 ppm, respectively. The ^{13}C NMR shift of the thiazoline methylene (C-35) in forazoline A (**72**) was 38.8 ppm, similar to that of apratoxin and indicating that the sulfoxide was most likely not part of the thiazoline moiety in forazoline A (**72**). To support this conclusion, low-energy conformers of the two possible structures were calculated with Spartan10,[14] and DFT calculations (Gaussian09[15]) were analyzed with the DP4 probability method.[16] Each of the two possible sulfoxide diastereomers was also investigated using Spartan10 and Gaussian09. After comparing the calculated ^{13}C chemical shifts of the two structures and the corresponding set of diastereomers with the observed chemical shifts of forazoline (**72**), the DP4 probability method predicted a 100.0% probability that the sulfoxide was attached to C-40 and C-42. Notably, for the structure with the sulfoxide in the thiazoline moiety, DFT calculations resulted in a ^{13}C chemical shift of 58.6 ppm for C-35, nearly identical to the methylene in apratoxin sulfoxide (Figure 7.3). Meanwhile, DFT calculations for forazoline A (**72**) predicted a ^{13}C chemical shift of 43.3 ppm at C-35. Thus, the location of the sulfoxide in forazoline A (**72**) was supported by chemical shifts of known compounds and DFT calculations.

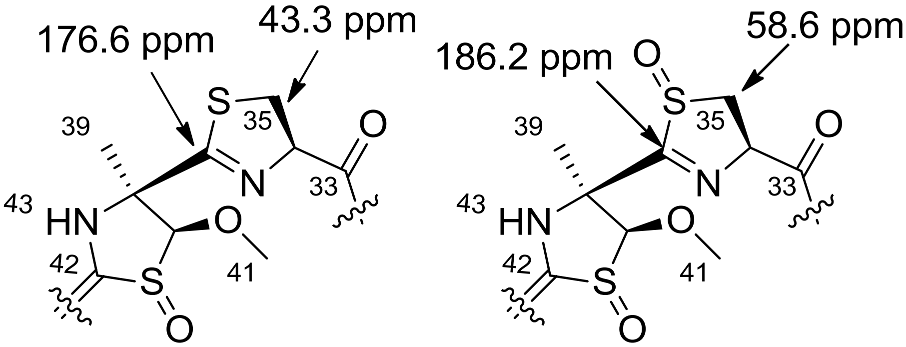

Figure 7.3. DFT calculated ^{13}C NMR shifts.

The configuration of forazoline A (**72**) was determined by a combination of NOE studies, coupling constant analysis, extensive molecular modeling, and DFT calculations. We began by determining the configuration of the two sugars by analyzing NOE correlations and coupling constants and comparing ^{13}C NMR shifts of sugars in known compounds. We then assigned the configuration of the chlorine-containing cyclohexane ring using a combination of NOE correlations and coupling constants (Figure 7.5). The configuration of the heterocyclic system (C-34 to C-42) was then addressed by molecular modeling and DPFGSE NOE studies. In parallel, the configuration between C-9 and C-11 was assigned based on extensive molecular modeling and careful NOE studies. Thus, convergent studies with NOE's, molecular modeling, and DFT caculations, which will be detailed in the following sections, allowed for assignment of the configuration of forazoline A (**72**).

The two sugar moieties were determined to be forosamine based on a comparison of ^{13}C chemical shifts of known compounds. A comparison of known natural products containing forosamine (spinosyn,[17] spiramycin,[18] shengjimycin A[19]) and ossamine (ossamycin,[20] dunaimycin D2S,[21] frigocyclinone[22]) sugars showed that C-1, C-2, and C-5, had characteristic ^{13}C chemical shifts (Figure 7.4). For example, the compounds containing forosamine sugars had a ^{13}C chemical shift of 40.6 ppm at C-1, while the ossamine sugars had a ^{13}C chemical shift of 43.2 ppm. The ^{13}C chemical shift of 40.9 ppm at C-1 for forazoline (**72**) suggested that the sugar was forosamine.

The relative configuration of the chlorine-containing cyclohexane ring was determined using a combination of ROE correlations and coupling constants (Figure 7.5). H-17 is a quartet with ^3J_H 9.8. The large coupling constant in a cyclohexane ring is indicative of a pair of axial protons. In this case, H-17 is coupled to H-16, H-18, and H-31, and therefore H-17, H-18, and H-31 are axial. Analysis of 2D ROESY NMR of forazoline A (**72**) showed an ROE correlation between H-17 and H-30. H-28 is a triplet with ^3J_H 2.7 and therefore, is equatorial. The axial H-17 demonstrated an ROE correlation with H-30; consequently, H-30 is also axial. The relative configuration between the forosamine sugar and chlorine-containing cyclohexane ring was determined by the ROE correlations between H-18 and H-19 and molecular modeling. The geometry of the olefin at C-16 was determined to be (*Z*) due to an NOE correlation between H-16 and H-15.

	forazoline A	spinosyns	spiramycin	shengjimycin A	ossamycin	dunaimycin D2S	frigocyclinone
	δ_C	δ_C	δ_C	δ_C	δ_C	δ_C	δ_C
1	101.8	103.5	100.0	100.1	98.7	98.4	63.6
2	74.3	73.4	74.0	73.6	72.8	72.3	70.9
3	19.4	18.9	19.3	18.8	13.6	13.4	11.5
4	65.0	65.3	65.9	64.9	63.1	61.9	63.5
5	40.9	40.4	40.9	40.6	43.5	43.3	42.9
6	18.7	18.1	18.6	18.55	20.85	20.0	22.3
7	31.8	31.2	32.1	31.17	30.75	29.2	31.4

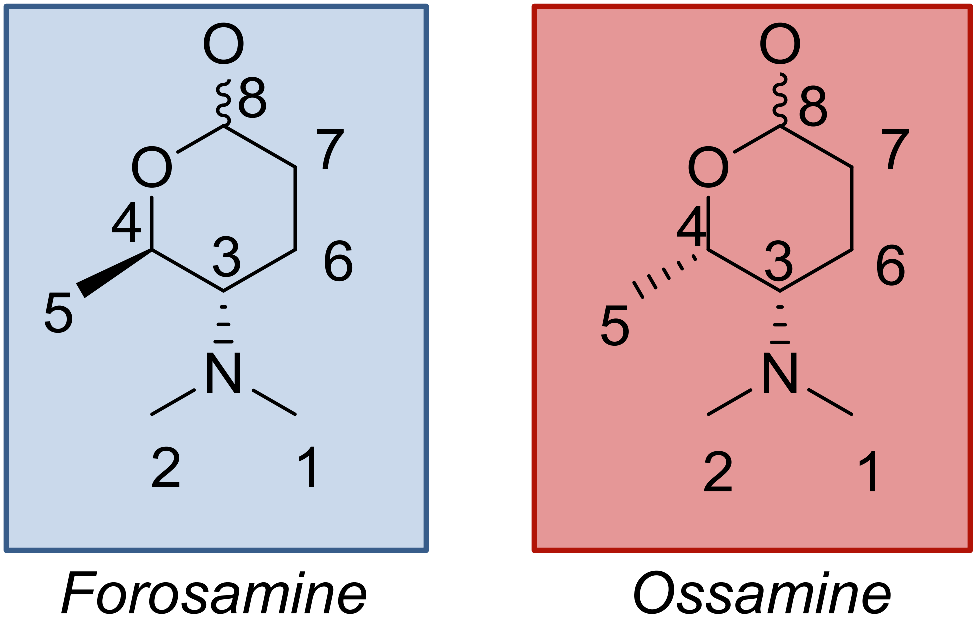

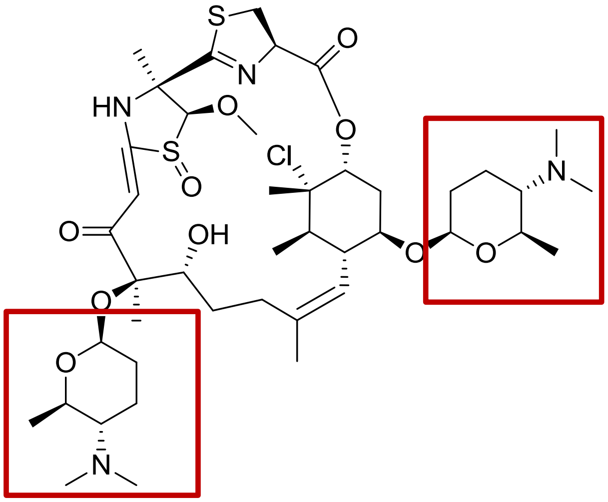

Figure 7.4. Forosamine/ossamine ^{13}C chemical shift comparison for relative configuration

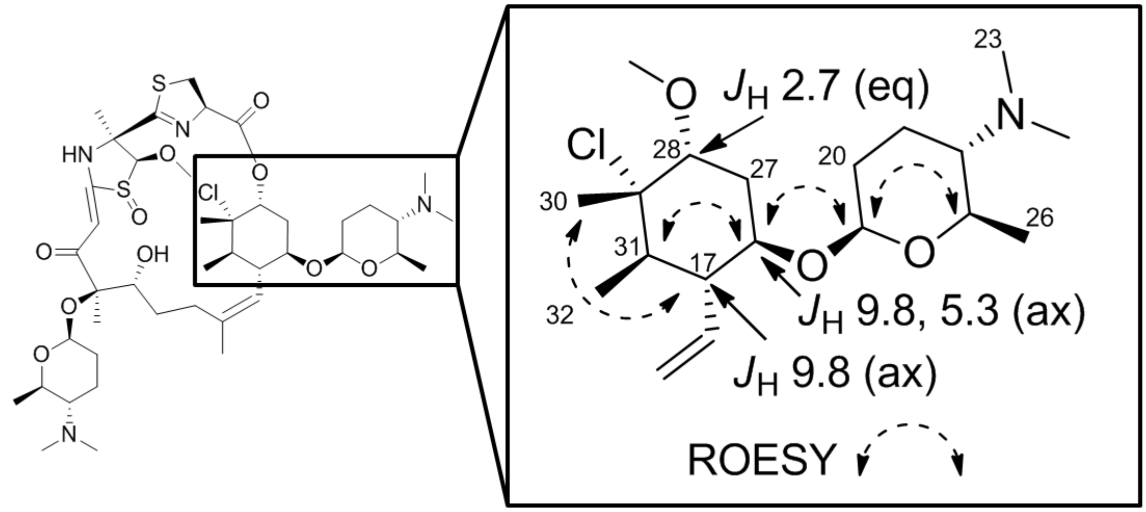

Figure 7.5. Key ROESY correlations and coupling constants

To determine the relative configuration at C-38 and C-40, 1D DPFGSE NOE experiments were used to calculate interproton distances and compared to molecular models. The interproton distances were calculated by determining the initial slope of the NOE build-up curve (50 – 250 ms mixing time); the slope is equal to the cross-relaxation rate constant between two spins, which is proportional to the inverse sixth power of the distance between the two protons (Figure 7.6A).[23] A selective pulse was applied to H-40 resulting in an NOE from H-39 and H-41 (Figure 7.6B) using an array of mixing times (50 to 250 ms), allowing for the construction of an NOE build-up curve (Figure 7.6C). For calibration using a known interproton distance, selective 1D NOE pulses were applied to H-8 resulting in NOE signal from H-4. The distance between H-4 and H-8, part of the forosamine sugar, is 2.34 Å, as characterized in several known compounds. After scaling the NOE integrals to account for the number of protons irradiated and observed in the NOE spectrum, the interproton distances were determined (Table 7.2). These distances were then compared to energy-minimized and

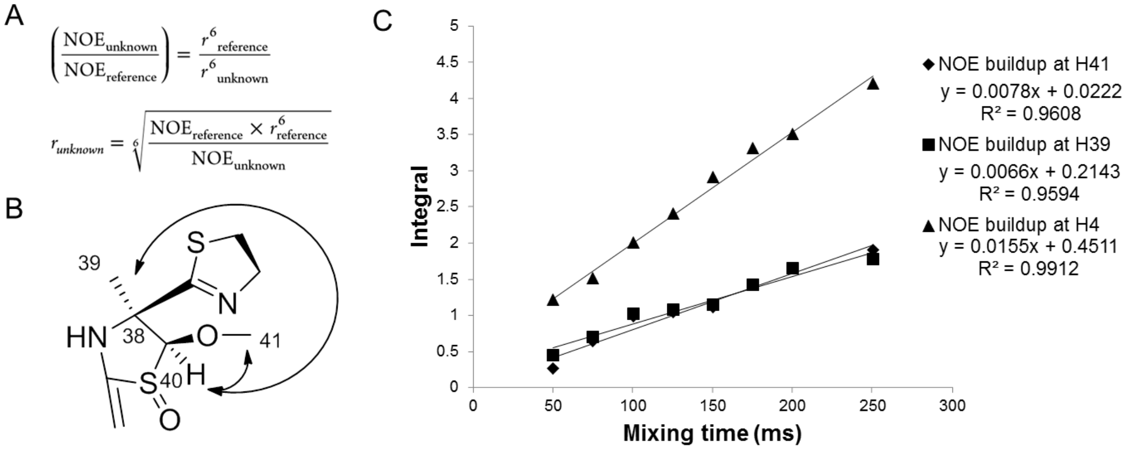

$$\left(\frac{\mathrm{NOE}_{\mathrm{unknown}}}{\mathrm{NOE}_{\mathrm{reference}}}\right) = \frac{r^{6}_{\mathrm{reference}}}{r^{6}_{\mathrm{unknown}}}$$

$$r_{unknown} = \sqrt[6]{\frac{\mathrm{NOE}_{\mathrm{reference}} \times r^{6}_{\mathrm{reference}}}{\mathrm{NOE}_{\mathrm{unknown}}}}$$

Figure 7.6. Relative configuration determination. (A) Equation relating interproton distance (*r*) and slope of NOE build-up curve (NOE). (B) NOE correlations (C) NOE build-up curve

geometry-optimized models of forazoline A (**72**) and its diastereomer. Forazoline A (**72**) and each of the diastereomers at C-38 and C-40 were subjected to a Monte Carlo low energy conformer search using Spartan10, and the geometry was optimized with Gaussian09. The interproton distance for the models with *syn* geometry (*S*,*S* or *R*,*R*) fit the NOE-calculated distances much better than the models with the *anti* geometry (*S*,*R* or *R*,*S*). Therefore, based on NOE distance calculations and molecular modeling, the relative configuration at C-38 and C-40 was determined to be *syn*.

Table 7.2. NOE and DFT calculated interproton distances.

	H-40 to H-39	**H-40 to H-41**
NOE Distance calculated	2.69 Å	2.62 Å
DFT calculations (*S*,*S*)	2.93 Å	2.94 Å
DFT calculations (*S*,*R*)	3.52 Å	2.84 Å

To determine the relative configuration between C-9 and C-11, modified Mosher's method[24] was attempted and formed two products with the expected *m/z*, but extensive 1D and 2D NMR data analysis suggested the reaction resulted in potential side reactions, preventing conclusive determination of the configuration by this method. Instead, extensive molecular modeling, DFT calculations, and ROESY correlations were used in combination with the NMR database for polyols[25] to propose the configuration. The *R*,*R* and *S*,*R* configurations at C-9 and C-11 were modeled with Spartan10 and Gaussian09, as described earlier. The experimentally calculated ^{13}C chemical shifts at C-9 and C-11 were 90.4 ppm and 78.3 ppm, respectively, for the *R*,*R* model, and 85.8 ppm and 78.0 ppm, respectively, for the *S*,*R* model. The chemical shifts of the *R*,*R* model, thus, matched the experimental chemical shifts better than the *S*,*R* model. In addition, nearby ^{13}C chemical shifts (C-45, C-8, C-9, C-10, C-11, and C-12) were compared using the DP4 probability method[16] and supported the same conclusion (100% probability for *R*,*R*). The NMR database for polyols[25] indicated that $\delta_{C\text{-}9}$ should be further upfield for the *S*,*R* configuration than the *R*,*R* relative configuration, in agreement with the ^{13}C calculated shifts. Additionally, a ROESY correlation between H-8 and H-44 in the experimental data matched only the *R*,*R* model; the distance between H-8 and H-44 in the *S*,*R* model was 5.3 Å and 3.4 Å in the *R*,*R* model. Although these data support the proposed configuration between C-9 and C-11, direct methods (e.g. modified Mosher's) would have been more reliable had they not failed.

After determining the relative configuration for several portions of the structure, several attempts at crystallization of forazoline A (**72**) resulted in yellow rod-shaped crystals from slow evaporation in ethyl acetate at 4 ˚C. X-ray diffraction of a single crystal provided the crystal structure for an analog of forazoline A (**74**). The analog closely resembled forazoline A (**72**) but contained two chlorine atoms and no sulfoxide. The crystal structure clearly did not fit the NMR and MS data for forazoline A (**72**), and therefore, we proposed that in the process of crystallization, forazoline A (**72**) underwent a transformation which made it more favorable for crystallization. Despite the minor difference in structure, the majority of the crystal structure of the analog matched the structure of forazoline A (**72**) as determined by NMR, MS, and the aforementioned methods. Additionally, the configuration that we determined experimentally matched the configuration of the crystal structure.

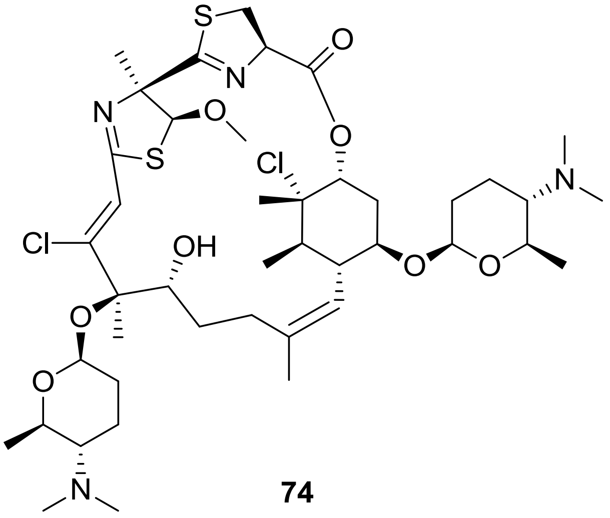

74

Forazoline A (**72**) and B (**73**) demonstrated *in vitro* activity against *C. albicans* K1 with a minimum inhibitory concentration of 16 μg/mL. Despite its moderate activity, *in vivo* studies were pursued due to the relatively high aqueous solubility (~5 mg/mL); antifungal agents such as amphotericin, suffer from solubility issues. Forazoline A (**72**) demonstrated *in vivo* efficacy in neutropenic (immunocompromised) mice in a disseminated candidiasis model against *Candida albicans* K1. Mice were treated with forazoline A (**72**) at concentrations of 2.5, 0.78, and 0.125 mg/kg. After 8 hours, the mice treated with the compound showed a decrease in greater than 1 $\log_{10}$ cfu/kidney (1.5 +/- 0.12) reduction in organism burden compared to control mice. No toxic effects from the compound were apparent.

Additionally, forazoline A (**72**) was treated in combination with amphotericin B against *C. albicans* K1 *in vitro*. These studies demonstrated that forazoline A (**72**) and amphotericin B (**71**) had a synergistic relationship indicating complementary mechanisms of action. Further investigation is necessary in order to better characterize the potential interaction of forazoline A (**72**) with amphotericin B (**71**).

Chemical genomic profiling with the yeast, *Saccharomyces cerevisiae*, was used to investigate the mechanism of action of forazoline A (**72**). This method has been used for determining the mechanism of action and molecular target for many bioactive compounds, including natural products.[26-29] Forazoline A (**72**) was screened against over four thousand deletion mutant yeast strains, genomic DNA was extracted, and mutant-specific DNA barcodes were amplified and sequenced by Illumina sequencing. Forazoline A (**72**) sensitive and resistant mutants were determined by quantification of DNA-barcodes, providing a chemical genomic profile, which was used to evaluate the mechanism of action.

Forazoline A (**72**) gave a distinct chemical genomic profile at 250 µg/mL (Table 7.3). The top sensitive mutant strains ($P<0.0001$) were significantly enriched for genes involved in phospholipid translocation (GO: 0045332, $P=0.0009$). This enrichment was driven by sensitive mutants with deletions of the genes *LEM3* and *FPK1*. Lem3p forms a complex with Dnf1p/Dnf2p that is responsible for maintaining phospholipid assymetry in membranes while Fpk1p is a Ser/Thr protein kinase that regulates Lem3p-Dnf1p/Dnf2p (Dnf1p is a phospholipid translocase).[30] These data suggest that forazoline A (**72**) either directly affects phospholipids or interacts with a protein target that complements the activity of the Lem3p complex. An important aspect of these data was that *LEM3*-Δ was not among the most sensitive strains for

Table 7.3. Forazoline responsive yeast deletion mutants. Fold change in abundance of the mutants relative to the solvent control was calculated with EdgeR. A fold change value <1 indicates sensitivity to forazoline A, while a value >1 indicates resistance.

	Disrupted gene	**Fold Change**	**Adj. P-value**	**Gene Function**
Sensitive	*JIP4*	0.0305	$6.14e^{-06}$	Protein of unknown function
	LEM3	0.0454	$3.13e^{-05}$	Membrane protein of the plasma membrane and ER; interacts specifically in vivo with the phospholipid translocase (flippase) Dnf1p
	PFA3	0.0612	$1.20e^{-05}$	Palmitoyltransferase for Vac8p; required for vacuolar membrane fusion; contains an Asp-His-His-Cys-cysteine rich (DHHC-CRD) domain
	MSH2	0.0664	$6.14e^{-06}$	Protein that binds to DNA mismatches; forms heterodimers with Msh3p and Msh6p that bind to DNA mismatches to initiate the mismatch repair process
	FPK1	0.0788	$4.51e^{-06}$	Ser/Thr protein kinase; regulates the putative phospholipid translocases Lem3p-Dnf1p/Dnf2p; phosphorylates and inhibits upstream inhibitory kinase, Ypk1p
Resistant	*GET1*	71.20	$1.70e^{-05}$	Subunit of the GET complex; involved in insertion of proteins into the ER membrane
	DEP1	28.27	$2.17e^{-05}$	Component of the Rpd3L histone deacetylase complex; required for diauxic shift-induced histone H2B deposition onto rDNA genes; transcriptional modulator involved in regulation of structural phospholipid biosynthesis genes and metabolically unrelated genes
	YMR010W	26.45	$3.76e^{-05}$	Putative protein of unknown function.
	IES2	19.77	$6.56e^{-05}$	Protein that associates with the INO80 chromatin remodeling complex
	SDS3	18.08	$3.13e^{-05}$	Component of the Rpd3L histone deacetylase complex; required for its structural integrity and catalytic activity, involved in transcriptional silencing and required for sporulation
	MON1	14.74	$4.52e^{-05}$	Protein required for cvt-vesicle/autophagosome fusion with the vacuole

caspofungin, fluconazole, or amphotericin, suggesting that forazoline A (**72**) has a unique mechanism of action from known antifungal agents.

Among the top mutant strains resistant to forazoline A (**72**) ($P<0.0001$), we saw significant enrichment for genes involved in negative regulation of chromatin silencing at rDNA (GO:0061188, $P=0.002$), driven by mutants of *SDS3* and *DEP1*, which encode proteins involved with the regulation of phospholipid biosynthesis. Dep1 is a transcriptional modulator involved in the regulation of phospholipid biosynthesis.[31]

We then compared the chemical genomic profile of forazoline A (**72**) to existing chemical genomic datasets[32] and our unpublished dataset, and found its profile significantly correlated with that of papuamide B and tyrocidine B ($P<0.0001$). Both of these compounds act by damaging cellular membranes and causing cell leakage.[33,34] Taken together, these data suggested that forazoline A (**72**) affected membrane integrity. On the other hand, the top 50 sensitive mutant strains for papuamide B, for example, did not contain deletions of *LEM3* or *FPK1*,[34] indicating that forazoline A (**72**) may have a different mechanism of action than papuamide B, which targets phosphatidylserine.

To investigate the membrane integrity of yeast cells treated with forazoline A (**72**), we evaluated membrane permability. Forazoline A (**72**) caused rapid, dose dependent permeabilization of fungal membranes after 4h of treatment (Figure 7.7) but was far less potent than amphotericin. Since chemical genomics suggested that forazoline A had a different mechanism compared to amphotericin, we further evaluated that hypothesis through synergy studies. Forazoline A (**72**) showed synergy when tested with amphotericin indicating a parallel and/or complementary mechanism of action. The data indicated that membrane integrity was affected by forazoline A (**72**), but additional studies will be necessary to fully unravel the details surrounding mechanism of action.

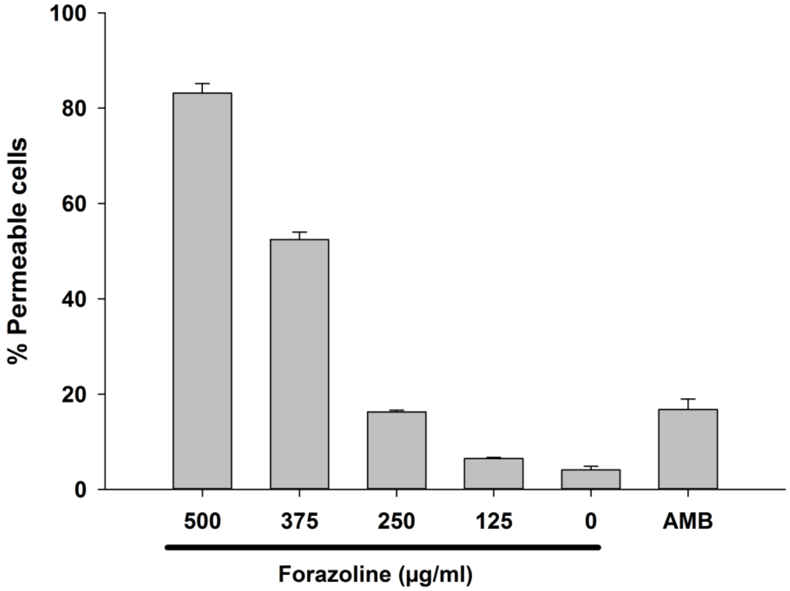

Figure 7.7. Cell leakage assay. Forazoline A compromises membrane integrity in a dose dependent manner. Forazoline A caused cell permeability after 4h of treatment, and membrane damage increased with the concentration. Amphotericin B (AMB) was included as a positive control which causes cell leakage by binding ergosterol in fungal membranes. (Mean ± S.E.)

7.3. Conclusion

Given the rising resistance to antifungal agents, there is a pressing need for new antifungal agents with novel mechanisms of action. Amphotericin (**71**) was first used over fifty years ago[4,5] and, despite its low solubility and dose limiting toxicity, remains the standard of treatment for fungal infections. The continued use of amphotericin demonstrates the struggle to discover novel antifungal drugs with new mechanisms of action. Forazoline A (**72**), a complex, novel natural product from a marine-derived *Actinomadura* sp., represents a new class of antifungal natural products. Forazoline A (**72**) demonstrated *in vivo* efficacy – comparable to that of amphotericin B – in a mouse model of *C. albicans* and no toxicity. Additionally, combination treatment of forazoline A (**72**) and amphotericin B demonstrated a synergistic effect *in vitro*. A chemical genomic approach suggested that forazoline A (**72**) affects cell membranes, possibly through disregulation of phospholipid homeostasis. While additional studies are necessary to better characterize the mechanism of action, forazoline A (**72**) represents a promising antifungal agent with a new mechanism of action compared to current clinically approved agents. Overall, these studies highlight the utility of metabolomics-based methods to enhance the discovery of novel natural products with therapeutic potential.

7.4. Materials and Methods

General Experimental Procedures. Optical rotations were measured on a Perkin–Elmer 241 Polarimeter. UV spectra were recorded on an Aminco/OLIS UV-Vis spectrophotometer. IR spectra were measured with a Bruker Equinox 55/S FT–IR spectrophotometer. NMR spectra were obtained in $CDCl_3$ with a Bruker Avance 600 MHz spectrometer equipped with a 1.7 mm $^{1}H\{^{13}C/^{15}N\}$ cryoprobe and a Bruker Avance 500 MHz spectrometer equipped with a $^{13}C/^{15}N\{^{1}H\}$ cryoprobe. HRMS data were acquired with a Bruker MaXis 4G QTOF mass spectrometer. RP HPLC was performed using a Shimadzu Prominence HPLC system with a Phenomenex Luna C18 column (250 × 10 mm, 5 µm) and a Gilson HPLC system with a Phenomenex Gemini C18 column (100 × 30 mm, 5 µm).

Strain Selection. Thirty-four marine derived bacterial strains were cultured and prepared for LCMS and PCA analysis according to previously published methods.[8] In the scores plot of the PCA analysis (PC5 versus PC10), strain WMMB499 demonstrated spatial separation from the other strains and led us to select the strain for further investigation.

Biological Material. Ascidian specimens were collected on August 10, 2011, in the Florida Keys (24° 39.591′, 81° 25.217′). A voucher specimen (FLK10-5-6) for *Ecteinascidia turbinata* (Herdman, 1880) is housed at the University of Wisconsin-Madison. For cultivation, a sample of ascidian (1 cm^3) was rinsed with sterile seawater, macerated using a sterile pestle in a micro-centrifuge tube, and dilutions were made in sterile seawater, with vortexing between steps to separate bacteria from heavier tissues. Dilutions were separately plated on three media: ISP2, R2A, and M4. Each medium was supplemented with 50 μg/mL cycloheximide and 25 μg/mL nalidixic acid. Plates were incubated at 28 °C for at least 28 days. WMMB499 was isolated from ISP2 medium.

Sequencing. 16S rDNA sequencing was conducted as previously described.[35] WMMB499 was identified as an *Actinomadura* sp. and demonstrated 99% sequence similarity to *Actinomadura* sp. 13679C (accession number EU741239). The 16S sequence for WMMB499 was deposited in GenBank (accession number JX101467).

Fermentation, Extraction, and Isolation. Two 10 mL seed cultures (25 × 150 mm tubes) in medium ASW-A (20 g soluble starch, 10 g glucose, 5 g peptone, 5 g yeast extract, 5 g $CaCO_3$ per liter of artificial seawater) were inoculated with strain WMMB499 and shaken (200 RPM, 28 °C) for seven days. Two hundred fifty mL baffled flasks (3 × 50 mL) containing ASW-A were inoculated with 1 mL seed culture and were incubated (200 RPM, 28 °C) for seven days. Two-liter flasks (6 × 500 mL) containing medium ASW-A with Diaion HP20 (4% by weight) were inoculated with 25 mL from the 50 mL culture and shaken (200 RPM, 28 °C) for seven days. Filtered HP20 and cells were washed with H_2O and extracted with acetone. The acetone extract (3.4 g) was subjected to liquid-liquid partitioning using 30% aqueous MeOH and $CHCl_3$ (1:1). The $CHCl_3$-soluble partition (1.2 g) was fractionated by Sephadex LH20 column chromatography ($CHCl_3$: MeOH, 1:1). Fractions containing **72** were subjected to RP HPLC (10/90% to 100/0% MeOH-H_2O containing 0.1% acetic acid, 22 min) using a Phenomenex Gemini C18 column (100 × 30 mm, 5 µm), yielding **72** (20.1 mg, RT 12.5 min). For ^{13}C and ^{15}N incorporation, the same procedure was used (1 × 250 mL) with labeled medium ASW-A (20 g soluble starch, 10 g $U^{13}C$-glucose, 2.5 g peptone, 2.5 g yeast extract, 5 g $^{15}NH_4Cl$, 5 g $CaCO_3$ per liter of artificial seawater). For the incorporation of bromine and the production of forazoline B (**73**), the same procedure was used with two-liter flasks (2 × 500 mL) containing medium ASW-A (with an increase of KBr from 0.1 g/L to 10 g/L and elimination of 20 g/L NaCl).

ICP Analysis. To confirm the number of sulfur atoms in the structure, forazoline A (**72**) was analyzed with a Perkin-Elmer Optima 2000 ICP-AES (Figure A5.7) and compared to a sulfur standard at known concentrations (10 and 100 mg/L). Forazoline A was dissolved in 1 N HCl. DI H_2O and HCl were analyzed by ICP as blanks. A calibration curve was constructed with the known sulfur concentrations (10 and 100 mg/L), allowing for the calculation of amount of sulfur in forazoline A (**72**).

Molecular Modeling and DFT calculations. Molecular modeling calculations were performed on a Dell Precision T5500 Linux workstation with a Xeon processor (3.3 GHz, 6-core). Low energy conformers were obtained using Spartan 10 software[14] (MMFF, 10000 conformers examined). The low energy conformer for each compound was analyzed using Gaussian 09[15] for geometry optimization and NMR calculations (B3LYP/6-31G(d,p)).[36] NMR shifts were referenced to TMS and benzene using the multi-standard (MSTD) approach.[37] Molecules were modeled in the gas phase. The chemical shifts (calculated vs. experimental) were compared using the DP4 probability method.[16]

NOE Build-up curve. A 1D NOE build-up curve was constructed by acquiring a 1D selective NOE NMR experiment with eight mixing times ranging 50 – 250 ms. H-40 was selectively irradiated, resulting in NOE signal from H-39 and H-41. Additionally, as a control, H-8 was selectively irradiated, resulting in NOE signal from H-4. NOE signal intensities were scaled to account for the difference in number of protons contributing to the signal. The scaled intensity of each peak was plotted with respect to the mixing time, and a best-fit line was assigned to each respective ^{1}H. The slope is equal to the cross-relaxation rate constant between two spins, which is proportional to the inverse sixth power of the distance between the two protons,[23] and the unknown distance ($r_{unknown}$) can be calculated according to the equation $[NOE_{unknown}/NOE_{reference}] = [r^6_{reference}/r^6_{unknown}]$. The $r_{reference}$ distance (H-8 to H-4) in the forosamine sugar has been well-characterized in other natural products[17-19] and by molecular modeling. Additionally, a molecular model for each of the *S*,*S* and *S*,*R* diastereomers at H-40 and H-39 was constructed with Spartan10 and Gaussian09 according to the previously mentioned protocol. The molecular model-calculated interproton distances were compared to the NOE build-up curve-calculated distances. The NOE build-up curve-calculated distances followed a similar trend of the molecular model-calculated distances for the *S*,*S* relative configuration.

Modified Mosher's method. To determine the relative configuration between C-9 and C-11, modified Mosher's method was attempted.[24] To form the *R*-MPA (methoxy-phenylacetic acid) chloride, 52 μL (0.6 mmol) oxalyl chloride was added to 10 mg (0.06 mmol) *R*-MPA and 0.5 μL DMF in 1 mL hexanes. The mixture was stirred at rt for 16 h. The product (*R*-MPA-Cl) was dried under argon and added to 2 mg (2 μmol) forazoline A (1) with 20 μL pyridine and 20 μL triethyl amine in 1 mL anhydrous CH_2Cl_2. The mixture was stirred at rt for 3 h and dried under argon. HPLC purification of the product (Phenomenex Phenyl-Hexyl column, 250 x 100 mm, 5 μm) and subsequent MS analysis suggested the MPA ester was formed, but the ^{1}H NMR spectrum of the MPA ester was complex with considerable overlap of signals, preventing conclusive determination of the configuration by this method.

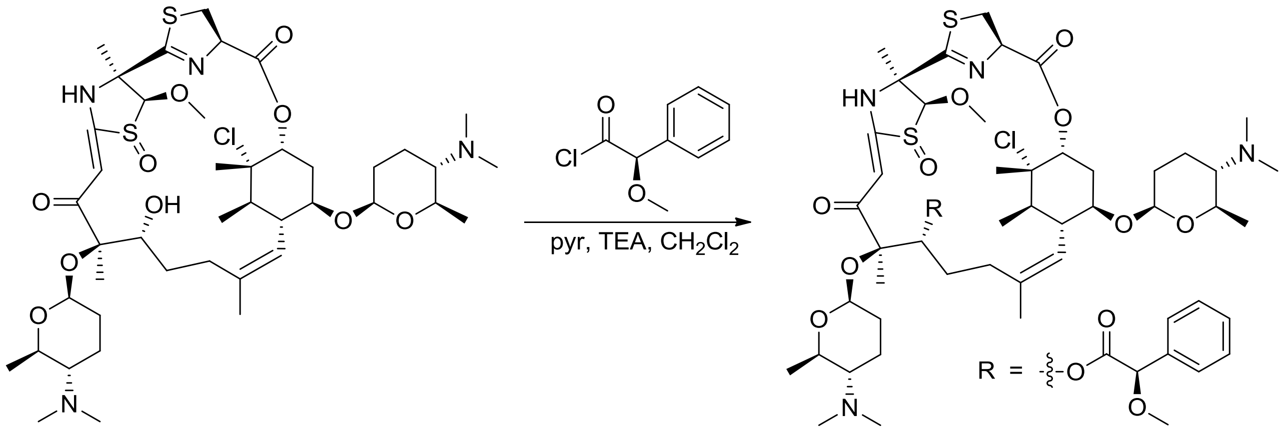

72

75

Figure 7.8. Modified Mosher's method

Acetylation. Acetic anhydride (50 μL) was added to 1 mg forazoline A (**72**) dissolved in pyridine (150 μL) and stirred at rt for 24 h. The product was evaporated under argon and analyzed by NMR.

***In vitro* Assay.** Forazoline A (**72**) and B (**73**) were tested for antifungal activity against a clinical isolate of *C. albicans* (K1), and MICs were determined using a dilution antifungal susceptibility test for yeasts.[38] Forazoline A (**72**) and B (**73**) were dissolved in DMSO, serially diluted to 10 concentrations (0.50 – 256 µg/mL), and tested in a 96-well plate. Amphotericin B was used as a positive control and exhibited an MIC of 0.5 µg/mL. Forazoline A (**72**), B (**73**) and amphotericin were tested in triplicate. Six untreated media controls were included on each plate. The plates were incubated at 33 °C for 48 h. The MIC was determined as the lowest concentration that inhibited visible growth. For synergistic testing with amphotericin B, the same antifungal susceptibility test for yeasts[38] was used, and amphotericin B (**71**) and forazoline A (**72**) were added in 96 well format (See Figure A5.9). One row of treatment with each compound by itself was used as a control. Three replicate plates were tested. Drug synergy is measured by the fractional inhibition concentration (FIC), where FIC = FIC(A) + FIC(B), for drug A (forazoline A) and drug B (amphotericin B). FIC(A) = MIC(A in the presence of B)/MIC(A alone). FIC(B) = MIC(B in the presence of A)/MIC(B alone). A drug combination is considered synergistic when $\text{FIC} \leq 0.5$. A drug is considered antagonistic when $\text{FIC} > 4$ and indifferent when $0.5 \leq \text{FIC} \leq 4$.[39]

Animals. Six-week-old ICR Swiss specific-pathogen-free female mice weighing 23 to 27 g were used for all studies. Animals were maintained in accordance with the American Association for Accreditation of Laboratory Care criteria. Animal studies were approved by the University of Wisconsin Animal Care Committee.

Infection model. A neutropenic, murine, disseminated candidiasis model was used for the treatment studies. Mice were rendered neutropenic (polymorphonuclear cell counts of <100 mm^3) by injecting cyclophosphamide subcutaneously 4 days before infection (150 mg/kg of body weight) and 1 day before infection (100 mg/kg). *Candida albicans* K1 was subcultured on Sabouraud dextrose agar (SDA) 24 h prior to infection. The inocula were prepared by placing three to five colonies into 5 ml of sterile 0.15 M NaCl warmed to 35 °C. The final inoculum was adjusted to 0.6 transmittance at 530 nm. Fungal counts of the inocula determined by viable counts on SDA were $5.63 \pm 0.38 \log_{10}$ CFU/ml (mean ± standard deviation).

Disseminated infection with *C. albicans* organisms was produced by injection of 0.1 mL of the inoculum via the lateral tail vein 2 h prior to the start of antifungal therapy. At the end of the study period (8 h), animals were sacrificed by CO_2 asphyxiation. After sacrifice, the kidneys of each mouse were immediately removed and placed in sterile 0.15 M NaCl at 4 °C. The organs were homogenized and then serially diluted 1:10. Aliquots were plated onto SDA for viable fungal colony counts after incubation for 24 h at 35 °C. The lower limit of detection was 100 CFU/kidney. The results are expressed as the mean and standard deviation of the $\log_{10}$ CFU/kidney from three mice.

Drug Treatment. Groups of three mice were treated with either an intravenous or intraperitoneal single of forazoline A at 0.125, 0.78, and 2.5 mg/kg. The intravenous dose was given by the lateral tail vein via a 200 µL infusion. The intraperitoneal dose was administered in 500 µL volume. Control mice were treated with saline. Groups of mice were sacrificed at the start of therapy and 8 hours after therapy for determination of organism burden in the kidney as described above.

Chemical genomic analysis. A chemical genomic analysis of forazoline A (**72**) was performed as described previously.[29,32] The optimal inhibitory concentration of forazoline A (**72**) for chemical genomic profiling (70-80% growth versus solvent control in YP-Glucose media after 24 h of growth) was determined. A concentration of 250 µg/mL inhibited growth within this range. Two hundred µL cultures of a pooled, genome wide collection of *S. cerevisiae* deletion mutants with 250 µg/mL forazoline A (**72**) or a DMSO control were grown in triplicate for 48 h at 30 °C. The genomic DNA was extracted using the Epicentre MasterPure™ Yeast DNA purification kit. Mutant-specific molecular barcodes were amplified with specially designed multiplex primers containing adapters for Illumina sequencing.[40] The barcodes were sequenced using an Illumina HiSeq2500 Rapid Run platform. Three replicates of each condition (forazoline A vs. DMSO) were sequenced. The barcode counts for each yeast deletion mutant in the presence of forazoline A (**72**) were normalized against the DMSO control conditions to generate a Z-score to define sensitivity or resistance of individual strains (the chemical genomic profile). In addition, differential abundance analysis was calculated for each mutant's response to the forazoline A (**72**) versus DMSO using edgeR.[41] The mutants with very low counts (<5) were filtered out before using the edgeR package (version 3.4.2) to calculate an adjusted P-value and log fold change for each mutant. A Bonferroni corrected hypergeometric distribution test was used to search for significant enrichment of GO terms among the top sensitive and resistant deletion mutants with a P-value less than 0.0001.[42] The chemical genomic profile of forazoline A (**72**) was compared against existing chemical genomic datasets by Pearson correlation.

Cell Leakage Assay. To determine if forazoline A (**72**) caused membrane damage a FungaLight^{TM} Cell Viability assay (Invitrogen L34952) and Guava Flow Cytometer (Millipore, USA) were used. This assay is based on the propidium iodide nucleic acid stain, which is not taken up by cells with intact membranes. If cellular membranes are damaged, the dye can enter the cell and bind nucleic acids. The population of stained cells (damaged membranes) versus non-stained can be determined by flow cytometer. We included amphotericin B as a positive control (10 μg/mL). Two hundred μL log phase populations of S288C yeast cells in YPD media were exposed to 5 dose points of forazoline A (**72**) and a DMSO control (n=3) for 4h at 30 °C. The cells were then stained with the FungaLight^{TM} kit and immediately read by flow cytometry.

Forazoline A (72): yellow solid; $[\alpha]^{25}_{D}$ +300 (*c* 0.6, MeOH); UV (MeOH) λ_{max} (log ε) 205 (4.11), 222 (3.91), 254 (3.74), 274 (3.54), 406 (4.05) nm; IR (ATR) υ_{max} 2940, 2359, 1733, 1533, 1472, 1060 cm^{-1}; ^{1}H and ^{13}C NMR (See Table 7.1); HRMS $[M+H]^+$ *m/z* 901.4205 (calcd for $C_{43}H_{70}ClN_4O_{10}S_2$, 901.4216).

Forazoline B (73): yellow solid; $[\alpha]^{25}_{D}$ +350 (*c* 0.1, MeOH); UV (MeOH) λ_{max} (log ε) 204 (4.14), 226 (4.00), 254 (3.85), 403 (4.02) nm; IR (ATR) υ_{max} 2940, 2359, 1733, 1533, 1471, 1060 cm^{-1}; ^{1}H and ^{13}C NMR (See Table 7.1); HRMS $[M+H]^+$ *m/z* 945.3702 (calcd for $C_{43}H_{70}BrN_4O_{10}S_2$, 945.3711).

7.5. References

1. Zaragoza, R.; Pemán, J. The diagnostic and therapeutic approach to fungal infections in critical care settings. *Adv. Sepsis*. **2008**, *6*, 90-98.

2. Giri, S.; Kindo, A.J. A review of Candida species causing blood stream infection. *Indian J. Med. Microbiol*. **2012**, *30*, 270-278.

3. Kathiravan, M.K.; Salake, A.B.; Chothe, A.S.; Dudhe, P.B.; Watode, R.P.; Mukta, M.S.; Gadhwe, S. The biology and chemistry of antifungal agents: a review. *Bioorg. Med. Chem*. **2012**, *20*, 5678-5698.

4. Barrett, J.P.; Vardulaki, K.A.; Conlon, C.; Cooke, J.; Daza-Ramirez, P.; Evans, E.G.; Hawkey, P.M.; Herbrecht, R.; Marks, D.I.; Moraleda, J.M.; Park, G.R.; Senn, S.J.; Viscoli, C. A systemic review of the antifungal effectiveness and tolerability of amphotericin B formulations. *Clin Ther*. **2003**, *25*, 1295-1320.

5. Laniado-Laborín, R.; Cabrales-Vargas, M.N. Amphotericin B: side effects and toxicity. *Rev. Iberoam Micol*, **2009**, *26*, 223-227.

6. Kanafani, Z.A.; Perfect, J.R. Antimicrobial resistance: resistance to antifungal agents: mechanisms and clinical impact. *Clin. Infect. Dis*. **2008**, *46*, 120-128.

7. Newman, D.J.; Cragg, G.M. Natural products as sources of new drugs over the 30 years from 1981 to 2010. *J. Nat. Prod*. **2012**, *75*, 311-335.

8. Hou, Y.; Braun, D.R.; Michel, C.R.; Klassen, J.L.; Adnani, N.; Wyche, T.P.; Bugni, T.S. Microbial strain prioritization using metabolomics tools for the discovery of natural products. *Anal. Chem*. **2012**, *84*, 4277-4283.

9. Zäehner, H.; Fiedler, H. P. The Need for New Antibiotics. In Fifty Years of Antimicrobials; Hunter, P. A., Darby, G. K., Russel, N. J., Eds.; Cambridge University Press: Cambridge, England, 1995; pp 67-84.

10. Wyche, T.P.; Standiford, M.; Hou, Y.; Braun, D.; Johnson, D.A.; Johnson, J.A.; Bugni, T.S. Activation of the nuclear factor E2-related factor 2 pathway by novel natural

products halomadurones A-D and a synthetic analogue. *Marine Drugs*, **2013**, *11*, 5089-5099.

11. Ellis, G.A.; Wyche, T.P.; Fry, C.G.; Braun, D.R.; Bugni, T.S. Solwaric acids A and B, antibacterial aromatic acids from a marine Solwaraspora sp. *Marine Drugs,* **2014**, *12*, 1013-1022.

12. Luesch, H.; Yoshida, W.Y.; Moore, R.E.; Paul, V.J.; Corbett, T.H. Total structure determination of apratoxin A, a potent novel cytotoxin from the marine cyanobacterium Lyngbya, majuscula. *J. Am. Chem. Soc*. **2001**, *123*, 5418-5423.

13. Thornbug, C.C.; Cowley, E.S.; Sikorska, J.; Shaala, L.A.; Ishmael, J.E.; Youssef, D.T.; McPhail, K.L. Aprotoxin H and apratoxin A sulfoxide from the Red Sea cyanobacterium Moorea producens. *J. Nat. Prod*. **2013**, *76*, 1781-1788.

14. Spartan 10, v. 1.0.2. Wavefunction Inc. 2011.

15. Gaussian 09, Revision A.1, Frisch, M. J.; Trucks, G. W.; Schlegel, H. B.; Scuseria, G. E.; Robb, M. A.; Cheeseman, J. R.; Scalmani, G.; Barone, V.; Mennucci, B.; Petersson, G. A.; Nakatsuji, H.; Caricato, M.; Li, X.; Hratchian, H. P.; Izmaylov, A. F.; Bloino, J.; Zheng, G.; Sonnenberg, J. L.; Hada, M.; Ehara, M.; Toyota, K.; Fukuda, R.; Hasegawa, J.; Ishida, M.; Nakajima, T.; Honda, Y.; Kitao, O.; Nakai, H.; Vreven, T.; Montgomery, Jr., J. A.; Peralta, J. E.; Ogliaro, F.; Bearpark, M.; Heyd, J. J.; Brothers, E.; Kudin, K. N.; Staroverov, V. N.; Kobayashi, R.; Normand, J.; Raghavachari, K.; Rendell, A.; Burant, J. C.; Iyengar, S. S.; Tomasi, J.; Cossi, M.; Rega, N.; Millam, N. J.; Klene, M.; Knox, J. E.; Cross, J. B.; Bakken, V.; Adamo, C.; Jaramillo, J.; Gomperts, R.; Stratmann, R. E.; Yazyev, O.; Austin, A. J.; Cammi, R.; Pomelli, C.; Ochterski, J. W.; Martin, R. L.; Morokuma, K.; Zakrzewski, V. G.; Voth, G. A.; Salvador, P.; Dannenberg, J. J.; Dapprich, S.; Daniels, A. D.; Farkas, Ö.; Foresman, J. B.; Ortiz, J. V.; Cioslowski, J.; Fox, D. J. Gaussian, Inc., Wallingford CT, 2009.

16. Smith, S.G.; Goodman, J.M. Assigning stereochemistry to single diastereomers by GIAO NMR calculation: the DP4 probability. *J. Am. Chem. Soc*. **2010**, *132*, 12946-12959.

17. Kirst, H.A.; Michel, K.H.; Martin, J.W.; Creemer, L.C.; Chio, E.H.; Yao, R.C.; Nakatsukasa, W.M.; Boek, L.D.; Occolowitz, J.L.; Paschal, J.W.; Deeter, J.B.; Jones, N.D.; Thompson, G.D. A83543A-D, unique fermentation-derived tetracyclic macrolides. *Tetrahedron Lett*. **1991**, *32*, 4839-4842.

18. Liu, L.; Roets, E.; Busson, R.; Vankeerberghen, A.; Janssen, G.; Hoogmartens, J. Two novel spiramycins ovtained from commercial samples: isolation and elucidation of structure. *J. Antibiot*. **1996**, *49*, 398-401.

19. Chenghang, S.; Wei, J.; Jie, H.; Wenzao, J.; Yiguang, W. Shengjimycins: a group of hyprid antibiotics, 4”-acylspiramycins. *Actinomycetologica* **1999**, *13*, 120-125.

20. Kirst, H.A.; Mynderse, J.S.; Martin, J.W.; Baker, P.J.; Paschal, J.W.; Rios Steiner, J.L.; Lobkovsky, E.; Clardy, J. Structure of the spiroketal-macrolide ossamycin. *J. Antibiot.* **1996**, *49*, 720-716.

21. Hochlowski, J.E.; Mullally, M.M.; Brill, G.M.; Whittern, D.N.; Buko, A.M.; Hill, P.; McAlpine, J.B. Dunaimycins, a new complex of spiroketal 24-membered macrolides with immunosuppressive activity. II. Isolation and elucidation of structures. *J. Antibiot*. **1991**, *44*, 1318-1330.

22. Bruntner, C.A.; Binder, T.; Pathom-aree, W.; Goodfellow, M.; Bull, A.T.; Potterat, O.; Puder, C.; Hörer, S.; Schmid, A.; Bolek, W.; Wagner, K.; Mihm, G.; Fiedler, H.P. Frigocyclinone, a novel angucyclinone antibiotic produced by a Streptomyces griseus strain from Antarctica. *J. Antibiot*. **2005**, *58*, 346-349.

23. Stott, K.; Keeler, J.; Van, Q.N.; Shaka, A.J. One-dimensional NOE experiments using pulsed field gradients. *J. Magn. Reson*. **1997**, *125*, 302-304.

24. Seco, J.M.; Quiñoá, E.; Riguera, R. The assignment of absolute configuration by NMR. *Chem. Rev*. **2004**, *104*, 17-117.

25. Higashibayashi, S.; Czechtizky, W.; Kobayashi, Y.; Kishi, Y. Universal NMR databases for contiguous polyols. *J. Am. Chem. Soc.* **2003**, *125*, 14379-14393.

26. Ho, C.H.; Piotrowski, J.; Dixon, S.J.; Baryshnikova, A.; Costanzo, M.; Boone, C. Combining functional genomics and chemical biology to identify targets of bioactive compounds. *Curr. Opin. Chem. Biol*. **15**, *2011*, 66-78.

27. Parsons, A.B.; Brost, R.L.; Ding, H.; Li, Z.; Zhang, C.; Sheikh, B.; Brown, G.W.; Kane, P.M.; Hughes, T.R.; Boone, C. Integration of chemical-genetic and genetic interaction data links bioactive compounds to cellular target pathways. *Nat. Biotechnol*. **2004**, *22*, 62-69.

28. Costanzo, M.; Baryshnikova, A.; Bellay, J.; Kim, Y.; Spear, E.D.; Sevier, C.S.; Ding, H.; Koh, J.L.; Toufighi, K.; Mostafavi, S.; Prinz, J.; St Onge, R.P.; VanderSluis, B.; Makhnevych, T.; Vizeacoumar, F.J.; Alizadeh, S.; Bahr, S.; Brost, R.L.; Chen, Y.; Cokol, M.; Deshpande, R.; Li, Z.; Lin, Z.Y.; Liang, W.; Marback M.; Paw, J.; San Luis, B.J.; Shuteriqi, E.; Tong, A.H.; van Dyk, N.; Wallace, I.M.; Whitney, J.A.; Weirauch, M.T.; Zhong, G.; Zhu, H.; Houry, W.A.; Brudno, M.; Ragibizadeh, S.; Papp, B.; Pál, C.; Roth, F.P.; Giaever, G.; Nislow, C.; Troyanskaya, O.G.; Bussey, H.; Bader, G.D.; Gingras, A.C.; Morris, Q.D.; Kim, P.M.; Kaiser, C.A.; Myers, C.L.; Andrews, B.J.; Boone, C. The genetic landscape of a cell. *Science* **2010**, *327*, 425-431.

29. Fung, S.-Y.; Sofiyev, V.; Schneiderman, J.; Hirschfeld, A.F.; Victor, R.E.; Woods, K.; Piotrowski, J.S.; Deshpande, R.; Li, S.C.; de Voogd, N.J.; Myers, C.L.; Boone, C.; Andersen, R.J.; Turvey. S.E. Unbiased screening of marine sponge extracts for anti-

inflammatory agents combined with chemical genomics identifies girolline as an inhibitor of protein synthesis. *ACS Chem. Biol*. **2014**, *9*, 247-257.

30. Nakano, K.; Yamamoto, T; Kishimoto, T.; Noji, T.; Tanaka, K. Protein kinases Fpk1p and Fpk2p are novel regulators of phospholipid asymmetry. *Mol. Cell. Biol.* **2008**, *19*, 1783-1797.

31. Lamping, E.; Lückl, J.; Paltauf, F.; Henry, S.A.; Kohlwein, S.D. Isolation and characterization of a mutant of Saccharomyces cerevisiae with pleiotropic deficiencies in transcriptional activation and repression. *Genetics* **1994**, *137*, 55–65.

32. Parsons, A.B.; Lopez, A.; Givoni, I.E.; Williams, D.E.; Gray, C.A.; Porter, J.; Chua, G.; Sopko, R.; Brost, R.L.; Ho, C.H.; Wang, J.; Ketela, T.; Brenner, C.; Brill, J.A.; Fernandez, G.E.; Lorenz, T.C.; Payne, G.S.; Ishihara, S.; Ohya, Y.; Andrews, B.; Hughes, T.R.; Frey, B.J.; Graham, T.R.; Andersen, R.J.; Boone, C. Exploring the mode-of-action of bioactive compounds by chemical-genetic profiling in yeast. *Cell* **2006**, *126*, 611-625.

33. Ford, P.W.; Gustafson, K.R.; McKee, T.C.; Shigematsu, N.; Maurizi, L.K.; Pannell, L.K.; Williams, D.E.; de Silva, E.D.; Lassota, P.; Allen, T.M.; Van Soest, R.; Anderson, R.J.; Boyd, M.R. Papuamides A-D, HIV-inhibitory and cytotoxic depsipeptides from the sponges Theonella mirabilis and Theonella swinhoei collected in Papua New Guinea. *J. Am. Chem. Soc*. **1999**, *121*, 5899-5909.

34. Merrick, J.M. Effect of polymyxin B, tyrocidine, gramicidin D, and other antibiotics on the enzymatic hydrolysis of poly-β-hydroxybutyrate. *J. Bacteriol*. **1965**, *90*, 965-969.

35. Wyche, T.P.; Hou, Y.; Braun, D.; Cohen, H.C.; Xiong, M.P.; Bugni, T.S. First natural analogs of the cytotoxic thiodepsipeptide thiocoraline A from a marine Verrucosispora sp. *J. Org. Chem*. **2011**, *76*, 6542–6547.

36. Stappen, I.; Buchbauer, G.; Robien, W.; Wolschann, P. ^{13}C NMR spectra of santalol derivatives: a comparison of DFT-based calculations and database-oriented prediction techniques. *Magn. Reson. Chem.* **2009**, *47*, 720-726.

37. Sarotti, A.M.; Pellegrinet, S.C. A multi-standard approach for GIAO ^{13}C NMR calculations. *J. Org. Chem.* **2009**, *74*, 7254-7260

38. National Committee for Clinical Laboratory Standards. *Reference Method for Broth Dilution Antifungal Susceptibility Testing of Yeasts* 3rd ed.; Clinical and Laboratory Standards Institute (CLSI): Wayne, PA, 2008; Approved standard M27-A3.

39. Eliopolous, G.M.; Moellering, R.C. In *Antibiotics in Laboratory Medicine*, 3rd ed.; V. Iorian, Ed.; Williams and Wilkins: Baltimore, MD, 1996; pp 330-396.

40. Smith, A.M.; Heisler, L.E.; Mellor, J.; Kaper, F.; Thompson, M.J.; Chee, M.; Roth, F.P.; Giaever, F.; Nislow, C. Quantitative phenotypes via deep barcode sequencing. *Genome Res*. **2009**, *19*, 1836– 1842.

41. Robinson, M.D.; McCarthy, D.J.; Smyth, G.K. edgeR: a Bioconductor package for differential expression analysis of digital gene exptression data. *Bioinformatics* **2010**, *26*, 139–140.

42. Boyle, E.I.; Weng, S.; Gollub, J.; Jin, H.; Botstein, D.; Cherry, J.M.; Sherlock, G. GO::TermFinder – open source software for accessing Gene Ontology information and finding significantly enriched Gene Ontology terms associated with a list of genes. *Bioinformatics* **2004**, *20*, 3710– 3715.

Chapter 8:

Concluding Remarks and Future Directions

8.1. Concluding Remarks

Natural products have historically played an important role in the development of therapeutics and therapeutic leads.[1] However, a bottleneck remains in the hit-to-lead process for natural products drug discovery.[2] At the same time, there is continued demand for new and effective therapeutics as a result of antibiotic resistance and other global health threats. Recent technological advancements in analytical chemistry – in the fields of MS and NMR – have helped spur new and efficient methods in natural products drug discovery, but additional progress is necessary.

In the field of mass spectrometry, LCMS-based metabolomics methods have begun to gain a foothold in natural products research. Principal component analysis (PCA) can be used to analyze large sets of data and therefore, can be useful for various aspects of the drug discovery timeline. For example, PCA can be used for bacterial strain selection (Chapter 4-7). Traditional methods in natural product isolation have relied on a brute force approach, isolating as many bacteria as possible and doing large scale fermentation on these bacteria. Instead, the bacteria can be grown on a small scale and the chemistry analyzed by LCMS. PCA can then take the *m/z*-RT time pairs and simplify data analysis for a large set of LCMS data. From a group of 34 strains, for example, the most chemically unique strains were selected (Chapter 5-7; Figure 8.1). Alternatively, strains often group based on chemistry, and one bacterial strain can be selected from an entire group (Chapter 4), rather than analyzing all the strains on large scale.

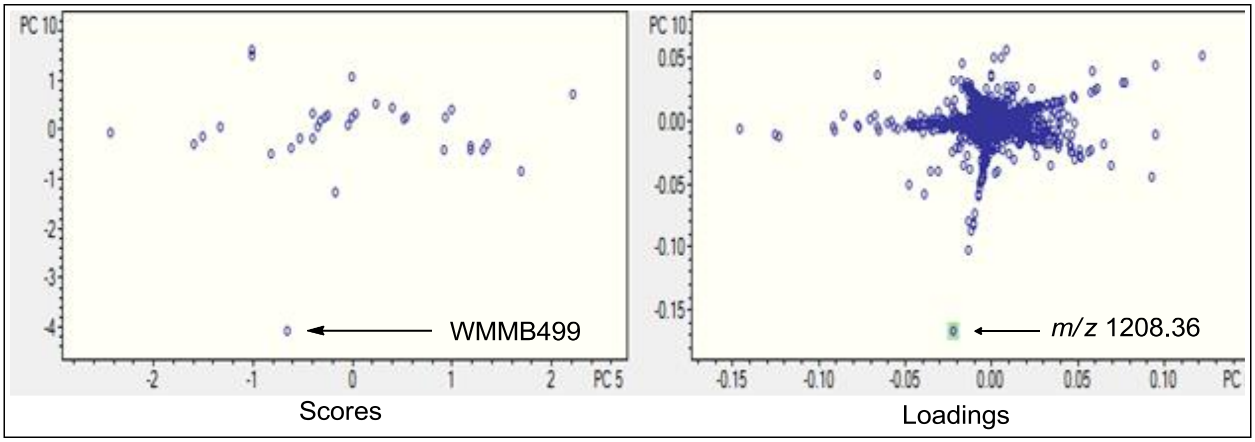

Figure 8.1. PCA analysis. Strain WMMB499 produced a diverse group of novel natural products with therapeutic potential (Chapters 5-7), but the compound that separated the farthest in the Loadings plot (*m/z* 1208.36) has not been thoroughly investigated. Initial attempts at isolation and structure elucidation suggested that the compound was a novel peptide, but low yield and potential chemical instability prevented further investigation at this point. Nevertheless, the aforementioned results (Chapters 5-7) demonstrated the power of PCA for bacterial strain selection.

The field of NMR has also seen major advancements in recent years – with the introduction of the cold probe, larger magnetic field strength, and smaller probes/sample volumes. Methods are needed to take advantage of these technological advancements. To make structure elucidation of natural products – one of the major bottlenecks in natural products research – more efficient, isotopic labeling can be a useful tool, especially in combination with the technological advancements of NMR. For example, ^{13}C-labeling of natural products with U^{13}C-glucose and acquisition of a ^{13}C-^{13}C COSY can provide direct carbon-carbon connectivity in the structure. Due to the low natural abundance of ^{13}C (1.1%), the ^{13}C-^{13}C COSY is not feasible on unlabeled compound. This method allows for rapid structure elucidation (Chapter 5-7). Additional isotopic labeling, such as ^{15}N, can also improve the efficiency for structure elucidation (Chapter 7).

Ultimately, the goal of these methods is to identify new and therapeutically relevant chemistry in an efficient manner. Seventeen novel natural products have been presented (Chapters 2, 4-7), all of which demonstrated therapeutic potential. These compounds demonstrated therapeutic potential in a variety of areas including anti-cancer (Chapter 2-3), antibacterial (Chapter 4, 6), antifungal (Chapter 7), and against neurodegenerative diseases (Chapter 5). Importantly, forazoline A (**72**) demonstrated *in vivo* efficacy in a mouse model of *Candida albicans* (Chapter 7).

In addition to the potential of novel natural products for the development of therapeutics, many known natural products have not been investigated fully, and therefore, investigating new therapeutic targets for known natural products may provide fruitful. The known natural product, thiocoraline, was originally isolated in 1997 and demonstrated potent cytotoxicity against a number of cancer cell lines. In this thesis, the isolation of thiocoraline is described (Chapter 2), and for the first time, the compound was investigated as a therapeutic against carcinoid tumors (Chapter 3). Additionally, the mechanism of action in carcinoid tumors was investigated, and a formulation method for delivery was developed. Ultimately, thiocoraline slowed carcinoid tumor progression *in vivo*. Although the focus of this thesis was the discovery of novel natural products from the marine environment, initial studies examining the mechanism of action and drug delivery of several of the compounds was completed and provides grounds for future work.

8.2. Future Directions

The work entailed in this thesis provides several examples of improving the efficiency of natural products drug discovery, as exemplified by seventeen novel structures. The future developments stemming from this work is two-fold.

First, the methods for improving the efficiency of natural products discovery – LCMS-based metabolomics for strain selection and isotopic labeling for structure elucidation – hold great promise not only for their use in natural products drug discovery but also for their extended application. For example, ^{13}C-labeling and acquisition of a ^{13}C-^{13}C COSY on a crude natural product extract can provide a great deal of information about the metabolites produced. This method spreads the chemistry out on a large sweep width (~200 ppm) and helps minimize the effect of media components, which would not be isotopically labeled. This method, which would examine the carbon-carbon connectivity of the compounds, could be used in combination with NMR metabolomics to rapidly compare multiple extracts, whether it be aimed at drug discovery, biochemical pathways, or other interests. While the ^{13}C-^{13}C COSY and ^{13}C-^{15}N HMQC were the focus for isotopically-labeled NMR experiments in this thesis, additional experiments, such as the ^{13}C-^{13}C TOCSY, could be beneficial.

Metabolomics tools will continue to expand its influence in natural products research in the coming years. While it has already exerted an impact in bacterial strain selection, these methods have only been used by a relatively small subset of the natural products community. However, as the utility of metabolomics for bacterial strain selection and other applications becomes more apparent, it will become more commonplace in natural products research. At the same time, these methods will be improved upon to gain even more efficiency – whether it is due to technological advancements or new ideas provoked by research progress. Thus, metabolomics and isotopic labeling should both help with future developments in natural products research.

Second, several of the novel structures hold exciting therapeutic potential. Forazoline A (**72**) demonstrated *in vivo* efficacy in a mouse model of *Candida albicans*, and initial studies suggested that the novel compound works by disrupting fungal cell membranes. However, the mechanism of action and *in vivo* studies were only preliminary evidence into the potential of the compound, and therefore, this work should be expanded greatly to include pharmacokinetic studies, among others. Additionally, medicinal chemistry work could ensue to improve the potency or solubility. The highly unusual and unprecedented skeleton puts it into a new class of compounds, which is exciting, especially considering the need for novel antifungal agents. Ecteinamycin (**65**) demonstrated potent *in vitro* activity against gram-positive bacteria, especially *C. difficile*, and initial studies suggested the compound is an ionophore antibiotic. Like forazoline A (**72**), the mechanism of action studies should be expanded and *in vivo* work pursued. Improving the solubility of ecteinamycin will be important for its delivery.

While on the surface, forazoline A (**72**) and ecteinamycin (**65**) appear to be the most promising drug leads – due to their novel structures and *in vitro* and *in vivo* efficacy – the other fifteen structures still hold potential, either as drug leads or as important stepping stones towards a new therapeutic. Therefore, in a way, none of the projects detailed in this thesis are complete. They are just the beginning of the long and winding path of the drug development timeline, which every drug on the market has to start at some point. Although many of these paths are cut short without success, hopefully this thesis will provide some guidance and inspiration along the way.

8.3. References

1. Newman, D.J.; Cragg, G.M. Natural products as sources of new drugs over the 30 years from 1981 to 2010. *J. Nat. Prod*. **2012**, *75,* 311-335.

2. Dias, D.A.; Urban, S.; Roessner, U. A historical overview of natural products in drug discovery. *Metabolites* **2012**, *2,* 303-336.

Appendix 1:

Supplementary Data for Chapter 2

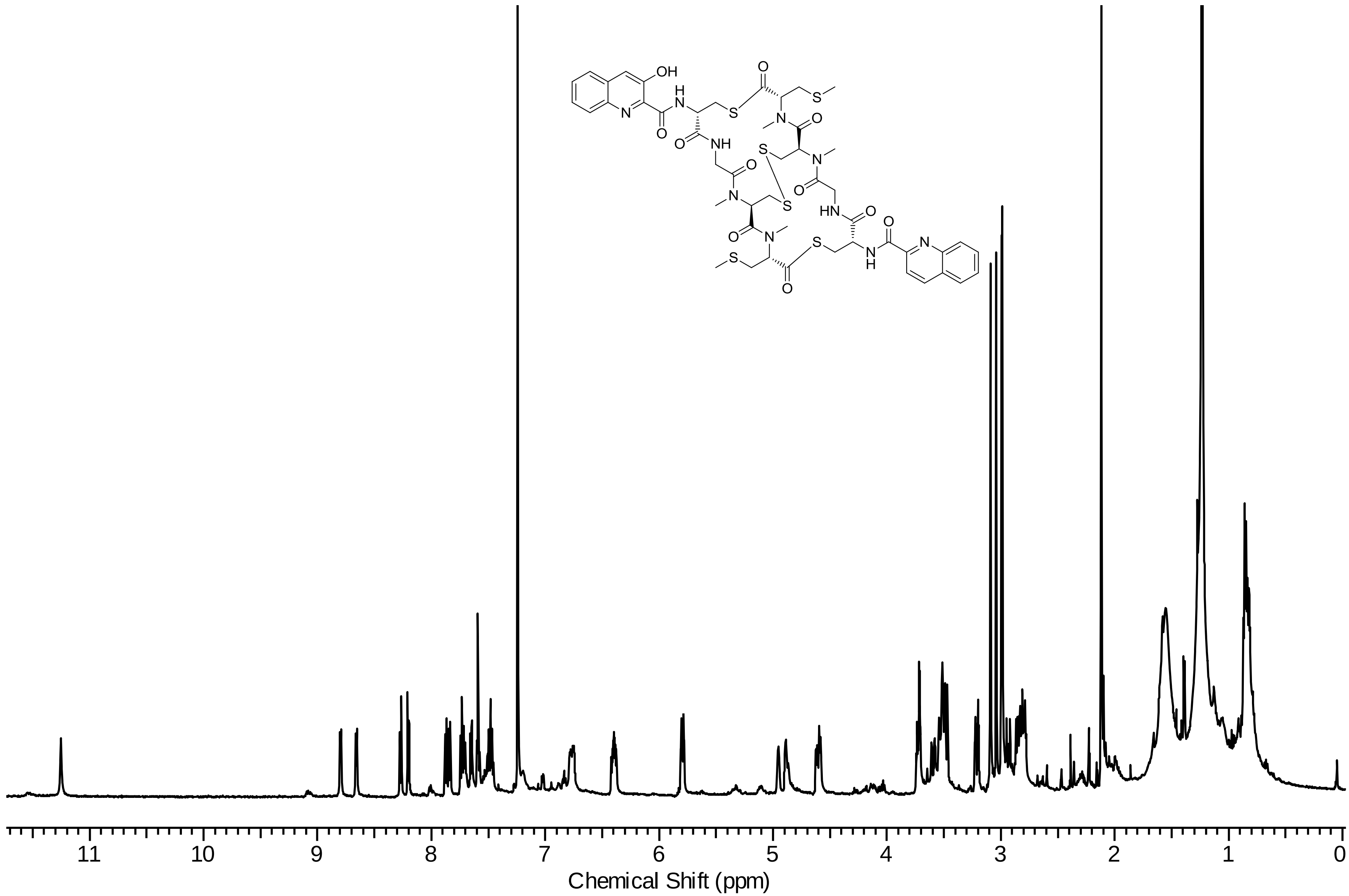

Figure A1.1. ^{1}H NMR (600 MHz, CDCl$_3$) of 22’-deoxythiocoraline (**38**)

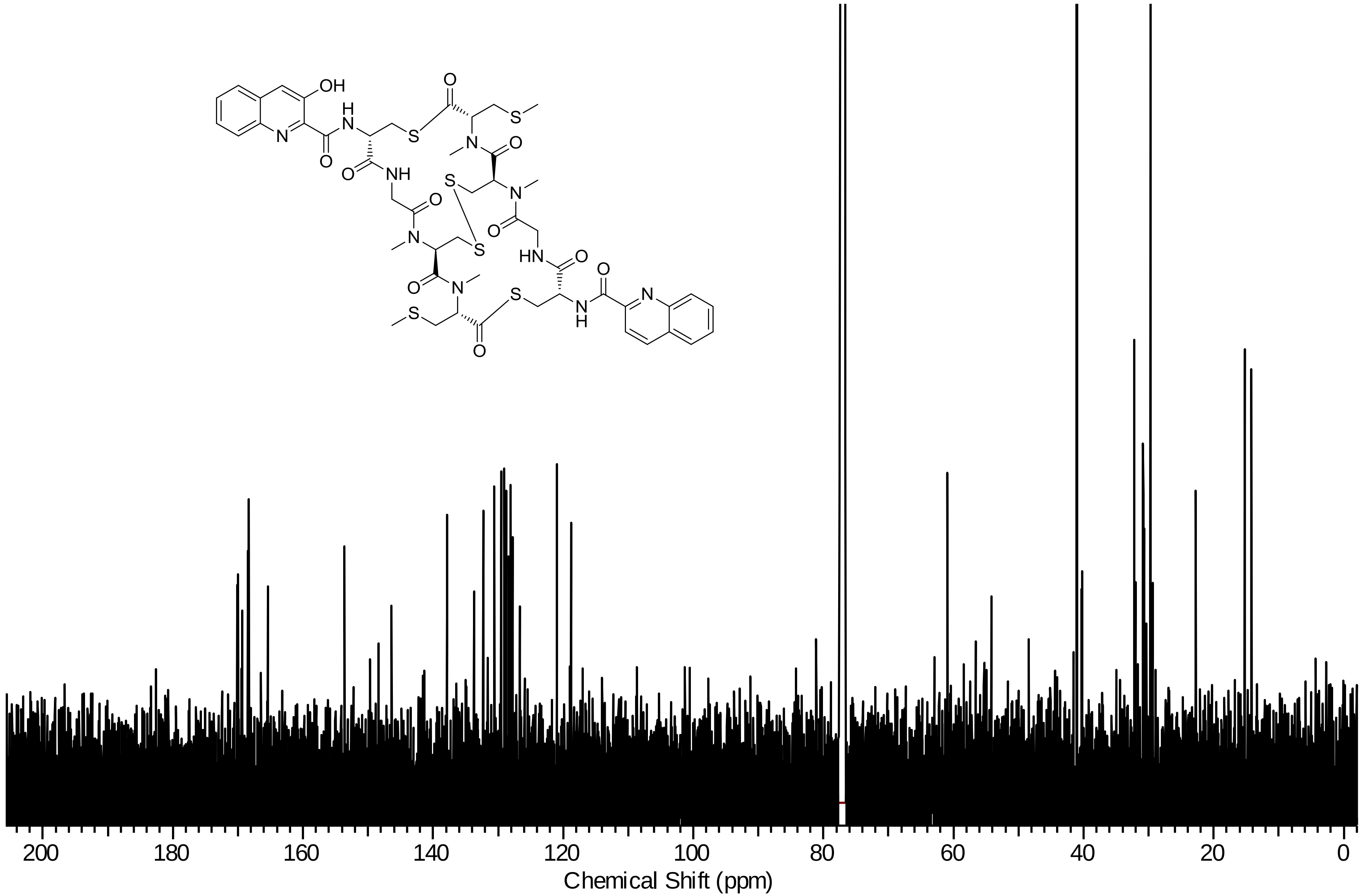

Figure A1.2. ^{13}C NMR (125 MHz, $CDCl_3$) of 22’-deoxythiocoraline (**38**)

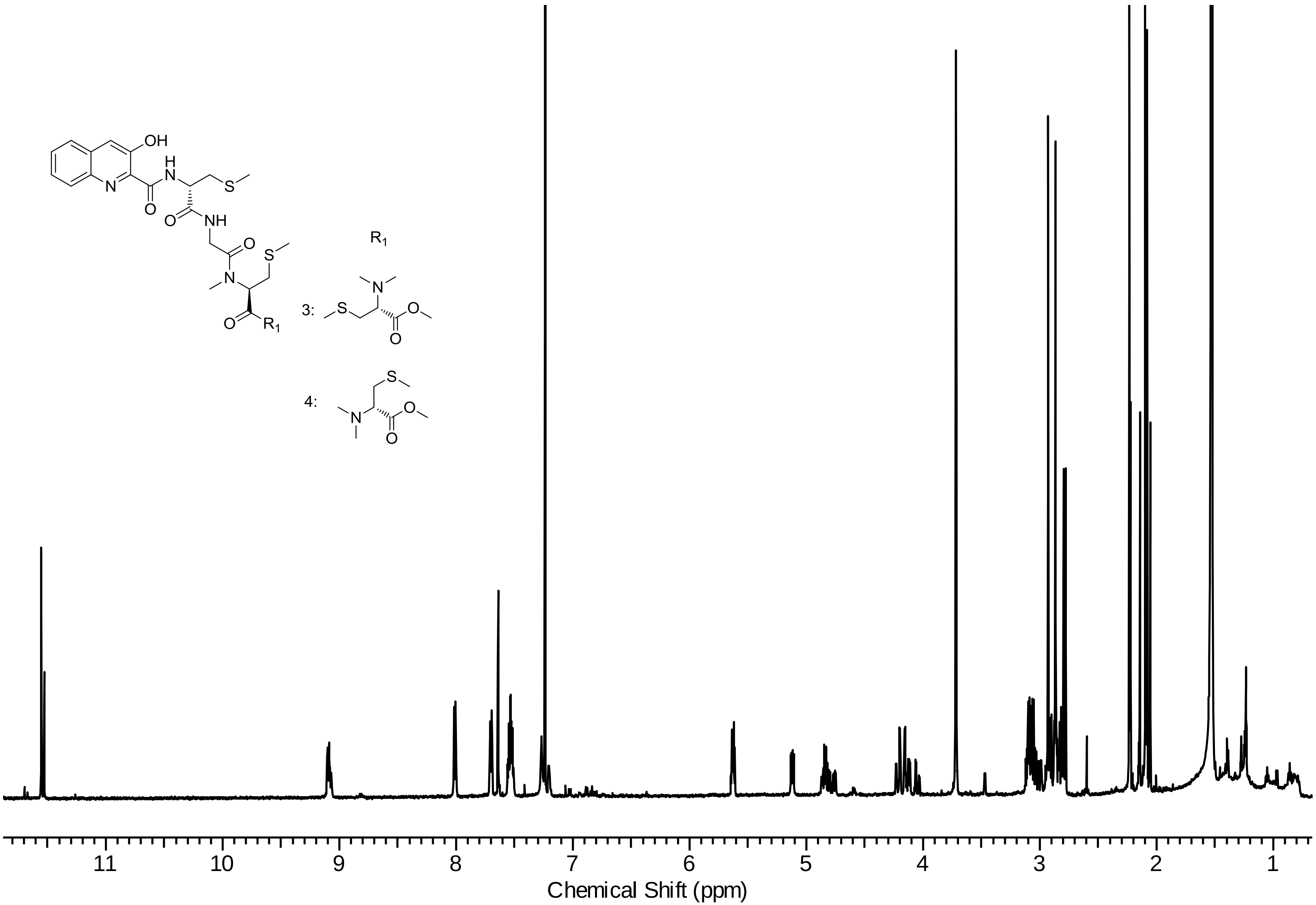

Figure A1.3. ^{1}H NMR (600 MHz, CDCl$_3$) of thiochondrilline A (**39**) & B (**40**)

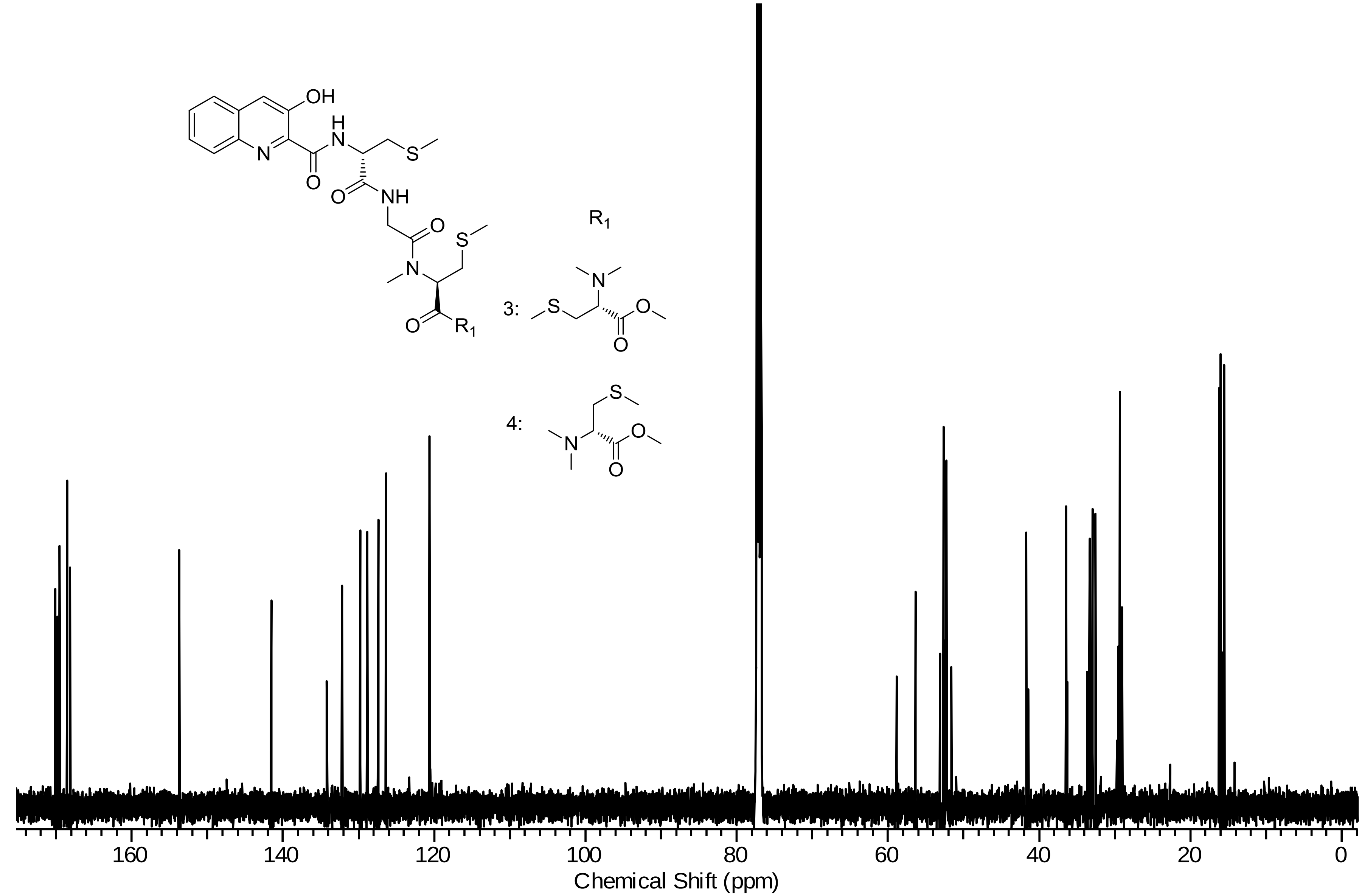

Figure A1.4. ^{13}C NMR (125 MHz, $CDCl_3$) of thiochondrilline A (**39**) & B (**40**)

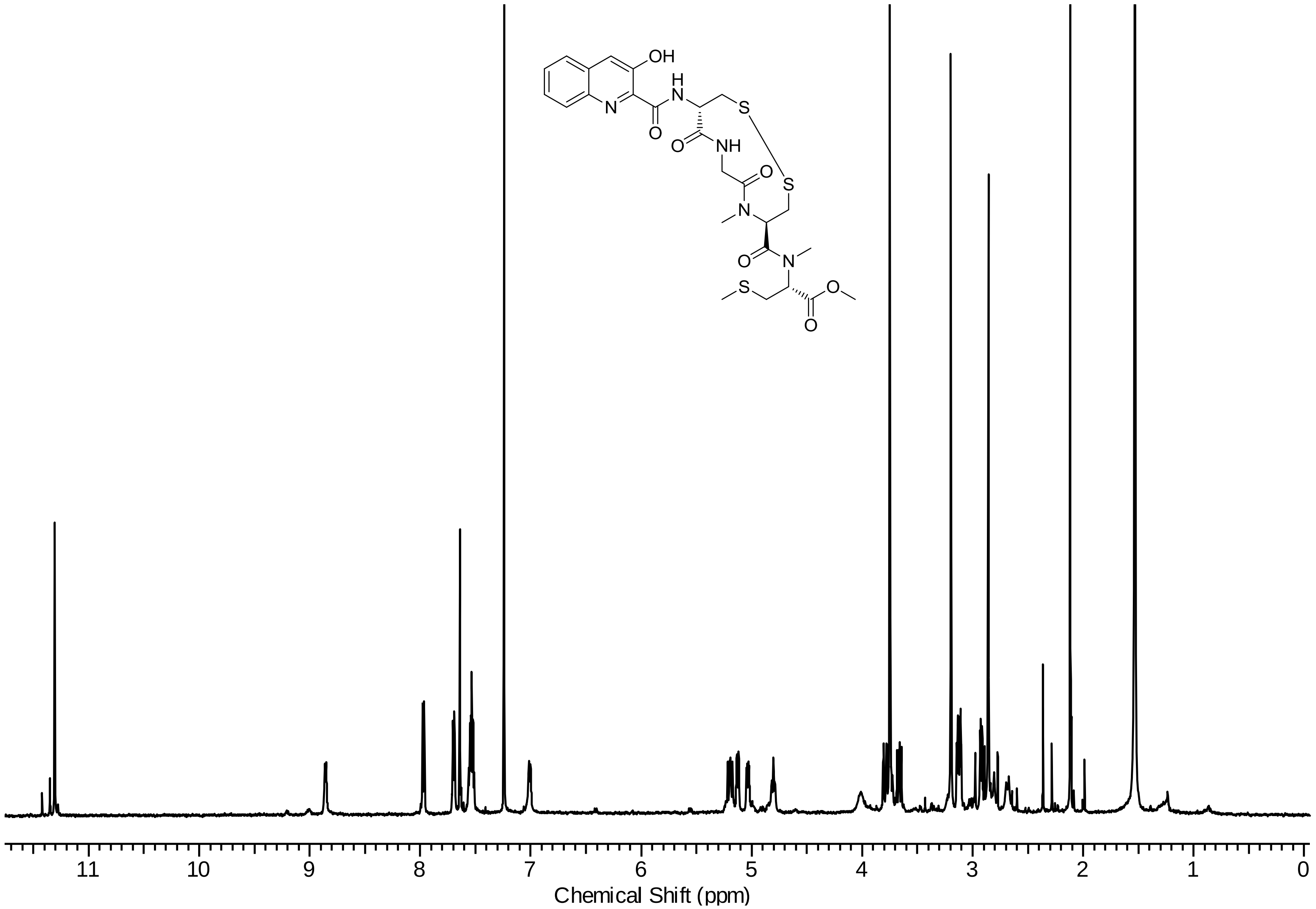

Figure A1.5. ^{1}H NMR (600 MHz, $CDCl_3$) of thiochondrilline C (**41**)

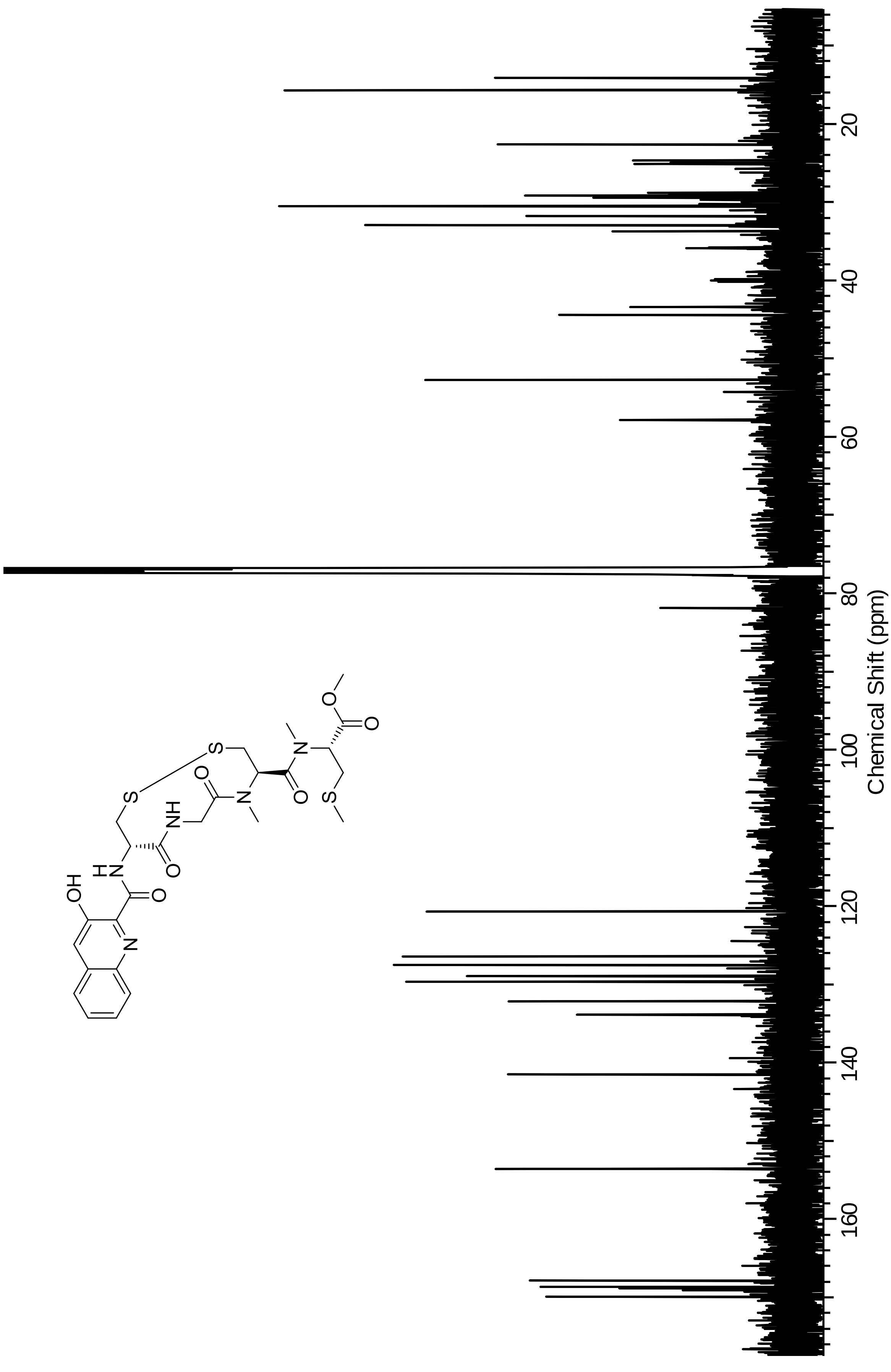

Figure A1.6. ^{13}C NMR (125 MHz, CDCl$_3$) of thiochondrilline C (**41**)

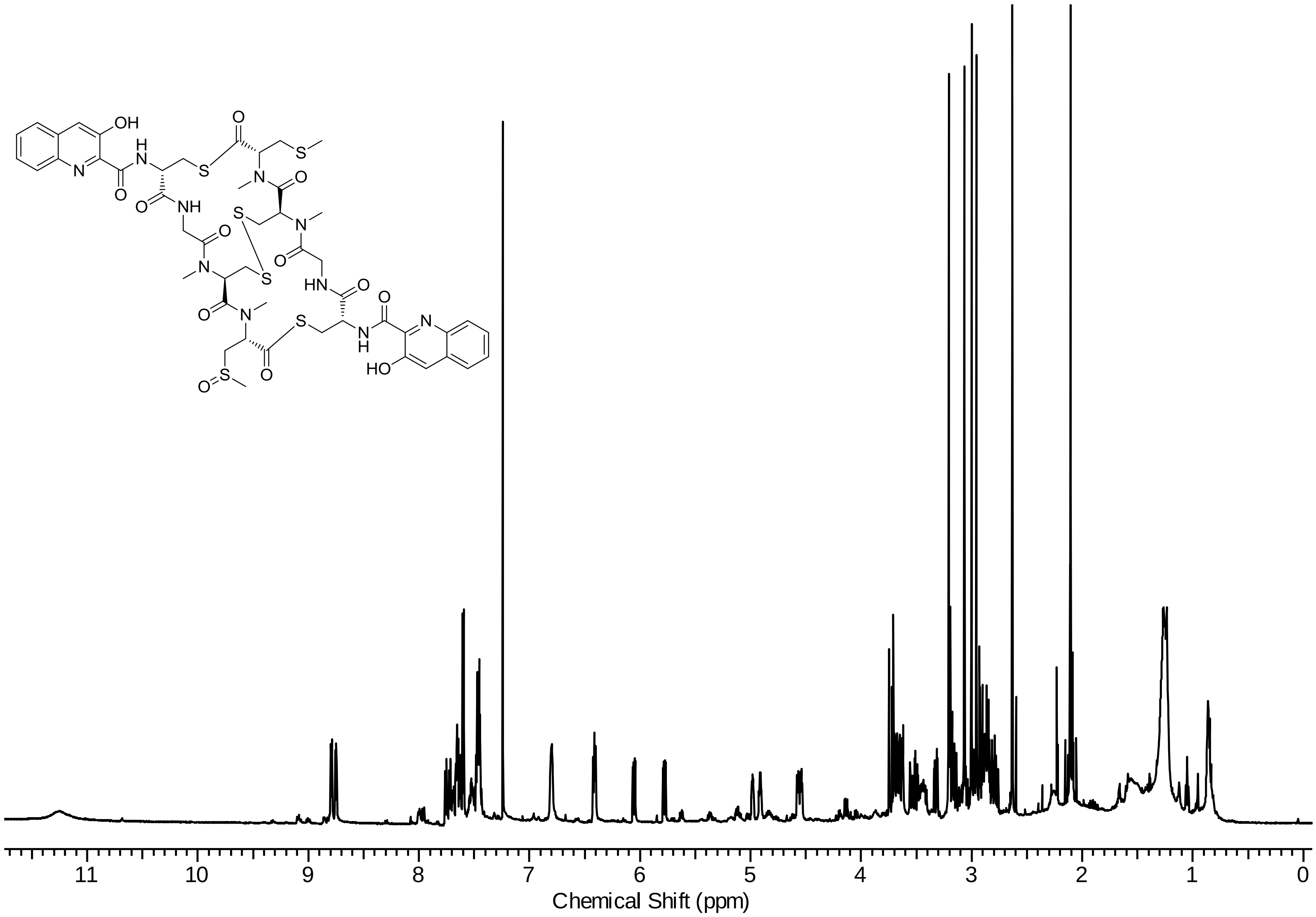

Figure A1.7. ^{1}H NMR (600 MHz, $CDCl_3$) of 12’-sulfoxythiocoraline (**42**)

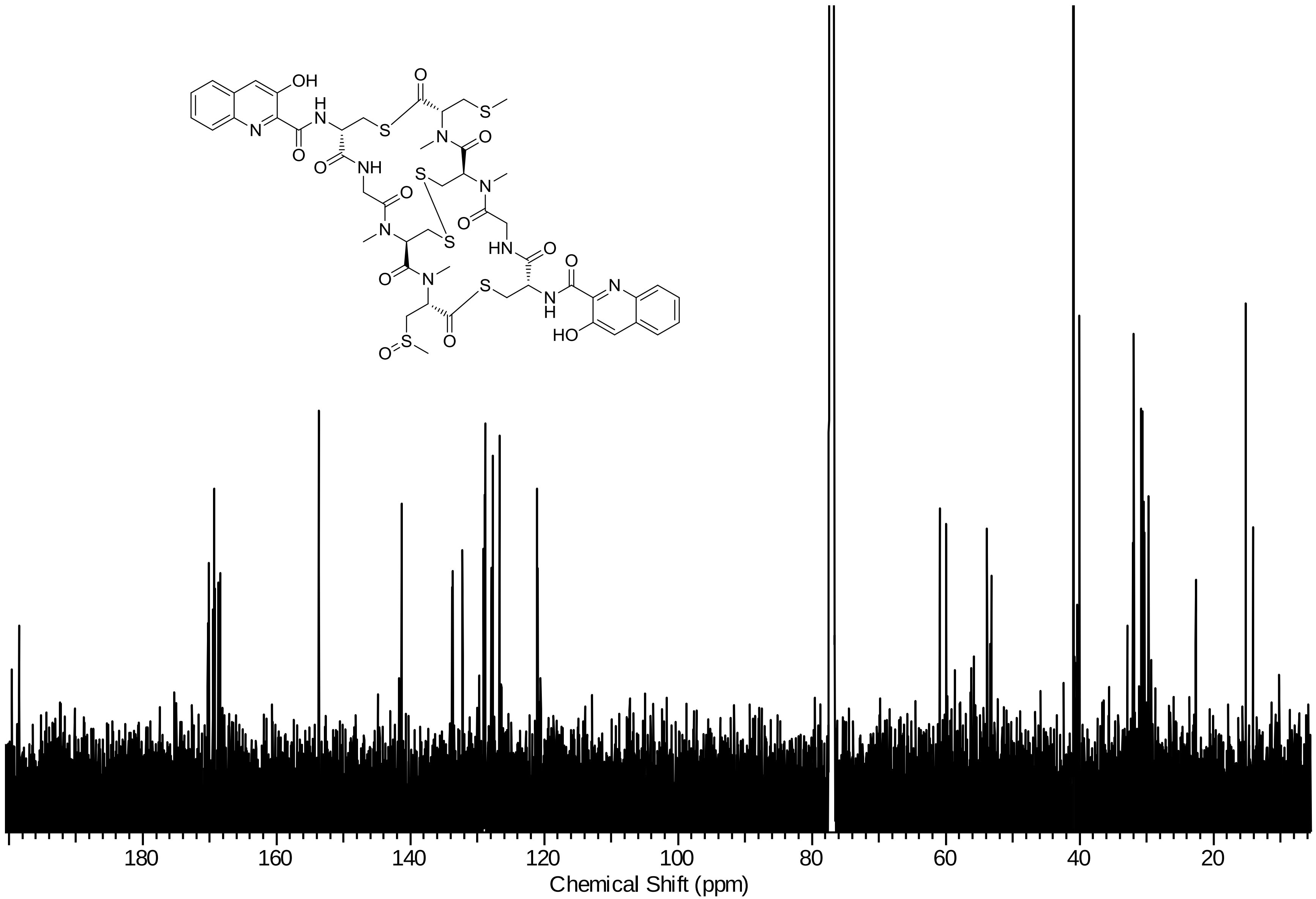

Figure A1.8. ^{13}C NMR (125 MHz, $CDCl_3$) of 12’-sulfoxythiocoraline (**42**)

Figure A1.9. DFT calculations for thiochondrilline A (**39**)

Thiochondrilline A			*R* (C-2)		*S* (C-2)		*Cis-trans R* (C-2)	
	Observed	Observed	Calc	Calc	Calc	Calc	Calc	Calc
Position	^{1}H	^{13}C	^{1}H	^{13}C	^{1}H	^{13}C	^{1}H	$^{\backslash3}$C
1		169.8		172.4		167		169.7
2	5.11	56.4	5.71	55.6	3.27	62.8	3.37	67.8
3		169.7		170.9		170.7		173.5
4	5.62	52.1	5.4	52.4	5.35	51.9	4.41	56.2
5		167.9		170.4		171		167.8
6	4.16	41.5	3.21	42	3.25	42.6	4.05	45.9
	4.2		5.03		4.77		4.14	
7-NH	7.27		7.59		7.4		8.36	
8		169.4		170.3	170.3			167.5
9	4.84	52.1	4.67	50.9	4.6	51.2	3.65	57.2
10-NH	9.09		8.41		8.47		8.73	
11		169.2		170.3		170.3		162
12	3.08	32.6	3.23	38.4	3.51	37.4	4.12	45
	2.88		2.61		2.45		2.45	
13	2.1	15.2	1.97	19.1	2.1	23.2	1.87	20.4
14	2.93	32.5	2.72	30.3	2.8	35.3	3.28	39.7
15	2.91	33.2	3.02	39.5	3.07	39.3	3.13	40.5
	2.83		2.27		2.24		2.54	
16	2.87	29.1	2.67	29.5	2.74	30.2	3.5	27.5
17	3.08	36.2	3.12	39	3.18	38.6	3.02	45.5
	3.04		2.96		2.88		2.87	
18	3.72	52.7	3.67	52.2		54	3.73	52.3
19	2.08	15.6	1.48	19	1.53	18.7	1.98	20.6
20	2.23	15.9	1.48	19	1.92	18	1.91	22
21		134		137.6		137.9		143.7
22		153.5		158.6		158.2		154
22-OH	11.55		12.57		12.53		4.22	
23	7.64	120.5	7.47	122.6	7.4	122.2	6.89	120.9
24		132.1		135		134.8		133.1
25	7.7	126.1	7.75	128.8	7.73	128.7	7.65	127.2
26	7.52	128.7	7.66	130.9	7.57	131	7.65	130.4
27	7.54	127.3	7.67	128.4	7.67	128.5	7.7	128.4
28	8.01	129.7	8.09	132.8	8.1	132.8	8.11	132.6
29		141.4		142.5		142.5		142.8

Using the DP4 Probability Method

	^{13}C data	^{1}H data	Both
R	78.00%	100%	100%
S	22.00%	0%	0%

	^{13}C data	^{1}H data	Both
R	100%	100%	100%
Cis-trans S	0%	0%	0%

Figure A1.10. DFT calculations for thiochondrilline B (**40**)

Thiochondrilline B			*R* (C-2)		*S* (C-2)		*Cis-Cis R* (C-2)	
	Observed	Observed	Calc	Calc	Calc	Calc	Calc	Calc
Position	^{1}H	^{13}C	^{1}H	^{13}C	^{1}H	^{13}C	^{1}H	^{13}C
1		169.8		170.8		166.8		170.1
2	4.76	58.8	6.04	62.3	3.91	64.4	4.3	61.2
3		169.6		169.2		172.4		171.2
4	5.63	51.7	5.62	53.2	5.92	53	3.92	56.7
5		167.9		168.3		170		165.5
6	4.06	41.3	3.61	44.6	3.77	45	3.39	43.3
	4.12		4.04		3.92		3.77	
7-NH	7.2		8		7.48		8.03	
8		169.4		167.7		166.5		169.2
9	4.81	52.2	4.63	50.8	4.66	50.7	4.89	53
10-NH	9.07		8.27		8.38		8.41	
11		169.2		169.5		168.7		161.1
12	2.84	33.3	2.59	40.5	2.59	39	2.85	40.5
	2.99		3.14		3.31		3.05	
13	2.05	15.4	2.39	20.4	2.69	24.4	1.95	26.3
14	2.78	29.3	2.71	33	2.93	36.1	3.02	26.3
15	2.91	33.2	3.28	40.7	3.21	43.9	3.12	40.9
	2.83		2.5		3		2.73	
16	2.8	29	2.94	28.4	2.77	28.4	3.5	27.9
17	3.08	36.2	3.06	39.1	3.3	38.7	3.39	41
	3.03		2.95		2.79		2.52	
18	3.71	52.7	3.76	52.2	3.71	54.6	3.67	54.3
19	2.14	15.8	1.79	20.1	1.78	20.6	1.96	20.3
20	2.22	15.9	1.99	18	1.9	20.6	1.92	20.7
21		134		137.2		137.5		142.5
22		153.5		158.5		158.6		153.8
22-OH	11.53		12.68		12.7		4.32	
23	7.64	120.5	7.45	122.8	7.42	122.5	6.94	121.2
24		132.1		135.1		135		133.3
25	7.7	126.1	7.76	128.9	7.74	128.8	7.69	127.4
26	7.52	128.7	7.66	131	7.64	130.6	7.69	130.6
27	7.54	127.3	7.65	128.5	7.64	128.1	7.72	128.7
28	8.01	129.7	8.07	132.7	8.09	132.8	8.13	133
29		141.4		142.5		142.4		137.2

Using the DP4 Probability Method

	^{1}H and ^{13}C	^{13}C only
R	99.9%	100%
S	0.1%	0%

	^{1}H and ^{13}C	^{13}C only
R	100%	100%
Cis-Cis R	0%	0%

Figure A1.11. DFT calculations for thiochondrilline C (**41**)

Thiochondrilline C			*R*		*S*		*SH-trans-R*		*SH-trans-S*	
Position	Observed	Observed	Calc	Calc	Calc	Calc	Calc	Calc	Calc	Calc
	^{1}H	^{13}C	^{1}H	^{13}C	^{1}H	^{13}C	^{1}H	^{13}C	^{1}H	^{13}C
1		170.1		174.4		170.2		172.2		166.8
2	5.04	58	4.17	64.4	5.31	61	5.68	55.7	3.28	62.8
3		169		172.5		166.5		170.4		170.5
4	5.13	58.1	4.33	60.5	4.68	55.7	5.34	56.3	5.28	56.1
5		168.8		171.3		165.6		170.5		171.3
6	5.2	44.6	4.59	45.1	5.32	46.2	5.02	42.1	4.95	42.2
	3.79		3.49		3.49		3.25		3.2	
7-NH	7.01		4.46		5.07		7.63		7.53	
8		169.2		169.5		169.3		169.2		169.5
9	4.8	54.4	4.47	55.5	4.61	56.4	4.31	57.4	4.3	63.4
10-NH	8.86		9.39		9.13		8.49		8.48	
11		168.1		166		168.8		170.2		170.3
12	2.92	33.9	3.46	42	2.68	41.8	2.6	38.4	2.43	37.5
	3.12		3.76		3.05		2.66		3.51	
13	2.12	15.9	1.94	18.1	2.47	23	1.97	19	2.07	22.9
14	3.2	33.2	3.13	39.8	3.19	38.6	2.72	30.3	2.83	35.2
15	4	43.2	3.65	41.6	3.48	42.8	2.83	32.3	2.87	32.3
	2.7		2.23		2.25		2.6		2.54	
16	2.86	30.7	2.75	32.8	2.8	31.1	2.74	34.8	2.8	29.9
17	3.66	43.6	4.33	46.4	4.3	47.2	3.23	32	3.18	31.8
	3.13		1.8		1.94		1.91		2.92	
18	3.75	52.9	3.67	51.3	4.2	55.3	1.97	52.2	3.5	54.1
21		134		139.4		136.8		137.4		137.6
22		153.7		153.7		158.4		158.5		158.4
22-OH	11.31		10.2		12.21		12.5		12.52	
23	7.64	120.9	7.59	126.9	7.5	123	7.48	122.7	7.45	122.5
24		132.4		129.2		135		135.1		135
25	7.7	126.6	7.8	128.9	7.79	129	7.78	128.9	7.75	128.7
26	7.54	129.1	7.7	130.1	7.69	131.4	7.68	131	7.67	131
27	7.56	127.7	7.8	128.8	7.73	128.9	7.69	128.6	7.7	128.6
28	7.97	129.8	8.22	131.3	8.18	132.9	8.1	132.8	8.12	132.9
29		141.7		138.7		142.8		142.6		142.5

Using the DP4 Probability Method

	^{13}C data
R	97.5%
SH-R	2.5%

Appendix 2:

Supplementary Data for Chapter 3

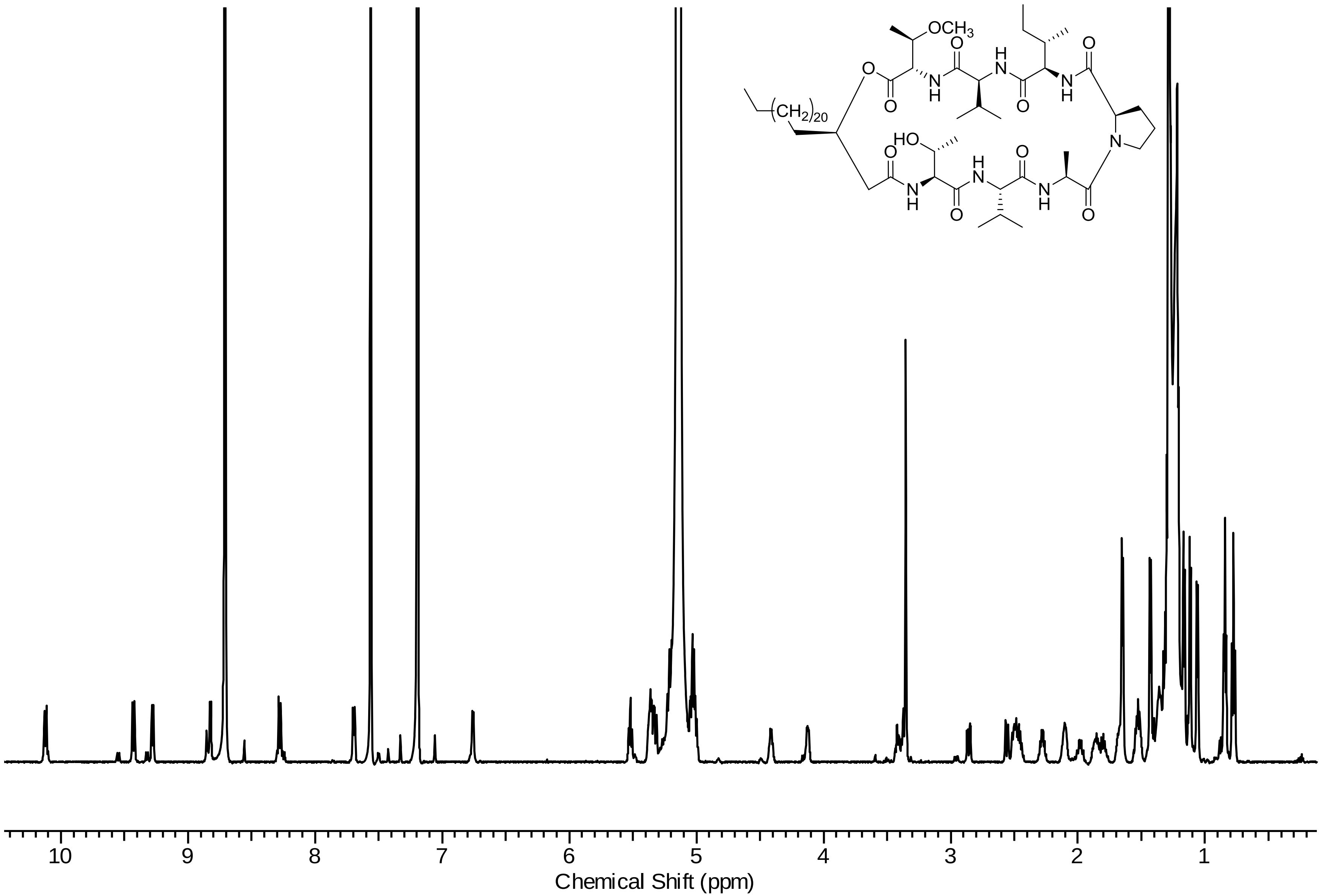

Figure A2.1. ^{1}H NMR (600 MHz, pyridine-d_5) of peptidolipin B (**45**)

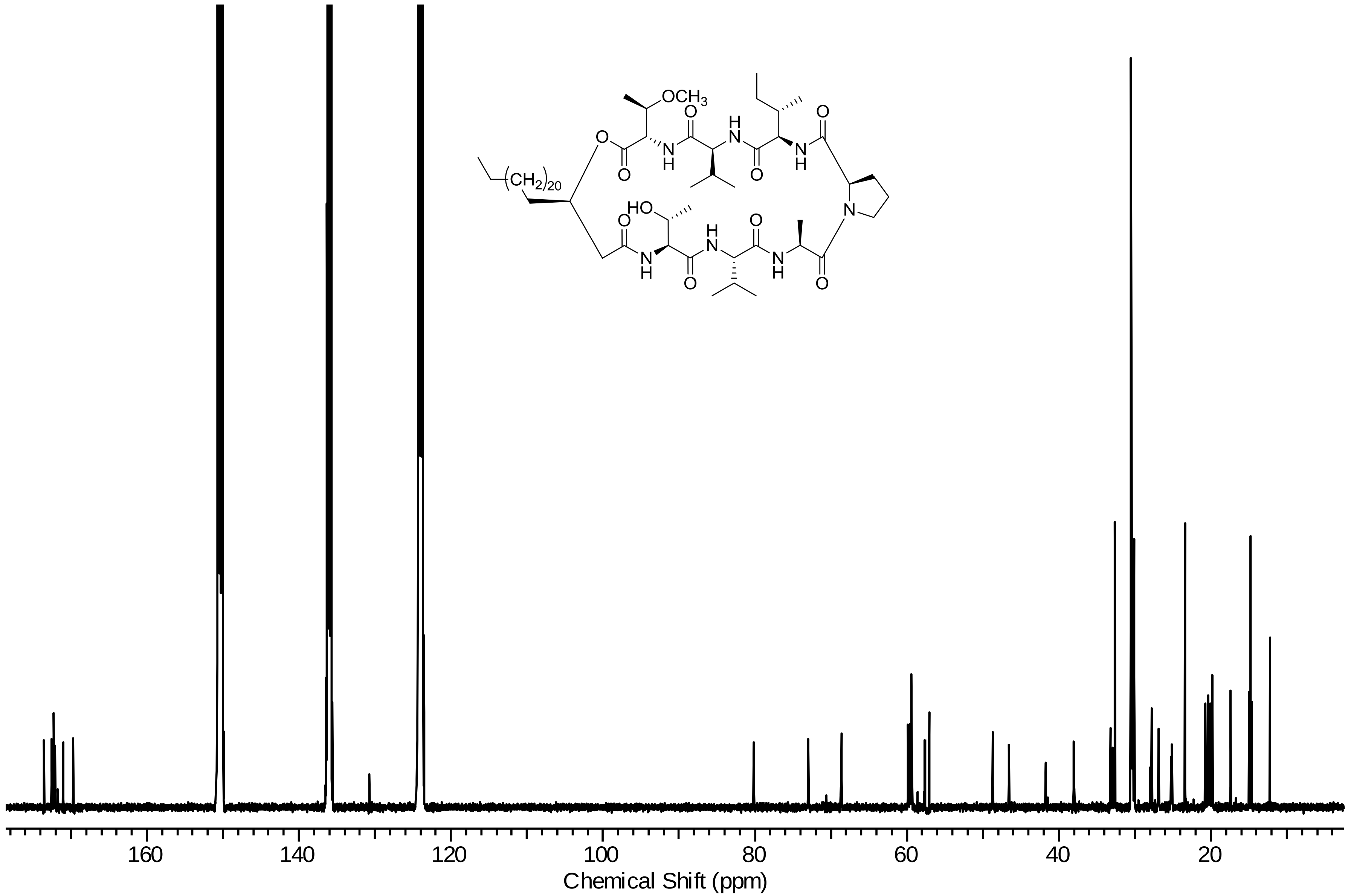

Figure A2.2. ^{13}C NMR (125 MHz, pyridine-d$_5$) of peptidolipin B (**45**)

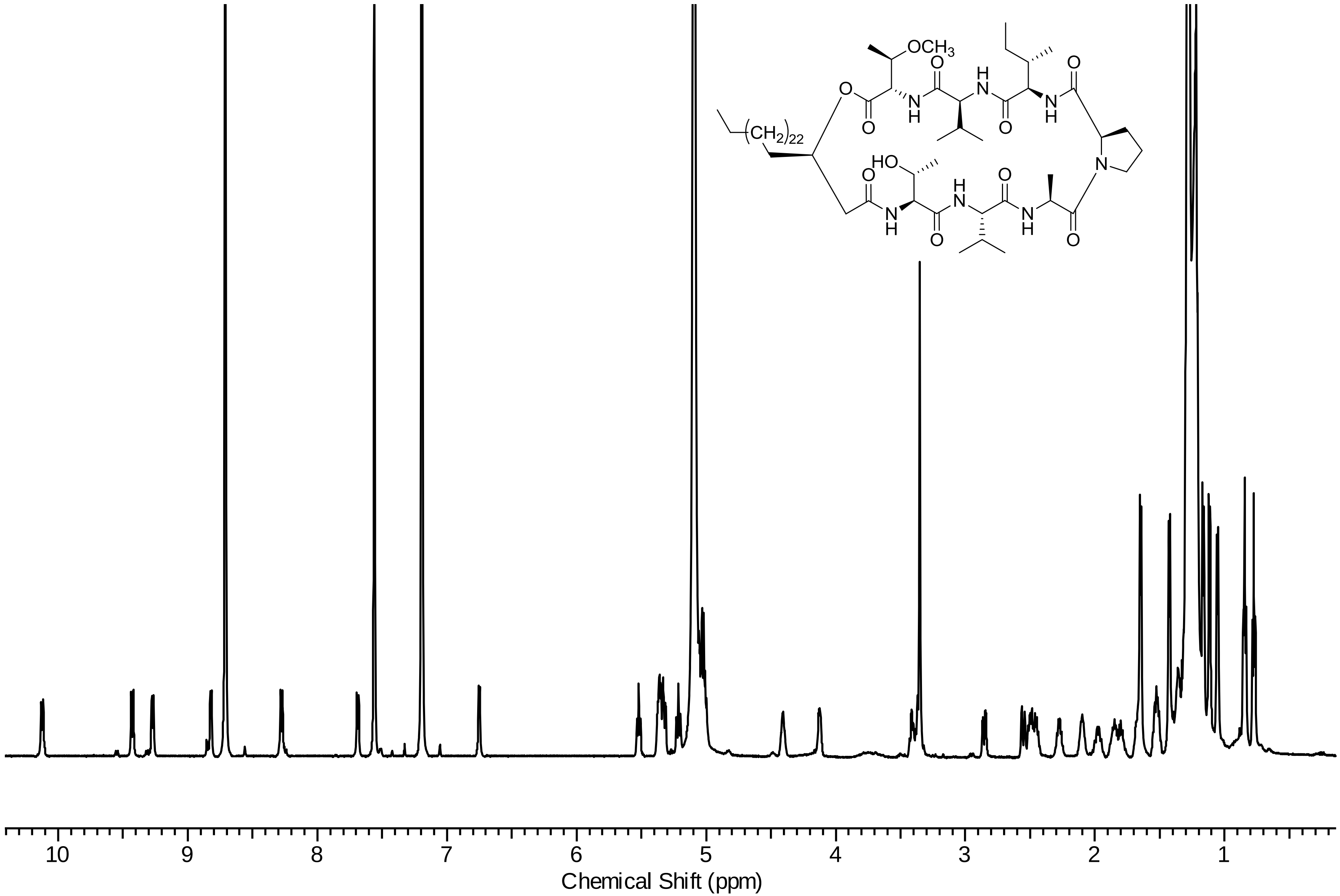

Figure A2.3. ^{1}H NMR (600 MHz, pyridine-d_5) of peptidolipin C (**46**)

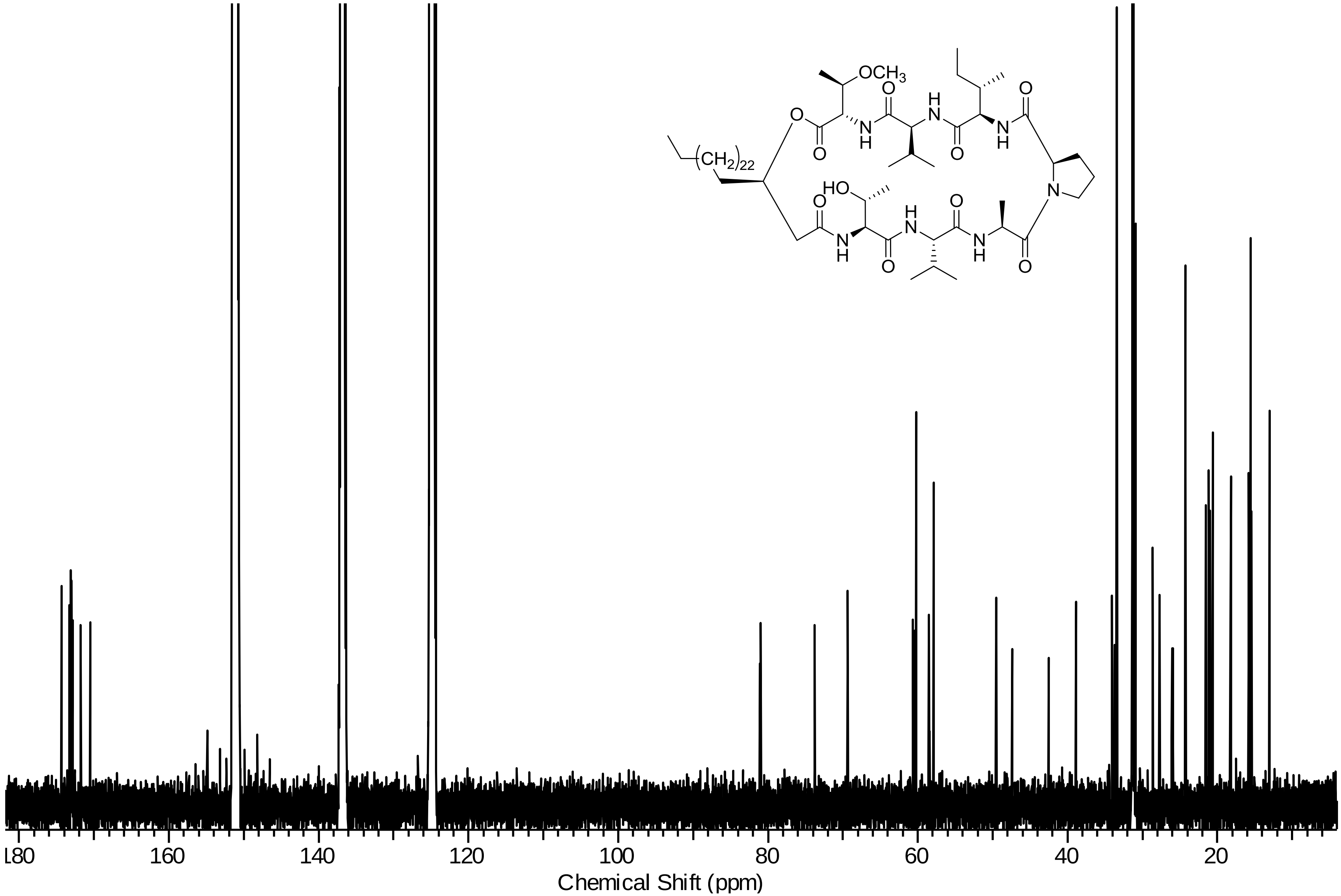

Figure A2.4. ^{13}C NMR (125 MHz, pyridine-d_5) of peptidolipin C (**46**)

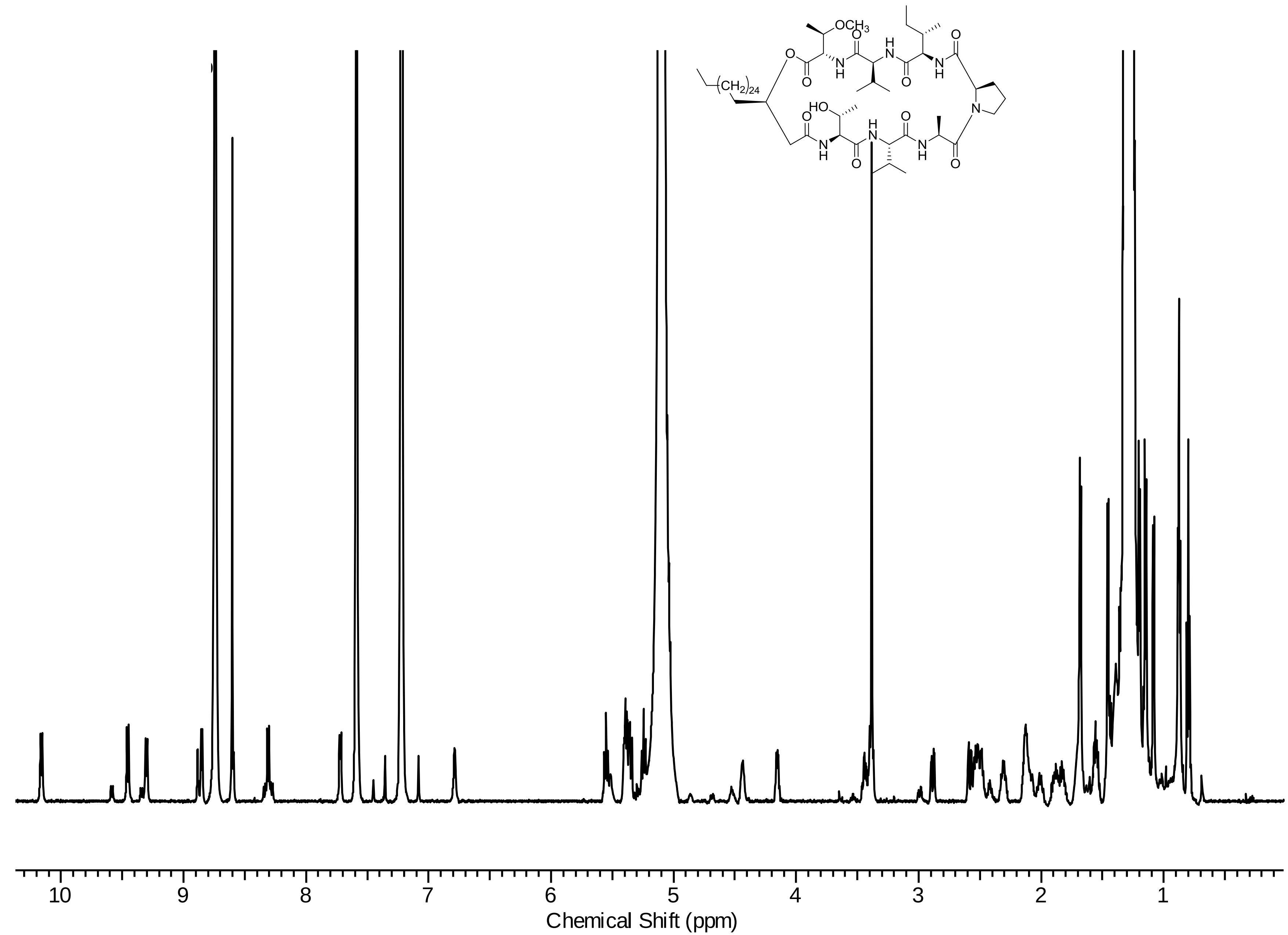

Figure A2.5. ^{1}H NMR (600 MHz, pyridine-d_5) of peptidolipin D (**47**)

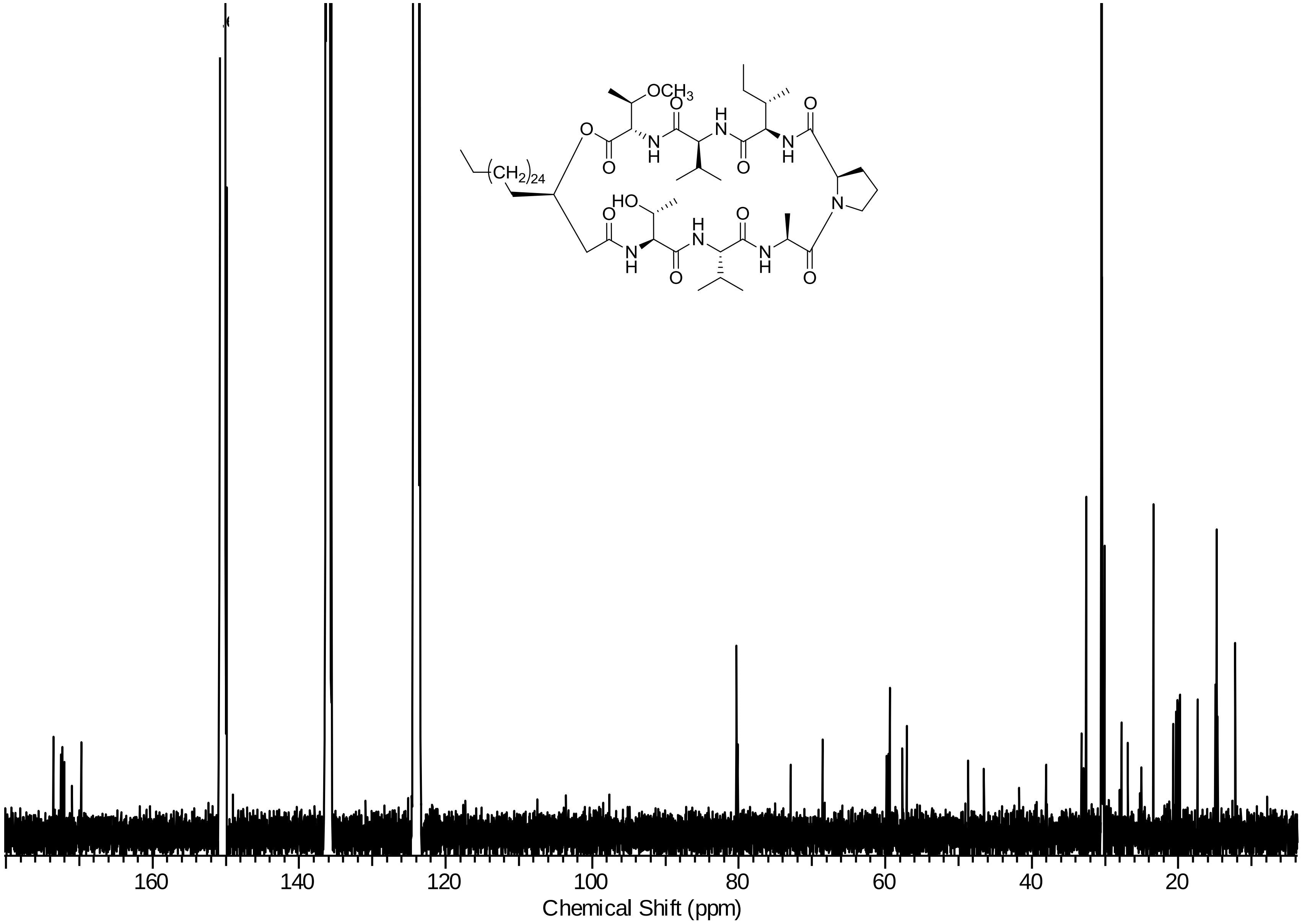

Figure A2.6. ^{13}C NMR (125 MHz, pyridine-d_5) of peptidolipin D (**47**)

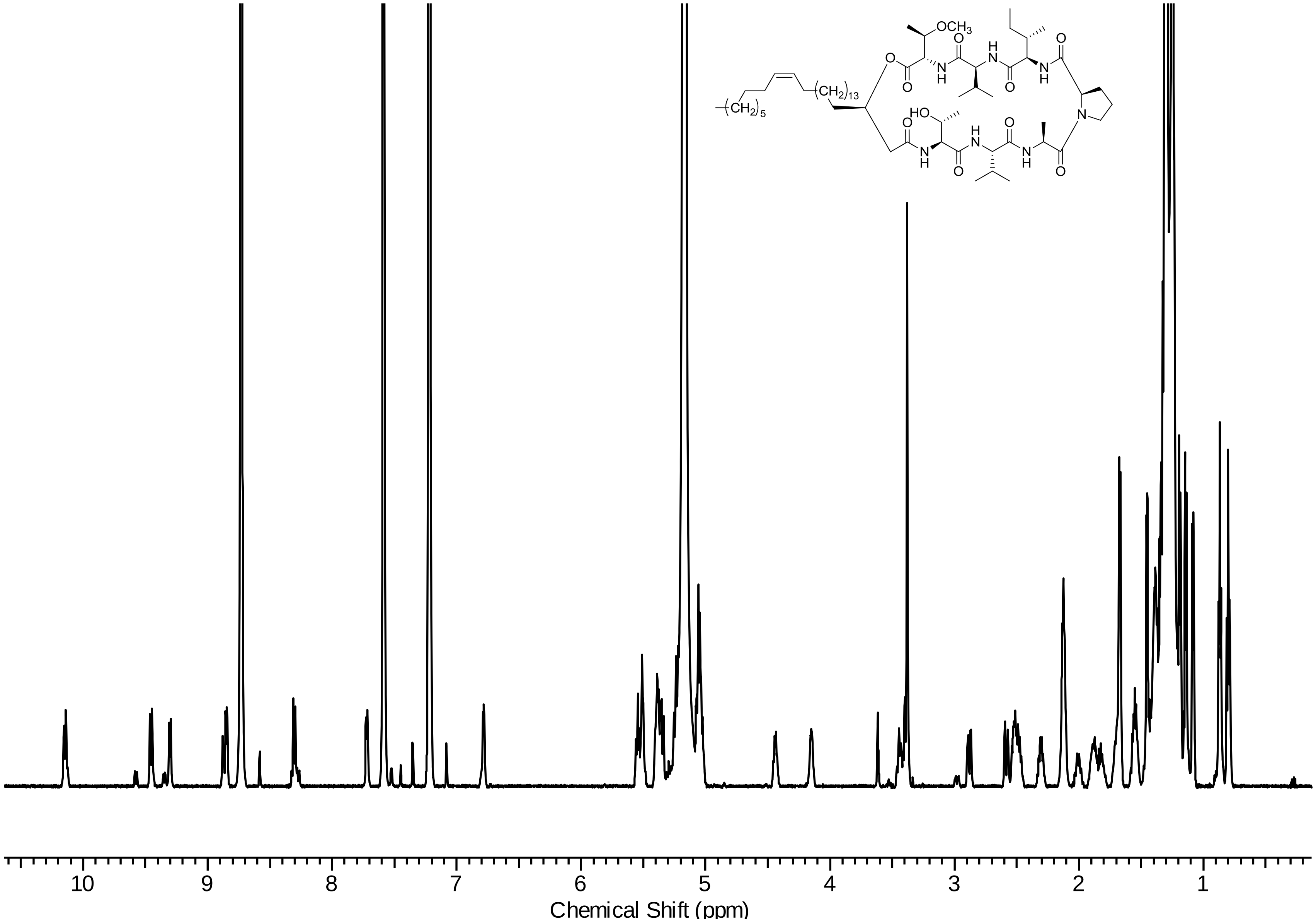

Figure A2.7. ^{1}H NMR (600 MHz, pyridine-d_5) of peptidolipin E (**48**)

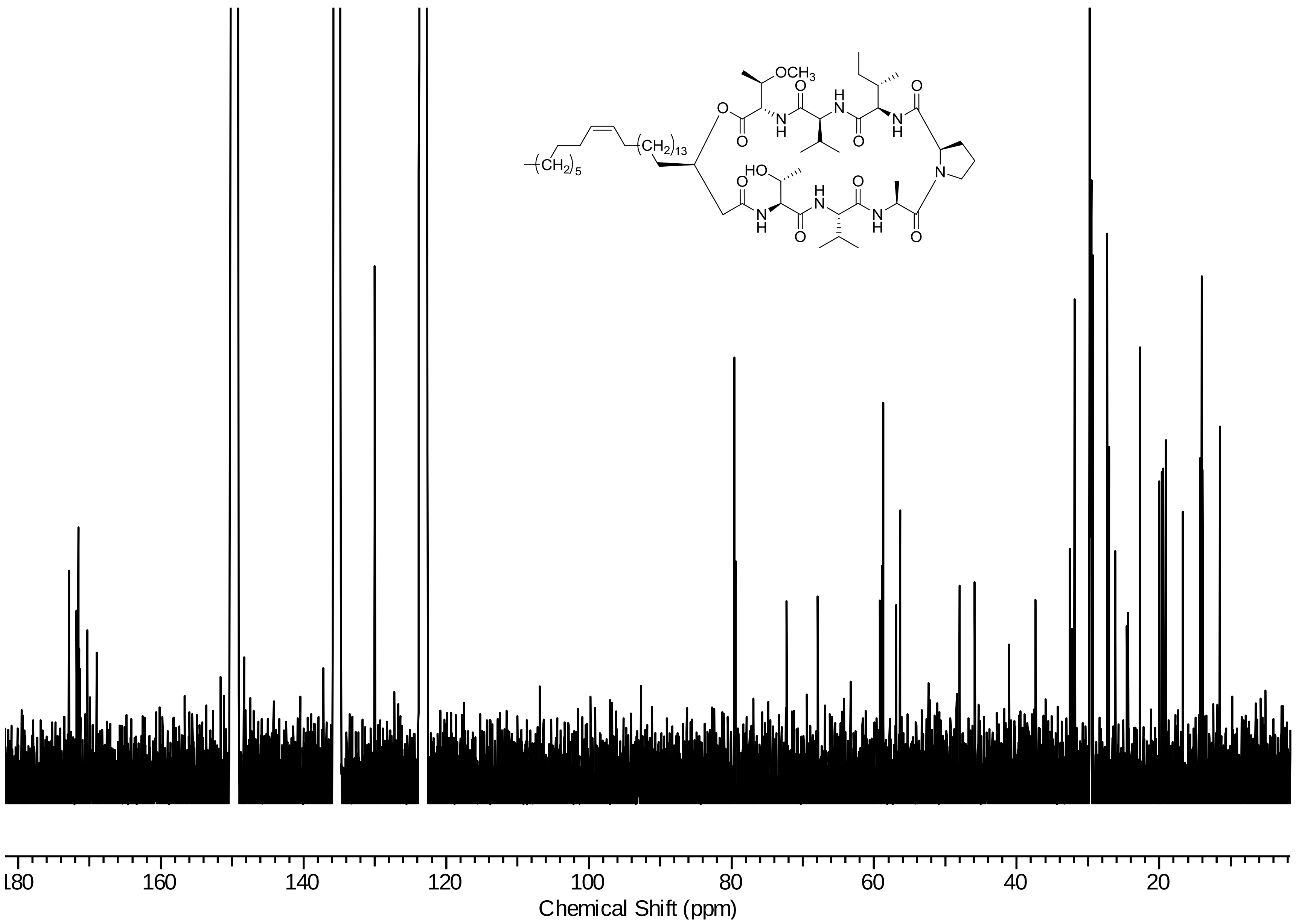

Figure A2.8. ^{13}C NMR (125 MHz, pyridine-d_5) of peptidolipin E (**48**)

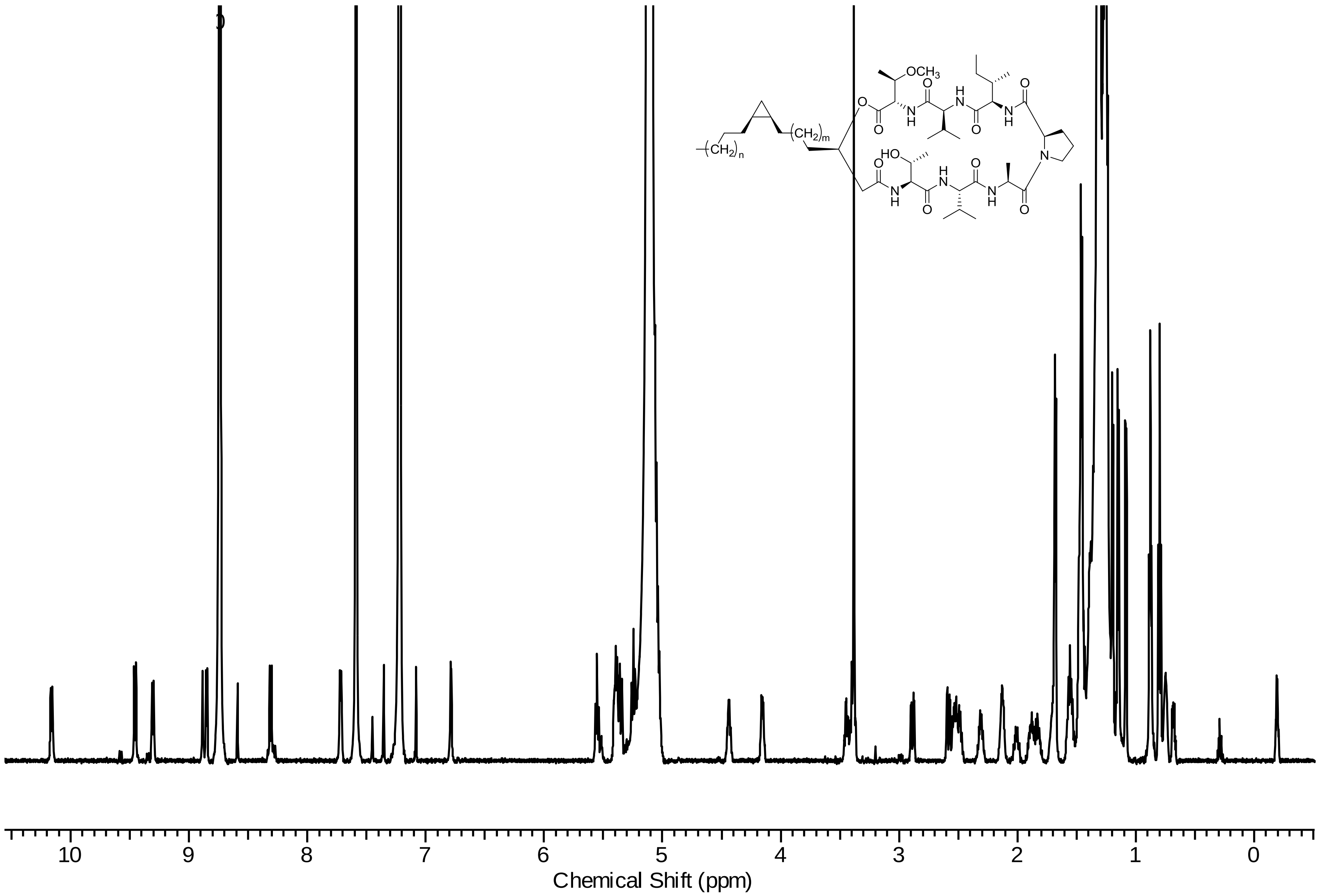

Figure A2.9. ^{1}H NMR (600 MHz, pyridine-d_5) of peptidolipin F (**49**)

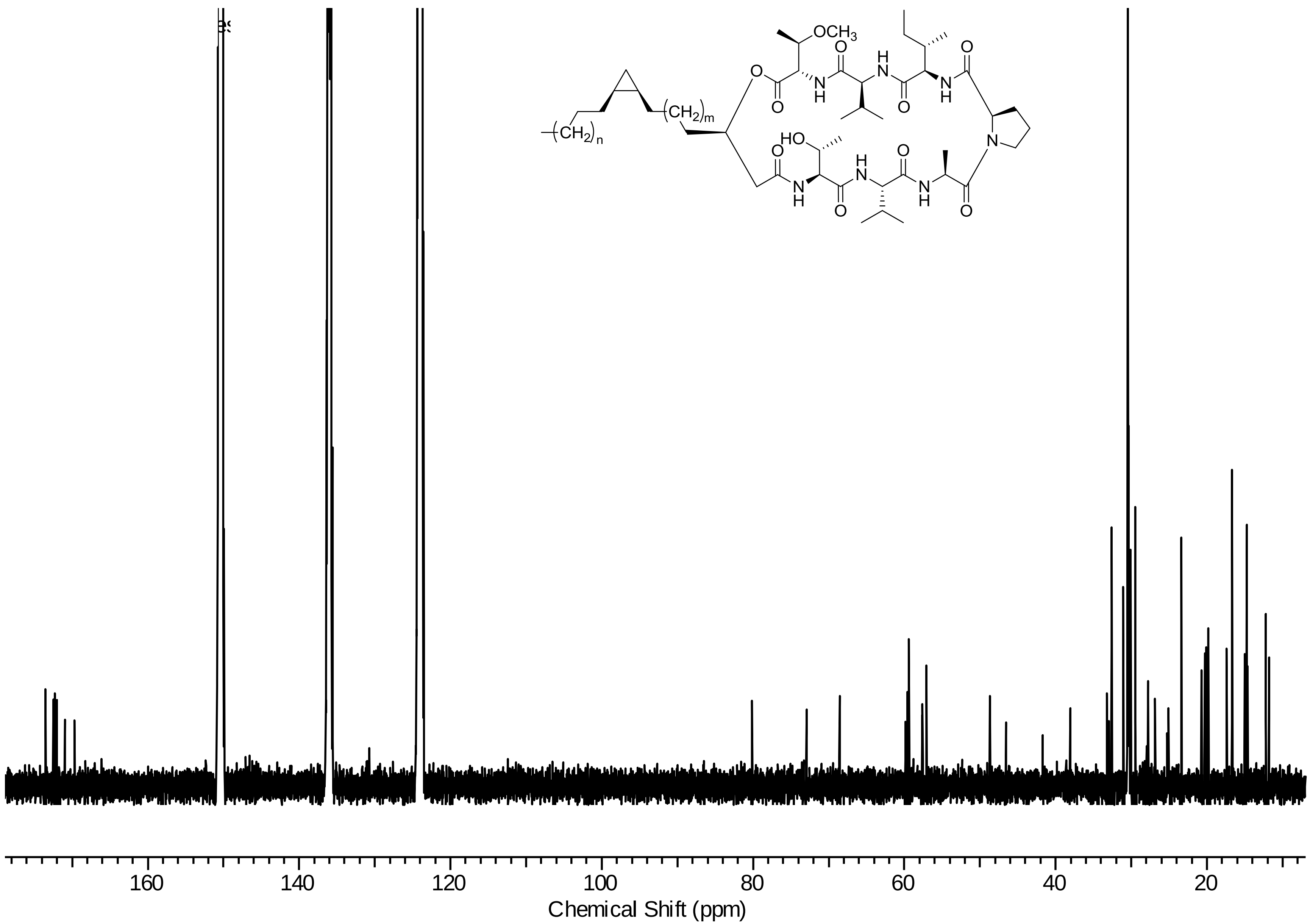

Figure A2.10. ^{13}C NMR (600 MHz, pyridine-d_5) of peptidolipin F (**49**)

Figure A2.11. DFT Calculations for configuration at C-43

Position	δ_C (Observed)	δ_C (*R* at C-43)	δ_C (*S* at C-43)
1	170.9	171.3	175.0
2	57.2	59.9	62.0
3	79.7	83.5	80.6
4	14.3	14.4	14.3
5	56.7	55.9	55.4
7	172.1	170.0	173.9
8	59.0	58.6	64.3
9	32.8	36.4	33.8
10	19.8	21.8	16.8
11	19.8	16.6	22.1
13	173.4	175.2	177.2
14	57.3	57.3	65.4
15	37.6	45.3	34.0
16	27.5	30.1	28.0
17	11.8	14.0	8.6
18	14.5	17.4	17.6
20	172.4	172.4	172.1
21	58.9	64.6	61.8
22	24.7	31.6	29.3
23	24.8	27.6	27.8
24	46.2	47.9	47.6
26	172.2	169.1	174.2
27	48.3	51.6	49.2
28	17.0	17.1	21.2
30	172.2	170.6	171.7
31	59.2	61.5	69.5
32	32.2	34.4	30.7
33	19.6	20.1	21.2
34	20.1	20.8	20.9
36	171.9	170.1	173.4
37	59.5	56.9	60.1
38	68.2	71.3	67.9
39	20.4	18.2	19.8
41	169.6	167.2	169.8
42	41.4	43.6	43.9
43	72.6	74.1	77.5
44	32.5	35.7	40.6

Using the DP4 Probability Method **(^{13}C NMR data)**

S at C-43	0.0%
R at C-43	100.0%

Appendix 3:

Supplementary Data for Chapter 5

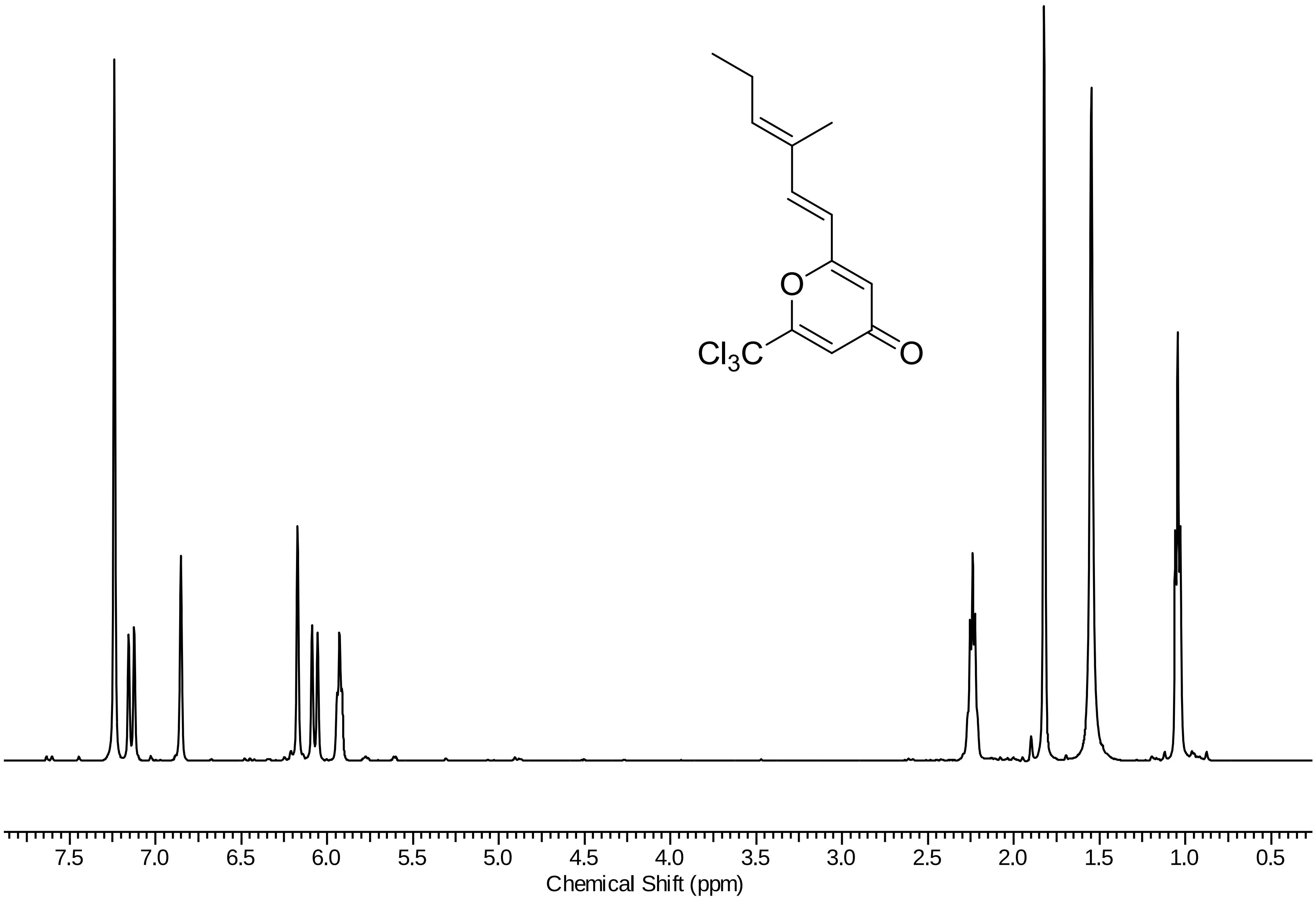

Figure A3.1. ^{1}H NMR (600 MHz, CDCl$_3$) of halomadurone A (**58**)

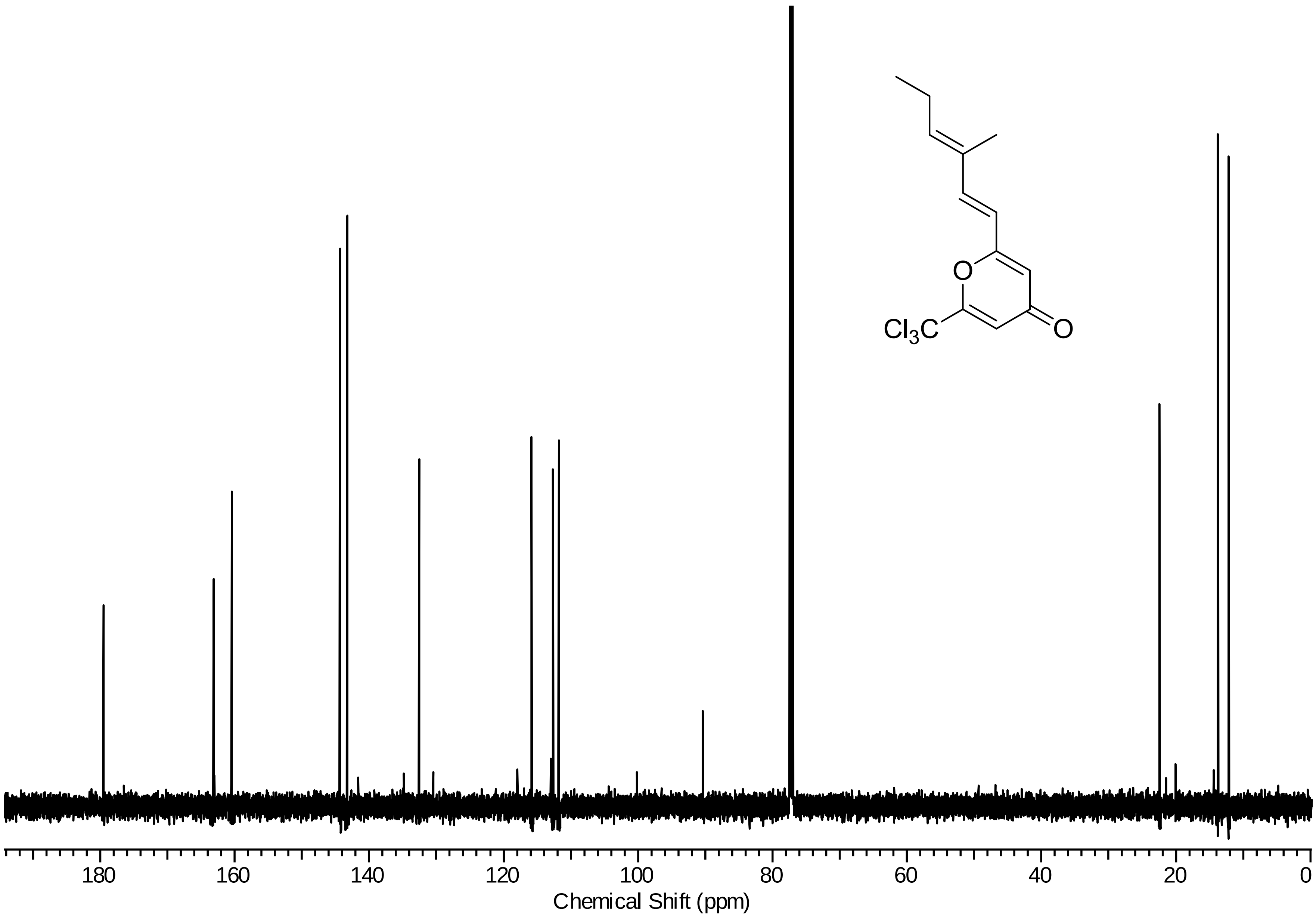

Figure A3.2. ^{13}C NMR (125 MHz, CDCl$_3$) of halomadurone A (**58**)

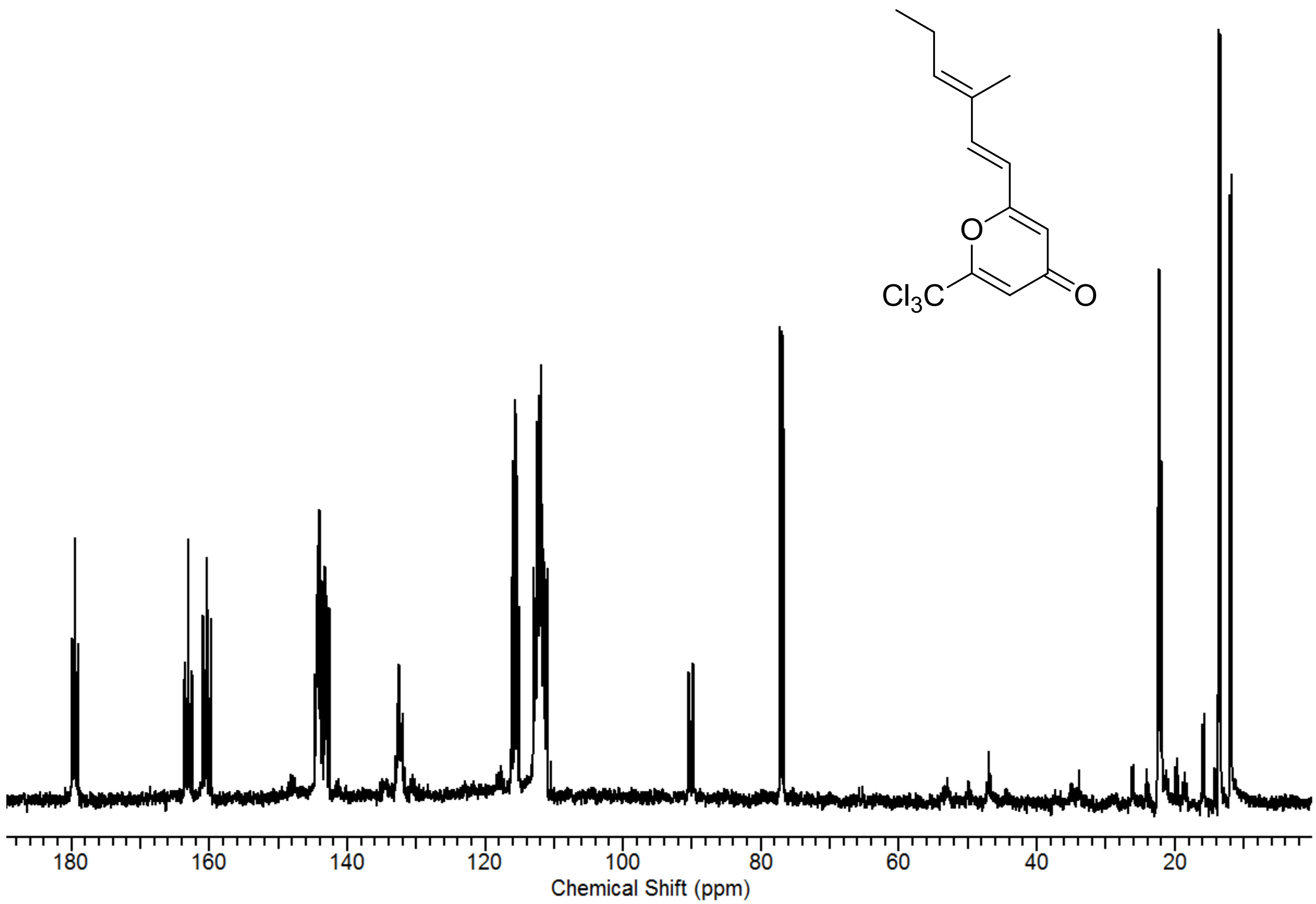

Figure A3.3. ^{13}C NMR (125 MHz, CDCl$_3$) of ^{13}C-labeled halomadurone A (**58**)

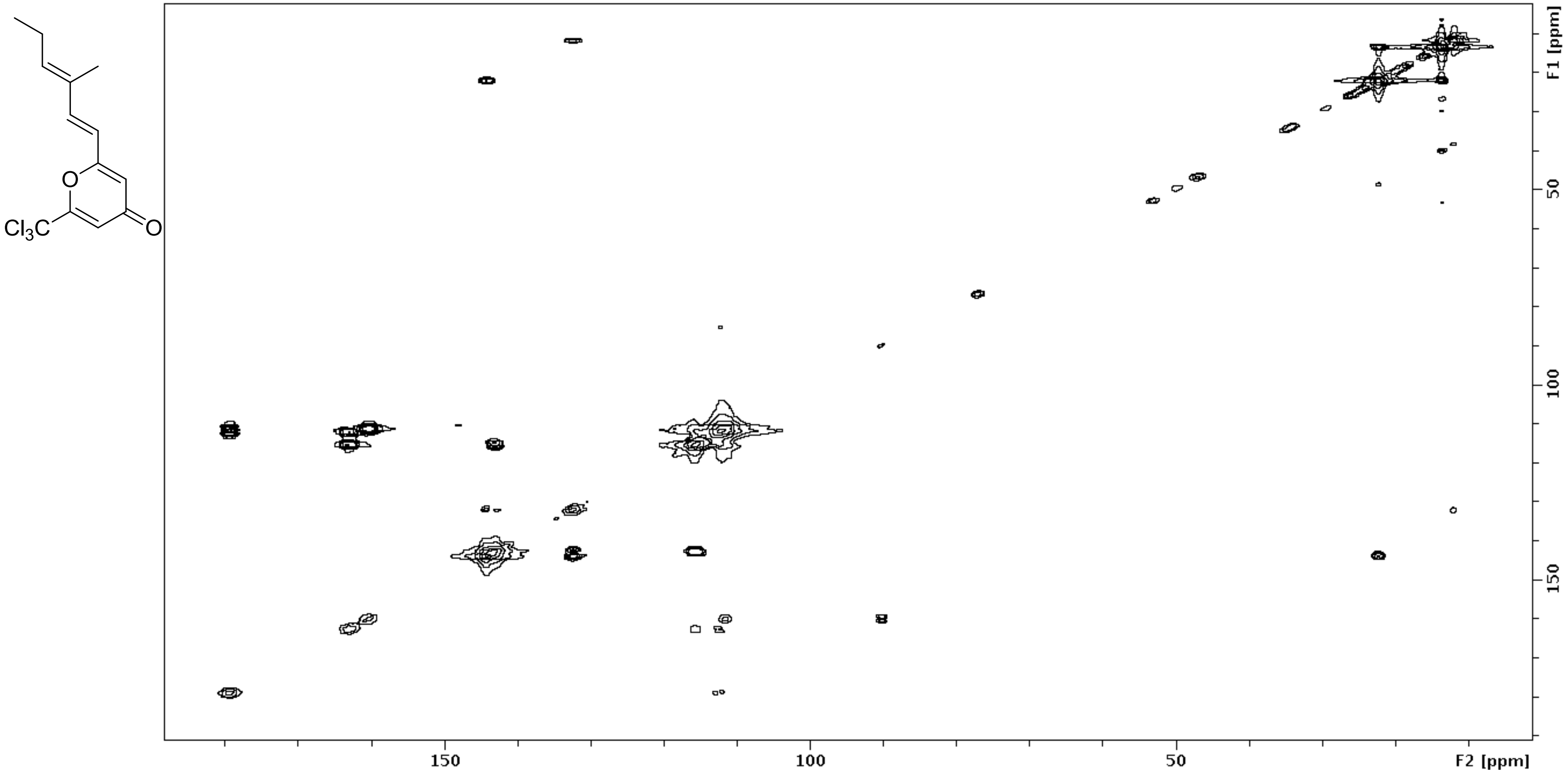

Figure A3.4. ^{13}C-^{13}C COSY NMR (125 MHz, CDCl$_3$) of ^{13}C-labeled halomadurone A (**58**)

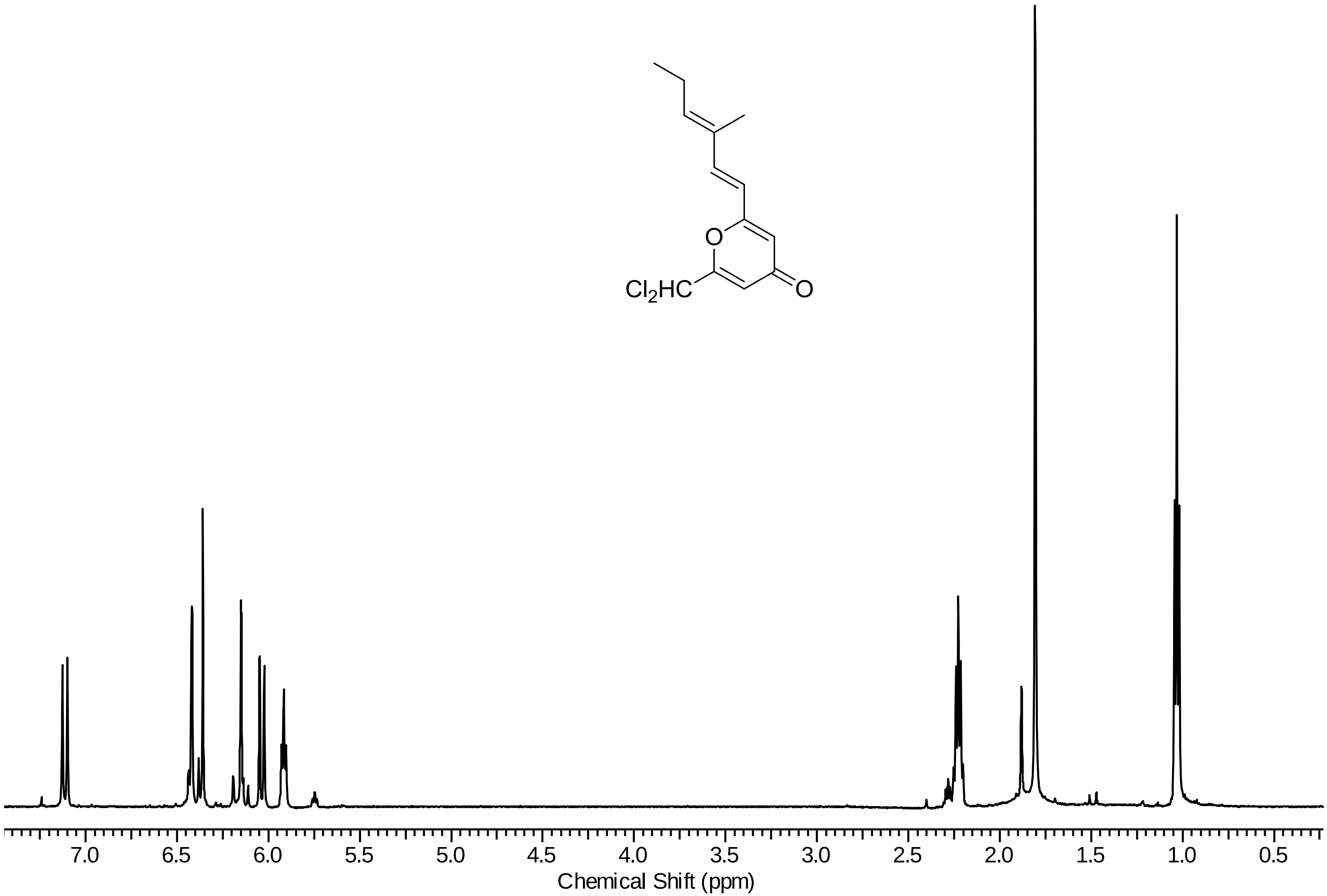

Figure A3.5. ^{1}H NMR (600 MHz, CDCl$_3$) of halomadurone B (**59**)

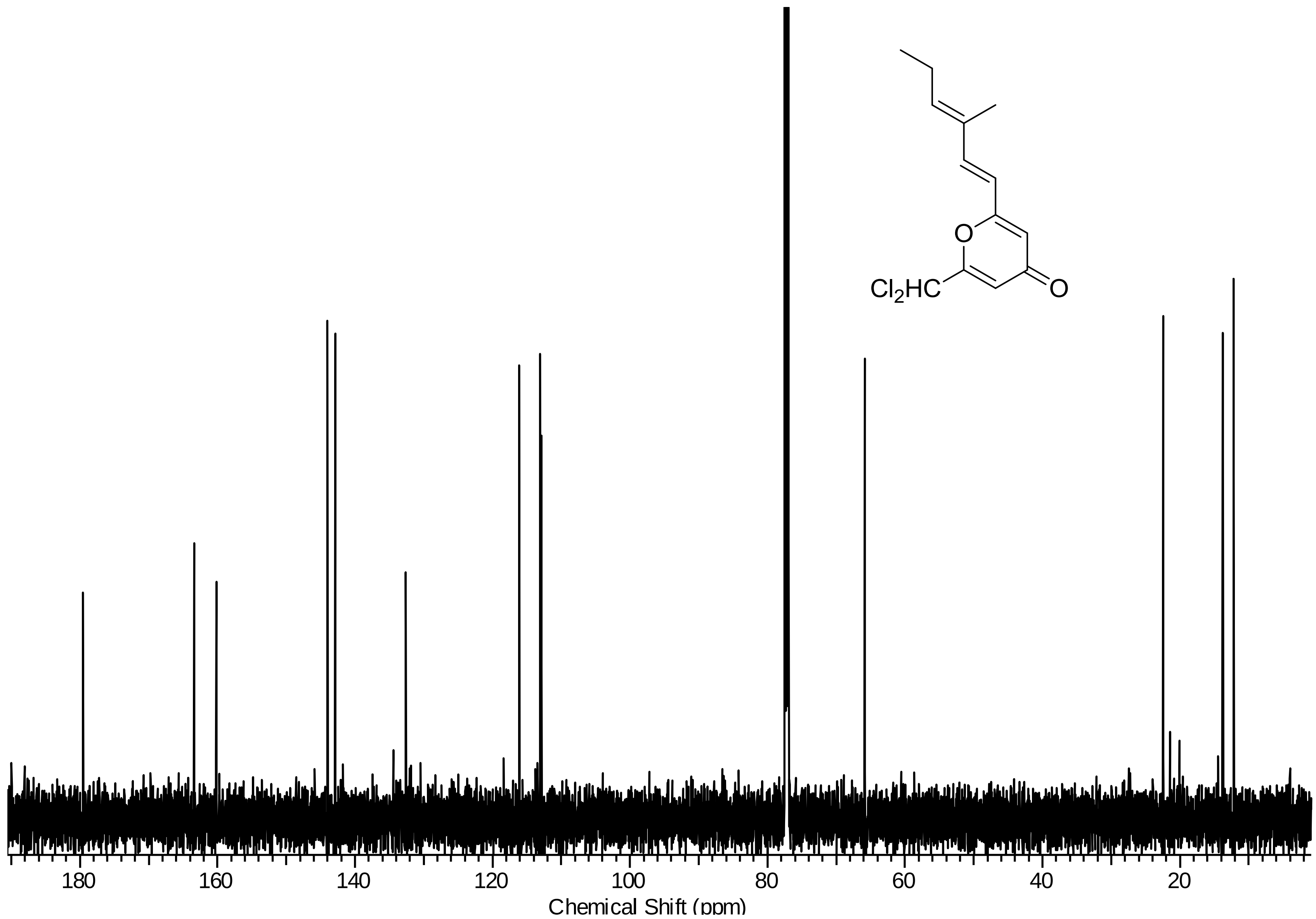

Figure A3.6. ^{13}C NMR (125 MHz, $CDCl_3$) of halomadurone B (**59**)

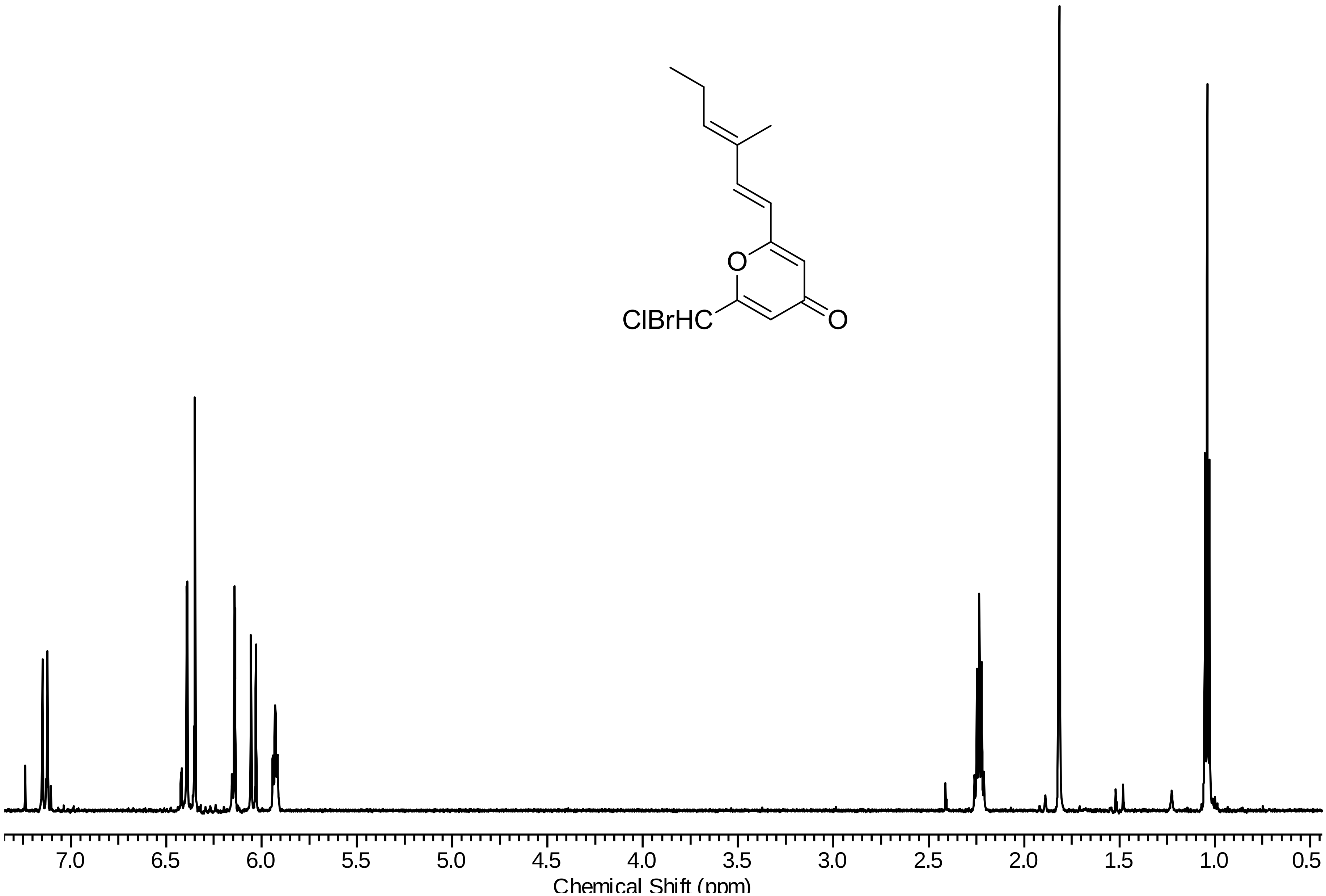

Figure A3.7. ^{1}H NMR (600 MHz, $CDCl_3$) of halomadurone C (**60**)

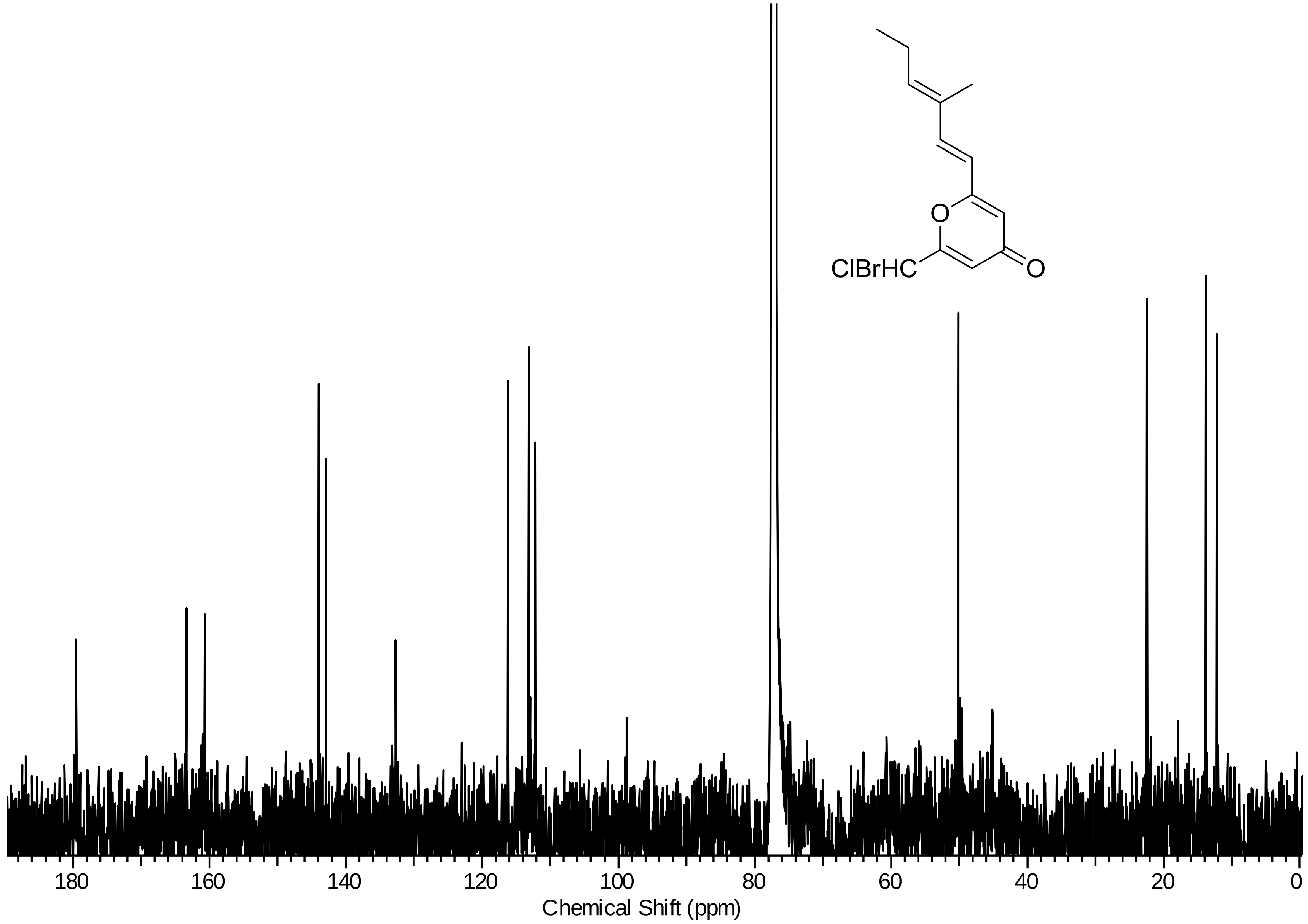

Figure A3.8. ^{13}C NMR (125 MHz, $CDCl_3$) of halomadurone C (**60**)

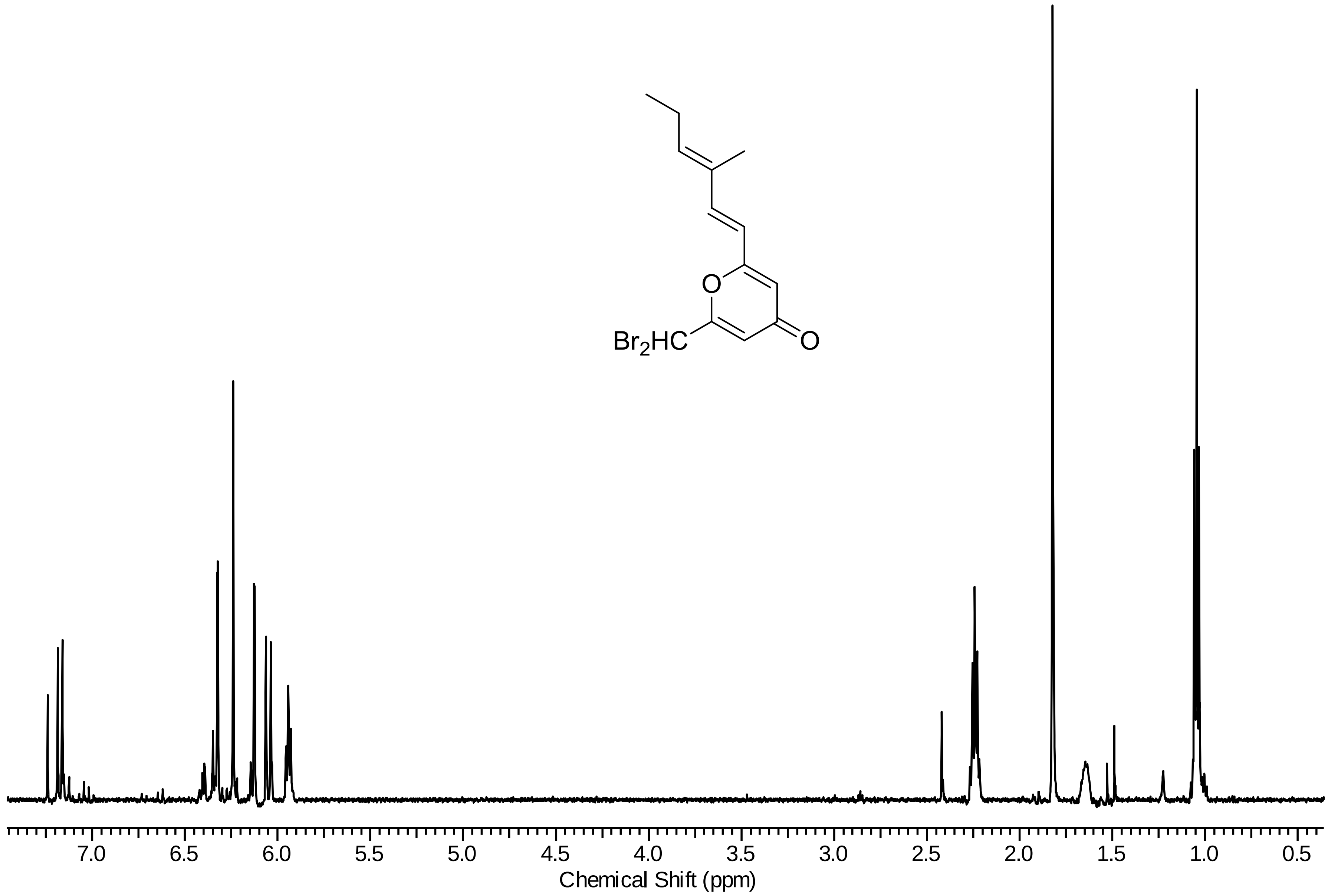

Figure A3.9. ^{1}H NMR (600 MHz, CDCl$_3$) of halomadurone D (**61**)

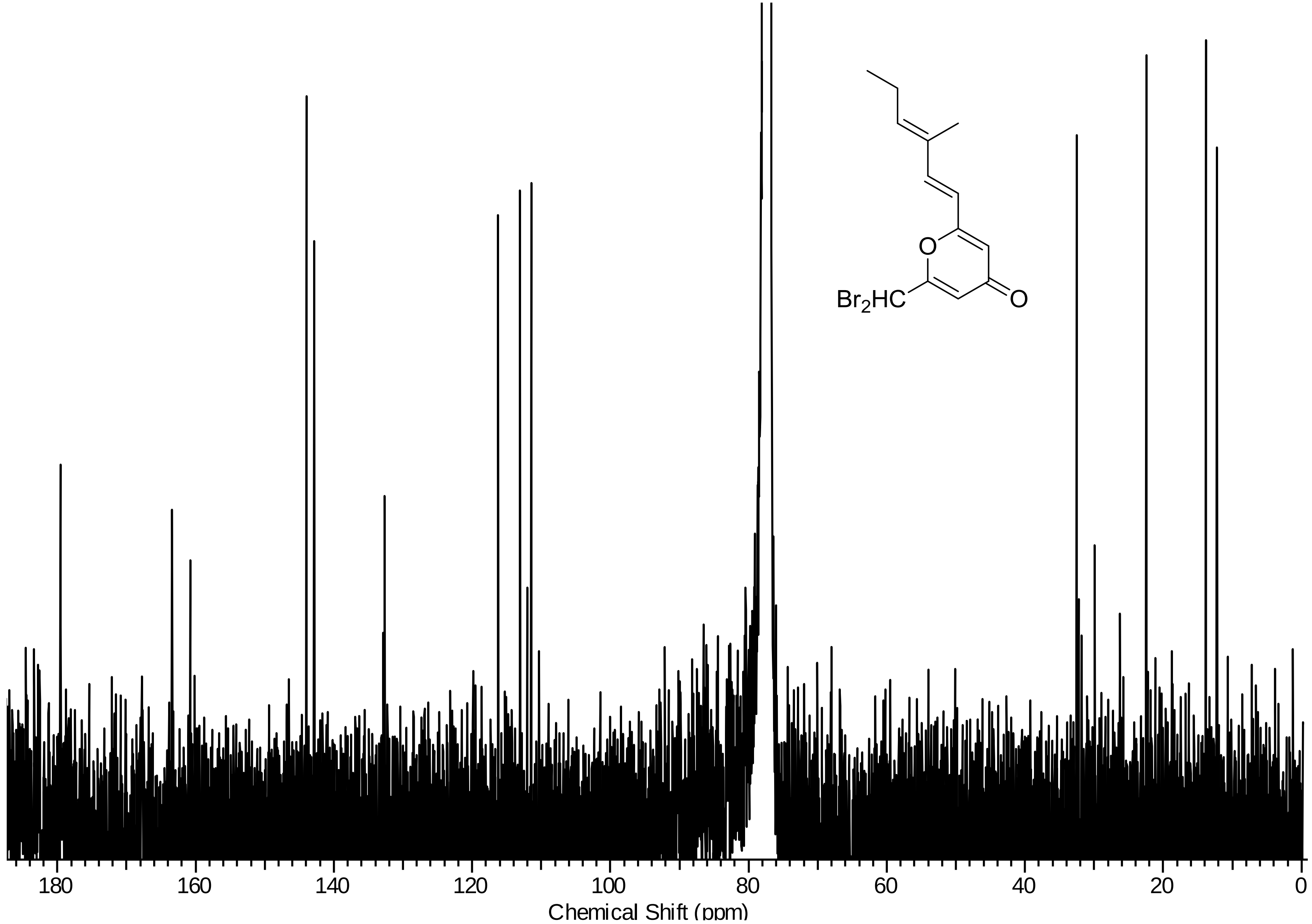

Figure A3.10. ^{13}C NMR (125 MHz, $CDCl_3$) of halomadurone D (**61**)

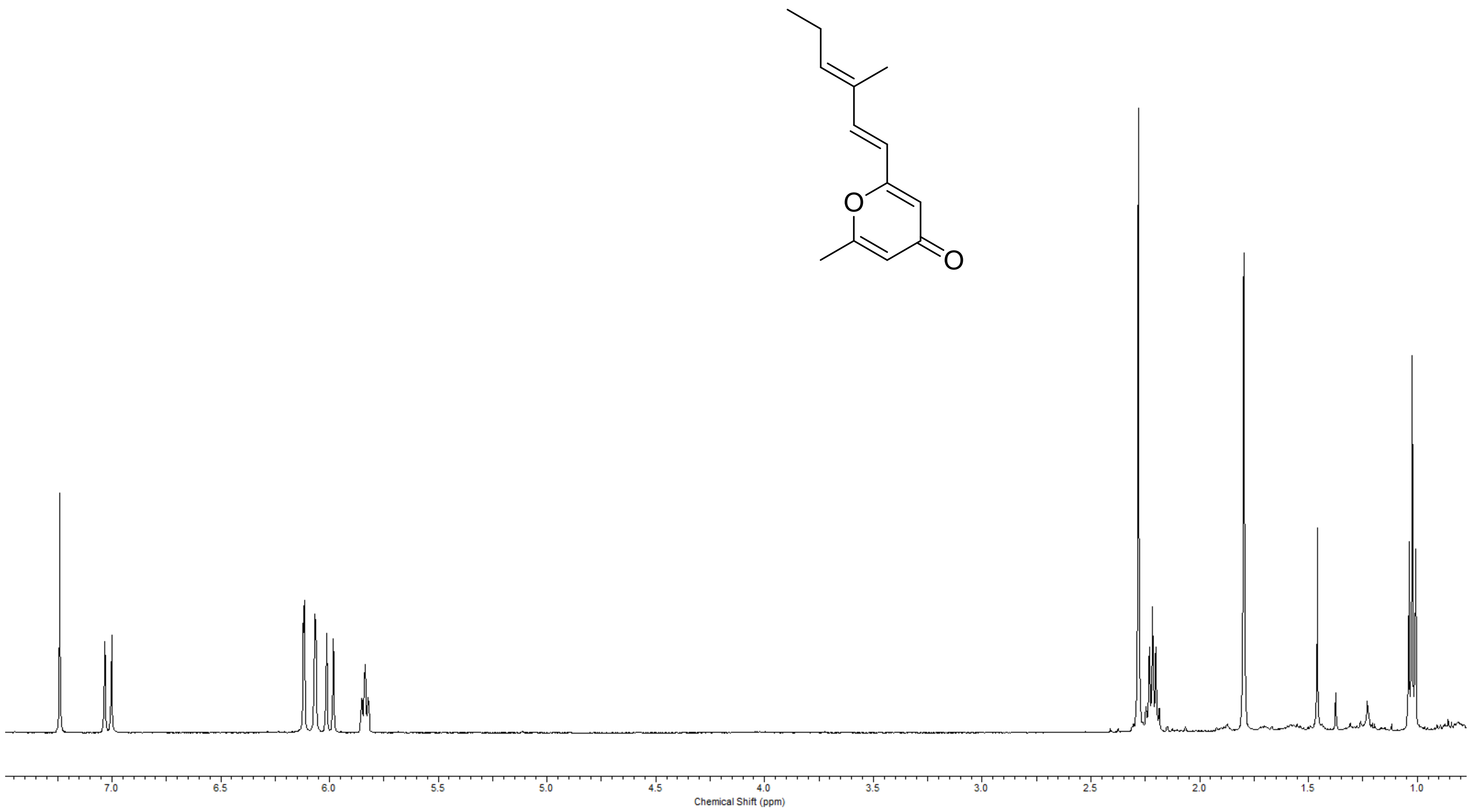

Figure A3.11. ^{1}H NMR (600 MHz, $CDCl_3$) of halomadurone synthetic analog (**62**)

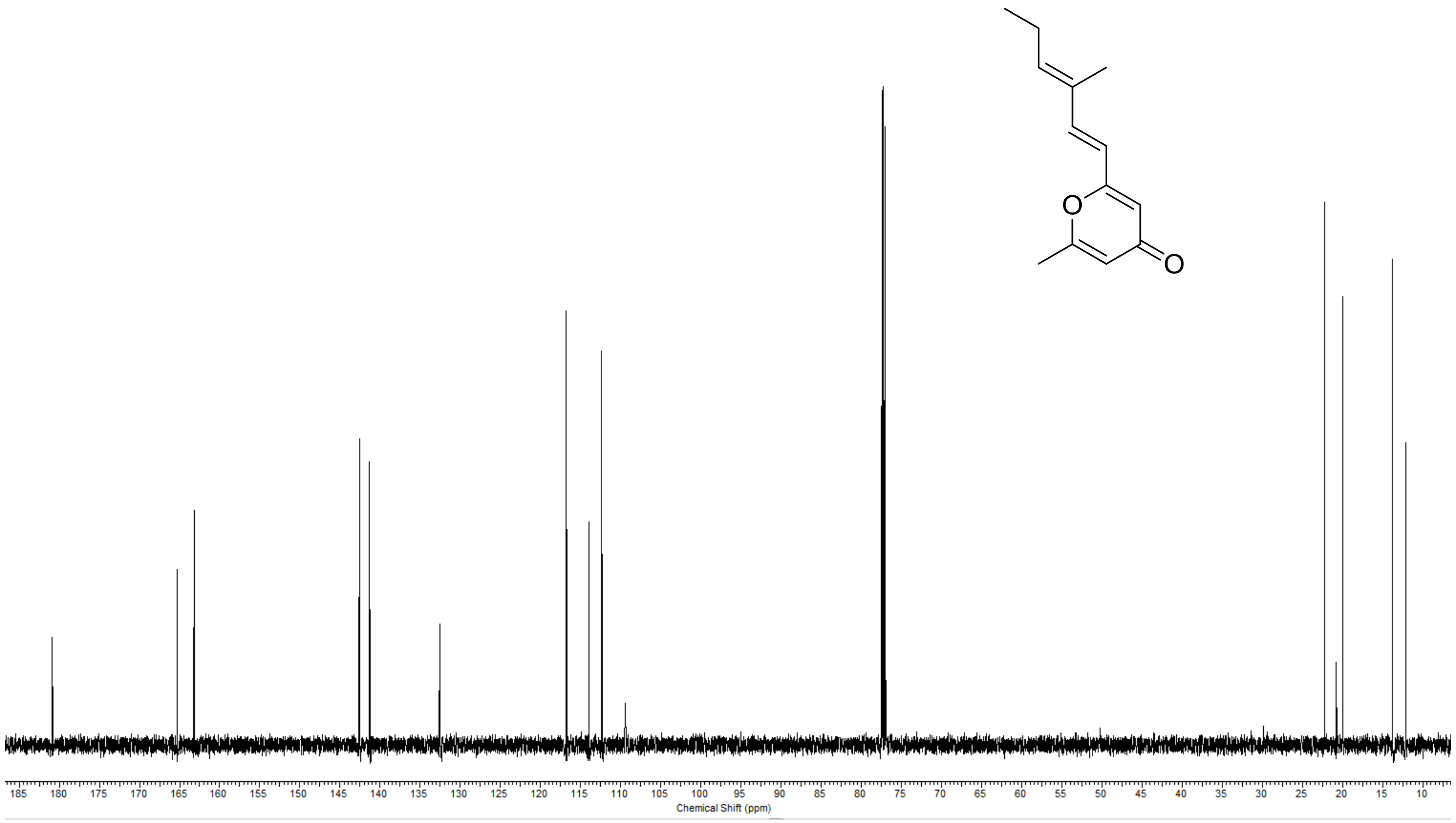

Figure A3.12. ^{13}C NMR (125 MHz, $CDCl_3$) of halomadurone synthetic analog (**62**)

Figure A3.13. ^{13}C-^{13}C gCOSY calculations

1. During t_1, each new fid increments t_1 by a dwell time of $dw1 = \frac{1}{sw1}$ (always true for each complex pair of FIDs, independent of type of acquisition, such as States or TPPI, etc.). For a ^{13}C–^{13}C cosy, $sw = sw1 \leq$ 220ppm, which = 125Hz/ppm×220ppm = 27.5kHz. Thus, $dw1$ = 1/27.5kHz = 36.4μs.

2. For J_{CC} ranging 30 to 60 Hz, maximum polarization transfer (largest crosspeak formation) will occur at 1/2J = 33 to 17 ms, respectively.

3. For an absolute-value cosy, where a sinebell or sinebell-squared apodization is applied, maximum crosspeaks (100% of the size of the ^{1}H 1D peak) will occur with a total acquisition time in the indirect dimension, $at1$ = 1/J, because sinebell-type functions are maximum at ½ the FID. So for maximum crosspeaks, the t_1 evolution would be at $at1$ = 66 to 33 ms, for J_{CC} = 30 to 60 Hz.

4. The total acquisition time in the indirect dimension equals the number of increments times the time per increment, or: $at1 = ni \times dw1$ Thus: $ni \equiv \mathrm{TD1} = \frac{at1}{dw1} = \frac{sw1}{J_{CC}}$ = 917 to 458 .

   Even smaller values (e.g., 256) can be used without much loss in sensitivity, since the crosspeaks intensities will follow something close to sinusoidal behavior close to 90°.

5. Resolution: If ni ≡ TD1 = 400, then sw1/ni = 27500/400 = 69 Hz = 0.55 ppm @ 500 MHz.

Figure A3.14. ^{13}C-^{13}C gCOSY pulse program (Bruker)

```
;cosygpqf - modified to have proton decoupling 2June2010
;avance-version (07/04/05)
;2D homonuclear shift correlation
;using gradient pulses for selection
;
;$CLASS=HighRes
;$DIM=2D
;$TYPE=
;$SUBTYPE=
;$COMMENT=

#include <Avance.incl>
#include <Grad.incl>

"d13=4u"

"d11=30m"

"in0=inf1"

"d0=3u"

1 ze
 d11 pl12:f2
2 30m do:f2
 d1 cpd2:f2
3 p1 ph1
 d0
 50u UNBLKGRAD
 p16:gp1
 d16
 p0 ph2
 p16:gp1
 d16
 4u BLKGRAD
 go=2 ph31
 30m do:f2 pl12:f2 mc #0 to 2 F1QF(id0)
exit

ph1=0 2
ph2=0 0 2 2
ph31=0 2
```

```
;pl1 : f1 channel - power level for pulse (default)
;p0 : f1 channel - 20 to 90 degree high power pulse
;p1 : f1 channel - 90 degree high power pulse
;p16: homospoil/gradient pulse
;d0 : incremented delay (2D) [3 usec]
;d1 : relaxation delay; 1-5 * T1
;d13: short delay [4 usec]
;d16: delay for homospoil/gradient recovery
;inf1: 1/SW = 2 * DW
;in0: 1/(1 * SW) = 2 * DW
;nd0: 1
;NS: 1 * n
;DS: 16
;td1: number of experiments
;FnMODE: QF

;use gradient ratio: gp 1
; 10
;for z-only gradients:
;gpz1: 10%
;use gradient files:
;gpnam1: SINE.100
;$Id: cosygpqf,v 1.5 2007/04/11 13:34:29 ber Exp $
```

Figure A3.15. Testing the Limits of the ^{13}C-^{13}C gCOSY with ^{13}C-labeled halomadurone A (**58**)

To determine the minimum amount of compound necessary to acquire the ^{13}C-^{13}C gCOSY, ^{13}C-labeled halomadurone A (**58**) was acquired for 18 hours (132 scans, 256 increments) on 200 µg (~3.7 mM) using a Bruker Avance 500 MHz spectrometer equipped with a ^{13}C/^{15}N\{^{1}H\} cryoprobe.

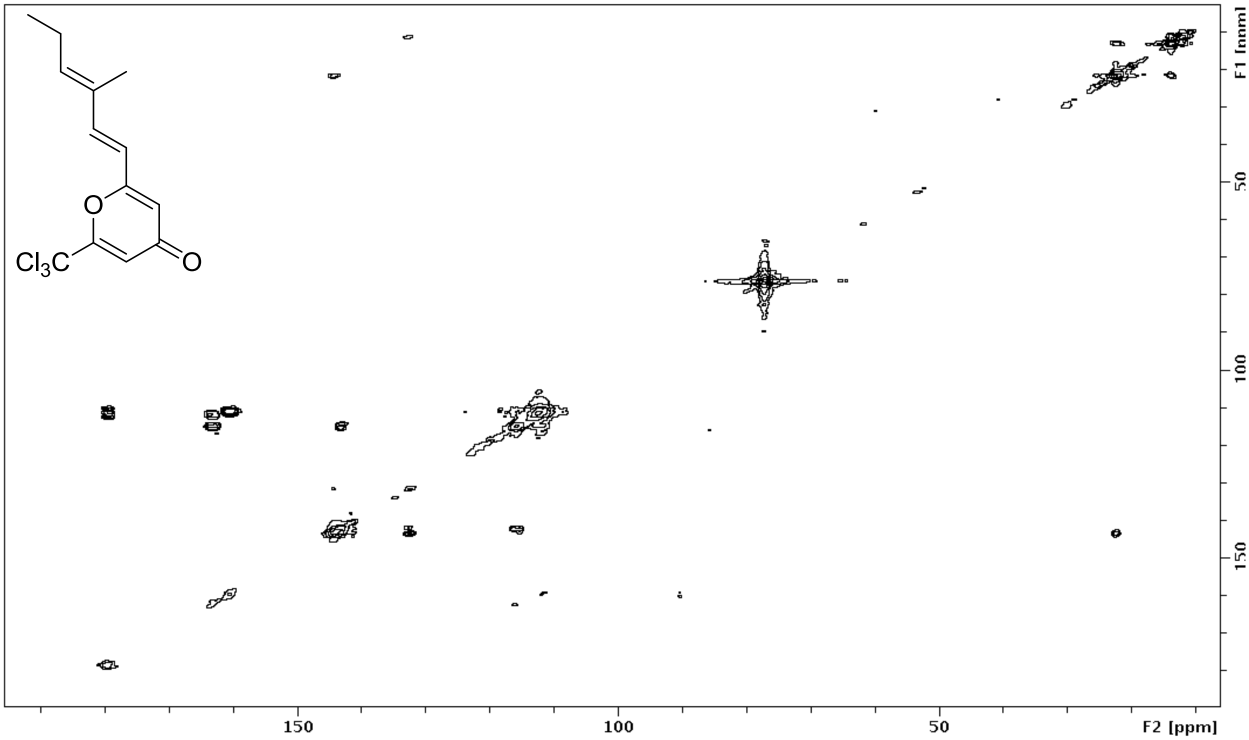

Figure A3.16. ^{13}C-^{13}C gCOSY for unlabeled halomadurone B (**59**)
(A) ^{13}C NMR of unlabeled halomadurone B. A 1D ^{13}C NMR spectrum was acquired on 5.3 mg of halomadurone B (0.11 M) in 175 μL $CDCl_3$ (3 mm tube) on a Bruker Avance 500 MHz spectrometer equipped with a ^{13}C/^{15}N{^{1}H} cryoprobe. For the spectrum shown, NS=32, D1=4. The experiment time was 2 minutes and appeared to have adequate signal-to-noise. (B) ^{13}C-^{13}C COSY of unlabeled halomadurone B. The same sample (0.11 M halomadurone B) was used to acquire a ^{13}C-^{13}C COSY. With NS=96 and 256 increments (14 hour experiment time), no cross-peaks were observed in the ^{13}C-^{13}C COSY.

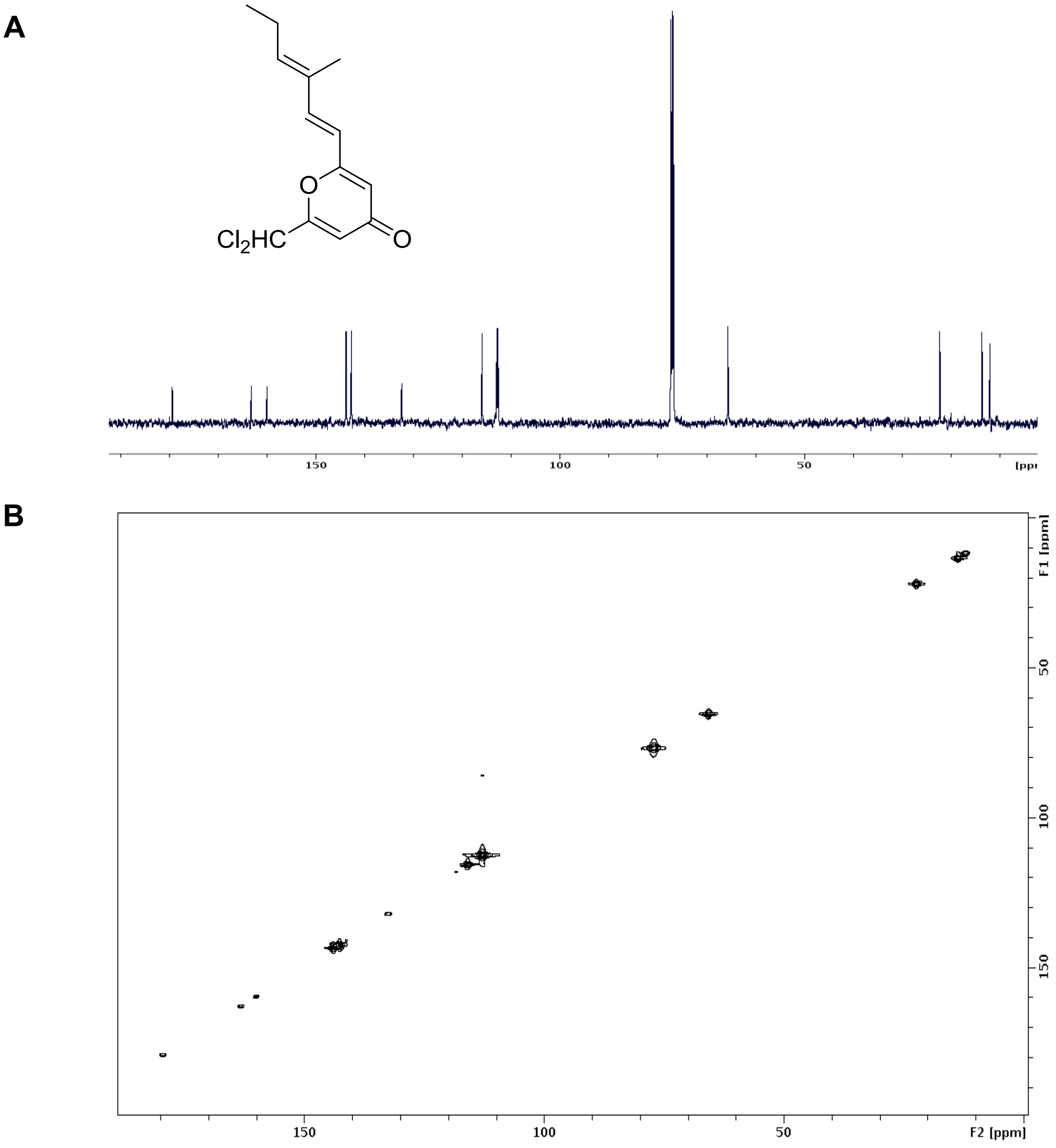

Figure A3.17. 2D INADEQUATE of ^{13}C-labeled halomadurone B (**59**)

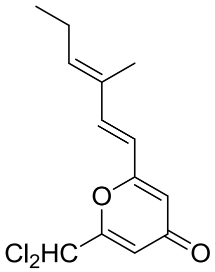

A 2D INADEQUATE (NS=32) was acquired on 1.1 mg ^{13}C-labeled halomadurone B (**59**).

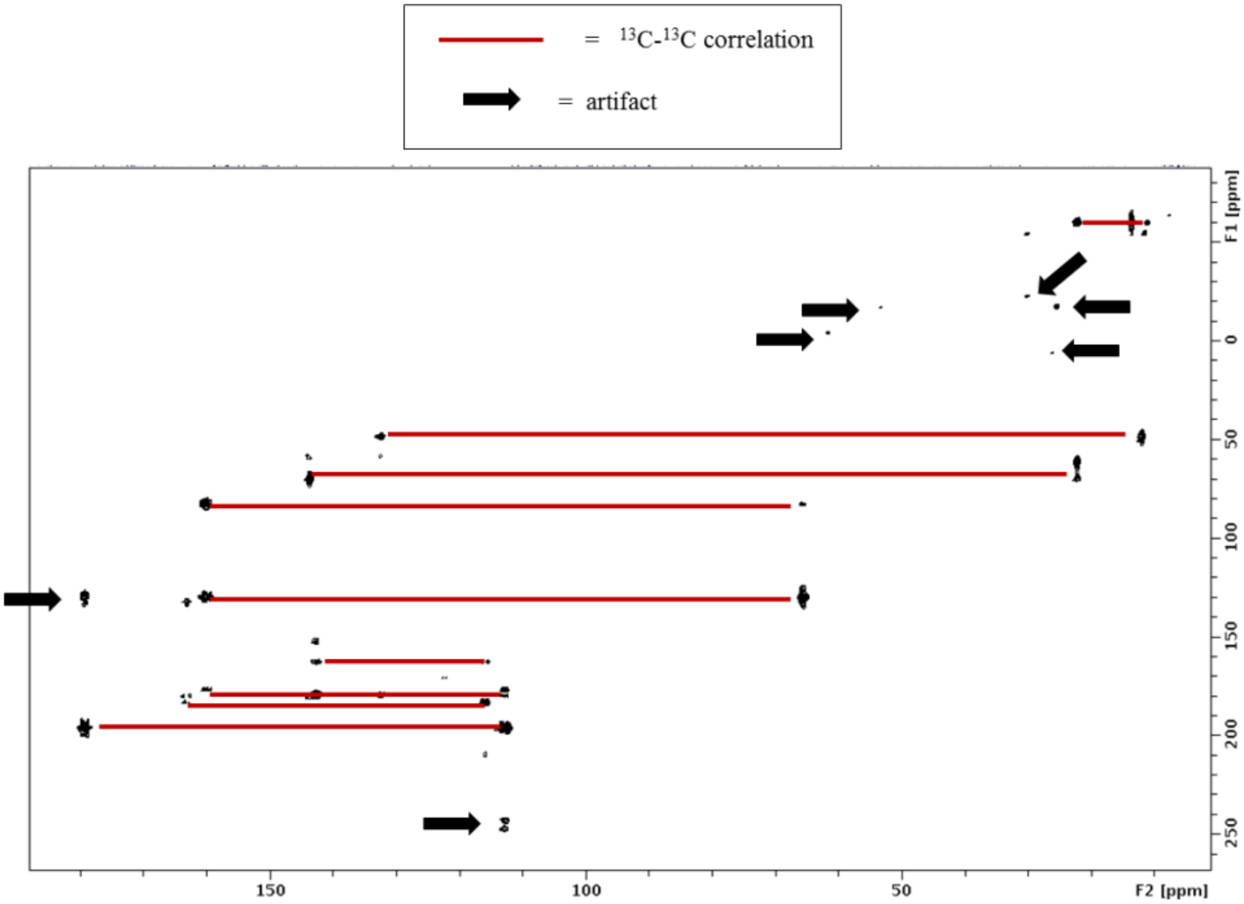

Figure A3.18. ^{13}C-^{13}C gCOSY (NS=32) of ^{13}C-labeled halomadurone B (**59**)

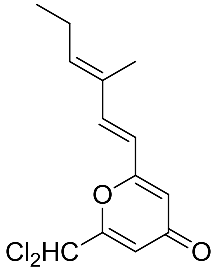

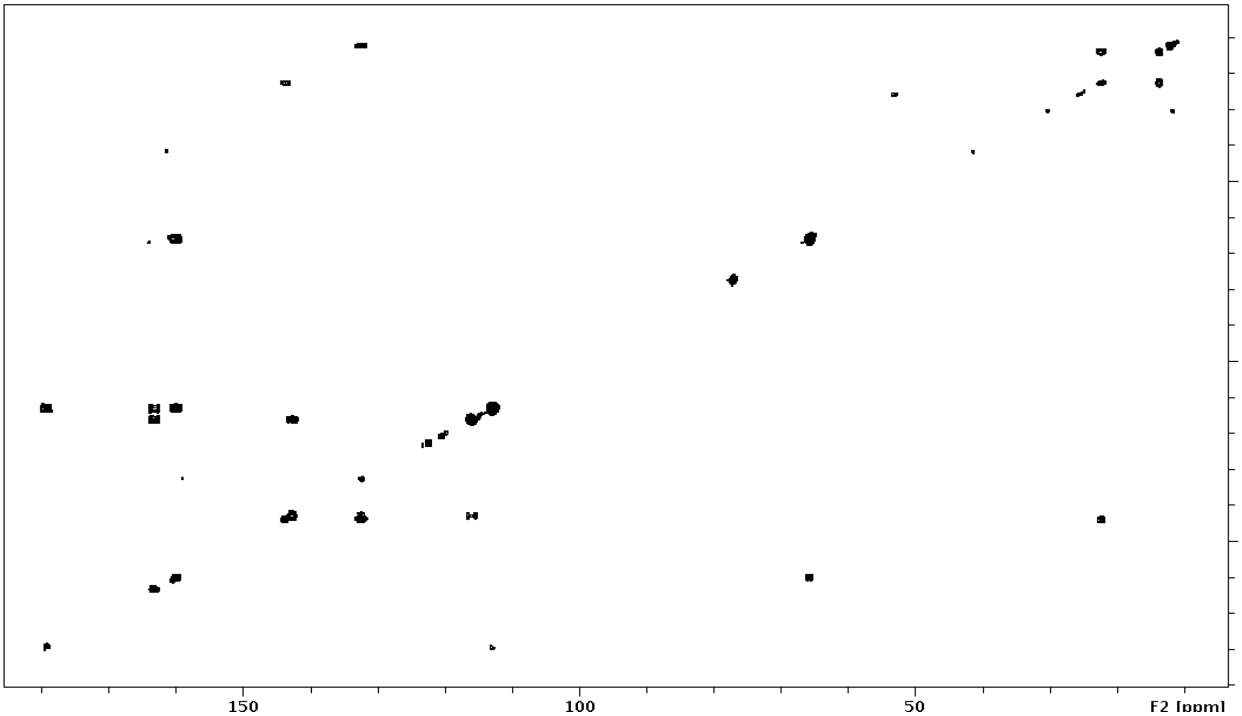

Figure A3.19. ^{13}C-^{13}C gCOSY (NS=4) of ^{13}C-labeled halomadurone B (**59**)

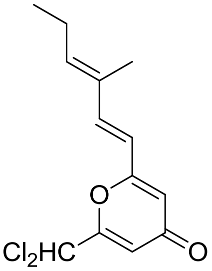

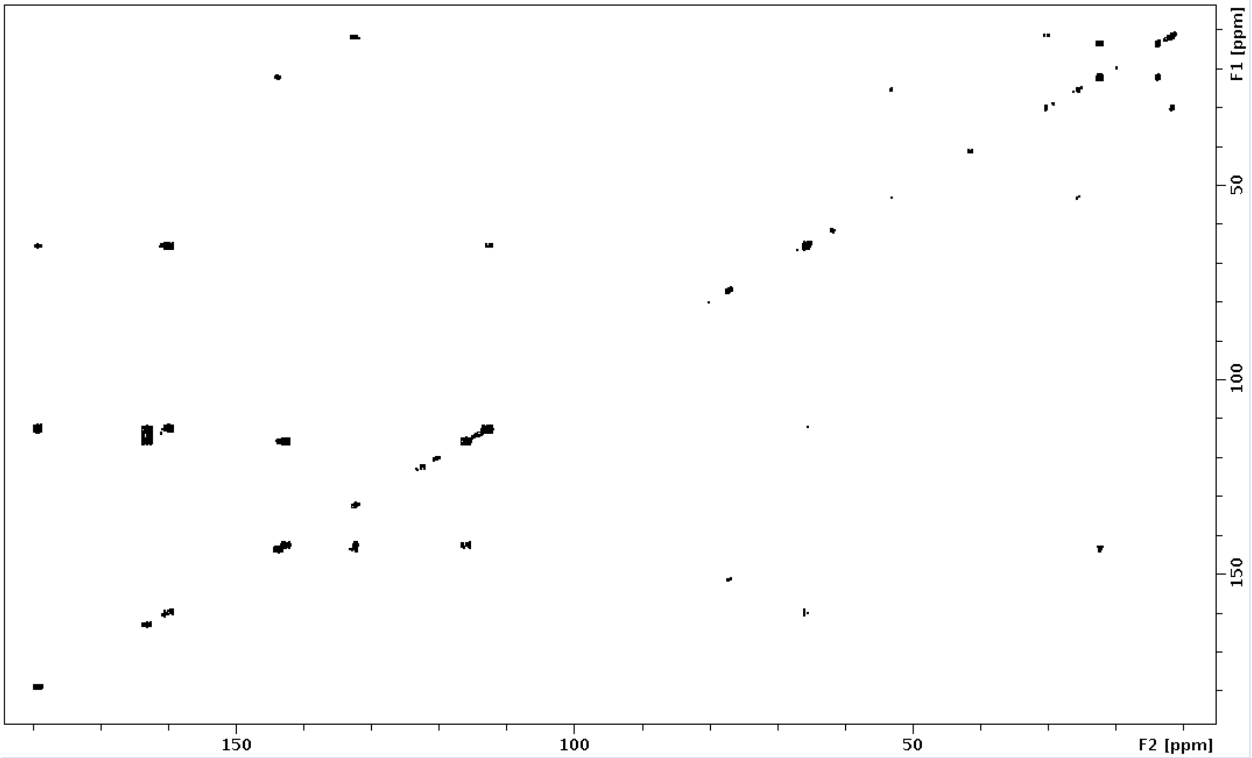

Figure A3.20. ^{13}C-^{13}C gCOSY (NS=175) of ^{13}C-labeled halomadurone B (**59**)

A ^{13}C-^{13}C COSY was acquired on 1.9 mg ^{13}C-labeled halomadurone B (**59**) in 12 hours on a Varian 500 MHz spectrometer with 5 mm room temperature probe.

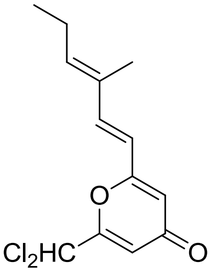

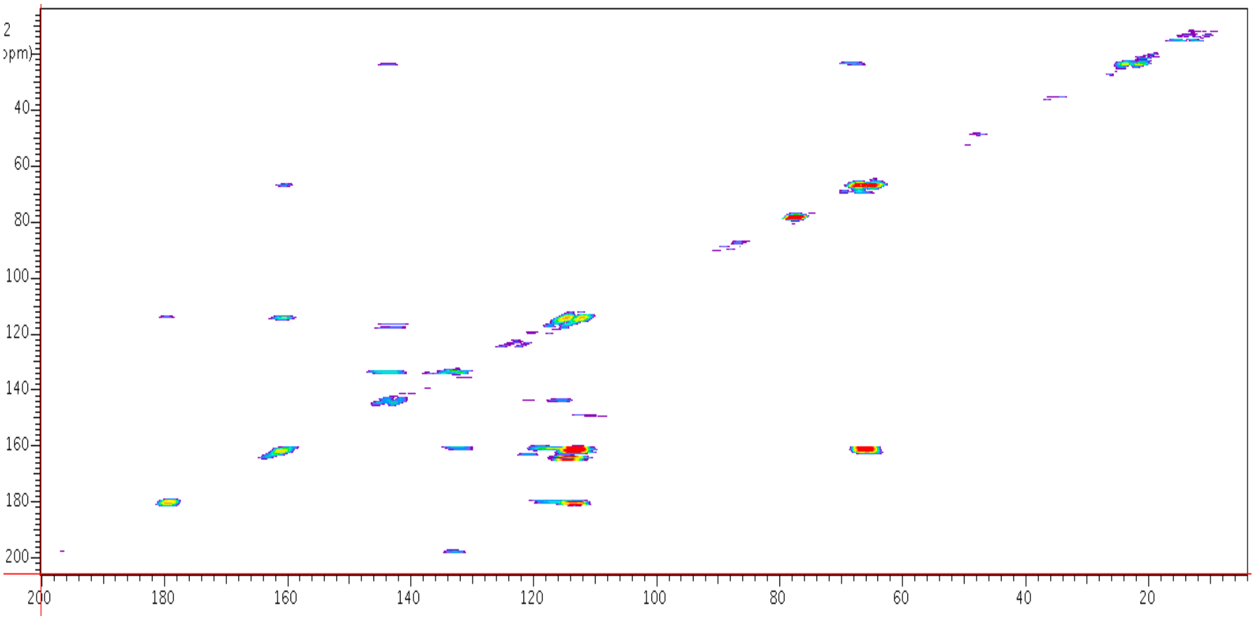

Appendix 4:

Supplementary Data for Chapter 6

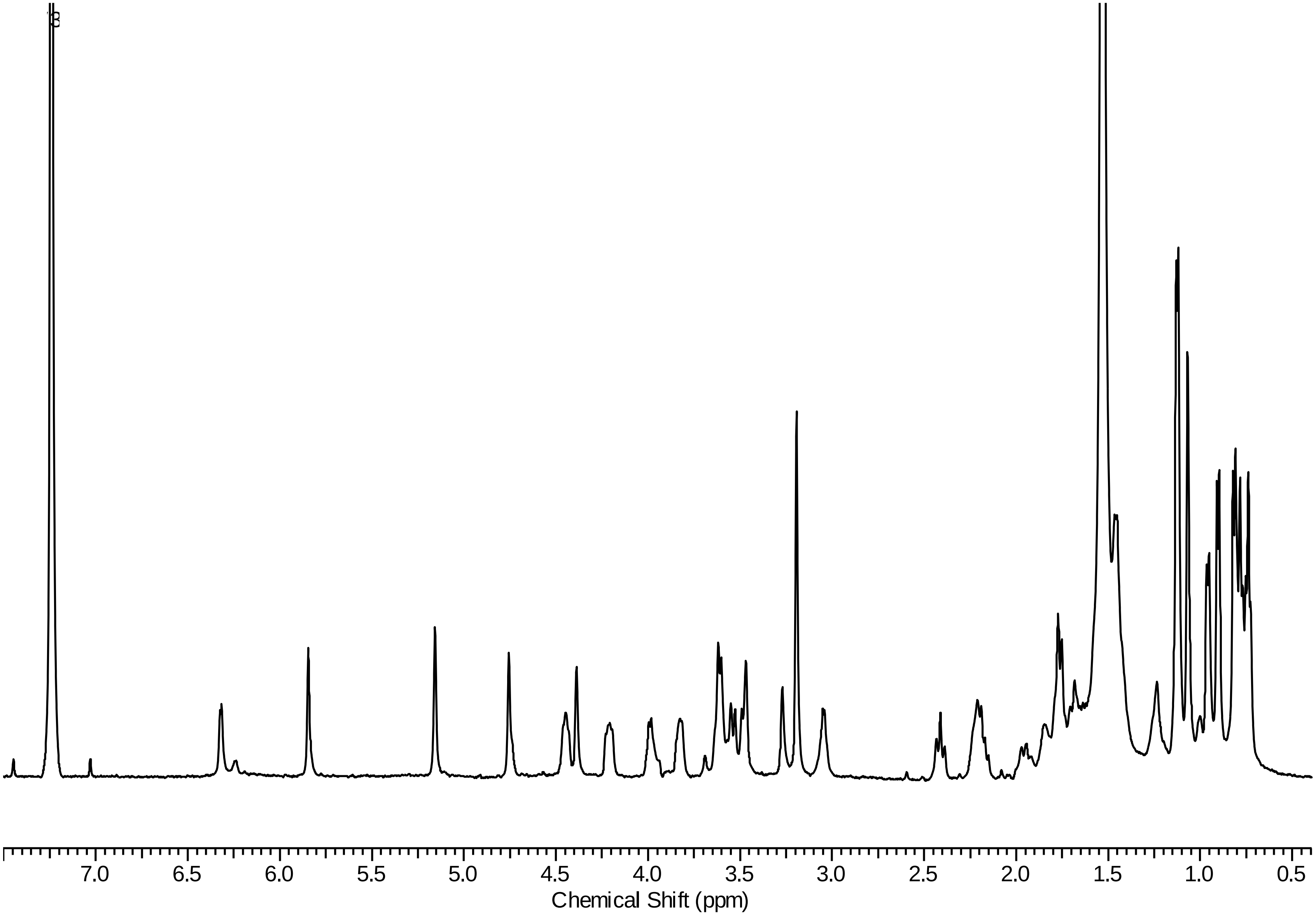

Figure A4.1. ^{1}H NMR (600 MHz, $CDCl_3$) of ecteinamycin (**65**)

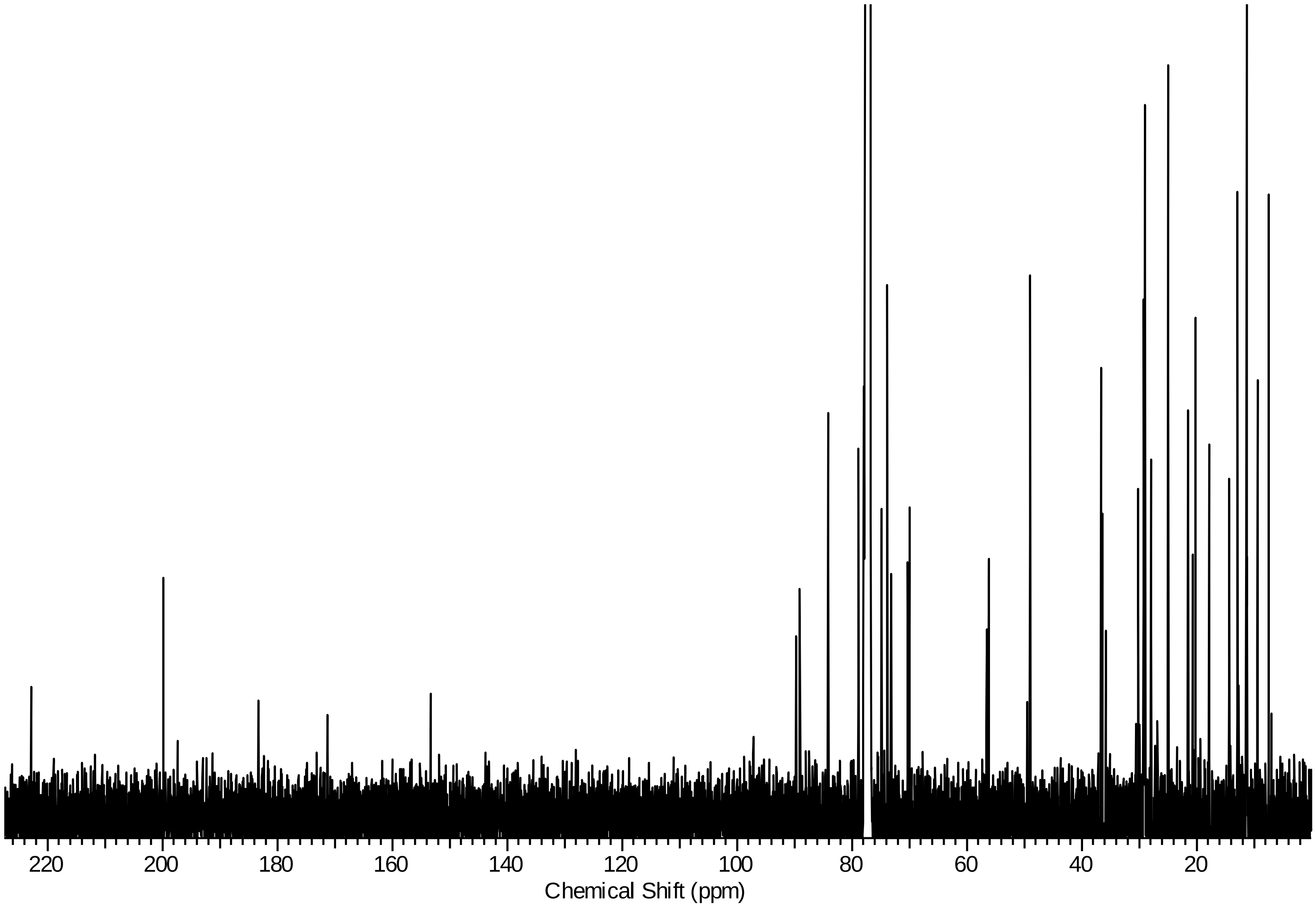

Figure A4.2. ^{13}C NMR (125 MHz, $CDCl_3$) of ecteinamycin (**65**)

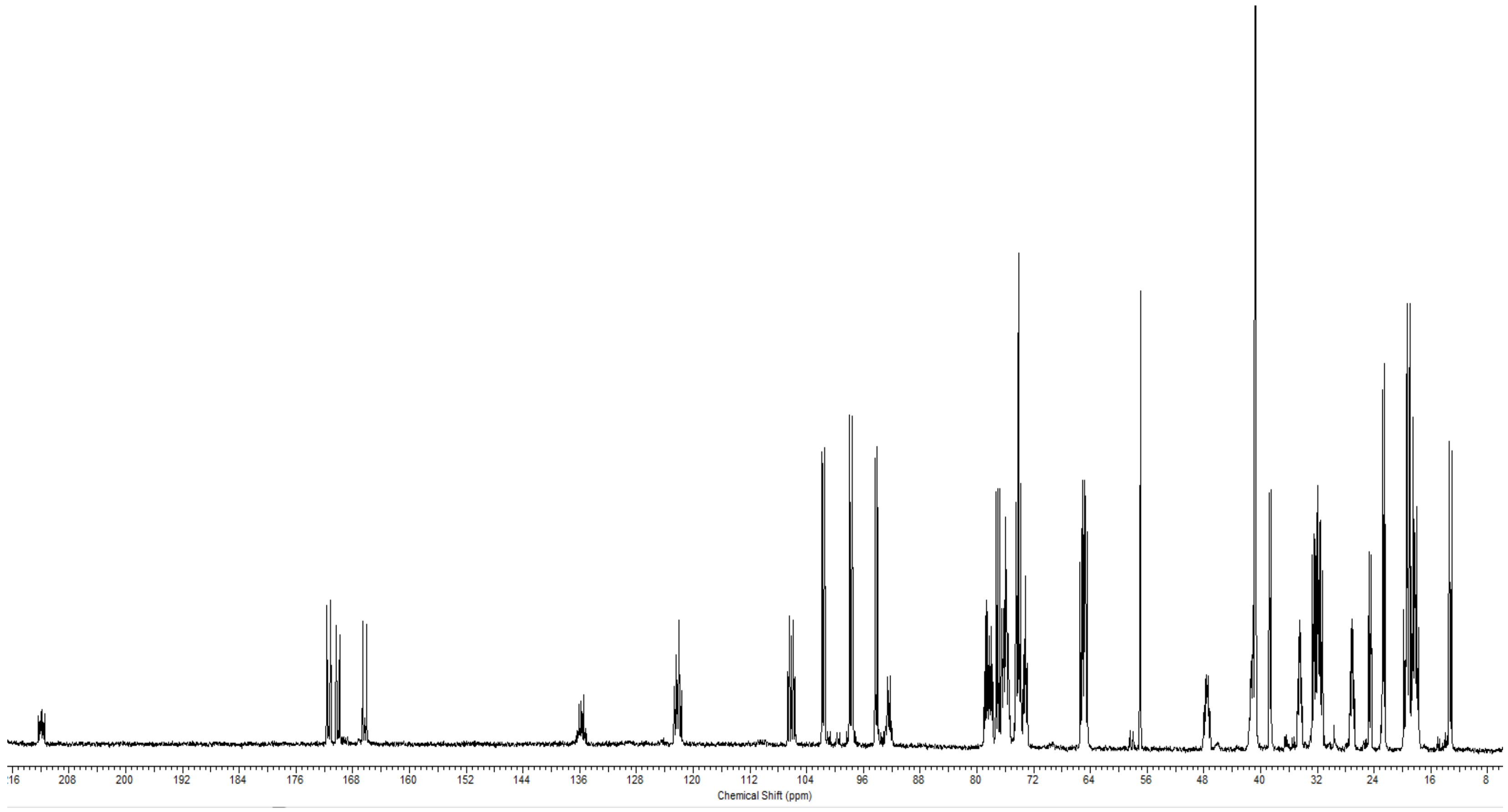

Figure A4.3. ^{13}C NMR (125 MHz, $CDCl_3$) of ^{13}C-labeled ecteinamycin (**65**)

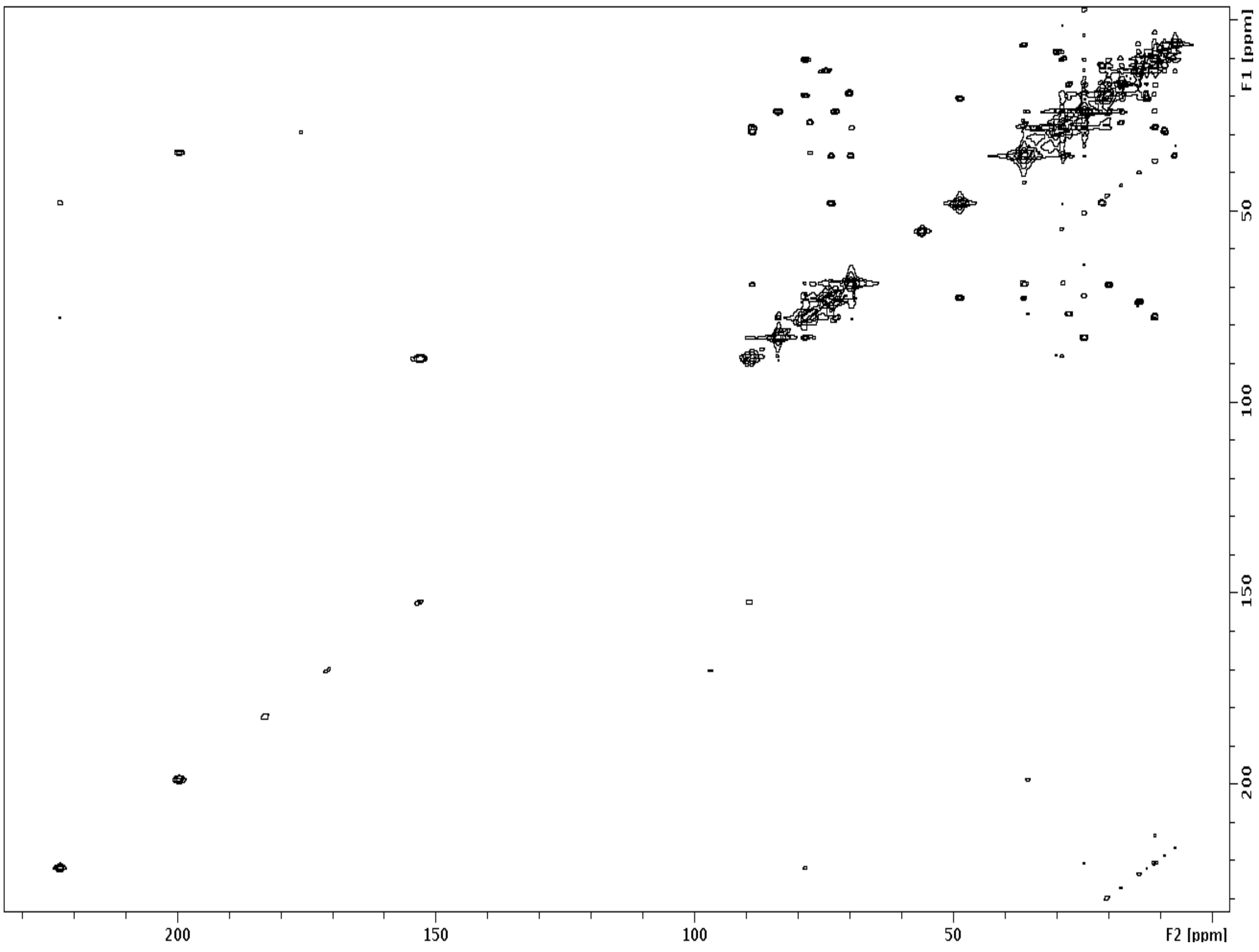

Figure A4.4. ^{13}C-^{13}C COSY NMR (125 MHz, CDCl$_3$) of ^{13}C-labeled ecteinamycin (**65**)

Appendix 5:

Supplementary Data for Chapter 7

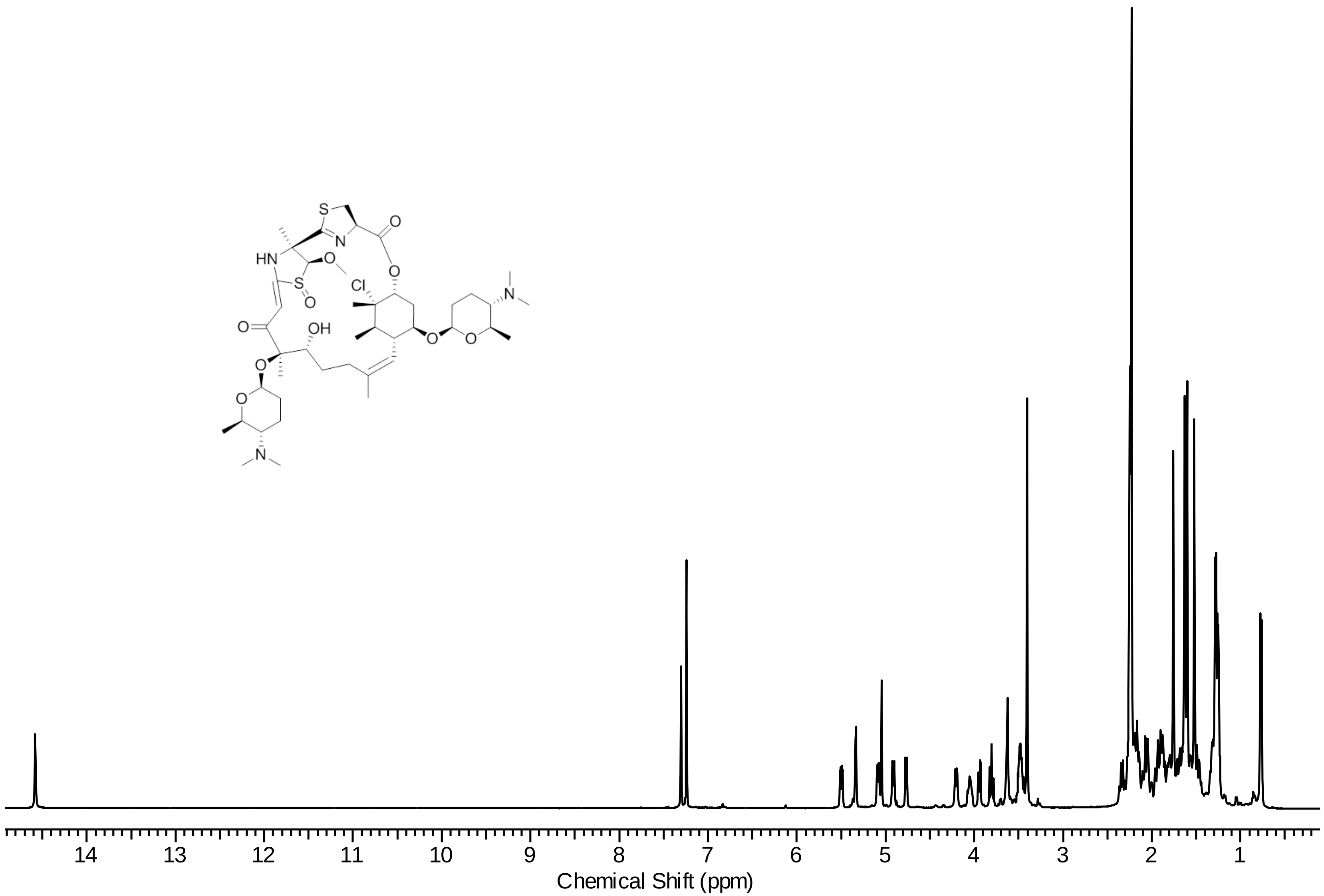

Figure A5.1. ^{1}H NMR (600 MHz, $CDCl_3$) of forazoline A (**72**)

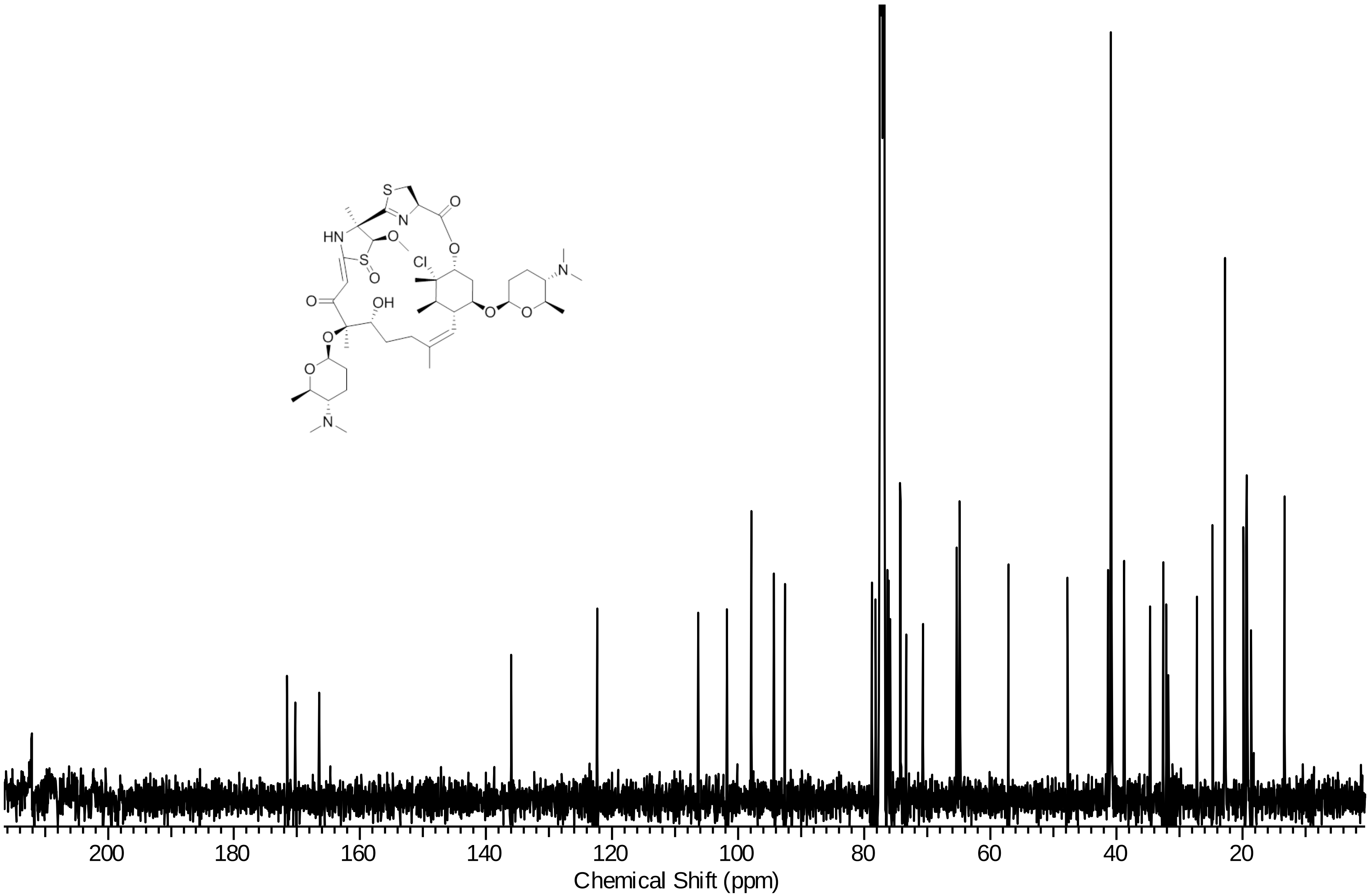

Figure A5.2. ^{13}C NMR (125 MHz, $CDCl_3$) of forazoline A (**72**)

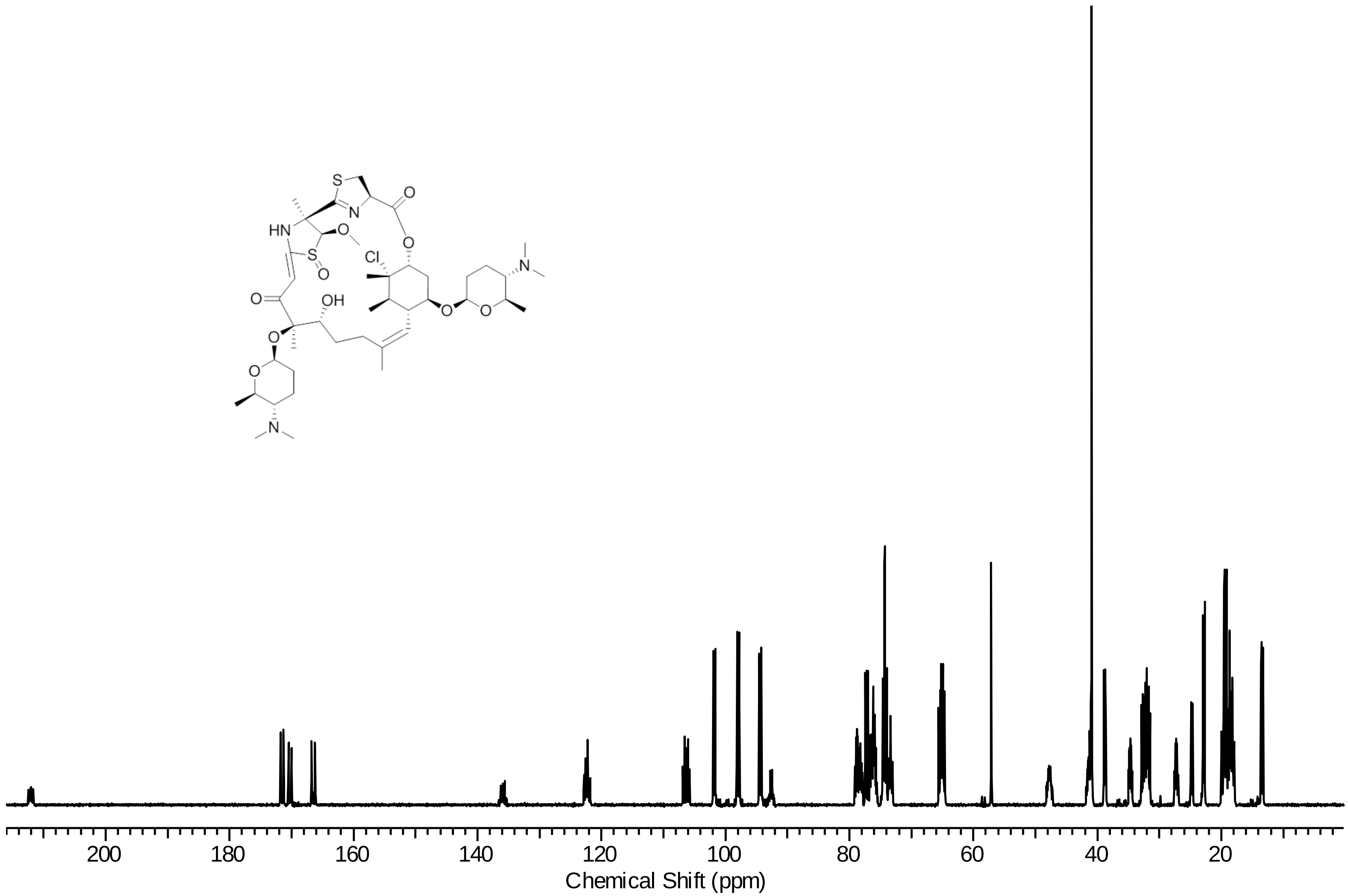

Figure A5.3. ^{13}C NMR (125 MHz, $CDCl_3$) of ^{13}C-labeled forazoline A (**72**)

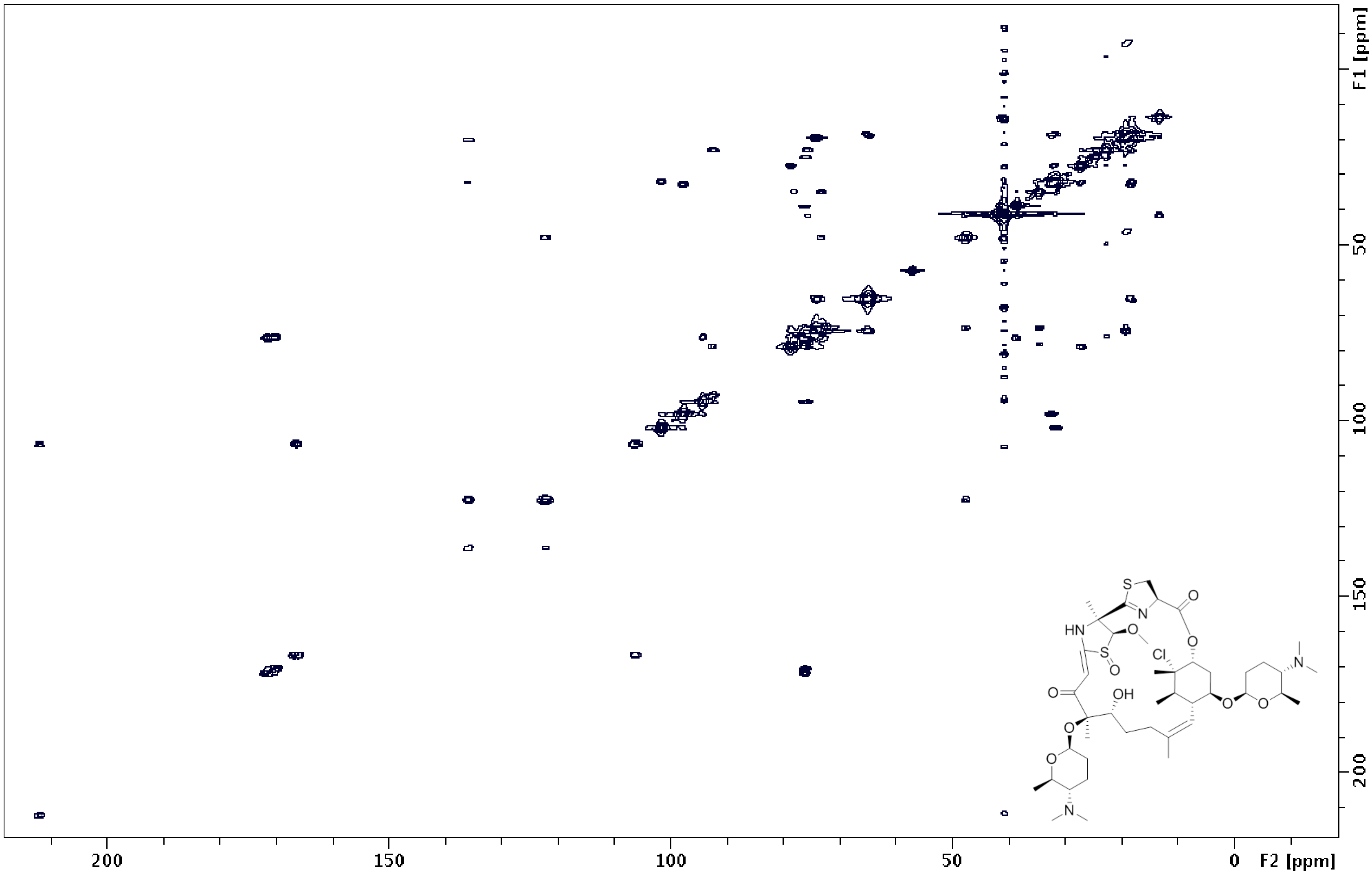

Figure A5.4. ^{13}C-^{13}C COSY NMR (125 MHz, $CDCl_3$) of ^{13}C-labeled forazoline A (**72**)

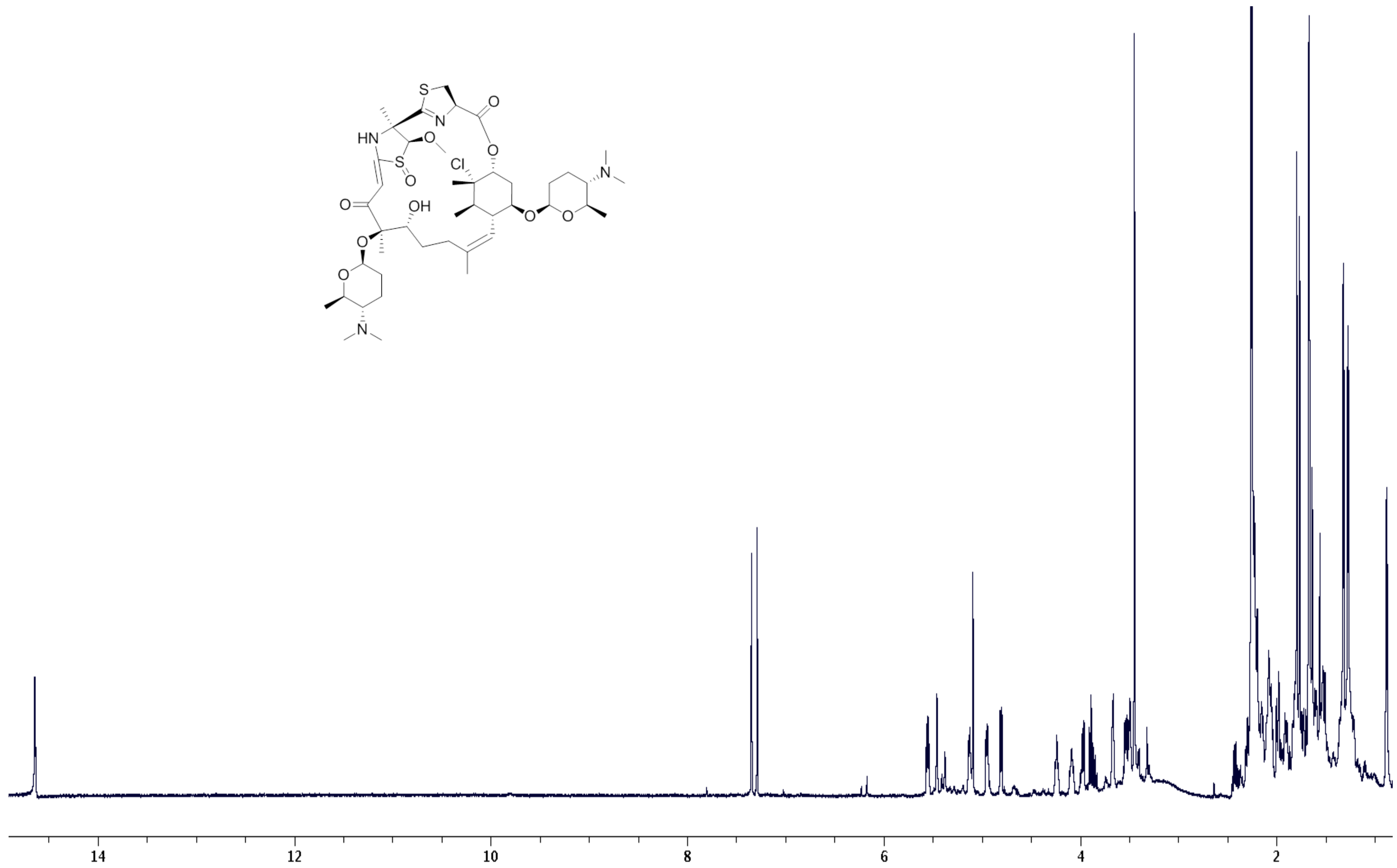

Figure A5.5. ^{1}H NMR (600 MHz, $CDCl_3$) of forazoline B (**73**)

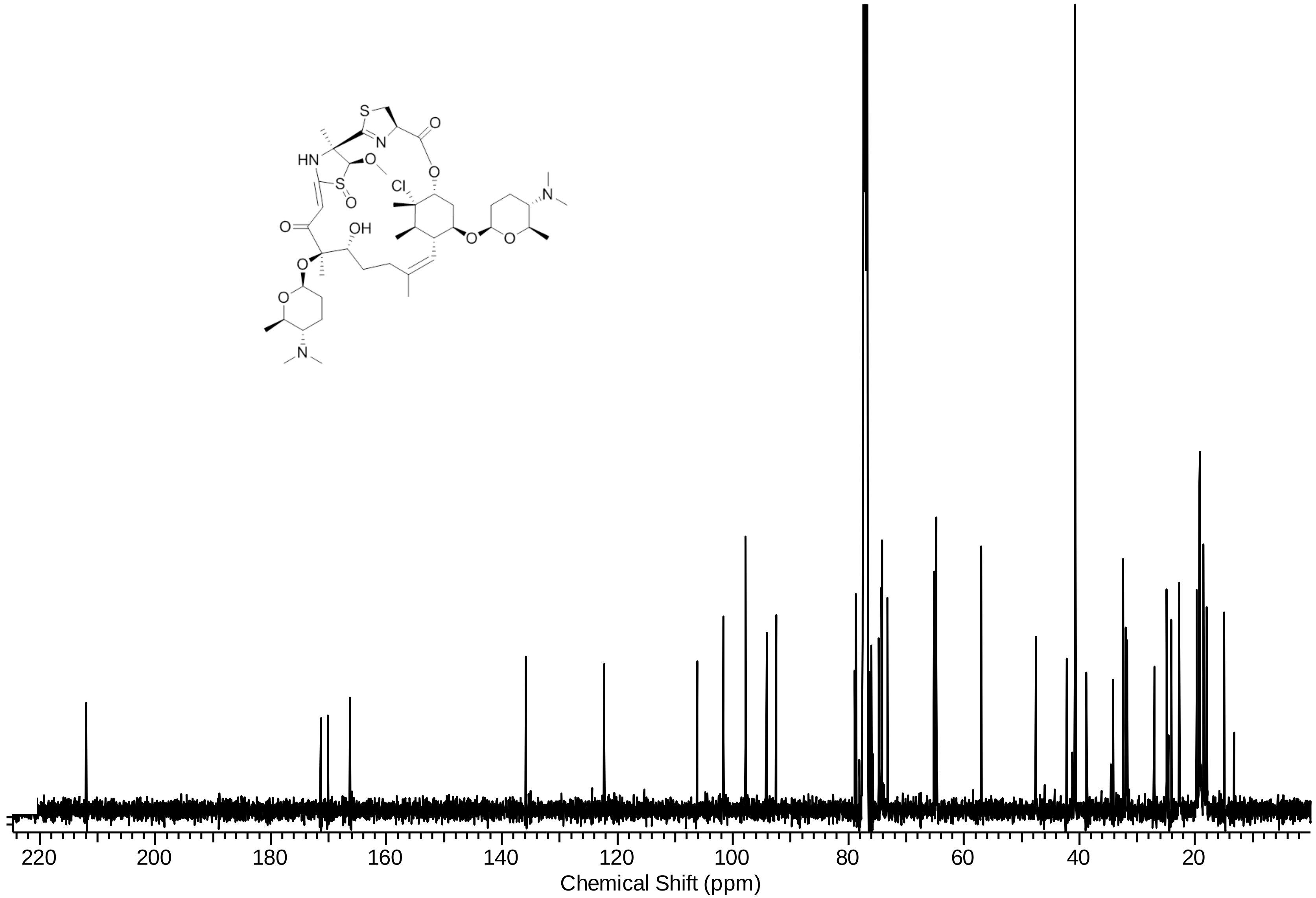

Figure A5.6. ^{13}C NMR (125 MHz, $CDCl_3$) of forazoline B (**73**)

Figure A5.7. ICP-AES of forazoline A (**72**)

A.

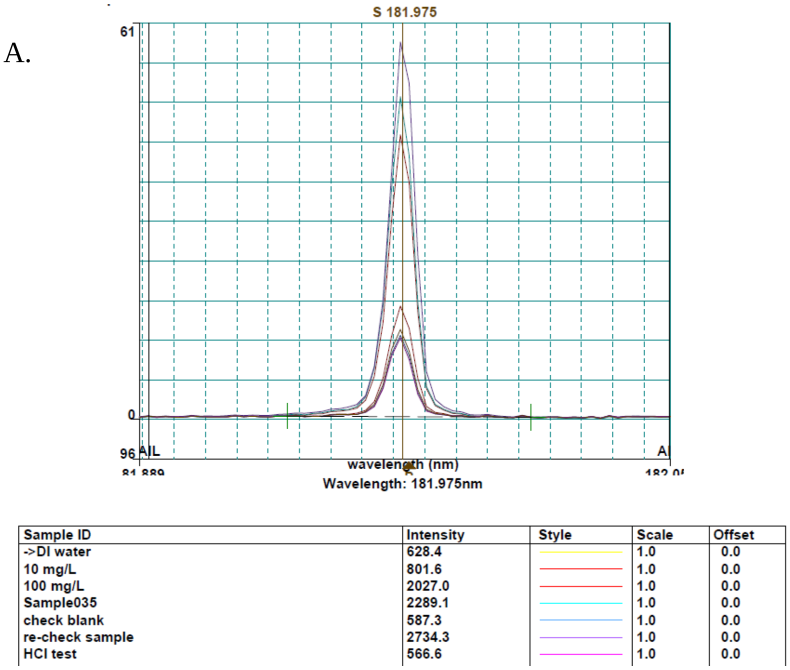

Sample ID	Intensity	Style	Scale	Offset
->DI water	628.4	—	1.0	0.0
10 mg/L	801.6	—	1.0	0.0
100 mg/L	2027.0	—	1.0	0.0
Sample035	2289.1	—	1.0	0.0
check blank	587.3	—	1.0	0.0
re-check sample	2734.3	—	1.0	0.0
HCl test	566.6	—	1.0	0.0

B.

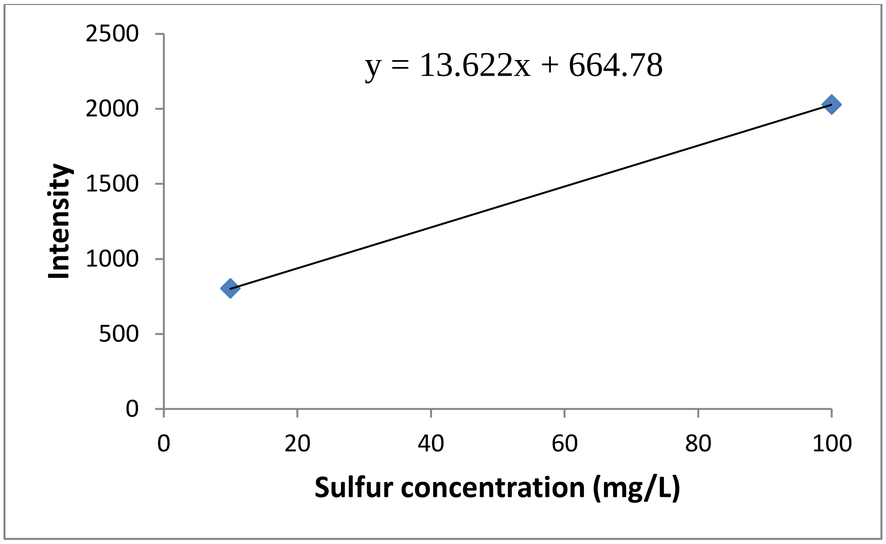

A. ICP analysis of forazoline A (**72**) with known concentrations of sulfur standards (10 and 100 mg/L).
B. A calibration curve was constructed based on the ICP intensity and sulfur standard concentrations. By inputting the ICP intensity of sulfur (2289.1) for forazoline A (**72**) into the equation, the concentration of sulfur could be determined (119.24 mg/L), converted to amount in that particular sample (1.19 mg), and atoms per molecule (~2).

Figure A5.8. DFT Calculations for sulfoxide location determination

	Measured	A (calcd)	B (calcd)	C (calcd)	D (calcd)
Position	δ_C, mult.	δ_C, mult.	δ_C, mult.	δ_C, mult.	δ_C, mult.
1	40.9	44.5	44.4	44.6	44.6
2	40.9	36.4	36.4	37.0	36.4
3	65.0	65.4	65.3	66.1	65.5
4	74.2	75.3	75.1	73.7	75.2
5	19.4	19.7	19.8	20.0	20.0
6	18.7	20.4	20.2	20.3	20.3
7	32.6	33.6	34.3	33.1	33.9
8	97.9	99.2	99.5	97.0	100.0
9	92.6	90.4	91.4	89.4	90.8
10	22.8	26.2	29.3	24.9	29.3
11	78.8	78.2	77.4	77.6	78.1
12	27.3	32.9	36.2	32.5	35.6
13	32.1	31.8	35.9	31.2	36.4
14	136.0	145.2	143.4	145.7	144.0
15	19.9	27.2	25.6	27.3	25.5
16	122.4	129.1	132.0	129.4	131.6
17	47.8	49.6	43.3	49.3	43.0
18	73.4	77.2	74.4	78.5	74.1
19	101.8	104.3	97.5	104.1	97.3
20	31.7	36.3	33.8	35.5	33.3
21	18.7	19.9	19.8	20.2	19.9
22	65.4	66.7	66.5	65.8	66.4
23	40.9	38.5	36.5	36.5	36.5
24	40.9	45.1	44.8	44.6	44.7
25	74.3	74.8	75.0	74.4	74.9
26	19.3	21.3	19.6	21.2	19.6
27	34.7	39.6	32.7	39.3	32.5
28	78.2	78.8	80.8	78.1	81.4
29	75.9	92.0	85.0	90.9	85.1
30	22.8	28.5	26.8	28.3	27.1
31	41.4	50.3	48.1	50.7	48.1
32	13.4	21.5	15.3	21.5	15.3
33	171.6	171.5	164.2	171.5	164.9
34	76.3	83.3	75.1	82.6	74.7
35	38.8	43.3	58.6	44.1	63.9
36	170.3	176.6	186.2	178.9	190.9
38	76.2	68.6	75.0	72.0	76.7
39	24.8	29.5	29.1	29.7	24.3
40	94.4	104.2	99.6	108.0	102.0
41	57.2	60.1	55.6	57.2	55.4
42	166.5	166.3	166.3	165.1	167.5
44	106.4	101.2	93.5	100.4	95.7
45	212.0	195.0	199.7	195.6	198.9

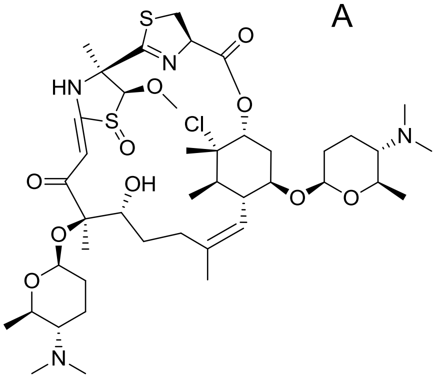
A

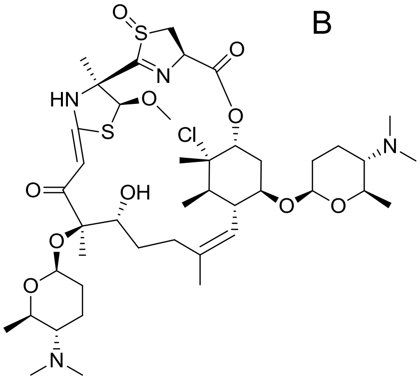
B

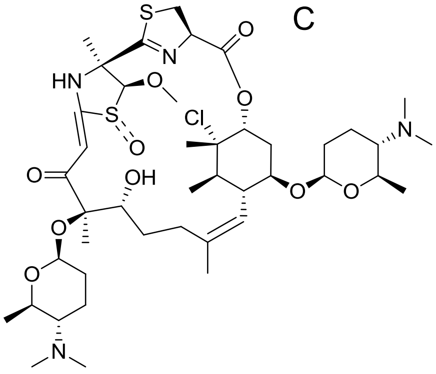
C

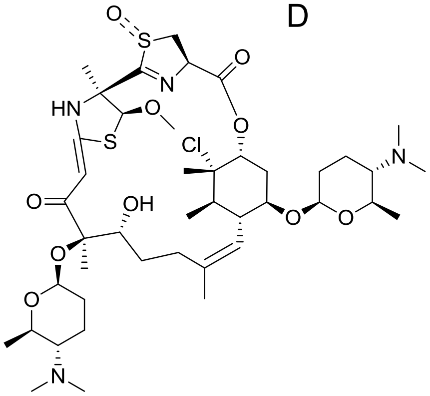
D

Figure A5.9. Synergy assay with amphotericin B

	▨ 64 µg/mL forA	▨ 32 µg/mL forA	▨ 16 µg/mL forA	8 µg/mL forA	4 µg/mL forA	2 µg/mL forA	1 µg/mL forA	0.5 µg/mL forA	0.25 µg/mL forA	0.125 µg/mL forA	0.06 µg/mL forA
▨ 1 µg/mL amphB	▨ 64 µg/mL forA 1 µg/mL amphB	▨ 32 µg/mL forA 1 µg/mL amphB	▨ 16 µg/mL forA 1 µg/mL amphB	▨ 8 µg/mL forA 1 µg/mL amphB	▨ 4 µg/mL forA 1 µg/mL amphB	▨ 2 µg/mL forA 1 µg/mL amphB	▨ 1 µg/mL forA 1 µg/mL amphB	▨ 0.5 µg/mL forA 1 µg/mL amphB	▨ 0.25 µg/mL forA 1 µg/mL amphB	▨ 0.125 µg/mL forA 1 µg/mL amphB	▨ 0.06 µg/mL forA 1 µg/mL amphB
▨ 0.5 µg/mL amphB	▨ 64 µg/mL forA 0.5 µg/mL amphB	▨ 32 µg/mL forA 0.5 µg/mL amphB	▨ 16 µg/mL forA 0.5 µg/mL amphB	▨ 8 µg/mL forA 0.5 µg/mL amphB	▨ 4 µg/mL forA 0.5 µg/mL amphB	▨ 2 µg/mL forA 0.5 µg/mL amphB	▨ 1 µg/mL forA 0.5 µg/mL amphB	▨ 0.5 µg/mL forA 0.5 µg/mL amphB	▨ 0.25 µg/mL forA 0.5 µg/mL amphB	▨ 0.125 µg/mL forA 0.5 µg/mL amphB	▨ 0.06 µg/mL forA 0.5 µg/mL amphB
0.25 µg/mL amphB	▨ 64 µg/mL forA 0.25 µg/mL amphB	▨ 32 µg/mL forA 0.25 µg/mL amphB	▨ 16 µg/mL forA 0.25 µg/mL amphB	▨ 8 µg/mL forA 0.25 µg/mL amphB	▨ 4 µg/mL forA 0.25 µg/mL amphB	▨ 2 µg/mL forA 0.25 µg/mL amphB	▨ 1 µg/mL forA 0.25 µg/mL amphB	0.5 µg/mL forA 0.25 µg/mL amphB	0.25 µg/mL forA 0.25 µg/mL amphB	0.125 µg/mL forA 0.25 µg/mL amphB	0.06 µg/mL forA 0.25 µg/mL amphB
0.125 µg/mL amphB	▨ 64 µg/mL forA 0.125 µg/mL amphB	▨ 32 µg/mL forA 0.125 µg/mL amphB	▨ 16 µg/mL forA 0.125 µg/mL amphB	▨ 8 µg/mL forA 0.125 µg/mL amphB	▨ 4 µg/mL forA 0.125 µg/mL amphB	▨ 2 µg/mL forA 0.125 µg/mL amphB	1 µg/mL forA 0.125 µg/mL amphB	0.5 µg/mL forA 0.125 µg/mL amphB	0.25 µg/mL forA 0.125 µg/mL amphB	0.125 µg/mL forA 0.125 µg/mL amphB	0.06 µg/mL forA 0.125 µg/mL amphB
0.06 µg/mL amphB	▨ 64 µg/mL forA 0.06 µg/mL amphB	▨ 32 µg/mL forA 0.06 µg/mL amphB	▨ 16 µg/mL forA 0.06 µg/mL amphB	▨ 8 µg/mL forA 0.06 µg/mL amphB	▨ 4 µg/mL forA 0.06 µg/mL amphB	2 µg/mL forA 0.06 µg/mL amphB	1 µg/mL forA 0.06 µg/mL amphB	0.5 µg/mL forA 0.06 µg/mL amphB	0.25 µg/mL forA 0.06 µg/mL amphB	0.125 µg/mL forA 0.06 µg/mL amphB	0.06 µg/mL forA 0.06 µg/mL amphB
0.03 µg/mL amphB	▨ 64 µg/mL forA 0.03 µg/mL amphB	▨ 32 µg/mL forA 0.03 µg/mL amphB	▨ 16 µg/mL forA 0.03 µg/mL amphB	▨ 8 µg/mL forA 0.03 µg/mL amphB	4 µg/mL forA 0.03 µg/mL amphB	2 µg/mL forA 0.03 µg/mL amphB	1 µg/ forA 0.03 µg/mL amphB	0.5 µg/mL forA 0.03 µg/mL amphB	0.25 µg/mL forA 0.03 µg/mL amphB	0.125 µg/mL forA 0.03 µg/mL amphB	0.06 µg/mL forA 0.03 µg/mL amphB
0.16 µg/mL amphB	▨ 64 µg/mL forA 0.016 µg/mL amphB	▨ 32 µg/mL forA 0.016 µg/mL amphB	▨ 16 µg/mL forA 0.016 µg/mL amphB	8 µg/mL forA 0.016 µg/mL amphB	4 µg/mL forA 0.016 µg/mL amphB	2 µg/mL forA 0.016 µg/mL amphB	1 µg/mL forA 0.016 µg/mL amphB	0.5 µg/mL forA 0.016 µg/mL amphB	0.25 µg/mL forA 0.016 µg/mL amphB	0.125 µg/mL forA 0.016 µg/mL amphB	0.06 µg/mL forA 0.016 µg/mL amphB

Forazoline A = forA Amphotericin B = amphB

▨ = inhibition

Synergism: $x \leq 0.5$ Indifference: $0.5 \leq x \leq 4$ Antagonism: $x > 4$

Example: Forazoline A: 4 µg/mL, Amphotericin B: 0.06 µg/mL FIC(A)= 4/16 FIC(B)= 0.06/0.5 FIC=FIC(A)+FIC(B)= 0.375 (synergistic)

Forazoline A: 2 µg/mL, Amphotericin B: 0.125 µg/mL FIC(A)= 2/16 FIC(B)= 0.125/0.5 FIC=FIC(A)+FIC(B)= 0.375 (synergistic)

Forazoline A: 1 µg/mL, Amphotericin B: 0.25 µg/mL FIC(A)= 1/16 FIC(B)= 0.25/0.5 FIC=FIC(A)+FIC(B)= 0.56 (synergistic/indifference)